UNIVERSITY OF SOUTHAMPTON

Faculty of Engineering and Physical Sciences
Aerodynamics and Flight Mechanics

High fidelity modelling of neighbourhood-scale environments

by

Matthew Coburn
MSc, BEng (Hons)

A thesis for the degree of
Doctor of Philosophy

March 2023

University of Southampton

Abstract

Faculty of Engineering and Physical Sciences
Aerodynamics and Flight Mechanics

Doctor of Philosophy

High fidelity modelling of neighbourhood-scale environments

by Matthew Coburn

Arrays of buildings with pitched roofs are common in urban and suburban areas of European cities. Large-eddy simulations are performed to predict the boundary-layer flows over flat and pitched-roof cuboids to gain a greater understanding of the impact of pitched roofs on urban boundary layers. The simulation methodology is validated for an array of flat roof cuboids. Further simulations show that changes in the type of grid conformity have a negligible effect on the mean flow field and turbulent stresses, while having a visible, but small, effect on the dispersive stresses for a given packing density. Comparisons are made for flat and 45° pitched roof cuboid arrays at packing densities of 16.7% and 33.3%. The interactions between pitched-roof buildings and their effect on the urban boundary layer are considerably different to those of flat-roof buildings. The pitched roofs at a packing density of 33.3% leads to significant changes in the mean flow field, the Reynolds stresses, and the aerodynamic drag. Further work investigates the effects of changes in turbulence level and atmospheric thermal stratification in the approaching flow. Importantly, in comparison to a flat-roof array, the pitched-roof one at a packing density of 33.3% evidently increases the friction velocity and greatly reduces the effects of stable stratification conditions and changes in inflow turbulence level.

Past work has shown that coupling can exist for urban flows between street scale (O(0.1 km)) and city scale (O(10 km)). Unfortunately, it is generally impractical at present to develop high-fidelity urban simulations capable of capturing such effects. This imposes a need to develop better parameterisations for meso-scale models but an information gap exists in that past work has generally focused on simplified urban geometries and generally assumed the buildings to be on flat ground. This study aimed to begin to address this gap in a systematic way by using the large eddy simulation method with synthetic turbulence inflow conditions to simulate atmospheric air flows over the University of Southampton campus using semi-realistic (i.e. flat terrain) and realistic geometries including significant local terrain features. The LES data were processed to obtain averaged vertical profiles of time-averaged velocities and second order turbulence statistics. The semi-realistic geometry simulation was validated against high resolution particle image velocimetry data. To address the uncertainty due to inflow turbulent intensity, the effects of different levels of inflow turbulence were assessed. The realistic geometry simulations conclusively showed that the inclusion of terrain can have a considerable effect on global quantities, such as the depth of the spanwise-averaged internal boundary layer and spatially-averaged turbulent kinetic energy (TKE). The terrain effects on local time-mean velocity and TKE at the same above-ground-level height can be even more significant. These findings demonstrate the crucial importance of local terrain features (O(0.1km)), and can have significant impact on near-field dispersion and urban micro-climate.

Contents

List of Figures

List of Tables

Declaration of Authorship

I declare that this thesis and the work presented in it is my own and has been generated by me as the result of my own original research.

I confirm that:

1. This work was done wholly or mainly while in candidature for a research degree at this University;
2. Where any part of this thesis has previously been submitted for a degree or any other qualification at this University or any other institution, this has been clearly stated;
3. Where I have consulted the published work of others, this is always clearly attributed;
4. Where I have quoted from the work of others, the source is always given. With the exception of such quotations, this thesis is entirely my own work;
5. I have acknowledged all main sources of help;
6. Where the thesis is based on work done by myself jointly with others, I have made clear exactly what was done by others and what I have contributed myself;
7. Parts of this work have been published as:
   M. Coburn, Z.-T. Xie, and S. J. Herring. Numerical simulations of boundary-layer airflow over pitched-roof buildings. *Boundary-Layer Meteorology*, 185(3):415–442, 2022
   M. Coburn, Z.-T. Xie, and C. Vanderwel. Modelling airflow over idealized, semi-realistic suburban and realistic urban areas, UFMSIG conference, 2021
   M. Coburn, Z.-T. Xie, and C. Vanderwel. Approaching city scale flows using les – an urban aerodynamics case study, UFMSIG conference, surrey, uk., 2019
   M. Coburn, Z.-T. Xie, and C. Vanderwel. Approching city scale flows, 13^{th} uk conference on wind engineering, leeds, uk., received award for *'top young presenter'*, 2018

Signed:..... Date:.....

Acknowledgements

I would like to take the opportunity to thank the following people, without whom I would not have been able to complete this thesis, words cannot express how grateful I am to the following people.

I would like to thank my supervisor Prof. Zheng-Tong Xie for his guidance throughout all aspects of the PhD. The support he has given me is immeasurable. I am extremely appreciative to have worked with him and learn from him. I would also like to thank Dr. Steven Herring, who has offered lots of his personal time and insightful comments and to which I am overwhelmingly thankful. Lastly, I am deeply grateful to Dr Steven Herring, Dr Christina Vanderwel, Prof Simon Cox, Dr Steven Johnston, and Dr Tim Foat for their comments and help throughout my PhD.

My biggest thanks to my mother and father for all the support they have shown me through my research, the culmination of four years of ups and downs, to Harry and Hannah, Balchin and friends that helped me through the past four years.

Without those mentioned and those I haven't, I would not be in the position that I am today.

I would like to acknowledge the funding I received the Faculty of Engineering and the Environment, University of Southampton and dstl towards my PhD research.

Definitions and Abbreviations

h	Canopy height (m)
H	Building depth (m)
$\overline{U}$	Time mean velocity (ms^{-1})
$\langle\overline{U}\rangle$	Spatial- time mean velocity (ms^{-1})
U	Instantaneous velocity (ms^{-1})
u'	Fluctuation velocity (ms^{-1})
u_*	Friction velocity (ms^{-1})
λ_p	Plan area packing density
λ_f	Frontal area packing density
d_0	Displacement height (m)
z_0	Roughness length (m)
A_T	Total plan area (m^2)
A_b	Building plan area (m^2)
A_F	Cross-sectional area (m^2)
δ_{ibl}	IBL depth (m)
Θ	Potential temperature ($^\circ C$)
P	Pressure (N/m^2)
R	Gas constant
c_p	Specific heat capacity ($Jkg^{-1}K^{-1}$))
Θ_v	Virtual potential temperature ($^\circ C$)
ρ	Density (kgm^{-3})
Ri	Richardson number
κ	von Karman constant

Chapter 1

Introduction

Past research in urban atmospheric problems have shown that coupling may exist between the boundary layer flow fields at City scale (O(10 km)), neighborhood scale (O(1 km)), and street scale (O(0.1 km)) (Barlow et al., 2017a; Fernando, 2010). This spatial coupling effect is particularly strong around urban forms such as groups of tall buildings (Han et al., 2017; Fuka et al., 2018; Hertwig et al., 2019), or around steep topographic changes. Little research has been carried out combining the effects of real complex urban areas and terrain effects. This study aims to take some steps to rectify this. To understand the importance of coupling effects we require a mapping between urban forms and flow field characteristics, such as mean velocity, turbulent statistics, momentum and heat fluxes.

Current research of idealised urban areas is very much focused on arrays of flat roof cubes and cuboids (Castro et al., 2017; Sessa et al., 2018; Marucci et al., 2018). This has led to significant insight into the interactions between buildings and has been used to inform current mesoscale models (Dudhia, 2014), such as the UK's Unified Model (Golding, 1987). As models increase in complexity and increased computational power becomes available, studies of idealised arrays should also complexity. Research on the effects of roof shapes within arrays of buildings has been neglected, with few published works (Holmes, 1994; Rafailidis, 1997). As suburban areas are littered with houses possessing 'pitched' roofs, the effect they have on the mean flow and turbulence statistics should not be ignored and can be used to assess the accuracy of current models for use in suburban areas. Acquiring such data for the varied range of geometries encountered in urban areas challenges both numerical and experimental simulations in many aspects.

1.1 Aims

This study has attempted to fill knowledge gaps and demonstrate capability in two key areas. The first of which is the effect of building roof shape, flat vs pitched roofs within the urban boundary layer. The second of which is to apply the methodologies developed in previous studies on idealised arrays to a real urban area case, to simulate flows around complex buildings in an area with significant changes in terrain (O(h)) in neutral and slightly thermally stable conditions, where h is the average building height.

1.1.1 Pitched roof buildings

This study aims to address three knowledge gaps with respect to roof shapes in urban areas:

1) How the urban boundary layer is affected by an array of buildings with pitched roofs?

2) How does the effect of pitched roofs vary with the array's packing density?

3) How the effect of pitched, rather than flat, roofs changes as the conditions vary from neutral to stable thermal stratification?

1.1.2 Real urban morphology and topology

This study aimed to bridge the knowledge gap by using the large eddy simulation method with synthetic turbulence inflow conditions to simulate atmospheric air flows over the University of Southampton campus. Semi-realistic (i.e. flat terrain) and realistic geometries, including significant local terrain features were compared to quantify the effects of terrain.

1) In order to capture appropriate details of the flow within the urban canopy, suitable inflow conditions are required. Are the flow quantities within and above the urban canopy sensitive to inflow turbulence intensities?

2) Small topographic features (compared to those present in mesoscale simulations) are present in many urban areas. The question is, what are the critical - small (O(0.01km)) to large (O(1km)) - topographical features which must be resolved?

3) To my knowledge, published work has considered only stratified flows over flat

terrain. Therefore, it is of crucial importance to quantify the stratification effect on urban flow over street-scale terrains (small topographic features).

1.2 Outline

This study first addresses how pitched roofs affect the local flow and coupling with the higher levels of the Boundary Layer (BL) compared to flat roofs. This has been examined through modelling three-dimensional arrays of blocks with either flat or pitched roofs. The aerodynamics are simulated using the well-developed large-eddy simulation (LES) method. Rigorous evaluation tests, e.g. mesh sensitivity, are carried out to ensure reliable results.

The effect terrain has on the flow is then assessed using LES of a real urban area with complex geometry, the University of Southampton's Highfield campus. The same buildings with the actual terrain elevation and with a flat ground plane. The case with a flat ground plane is simulated numerically and experimentally in a water tunnel using Particle Image Velocimetry (PIV). This can provide confidence in results that would otherwise be absent. Sensitivity tests on the inflow turbulence level have also been carried out to address the issue that the inflow turbulence quantities are not easily obtained from observations, theoretical estimation, or downscaling from the mesoscale models. The effects of weakly stable thermal stratification were assessed for both flat and real terrain cases.

Section 2.1 presents details of the numerical methods. Section 2.3.1 describes the cases and simulation settings. Section 3.1.1 details the verification and validation of the Computational Fluid Dynamics (CFD) model. Section 3.1.2 examines the effect of using conformal and non-conformal meshes, Section 3.2 presents a comparison between arrays of building blocks with and without pitched roofs, which includes spatially-averaged velocities, Reynolds stresses and surface pressures. Section 3.2.2 reports the effect of packing density in neutral stratification. Section 3.3 raises a discussion associated to the Eurocode on pitched roofs. Section 3.4.1 reports the stratification effects on flow over pitched-roof buildings. Section 5.1 summarises the conclusions from the research undertaken.

1.3 Review

1.3.1 Atmospheric Boundary Layer

The atmosphere can be up to 100km thick (Stull, 1988). Occupying the first 10km from the ground is the troposphere. The troposphere consists of the atmospheric boundary layer (ABL) and the free atmosphere (Stull, 1988). The ABL extends up to (O(1km)) from the earth's surface.

The ABL is the region of the troposphere that is directly affected by the earth's surface, the region or layer which "responds to surface forcings with a timescale of about an hour or less." (Stull, 1988). Forcings can include friction drag due to the effect of the surface on the fluid, heat transfer from the surface and changes in the flow direction due to changes in the underlying terrain. The ABL can vary greatly in height, from a few hundred meters to more than one kilometer. This depends on the time of day, the season and the weather. It has been shown that the height of the ABL is strongly associated to the temperature of the underlying surface and mean wind speed (Georgoulias et al., 2009).

1.3.2 Urban Boundary Layer

The Urban Boundary Layer (UBL) consists of several layers which possess unique characteristics. Therefore, when considering the different layers of the UBL, it is best to use a schematic to show the idealised structure of these layers, as in Fig. 1.1.

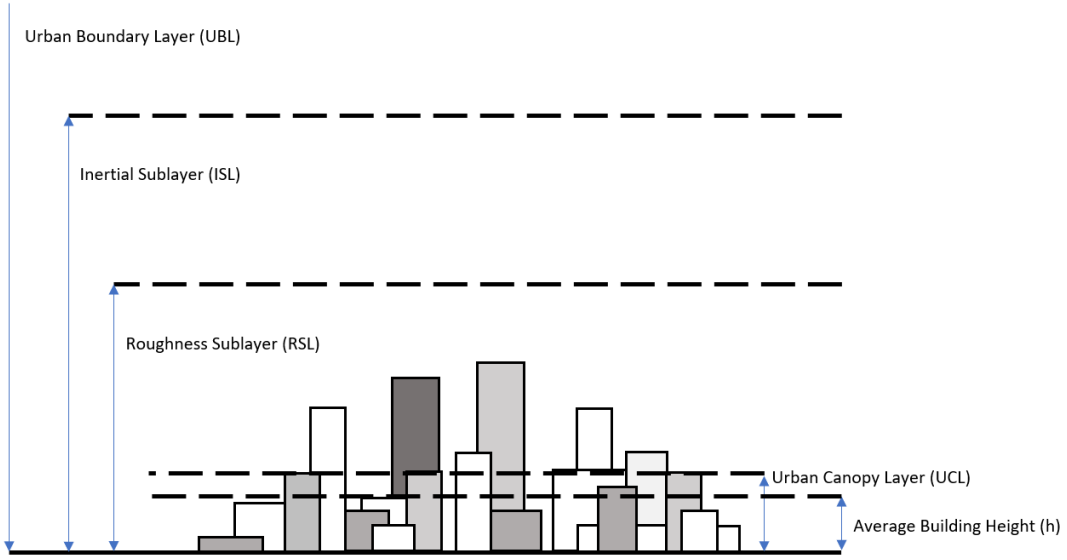

FIGURE 1.1: A schematic for the different heights of different layers within the Urban Boundary Layer above large urban roughness

The UBL develops as the wind passes from rural to urban areas. Each layer within the UBL can be characterised. The UBL consists of, from the ground, the Urban Canopy Layer (UCL), the Roughness Sublayer (RSL) and the Inertial Sublayer (ISL). Above which is either a mixed layer during daytime hours or a residual layer.

The UCL extends from the ground up to the average building height for buildings with non-uniform vertical extents or canopy height for arrays of buildings with uniform height. It is characterised by substantial heterogeneity in the flow field and sensitivity to changes in local morphology and or topography. The surrounding buildings and topology directly affect flow quantities within this layer.

The RSL, which includes the UCL is the layer within which the underlying roughness statically and dynamically influences the flow. It envelops all roughness elements and has been shown to have a depth of between two and five building heights (Pelliccioni et al., 2016). The effects of individual buildings can still be 'seen' within this layer. Increasing in height where the influence of the individual roughness elements is 'mixed up' by the turbulence (Raupach et al., 1991).

Above the height of the RSL exists the ISL, sometimes referred to as the constant-flux layer. Within the ISL, the flow can be considered spatially homogeneous if the region does not vary greatly in density, height and distribution of the roughness elements. The mean velocity profile within the ISL is characterised by a logarithmic profile, (Britter and Hanna, 2003):

$$U_z = \frac{u_*}{\kappa} ln \left(\frac{z - d_0}{z_0} \right), \tag{1.1}$$

where, U_z = mean velocity at height z, u_* is friction velocity, κ is the von Karman constant, d_0 is the displacement height and z_0 is the roughness length. The displacement height, also called zero-plane displacement, is the height at which zero mean wind velocity occurs if the logarithmic wind profile is continued down to zero velocity due to the surface (i.e. buildings and or vegetation). Jackson (1981) equates this physically to the level that would be attained by flattening the roughness to a flat plane. The roughness length, z_0, characterises the roughness of the underlying urban surface. The typical values for different surfaces are shown in Table 1.1.

TABLE 1.1: Roughness classification and z_0 according to Stull (1988)

z_0 **(m)**	**Classification**	C_D	**Landscape**
0.0002	sea	0.0014	sea, paved areas, snow covered flat plain, tide flat, smooth desert
0.005	smooth	0.0028	beaches, pack ice, morass, snow-covered fields
0.03	open	0.0047	grass prairie or farm field, tundra, airports, heather
0.1	roughly open	0.0075	cultivated area with low crops & occasional obstacles (single bushes)
0.25	rough	0.012	high crops, crops of varied height, scattered obstacles such as tress or hedgerows, vineyards
0.5	very rough	0.018	mixed farm fields and forest clumps, orchards, scattered buildings
1.0	closed	0.030	regular coverage with large-sized obstacles with open spaces roughly equal to obstacle heights, suburban houses, villages, mature forests
≥ 2	chaotic	$\geq$ 0.062	centers of large towns and cities, irregular forests with scattered clearing

With respect to the urban surface, the roughness can be categorised by the packing density of the roughness elements (buildings) and the relative height of the urban canopy. One method of categorisation is the plan area density, λ_p. This is the plan view percentage of the area of the buildings (Barlow and Coceal, 2008), given in Eq. 1.2. This is referred to as packing density and consists of the plan area of the buildings A_b and the total plan area of repeating unit of region of interest, A_T,

$$\lambda_p = \frac{A_b}{A_T}. \tag{1.2}$$

Another method of quantifying the building spacing density is using the frontal area density, λ_F. Here, A_F is the cross-sectional area of all buildings normal to the incoming flow direction,

$$\lambda_F = \frac{A_F}{A_T}. \tag{1.3}$$

The frontal area density has the added benefit of taking into the wind direction, where λ_p does not. Another factor that is important in the classification of urban roughness is the aspect ratio, h_i/W_x, where W_x is the downstream extent of the street canyon, H_i is the building height, see Fig. 1.2. The buildings can also be different heights as denoted in Fig. 1.2. Aspect ratio is of particular importance for flows in and over street canyons (Barlow et al., 2004; Harman et al., 2004). Wind incidence to the street canyon has great importance on the flow within the canyon (Soulhac et al., 2008). Building aspect ratio, typically given as L_x/h, will also considerably affect the flow pattern locally (Oke, 1988).

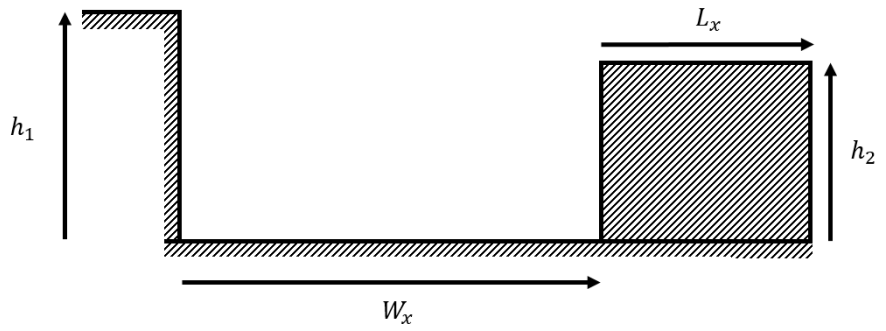

FIGURE 1.2: Definition of quantities of building height, h_i, building length, L_x and canyon fetch W_x for aspect ratios of street canyons and buildings

Flows within street canyons themselves can be categorised by the behaviour of their mean flow pattern within the canopy as a function of the street canyon morphology given above. Oke (2002) describes the three different flow patterns or regimes. Fig. 1.3 shows the three flow regimes. The presence of a thin shear layer at the canopy top, and a recirculation zone within the street canyon categorises the skimming flow. The wake interference regime has a bifurcation in the flow at the windward side of the building, with a reticulation zone upstream. The isolated roughness flow, has similar recirculation zones to that of a single wall mounted roughness element, e.g. flow around a wall mounted cube (Yakhot et al., 2006) across a centre span, streamwise-wall-normal-plane.

Skimming flow exists for aspect ratios of less than $h/W_x > 1$, wake interference flow which exists for $h/W_x \approx 0.5$ and individual roughness flow for aspect ratios of $h/W_x < 0.3$ (Oke, 1988). Flow regimes are also categorised by packing density (Grimmond and Oke, 1999), λ_p. Skimming flow occurs when $\lambda_p > 0.3$. The wake interference (W.I.) regime occurs for $0.15 \lessapprox W.I. \lessapprox 0.33$. These definitions shown are for flat roofed buildings.

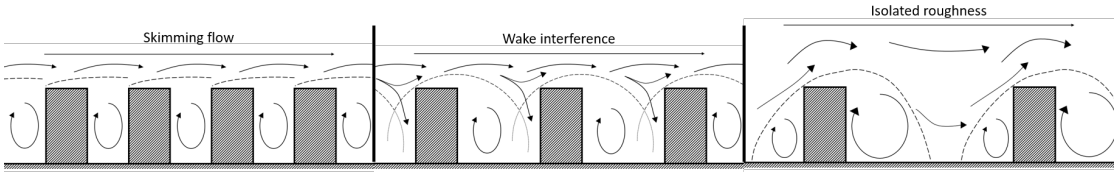

FIGURE 1.3: Definitions of flow regimes that are associated with different urban street canyon aspect ratios, based on that shown by Oke (1988)

1.3.3 Urban Internal Boundary layer

Urban surfaces are typically heterogeneous in their surface roughness distribution, i.e., differently shaped buildings with different maximum heights (Xie and Castro, 2009; Barlow et al., 2017b). Urban areas also consist of regions with different but consistent surface roughness, for example, a large park surrounded by suburban housing or suburban housing which may surround housing estates with tower blocks. There exists a transition region downstream of the roughness change, called the internal boundary layer (IBL). This is visualised in Fig. 1.4. This change in roughness can be quantified as a ratio of the upstream to downstream roughness lengths, z_{01}/z_{02} (Smits and Wood, 1985).

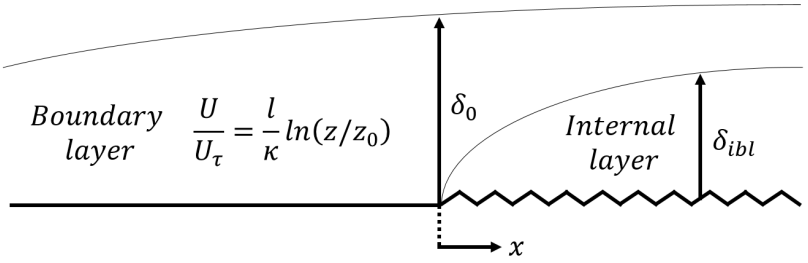

FIGURE 1.4: A schematic demonstrating the effect of a change in roughness and the growth of the internal boundary layer

The IBL develops (grows vertically) downstream (Smits and Wood, 1985; Antonia and Luxton, 1971b; Kaimal and Finnigan, 1994; Plate, 1995; Sessa et al., 2018). Above the IBL, the turbulence and flow field characteristics are consistent with the upstream roughness (Garratt, 1990). The IBL, also called the equilibrium layer has turbulence and flow field characteristics consistent with the underlying surface roughness. There exists a transition region or interface between the IBL and BL above. Quantifying the height of this interface and, as such, the height of the IBL has been an ongoing topic. Antonia and Luxton (1971a) developed a method of quantifying the IBL depth using normalised velocity profiles, noting that the velocity profiles follow half-power relationships of $U = z^{1/2}$ with differing slopes. The knee point lies just within the IBL, making it worthwhile to describe the IBL thickness, as seen in Fig. 1.5. Antonia and Luxton (1971a) notes that downstream, the 'knee' point moves further away from the

surface and becomes less clearly defined. The IBL growth was shown to be similar to that of a smooth wall turbulent boundary layer, (Wood, 1981, 1982) and is shown in Eq. 1.4.

$$\frac{\delta_{ibl}}{z_{0r}} = 0.28 \left(\frac{x}{z_{0r}} \right)^{0.8}, \tag{1.4}$$

where δ_{ibl} is the IBL depth, x is the downstream distance. z_{0r} is the larger of the two roughness lengths, z_{01} and z_{02}. This was shown by Elliott (1958) to be valid only for $x/z_{0r} > 1000$, and notes that for greater distance from the roughness step change, the exponent will be smaller and the coefficient will be greater.

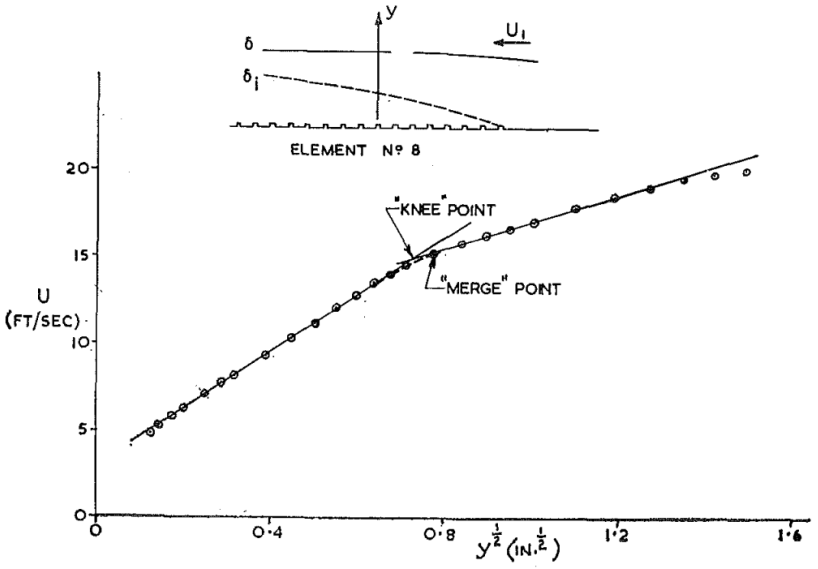

FIGURE 1.5: The 'knee' point which marks the interface between the IBL and BL (Antonia and Luxton, 1971a)

The second method developed by Efros and Krogstad (2011) for quantifying the IBL depth uses vertical profiles in common with Antonia and Luxton (1971a). Instead of using the mean velocity profile, the normalised streamwise Reynolds stress component is used, $\overline{u'u'}^{+}$. The knee point is then used to quantify the vertical extent, h, of the IBL. The third method, suggested by Sessa et al. (2018) again uses vertical profiles but substitutes the streamwise Reynolds stress for the vertical Reynolds normal stress component, $\overline{w'w'}^{+}$. For an array of 3-dimensional cuboids, with packing density $\lambda_p = 1/3$ and a building aspect ratio of $L_x/h = 1$ the IBL growth using the method of Sessa et al. (2018) is given as

$$\frac{\delta_{ibl}}{z_{0r}} = 12.71 \left(\frac{X}{z_{0r}} \right)^{0.21}. \tag{1.5}$$

This confirms the suggestions of Elliott (1958) in the changes of the exponent and coefficient, where the distance downstream here is $X/z_{0r} < 300$. Sessa et al. (2018) gives the IBL growth for simplified cuboids with uniform plan area packing density across the height of the canopy. The above coefficient in eq. 1.5 calculated by Sessa et al. (2018) is similar to that obtained by Cheng and Castro (2002), 12.71 and 10.56 respectively. The exponent generated by Cheng and Castro (2002) was 0.33. Sessa et al. (2018) cites the difference in roughness being examined as the reason for the difference in coefficient and exponent. It should be noted, Cheng and Castro (2002) investigated 2-dimensional rib-type roughness, compared to the 3-dimensional cuboid array of Sessa et al. (2018).

The method of Sessa et al. (2018) will be applied to that of the pitched roof cuboids, which is of particular importance in suburban regions in which the vast majority of buildings have pitched roofs, i.e. residential housing (Department for Communities and Local Government, 2008).

1.3.4 Stratification

Up to now, the discussion of urban boundary layers has been concerned with purely neutral conditions, i.e. no density gradient across the boundary layer (Stull, 1988). Stratification is caused by changes in density, which is dependent on temperature, humidity and pressure (Stull, 1988). There are three situations in which the UBL can reside. Neutral (NBL), stable (SBL) and convective or unstable (CBL). Stable stratification occurs when the highest density is closest to the ground, with density decreasing as height increases. Convective or unstable conditions occur when the density closest to the ground is lower than above.

Here the concept of virtual potential temperature is introduced. The definition of potential temperature is the temperature of an air parcel adiabatically displaced to a height where the pressure is 1 bar. The potential temperature is defined as:

$$\Theta = T\left(\frac{P_0}{P}\right)^{R/c_p}, \tag{1.6}$$

where Θ is the potential temperature, T is absolute temperature, P is pressure, R is the gas constant and c_p is the specific heat capacity of the fluid at constant pressure. Within the low ABL, the potential temperature is the same as the absolute temperature T.

In order to categorise the strength of the stratification, it is helpful to examine the turbulent kinetic energy budget within the urban boundary layer, Stull (1988) gives the following.

$$\frac{\partial k}{\partial t} + \overline{U_j}\frac{\partial k}{\partial x_j} = -\frac{1}{\rho_0}\frac{\partial \overline{u_i' p'}}{\partial x_i} - \frac{1}{2}\frac{\partial \overline{u_j' u_j' u_i'}}{\partial x_i} + \nu\frac{\partial^2 k}{\partial {x_j}^2} - \overline{u_i' u_j'}\frac{\partial \overline{u_i}}{\partial x_j} - \nu\frac{\overline{\partial u_i' \partial u_i'}}{\partial x_j \partial x_j} - \frac{g}{\overline{\Theta}}\overline{\Theta' u_i'}\delta_{i3} - \epsilon. \tag{1.7}$$

The important terms are as follows. The second term on the l.h.s. describes the advection of kinetic energy, k, due to the mean velocity, $\overline{U_j}$. Where the kinetic energy is defined as $k = \frac{1}{2}\left(\overline{u_i'^2} + \overline{u_j'^2} + \overline{u_k'^2}\right)$. The second term on the r.h.s. describes the transport of kinetic energy due to turbulent velocity fluctuations, u_j' and u_i'. The fourth term on the r.h.s. describes the shear production due to the Reynolds shear stress, $\overline{u_i' u_j'}$, associated with the mean velocity gradient, $\frac{\partial u_i}{\partial x_j}$. This is the mechanical production component and is nearly always positive. The second to last term on the right describes the buoyant production or consumption of the kinetic energy due to differences in density, Θ_v', which is caused by temperature differences. It is dependent on the sign of the heat flux, $\overline{\Theta_v' u_i'}$, as to whether it contributes to production or consumption.

It is possible to quantify the ratio of buoyant production and mechanical production of turbulent kinetic energy using the flux Richardson number, which takes terms 8 and 6 from Eq. 1.7. Following Stull (1988), if horizontal homogeneity is assumed and subsidence is neglected, then a more common form of the flux Richardson number is produced,

$$Ri_f = \frac{\frac{g}{\overline{\Theta_v}}\overline{\Theta_v' u_k'}}{\overline{u_i' u_j'}\frac{\partial \overline{U_i}}{\partial x_k}}. \tag{1.8}$$

It is expected that when $Ri_f < +1$ the flow is turbulent (dynamically unstable); if $Ri_f > +1$, the flow becomes laminar (dynamically stable). When $Ri_f < 0$, the buoyancy contributes to turbulence generation. However, the limitation here is that the flux Richardson number can only highlight when the flow will become laminar and not when the flow will become turbulent. This is due to the equation containing turbulent correlations, $\overline{\Theta_v' u_k'}$. Assuming $-\overline{\Theta_v' u_k'}$ is proportional to the lapse rate, $\partial\overline{\Theta_v}/\partial x_k$, and that $\overline{u_i' u_k'}$ is proportional to $\partial\overline{U_k}/\partial x_k$. This gives a new ratio which is known as the gradient Richardson number, Ri_g,

$$Ri_g = \frac{\frac{g}{\overline{\Theta_v}}\frac{\partial \overline{\Theta_v'}}{\partial x_k}}{\left[\left(\frac{\partial \overline{U_i}}{\partial x_k}\right)^2 + \left(\frac{\partial \overline{U_j}}{\partial x_k}\right)^2\right]}. \tag{1.9}$$

The gradient Richardson number is useful as it can describe when a turbulent flow will become laminar and determine if a laminar flow will become turbulent. When

$Ri_g > R_T$ turbulent flow becomes laminar, and when $Ri_g < R_c$ laminar flow becomes turbulent. R_c is the critical Richardson number, which can be approximated to $R_c \cong 0.25$. The Richardson termination, $R_T \cong 1$, describes the point at which turbulence is terminated. In real cases, meteorologists rarely know actual local gradients but can approximate them using observations made at discrete heights. Through approximating $\partial\overline{\Theta_v'}\partial u_k'$ with $\Delta\Theta_v/\Delta x_k$ and $\partial\overline{U_k}/\partial x_k$ with $\Delta U_i/\Delta x_k$, gives a new ratio called the bulk Richardson number, Ri_b,

$$Ri_b = \frac{g\Delta\overline{\Theta_v}\Delta x_k}{\overline{\Theta_v}\left[\left(\Delta\overline{U_i}^2\right)\left(\Delta\overline{U_j}^2\right)\right]}. \tag{1.10}$$

Where Δx_k, is the characteristic length-scale. Due to its simplicity, the bulk Richardson number is the most commonly used. For stable stratification within the boundary layer, the bulk Richardson number is always positive and negative for convective boundary layers. The bulk Richardson number is a useful simplified quantification of the strength of stratification and clarifies clearly, the effect it has on the turbulence. Where stable-stratified flows are concerned, it will lead to low turbulence kinetic energy, and the opposite is true for convective boundary layers by increasing production in TKE.

1.3.5 Simplified arrays of buildings

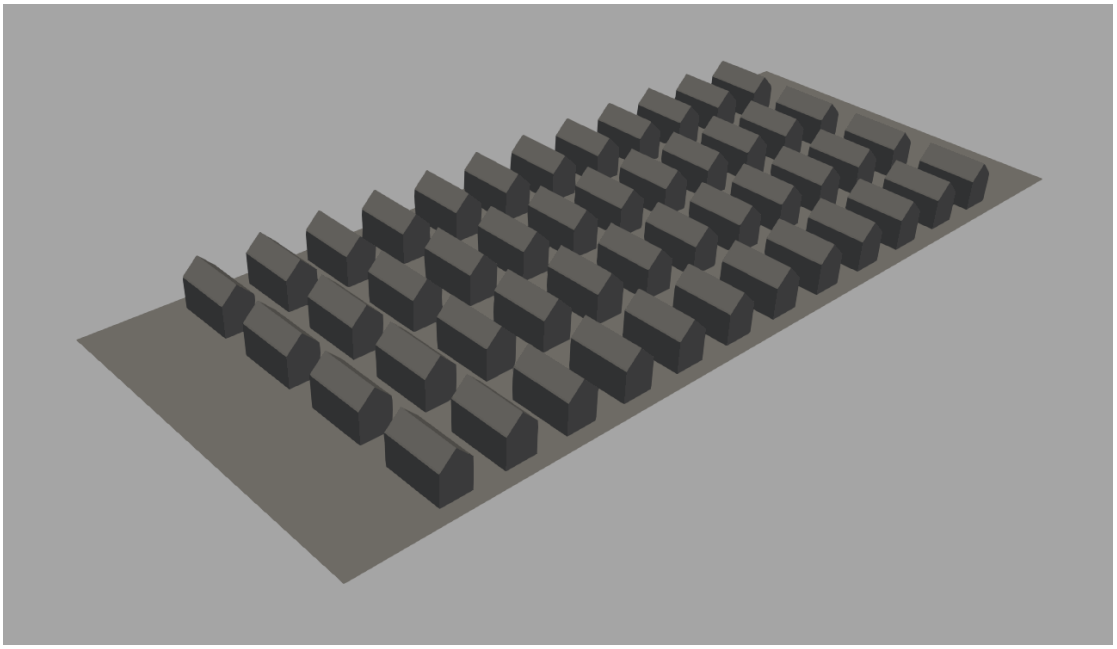

FIGURE 1.6: Pitched roof geometry for cases with synthetically generated inlet turbulence

Most of the published experimental and numerical studies on idealized buildings (e.g. Cheng and Castro, 2002; Stoesser et al., 2003; Coceal et al., 2006; Xie and Castro, 2006) have focused on arrays of cuboid blocks with flat roofs, which are placed in an aligned or staggered arrangement with uniform or non-uniform heights. These studies are most relevant to urban flows over city centres, where most buildings are likely to have flat roofs. However, most of the residential houses have pitched roofs in the surrounding urban and suburban areas of European cities. It is, therefore, of great interest to assess the effect of having pitched, rather than flat roofs, on both the local flow field and large-scale boundary layer flow. For example, in 2008 it was recorded that 93% of the dwellings in England had pitched roofs (Department for Communities and Local Government, 2008). It is therefore of great interest to assess the effect of having pitched, rather than flat roofs, on the local flow field and large-scale boundary-layer flow.

There are a small number of published papers (Rafailidis and Schatzmann, 1996; Rafailidis, 1997; Barlow et al., 2004; Yassin, 2011; Ferrari et al., 2016; Nosek et al., 2016, 2017; Llaguno-Munitxa et al., 2017; Badas et al., 2017; Woodward et al., 2021) in which different roof shapes and their effect on the flow field has been investigated. Most of these studies (Barlow et al., 2004; Yassin, 2011) have investigated two-dimensional street canyons with various roof shapes. This neglects the mean convection that is present within a three-dimensional urban canopy. Something that has been accounted for with arrays of flat roof cuboids, but the effect of the pitched roof in three-dimensional arrays for fully developed flows and flows with roughness step changes is unknown.

A few studies (Holmes, 1994; Tominaga et al., 2015; Ozmen et al., 2016; Fouad et al., 2018; Woodward et al., 2021) have also examined a single isolated building with a pitched roof and these have provided an understanding of the mean surface pressure (Ginger and Letchford, 1995; Oliveira and Younis, 2000; Tominaga et al., 2015) which has supported the development of building regulation codes.

Rafailidis (1997) demonstrated a velocity deficit just above the canopy for an array of two-dimensional 'slanted' roof buildings compared to flat roofs. They found that the pitched roof also increases the vertical turbulent momentum flux at the roof height as shown in Fig. 1.7. Rafailidis (1997) suggests the two significant quantities here are: 1) horizontal advection by the mean wind and 2) the vertical momentum flux. The vertical turbulence intensity was shown to be larger than the mean vertical velocity at and just above the canopy height.

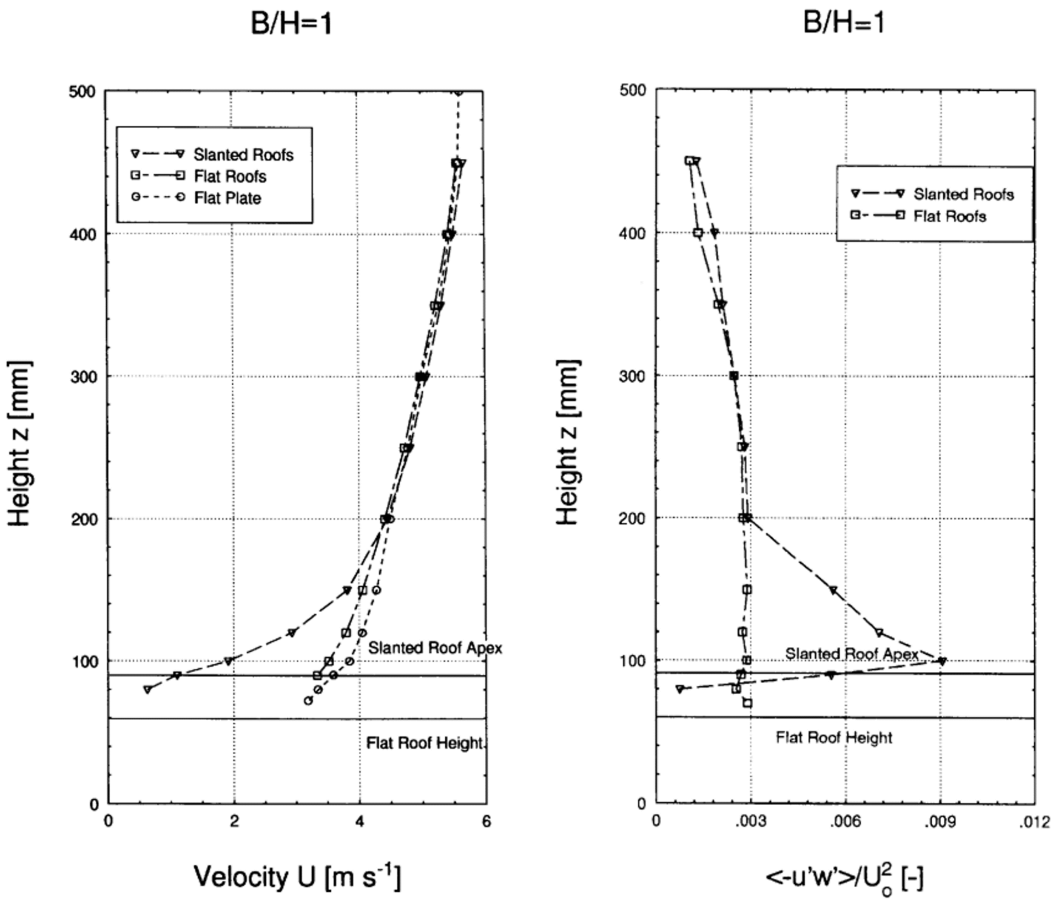

FIGURE 1.7: Mean streamwise velocity profiles for slanted and flat roofs (left) and normalised vertical turbulent momentum flux (right), Rafailidis (1997)

Rafailidis (1997) also showed that above $2-3h$, the vertical profiles shown in Fig. 1.7 collapse, suggesting that it is only the lowest portion of the UBL that is directly affected by the building shape. Above $2-3h$, they have shown that the downstream distance between subsequent rows of buildings, effectively packing density, causes the difference between the vertical profiles. The vertical momentum transfer caused by the free shear layer from the apex of each pitched roof roughness element causes a more significant velocity deficit across the long street locations. Rafailidis (1997) did not produce data within the canopy, so this cannot be commented upon. For three-dimensional roughness, the recirculation velocity will decrease somewhat compared to two-dimensional roughness. The effect of the pitched roof on the mean flow and turbulent statistics within the canopy for a fully developed flow remains unknown.

Tominaga et al. (2015) investigated the flow field and surface pressure on an isolated building for one aspect ratio and three roof pitch angles using PIV and CFD. They found large differences in the flow fields produced by the smaller and larger pitch angles, and suggested that a critical angle existed around the pitch angle 20°. Holmes

(1994) found that a 30° pitched roof on a single tropical house considerably affected the mean roof pressures. He found that the mean pressure coefficient on the upwind half of the roof was all positive, while on the leeward side, the flow did not re-attach on the roof, resulting in a near-uniform surface pressure. On the other hand, Reardon and Holmes (1981) found that roof pitches up to 10° in winds normal to the ridge yielded a small separation bubble at the leading edge with high shear-layer curvatures, which were associated with high suction pressure, and rapid pressure recovery downwind to the flow reattachment position. They suggest that roof pitches up to 10° with the wind normal to the ridge be called "aerodynamically flat". These results suggest that modest changes in the angle of pitched roofs may strongly affect the flow field around the building and building surface pressures.

Fouad et al. (2018) investigated isolated pitched-roof buildings to explore the potential for obtaining useful design data using CFD methods by comparing their results to the Eurocode (Comm., 2005) and ASCE 7-10 (of Civil Engineers, 2013) standards. They concluded, "the application of CFD techniques show great potential to offer very good wind design data for structures with shapes not listed in the existing codes."

While building regulations are based on considering a single isolated building, it is probable that the flow within the canopy of an array of pitched roof buildings will be considerably different to that around an isolated building, with consequent effects on the surface pressure distribution. However, published studies on the effect of interference between buildings have typically only focused on two buildings (e.g. Bailey and Vincent, 1943; Holmes, 2007).

Bailey and Vincent (1943) suggested that having a maximum of two buildings upstream of the instrumented model was sufficient to represent built-up areas. Holmes (2007) concluded that the building spacing was a key parameter and the number of shielding rows was of lesser importance. It is now well established that two building rows upstream of the measurement location are insufficient for a simulation of a fully-developed internal boundary layer (IBL) over a very large array (e.g. Hanna et al., 2002; Xie and Castro, 2008; Sessa et al., 2018). For arrays of building blocks placed in a fully developed turbulent boundary layer in the scenarios typically studied (e.g. low-rise buildings and small roughness length upstream of the array), it requires a fetch length of about ten average building heights (e.g. Hanna et al., 2002; Xie and Castro, 2008). The required fetch length is much greater for arrays of buildings placed in a smooth laminar boundary layer. It is to be noted that while generating near equilibrium and fully developed urban boundary layer flows is necessary for reducing the uncertainty of the research data, such conditions are not generally established in real urban atmospheric airflows.

More recently Garau et al. (2018) studied the effect of downstream spacing (street canyon aspect ratio) of two-dimensional flat and pitched roof buildings using PIV.

They show that the pitched roof causes the wake interference flow regime to be present for smaller aspect ratios than for the flat roof building but determine this effect is a result of the height difference between their flat and pitched roof buildings. They also note that for high packing density, the vertical momentum flux is increased by the pitched roof buildings. Due to the mean convection present within three-dimensional arrays, it remains to be seen how these results will compare to an array of three-dimensional pitched roof buildings.

Two parameters frequently used to characterise the morphology of urban areas are the frontal and plan solidities (e.g. Placidi and Ganapathisubramani, 2015). The latter is more often termed the 'packing density' λ_p. The effect of packing density in arrays of simplified buildings with flat roofs has been intensively studied (e.g. Cheng et al., 2007; Placidi and Ganapathisubramani, 2015, 2018), and it has been shown that their total drag coefficient based on the freestream velocity is a function of the packing density. The drag coefficient function has minima at $\lambda_p = 0$ or 100% and a maximum in the lower half of the packing density range. Cheng et al. (2007) showed that the maximum drag coefficient was closer to $\lambda_p = 6.25\%$ than 25% for aligned arrays of cubes.

Characterising flat roof buildings is relatively straightforward, especially for simple cuboids. For pitched roof buildings, the frontal area density remains the same as that for flat roof cuboid roughness elements assuming the same overall canopy height. In contrast, the cross-sectional plan area changes with height within the canopy above the building's side face-roof face transition height. Fig. 1.8 shows this effect graphically. Above C, the cross-sectional area for pitched roof buildings goes linearly to zero as a function of the pitch angle. D denotes the half roof height; at this height, the packing density would be 50% assuming a 45° pitch angle. Whereas for the flat roof building, the packing density remains constant across its entire vertical extent.

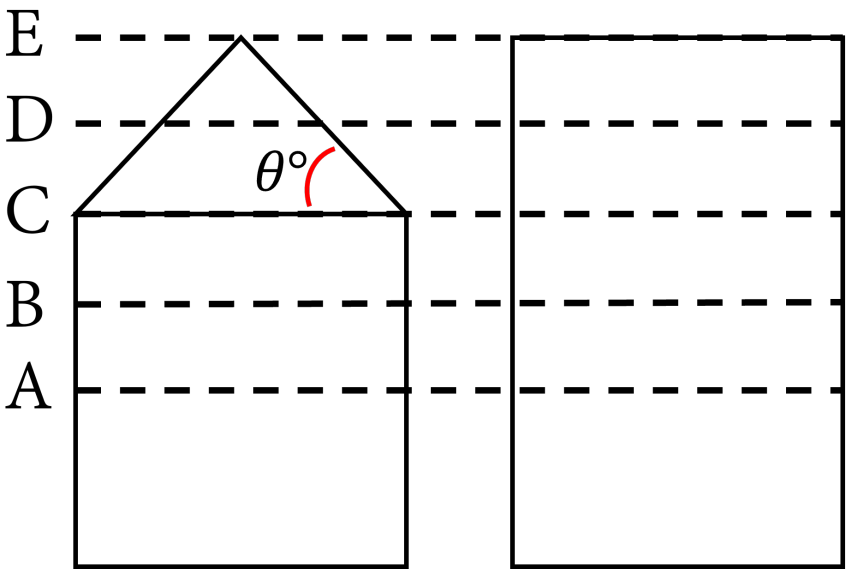

FIGURE 1.8: A) eaves half height, B) canopy half height, C) eaves height, D) roof half height and E) canopy maximum height. θ° denotes the pitch angle definition in degrees.

There is a need to understand whether the drag coefficient function shows similar or different behaviour for arrays of blocks with pitched roofs. Although it must be noted that the frontal solidity and packing density provide adequate descriptions of arrays for developing parameterisations for the effects of flat roofed buildings in mesoscale models, at least one additional parameter is required to differentiate between arrays with different roof geometries.

Further, the effect of the roof gives rise to the question of parameterisation for the characterisation of the flow regime. Fig. 1.3 shows definitions of each flow regime, and section1.3.2 discusses characterisation based on flat roof building dimensions.

1.3.6 Effect of stratification

The effect of stratification has yet to be investigated with buildings with pitched roofs, particularly regarding arrays of buildings. Very few experimental studies have investigated the effects of stratification over rough and urban-like surfaces (e.g. Ohya, 2001; Marucci et al., 2018). Few studies using numerical methods have investigated stratified flow over urban-like surfaces (e.g. Xie et al., 2013; Boppana et al., 2014; Tomas et al., 2016; Sessa et al., 2020). Weak SBLs tend to decrease the depth of the IBL. Tomas et al. (2016) showed a decrease of 14% in the IBL depth compared to a NBL. The bulk Richardson number for the SBL was 0.147 and the *tke* was reduced by 21% for the SBL compared to the NBL. Sessa et al. (2020) showed the IBL depth for a range of bulk Richardson numbers, from 0.21 up to 1, with consistent inflow conditions. The

depth of the IBL was shown to vary up to 30%, shown in Fig. 1.9. This shows the considerable effect of even weakly stably stratified stable boundary layers.

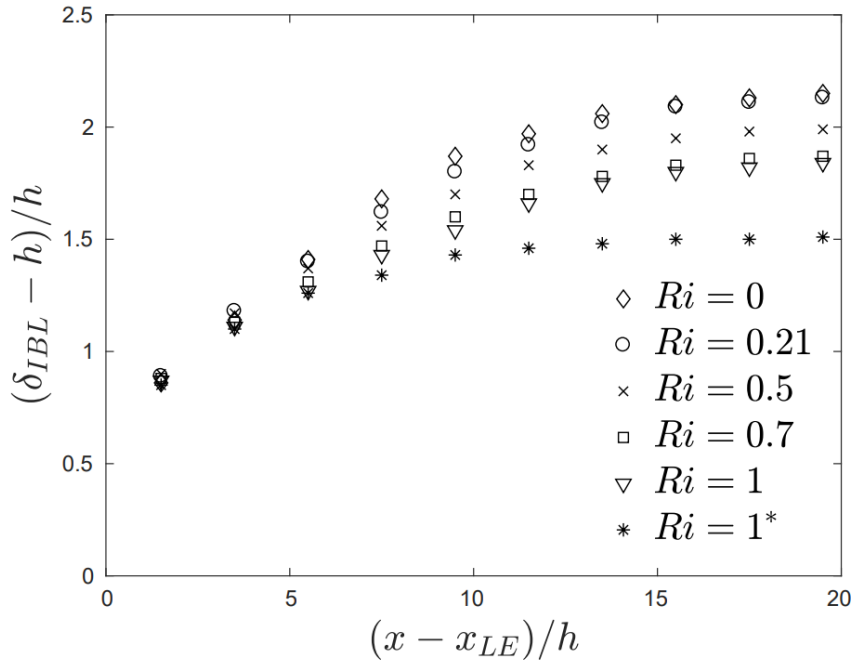

FIGURE 1.9: IBL depth for various strengths of stratification from Sessa et al. (2020)

1.3.6.1 Research Needs

The existing body of literature shows a clear need to investigate the effect of pitched roofs in building arrays at different frontal solidities, packing densities and aspect ratios with fetches sufficient to develop realistic urban boundary layers; to demonstrate improved methods for predicting the airflow and dispersion at neighbourhood scales; and to obtain spatially averaged momentum and scalar flux data which may be used to develop parameterisations for mesoscale models.

In addition to the above, there is the question of thermal stratification effects in urban areas. This attracted little attention until recently (Sessa et al., 2018). The studies published since then have focused on arrays of idealised cuboid-shape buildings (e.g. Boppana et al., 2014; Kanda and Yamao, 2016; Tomas et al., 2016; Sessa et al., 2018; Marucci et al., 2018; Marucci and Carpentieri, 2020), or much simplified realistic urban geometries with flat roofs (e.g. Xie et al., 2013). They have concluded that even weakly stable stratification conditions (i.e. the bulk Richardson number ≤ 1) considerably impact the urban boundary layer turbulence and significantly impact pollutant dispersion.

A thorough search of the relevant literature yielded no research into the nature of the flow over arrays of pitched-roof buildings in thermally stratified conditions. The few

studies performed on pitched roof geometries have shown that a pitched roof can generate a very different flow within and above the canopy top in neutral stratification, with more three-dimensional flow structures than those in flows over flat-roof buildings. The question arises as to whether the effects of changes in thermal stratification are similar over pitched-roof buildings as those over flat roofs.

With respect to producing numerical simulations of the flow around buildings, it is the case that rather than using conformal meshes (Fig. 2.5) to accurately capture the geometric details of buildings (such as pitched roofs), two widely used urban CFD codes PALM-4U (Maronga et al., 2020; Krč et al., 2021) and DALES-Urban (Heus et al., 2010; Grylls et al., 2020) use non-conformal cartesian meshes. This simple treatment is attractive as it leads to significant improvements in computational efficiency but raises the question of what the penalty in accuracy is compared to using conformal (body-fitted) meshes. This study also addresses this question.

1.3.7 Flows over realistic urban areas

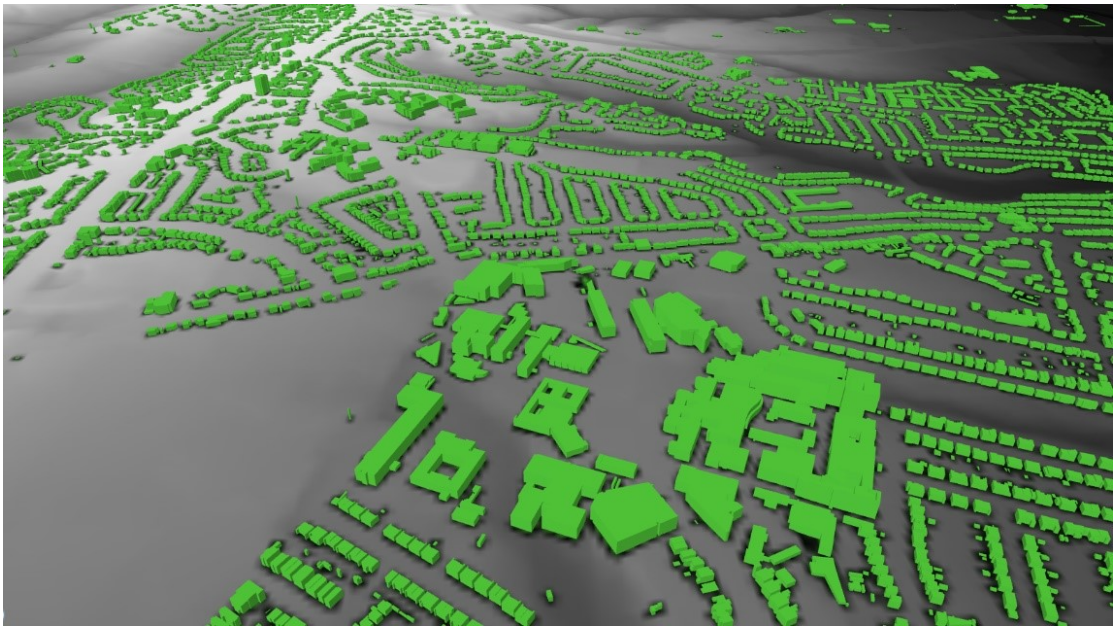

FIGURE 1.10: Highfield campus (centre) University of Southampton and surrounding suburban areas, with real terrain topology

At present operational mesoscale models are unable to predict the details of urban flows at street and neighbourhood scale (i.e. O(1 km)). Finely resolved urban simulations over scales from 1 m to neighbourhood scale generated by engineering computational fluid dynamics (CFD) codes (e.g. Xie and Castro, 2009; Han et al., 2017; Antoniou et al., 2017; Inagaki et al., 2017; Tolias et al., 2018; Gronemeier et al., 2020) but more extensive city-scale simulations (i.e. O(10 km)) are generally impractical. This presents a significant limitation, as past work has shown that a two-way coupling

can exist not just between the urban boundary layer properties measured at street scale (O(0.1 km)) and neighbourhood scale (O(1 km)), but also between street scale and city scale (O(10 km)) (Barlow et al., 2017a; Fernando, 2010). Such coupling effects can be particularly pronounced when the urban area includes features such as a single or cluster of tall buildings (Han et al., 2017; Fuka et al., 2018; Hertwig et al., 2019) or a sharp change in topography (Conan et al., 2016; Blocken et al., 2015; Limbrey et al.).

The development of simulations which can accurately capture the coupling between street and city scales challenges both numerical and experimental approaches in many aspects. This study aims to use numerical simulations to examine the effect of terrain, which includes real, heterogeneous, urban geometry and small sharp changes in topography (O(0.1 km)) in a systematic way which is difficult to achieve in wind and water tunnel experiments or through field observations.

A number of studies have been published since 2000 in which the air flows around arrays of buildings with complex geometries have been investigated, for example, (e.g. Arnold et al., 2004; Xie and Castro, 2009; Hertwig et al., 2012; Han et al., 2017; Antoniou et al., 2017; Inagaki et al., 2017; Tolias et al., 2018; Hertwig et al., 2019; Gronemeier et al., 2020; Sessa et al., 2020; Goulart et al., 2019; Ricci et al., 2020; Liu et al., 2023). These studies address two big challenging issues – heterogeneity and anthropogenic drivers as identified in Barlow et al. (2017a), which can be associated with such as step-change of urban roughness height, a cluster of tall buildings, local thermal stratification, and internal urban boundary layer. However, they generally neglected the terrain and assumed the buildings to be on flat ground.

Those studies which have considered the effects of urban terrain have focused on city-scale (O(10 km)) topographic changes (e.g. Fernando, 2010; Oke et al., 2017), perhaps because they have aimed to support mesoscale model developers striving to increase their spatial resolution (e.g. to O(1 km)) and account for the average effects of small topographic features without resolving them. A small number of papers in the literature (Apsley and Castro, 1997; Blocken et al., 2015; Conan et al., 2016) studied the airflow over small-scale terrain only without buildings and emphasized the crucial role of the small terrain features.

Tominaga et al. (2004) investigated the effect of the neighbouring urban canopy on a single tall building in an attempt to validate several codes and meshing strategies. No significant difference was seen between structured, unstructured and an overlapping structured grid (Tominaga et al., 2004). All three were able to suitably predict the pedestrian level velocity, except in the wake and far from target buildings where the resolution was coarser. The resolution, however, was not reported.

Work by Xie and Castro (2009) has shown that resolving the flow at street scale requires a grid resolution of a metre or less, but to use that level of resolution for city scale simulations challenges both current computational tools and resources. A

further issue is that due to the resolution limits imposed by current computational resources, the complex geometries of real buildings must be simplified without losing those features which have a critical effect on the flow. A similar challenge applies to small topographic features (O(0.1km)), which are typically smoothed and simplified in numerical models (e.g. by choosing the resolution of digital terrain elevation data to be used). The question is what are the critical - but perhaps small - features of buildings and terrain which must be resolved?

More recently, Tolias et al. (2018) investigated the flow around the Michelstadt model, this emulates a typical European-type city and compared CFD to wind tunnel results. In comparison to Xie and Castro (2009), the building alignments were far more random. The angles between streets vary considerably throughout the domain, emulating the random nature of real urban areas. Fig. 1.11 shows the flow patterns in and above the urban canopy from Tolias et al. (2018). Certain flow structures are immediately obvious, the presence of a long axial vortex along the street shown by streamtrace 6. It is worth noting that streamtraces that start in very similar locations can finish in rather different places, streamtraces 1 and 2, and streamtraces 6 and 7. Streamtrace 8 shows a typical flow bifurcation, and a similar streamtrace could turn in the opposite direction, $-y$. Streamtrace 5 shows the complex nature of urban canopy flows, following a very complex path through and sometimes above the canopy.

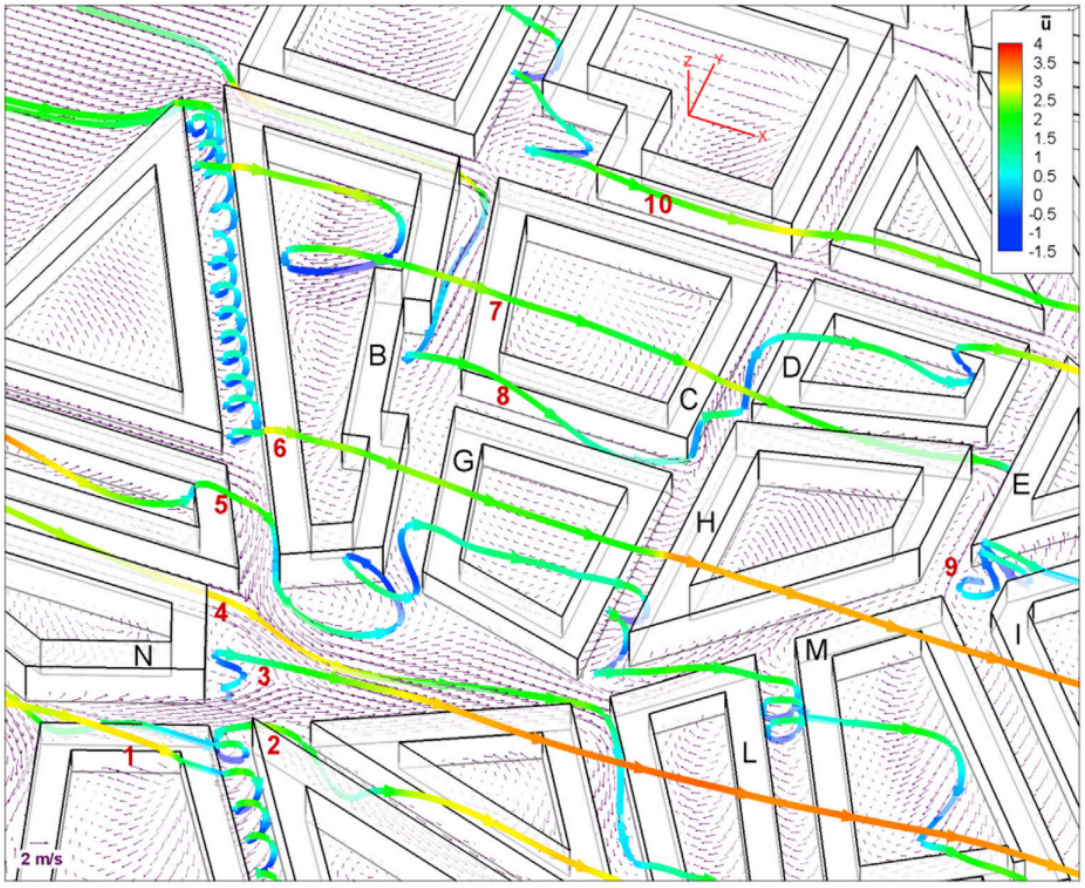

FIGURE 1.11: Streamtraces extracted from the mean flow (coloured by mean streamwise velocity). Horizontal velocity vectors shown across a plane at $z = 4.1$m. The grid size at ground level is 0.5m. Streamlines are numbered 1-10 for ease of identification. Figure from Tolias et al. (2018)

Hertwig et al. (2019) showed the effects of tall buildings and their wakes on the flow within the urban canopy. It was shown that the tall buildings cause strong interactions between the RSL and UCL that wake models, such as ADMS 5, do not take into account. Comparing the full urban area with tall buildings and tall buildings only showed an increase in both the turbulent kinetic energy and vertical momentum flux at the top of the tall buildings for the former setup.

So far, little is understood about the effects of topographic features on street scale (O(0.1km)) to neighbourhood scale (O(1km)) on urban flows. The prediction of these scales of flow is beyond the capability of the current operational mesoscale models. Nevertheless, these models are striving to increase their spatial resolution (e.g. O(0.1km)) and to account for the average effects of these small topographic features without resolving them. There is a clear need to simulate the effects of topographic features on street scale (O(0.1km)) to neighbourhood scale (O(1km)). On the other hand, engineering CFD-type codes have been developing rapidly. They have demonstrated the capability of resolving the buildings as well as a broad spectrum of

scales from 1m to O(1 km) (e.g. Xie and Castro, 2009; Han et al., 2017; Antoniou et al., 2017; Inagaki et al., 2017; Tolias et al., 2018; Gronemeier et al., 2020). Before understanding these large scale flows due to the terrain variations, a more complex variant of cuboid arrays must first be investigated. One aspect of interest is the spatially averaged profiles of the domain.

1.3.7.1 Research Needs

To appropriately capture the vast array of scales within the city, from (O(1m)) to (O(1km)), it should be determined what resolution is sufficient. These tests have been carried out previously (Xie and Castro, 2009) but applied to flat domains only. The increase in building complexity may require finer grid resolutions in order to capture the relevant flow features.

The only neighbourhood or larger scale investigation using LES of a region above $25km^2$ that could be found is that of Fossum and Helgeland (2020). Fossum and Helgeland (2020) carried out ambitious large-eddy simulations (LES) with a domain of $150km^2$ area of the hilly Norwegian city of Oslo, in which the difference between the CFD and operational hazmat dispersion tool (CT-Analyst®) was shown. The work aims to demonstrate the capability of LES, and to provide detailed data for parameterisation to be used in a fast-response tool. A resolution of $2-4m$ was achieved with a cell count of between $315,000$ and $922,000$ within the area of interest of 14.5x11km. They, in particular, emphasised the importance of setting the wall boundary conditions, again suggesting the critical role of small-scale topographic features.

The complete lack of inclusion of neighbourhood-scale topography has left a significant gap in the understanding of flows within urban areas. Terrain effects on their own have been published widely, but the effect that even small changes in terrain height ($O(h)$) would have within an urban setting are unknown. Even the University of Southampton's Highfield campus has terrain changes of this order of magnitude compared to the average canopy height and greater in some locations. Fig. 1.10 highlights this. The terrain is coloured by height, black being lowest at 0m above sea level (ASL) and white being the highest, at 73m ASL. Within the campus, there is a large dark region running down the image. The depth of this region is around $h = 16$m compared to the open region within the campus or the larger open region to the left. The question is whether it is necessary to include these terrain features to predict the flow field sufficiently.

These studies suggest, that although it is known coupling may exist between street and city scale flows, considerable uncertainty remains regarding the importance of small-scale topographic features in influencing street scale (O(0.1km)) and

neighbourhood scale (O(1km)) urban flows. This highlights a need for new studies to investigate and understand the effects of small-scale topographic features on street (O(0.1 km)) to neighbourhood (O(1km)) scales before considering the coupling between neighbourhood and city scales.

The effect of stratification for complex, more 'realistic' arrays has been reported for flat urban regions only (e.g. Xie et al., 2013). Xie et al. (2013) discussed the use of thermally stratified flows with more realistic urban canopies as producing results closer to field measurements. This is due to the somewhat rarity of purely neutral conditions within the UBL. It was shown that in the case with a weakly stratified $Ri_b = -0.2$ convective UBL, the agreement with field measurements was significantly closer. However, they note that in the near field, the situation is far more complex than simply matching the stratification strength (i.e. small scale roughness elements and local heat transfer). It is therefore vital that, due to the lack of cases reported using realistic urban morphology and thermal stratification, research is undertaken to mitigate this lack of knowledge.

To briefly summarise, this study aims to address the gap in current literature, i.e. to quantify and understand g the effect of pitching roof of cuboids, and the effect of street-scale real terrain on the urban canopy flows in neutral and weakly stable thermal stratification. In an attempt to generalise some of the results, it is required to define which are the critical - small (O(0.01km)) to large (O(1km)) - topographical features to be resolved.

Chapter 2

Methodology

What follows is a description of the process of generating and running numerical simulations of urban areas to gain new insight into the complex flows within and above the urban canopy.

2.1 Numerical Methods

2.1.1 Governing Equations

2.1.1.1 Coordinate system

The research undertaken uses a Cartesian coordinate system, utilising x, y, z, where x is the streamwise direction, y is the spanwise direction and z is the wall normal or vertical direction. This is the typical convention for meteorological flows (Stull, 1988). The velocities associated with x, y, z are u, v, w respectively.

2.1.1.2 Large Eddy Simulation

The flow which develops over arrays of blocks is innately unsteady and so is best resolved by adopting a large eddy simulation (LES) approach (e.g. Kanda et al., 2004; Xie and Castro, 2006; Castro, 2017). Equations 2.1 and 2.2 are respectively the filtered continuity and Navier-Stokes equations LES:

$$\frac{\partial \overline{u}_i}{\partial x_i} = 0 \tag{2.1}$$

$$\frac{\partial \overline{u}_i}{\partial t} + \frac{\partial \overline{u}_i \overline{u}_j}{\partial x_j} = -\frac{1}{\rho}\frac{\partial \overline{p}}{\partial x_i} + \nu \frac{\partial^2 \overline{u}_i}{\partial x_j \partial x_j} - \frac{\partial \tau_{ij}}{\rho \partial x_j} - \frac{1}{\rho}\frac{\partial P}{\partial x_i}\delta_{i1} + f\delta_{i3}, \tag{2.2}$$

where x_i and t are respectively spatial coordinate and time, $\overline{u_i}$ and $\overline{p}$ are respectively the resolved or filtered velocity and pressure, in the following sections /chapters, if otherwise stated, stress, u_i and p also respectively denote the filtered velocity and pressure, ρ is the density, ν is the kinematic viscosity, τ_{ij} is the Subgrid-scale (SGS) stress. δ_{i1} is the Kronecker-delta and $\partial P/\partial x_i$ is the pressure gradient or body force term which drives the flow when periodic boundary conditions are used in LES. The term $f\delta_{i3}$ is the body force in the vertical direction due to applied thermal buoyancy and is calculated by using the Boussinesq approximation based on the estimated temperature from Eq. 2.15. The mixed time scale SGS model (Inagaki et al., 2005) was used to avoid using the near-wall damping functions as used in the Smagorinsky SGS model. Nevertheless, Xie and Castro (2006) suggested that the flow is very much building block-scale dependent and that the results are not sensitive to the precise nature of the SGS model, subject to a requirement that the grid sufficiently resolves the inertial range of the turbulent spectra.

2.1.1.3 Subgrid-scale Modelling

The closure of the LES method is achieved by modelling the smallest scales of turbulence. It is the SGS stress generated through the filtering operation that has to be modelled. The SGS stress term, τ_{ij}, is the anisotropic residual stress tensor:

$$\tau_{ij} = \overline{u_i u_j} - \overline{u}_i \overline{u}_j - \frac{2}{3} k_r \delta_{ij}. \tag{2.3}$$

This process is very similar to the methodology followed in modelling the Reynolds stresses for the RANS turbulence models, and this method also is formed from the basis of relating the sub-grid stress to the mean strain rates, as was done with RANS closure. As the Boussinesq hypothesis works well for RANS, Smagorinsky postulated that a similar technique would work well to describe the effects of the unresolved eddies on the flow. Smagorinsky then proposed his SGS model in which the local SGS stress is proportional to the local strain rate of the fully resolved flow, given as:

$$\tau_{ij} = -2\nu_{SGS}\overline{S_{ij}}, \tag{2.4}$$

where $\overline{S_{ij}} = \frac{1}{2}\left(\frac{\partial \overline{u}_i}{\partial x_j} + \frac{\partial \overline{u}_j}{\partial x_i}\right)$ and $\nu_{SGS}(x,t)$ is the eddy viscosity. The eddy viscosity is given as:

$$\nu_{SGS} = (C_{SGS}\Delta)^2 \left|\overline{S}\right|, \tag{2.5}$$

where C_{SGS} is the Smagorinsky coefficient, Δ is the filter width and $(|\overline{S}|) = \sqrt{2\overline{S}_{ij}\overline{S}_{ij}}$. The Smagorinsky length scale is defined as $\ell = C_{SGS}\Delta$. The Smagorinsky model

requires that the Reynolds number be sufficiently high enough so that energy is transferred from large to small eddies, i.e. there is no backscatter (Katopodes, 2018).

At the wall the gradient, $\frac{\partial u}{\partial y}$, becomes very large within a turbulent boundary layer. This means that the turbulence at smaller scales than the grid become very large also. This can produce turbulence within the viscous sublayer, which is non-physical, due to the high viscous force. Therefore, the prediction of the turbulent stress becomes incorrect, thus the need for a function to reduce the turbulent viscosity to 0 in the close wall region. The Van Driest damping function (f_{VD}) can be seen below:

$$D = 1 - e^{\frac{-y^+}{A^+}}, \tag{2.6}$$

where, y^+ is $\rho \hat{u_\tau} y/\mu$ and A^+ is a constant. The adaptation used for this project, put forward by Krogstad (1991). The damping variable given above is then usually multiplied into the ν_{SGS} using the same C_{SGS} as before, which gives the Van Driest constant, $C_{SGS-VD} = C_{SGS}D$. This means that when $y^+ = 0, D = 0$, which makes $C_{SGS-VD} = 0$. This forces $\nu_{SGS} = 0$. This does, however, mean that the Smagorinsky can be over-dissipative in other shear regions too.

The dynamic Smagorinsky model (Germano et al., 1991) attempts to change C_{SGS} to $C_d(x,t)$ during the solution by interpreting SGS and resolved turbulence within the inertial range at different points. This is done by utilising a test filter, $\hat{\Delta}$, which is a grid filter larger than the standard grid filter, Δ. The newly formulated subgrid-scale is now:

$$T_{ij} = \widehat{\overline{u_i}\overline{u_j}} - \hat{\overline{u}}_i \hat{\overline{u}}_j, \tag{2.7}$$

and the resolved turbulent stress, ℓ_{ij} is defined as

$$\ell_{ij} = T_{ij} - \hat{\tau}_{ij} = \widehat{\overline{u_i}\overline{u_j}} - \hat{\overline{u}}_i \hat{\overline{u}}_j, \tag{2.8}$$

where the test filter is denoted by $\hat{}$. This relates the resolved turbulent stress, ℓ_{ij}, to the subgrid-scale stress at both test, T_{ij}, and grid levels, $\hat{\tau}_{ij}$. The Smagorinsky model, Eq. 2.5, can be applied now:

$$\ell_{ij} = -2\left(C_d \Delta\right) M_{ij}, \tag{2.9}$$

where $M_{ij} = \left(\frac{\hat{\Delta}}{\Delta}\right) |\hat{\overline{S}}|\hat{\overline{S}}_{ij} - \widehat{|\overline{S}|\overline{S}_{ij}}$. The Smagorinsky constant is a function of the test filter stresses:

$$C_d \Delta^2 = -\frac{1}{2} \frac{\langle \ell_{ij} M_{ij} \rangle}{\langle M_{ij} M_{ij} \rangle}, \tag{2.10}$$

where the angle brackets denote averaging in homogeneous directions of the grid. C_d is a function of time and inhomogeneous grid direction and there is no need for a damping function. The SGS eddy viscosity is still not guaranteed to be positive.

The mixed time scale of Inagaki et al. (2005) is based on the dynamic Smagorinsky model that uses the scale similarity hypothesis. The hypothesis states that the statistics of the SGS turbulent structures are like those of the higher frequencies within the resolved turbulent energy spectra. This means it may be possible to extrapolate the higher frequencies of the resolved energy spectra to predict the frequencies of the sub-grid scale turbulence, the modelled turbulence. The SGS eddy viscosity is expressed typically as:

$$\nu_{SGS}\,(\text{Velocity Scale}) \times (\text{Length Scale})\,, \tag{2.11}$$

.

Smagorinsky defines the velocity scale as $\overline{\Delta}|\overline{S}|$ and the length scale is defined as $\overline{\Delta}$. The velocity can be replaced with $\sqrt{k}$, where k is the SGS turbulent energy. This is often estimated by solving the modelled k-equation. It is possible to estimate k by filtering a velocity field:

$$k_{es} = \left(\overline{u}_k - \hat{\overline{u}}_k\right)^2, \tag{2.12}$$

here $\hat{()}$ denotes the filtering operator. The merit of this method is that ν_{SGS} is consistently guaranteed to approach zero in the laminar flow regions because k_{es} approaches zero. The SGS viscosity for the mixed time scale is given below:

$$v_{SGS} = C_{MTS} k_{es} T_S, \tag{2.13}$$

and

$$T_s{}^{-1} = \left(\frac{\Delta}{\sqrt{k_{es}}}\right)^{-1} + \left(\frac{C_T}{|\overline{S}|}\right)^{-1}. \tag{2.14}$$

The model constants C_{MTS} and C_T are usually set as 0.05 and 10 respectively (Inagaki et al., 2005). The time scale is defined as the harmonic average of $\overline{\Delta}/\sqrt{k_{es}}$ and $1/|\overline{S}|$. $\overline{\Delta}/\sqrt{k_{es}}$ is the characteristic time scale of the small-scale turbulence corresponding to the cut-off scale, whereas $1/|\overline{S}|$ stands for the large scales. In the region away from the wall, if $|\overline{S}|$ approaches zero, ν_{SGS} approaches $C_{MTS}\overline{\Delta}\sqrt{k_{es}}$. All of the cases shown throughout this research make use of the mixed time scale SGS model.

2.1.1.4 Temperature Transport

The filtered transport equation of temperature is:

$$\frac{\partial T}{\partial t} + \frac{\partial \overline{u}_j T}{\partial x_j} = \frac{\partial}{\partial x_j}\left[(D + D_r)\frac{\partial T}{\partial x_j}\right], \tag{2.15}$$

where T is the resolved-scale temperature. D is the molecular diffusivity of temperature, D_r is the SGS diffusivity and is given by ν_{SGS}/Pr_r, where ν_{SGS} is the SGS kinematic viscosity, Pr_r is the subgrid Prandtl number set to 0.9. The Prandtl number is calculated as the ratio of thermal diffusivity, d, and the eddy diffusivity, ν:

$$Pr = \frac{\nu}{D} \tag{2.16}$$

2.1.2 Thermal Stratification

2.1.2.1 Boussinesq assumption

The Boussinesq assumption assumes the variations in density do not apply any forces to the flow except buoyancy. This assumption is valid where temperature differences vary little, and as such, density varies little. For thermally stratified flows, the kinematic density, ρ_k, where the temperature change is small, is given as:

$$\rho_k = \rho\left[1 - \beta\left(T - T_{\text{ref}}\right)\right], \tag{2.17}$$

where β is the thermal expansion coefficient and T_{ref} is the reference temperature. It is important that $|\rho_k - \rho|/\rho \ll 1$ so that incompressible flow assumptions remain true.

The final term of Eq. 2.2 is:

$$f\delta_{i3}, \tag{2.18}$$

which is the term defining the force due to buoyancy in the vertical direction. Substituting $f = \rho_k g$ from the Boussinesq assumption gives a new final term to Eq. 2.2:

$$\frac{\rho_k g}{\rho}\delta_{i3}, \tag{2.19}$$

$$\frac{\partial u_i}{\partial t} + \frac{\partial u_i u_j}{\partial x_j} = -\frac{1}{\rho}\frac{\partial p}{\partial x_i} + \nu\frac{\partial^2 u_i}{\partial x_j \partial x_j} - \frac{\partial \tau_{ij}}{\rho \partial x_j} - \frac{1}{\rho}\frac{\partial P}{\partial x_i}\delta_{i1} + \frac{\rho_k g}{\rho}\delta_{i3}, \tag{2.20}$$

This gives a general form of the equation for momentum conservation in buoyancy-driven flows, in which the incompressible flow assumptions are still valid.

2.1.2.2 Setting of Thermal Stratification

In this study, thermal stratification effects are set using the bulk Richardson number, which offers a convenient approach for quantifying the strength of stratification due to the vertical temperature gradient in numerical simulations. The bulk Richardson number re-written from Eq. 1.10 to the form:

$$Ri_b = \frac{g\delta(\overline{T}_{\text{ref}} - \overline{T}_0)}{\overline{T}_0 \overline{U}_\infty^2}, \tag{2.21}$$

where g is acceleration due to gravity, δ is the boundary layer depth or domain height, $\overline{T}_{\text{ref}}$ is the mean freestream temperature, $\overline{T}_0$ is the mean ground temperature and $\overline{U}_\infty$ is the mean freestream velocity at the inlet.

2.1.3 Boundary Conditions

The LES model must be used with boundary conditions appropriate to the problem. For urban flow simulations, the inflow and outflow faces typically have periodic boundary conditions (PBC) (e.g. Coceal et al., 2006) or synthetic turbulence inflow conditions (STI) (e.g. Xie and Castro, 2008). An LES simulation with PBC is based on the assumption that the simulated domain is a repeat unit of a much greater region. This approach can substantially reduce the computational cost. However, when modelling a 'real' urban geometry, the PBC approach could lead to an inaccurate representation of the flow in some scenarios because, as stated in Xie and Castro (2009), the repeat unit creates wakes that impact itself.

The synthetic turbulence inflow (STI) method has been well documented (Xie and Castro, 2008; Sessa et al., 2018) and simulations using it have compared very well to data from experiments (Marucci et al., 2018; Marucci and Carpentieri, 2020). As inputs, STI requires vertical profiles of mean velocity, Reynolds stresses, and integral length scales. Furthermore, to apply thermal stratification at the inlet, STI requires vertical profiles of the mean and variance of temperature and integral length of temperature fluctuations as additional inputs.

2.1.3.1 Periodic Boundary Condition

The cyclic or periodic boundary condition (PBC) provides a coupling condition between a pair of patches (domain surfaces). In this research, the translation case is

used. The PBC allows flows to exit one patch and enter the paired patch at the same patch location. The PBC will be applied on both the side patches of all cases. In some cases, the PBC will be applied to the inlet and outlet boundaries. For the cuboid cases, this means all horizontal boundaries will use PBCs. Giving essentially an infinitely long and wide array of cubes. As the cubes used are all the same size, the inflow will be able to produce a fully developed turbulent urban boundary layer, given enough time for the simulation to initialise.

2.1.3.2 Synthetic Turbulence Generation

This technique was developed by Xie and Castro (2008) to generate incoming turbulence to simulate the structure of the urban boundary layer. It should be noted that this synthetic turbulence generation requires the wall normal direction to be $+y$, which is not aligned with the conventions within this thesis. Therefore, in the following paragraphs for outlining the turbulence generator methodology, the coordinate system will use the $+y$ for the wall normal direction.

The turbulence generator uses an exponential velocity correlation, which assumes the auto-correlation function of the velocity component decays exponentially. The correlation function can be written as:

$$\frac{\overline{u_m u_{m+k}}}{\overline{u_m u_m}} = R_{uu}(k\Delta x) = exp(-\frac{\pi|k|}{2n}), \tag{2.22}$$

given that $L = n\Delta x$ is the length scale of the flow. Therefore, the exponential correlation function is used to create a filter to process a set of random data. This is described using a one-dimensional data set, where Δx is the grid size. Where a filter function is used to generate a spatial correlation:

$$u_m = \sum_{j=-N}^{N} b_j r_{m+j}, \tag{2.23}$$

where r_m is a 1-dimensional random set of data with the mean $\overline{r}_m = 0$ and the variance $\overline{r_m r_m} = 1$. b_j is the filter coefficient, and N is related to the length scale of the filter, where $N = 2n$, $n = L/\Delta x$. u_m is a 1-dimensional number sequence, with a mean value given as $\overline{u}_m = 0$, and $\overline{r_m r_n} = 1$, when $m \neq n$, meaning zero cross-correlation and u_m has spatial correlation. It is possible to guess a filter coefficient in the form, which is re-written to satisfy $\overline{u_m u_m} = 1$:

$$b_k = \frac{\tilde{b}_k}{(\sum_{j=-N}^{N} \tilde{b}_l{}^2)^{1/2}} \tag{2.24}$$

where,

$$\tilde{b}_k \approx exp(-\frac{\pi|k|}{2n}) \tag{2.25}$$

Only a single 2-dimensional slice is produced per time step for all the zones for one velocity component. The next time step is described by:

$$\psi_\beta(t+\Delta t) = \psi_\beta(t)exp(-\frac{\pi\Delta t}{2T}) + \psi_i(t)[1-exp(-\frac{\pi\Delta t}{T})]^{0.5}, \tag{2.26}$$

where T is the Lagrangian time and $\psi_\beta(t)$ is the un-scaled fluctuation with zero mean, zero cross-correlations and variance equal to 1. The velocity components can then be calculated by considering the transformation given:

$$u_i = \overline{u}_i + a_{ij}\psi_j, \tag{2.27}$$

where

$$[a_{ij}] = \begin{bmatrix} (\hat{R}_{11})^{1/2} & 0 & 0 \\ \hat{R}_{21}/a11 & (\hat{R}_{22}-(a_{21})^2)^{1/2} & 0 \\ \hat{R}_{31}/a11 & (\hat{R}_{32}-a_{21}a_{31})/a_{22} & (\hat{R}_{33}-a_{31}^2-a_{32}^2)^{1/2} \end{bmatrix}, \tag{2.28}$$

where u_i is the instantaneous velocity, $\overline{u}_i$ is the mean velocity and a_{ij} is the Cholesky decomposition of the Reynolds stress tensor, R_{ij} suggested by Lund et al. (1998). For a boundary layer flow which is homogeneous in the spanwise direction, i.e. z, $\hat{R}_{31} = 0$, therefore a_{31} and a_{32} vanish.

The inflow generation technique allows the user to prescribe the turbulent stresses, the mean velocity profile and the turbulent length scales at the inlet. The length scales, defined as L_x, L_y, L_z are given as constants in the code. However, it is possible to use length scales that change in a certain direction. The code creates a 2-dimensional slice mesh on which the spatially correlated inflow is generated. Length scales are given as the number of cells in the code. For simulations herein, the length scales are the same for the L_y and L_z directions.

Throughout this work, the PBC and STI boundary conditions are used for two different sets of simulation cases. The choice of boundary condition was driven by the physics to be simulated. STI boundary conditions were used for examining the effect of thermal stratification and the change in roughness flows. So that the results could be compared with past work on block arrays with flat roofs, the same STI inputs were used for the thermal stratification cases as in Sessa et al. (2020). This meant that the

prescribed vertical profiles of mean velocity, Reynolds stresses, mean temperature and temperature fluctuations for simulating $Ri_b = 0,\ 0.2,\ 0.5$ and 1 were identical to those used in Sessa et al. (2018), which matched the experimental data in Marucci et al. (2018). It should be noted that the same prescribed inflow data were used for $Ri_b = 0.2,\ 0.5$ and 1. This was because, as stated in Sessa et al. (2018), using the same settings allows the effect of thermal stratification to be isolated for investigation.

2.1.4 Spatial Averaging

The spatial averaging method was adopted for processing the outputs from all simulations. Using spatially averaging over a whole $(x-y)$ plane (e.g. Fig. 2.6), a resolved instantaneous flow quantity ϕ in LES can be further decomposed into space-time average $\langle\overline{\phi}\rangle$ (Eq. 4.2) , spatial variation of the time average $\tilde{\phi}$, and resolved turbulence fluctuation ϕ' which is the deviation of the resolved instantaneous quantity ϕ from the time average $\overline{\phi}$,

$$\phi = \langle\overline{\phi}\rangle + \tilde{\phi} + \phi', \tag{2.29a}$$

$$\text{and} \quad \overline{\phi} = \langle\overline{\phi}\rangle + \tilde{\phi}, \tag{2.29b}$$

where the time-averaged quantity $\overline{\phi}$ is equivalent to ϕ for simplicity, such as $\bar{u}_i$ being equivalent to U_i. In particular, the comprehensive spatial average (Xie and Fuka, 2018) was selected. This method includes the solid regions in the total volume but ascribes zero values to the output quantities in them (i.e. the volume occupied by the building blocks shown as the grey area in Fig. 2.3d), while the solid regions within the domain are included in the total volume. Equation 4.2 defines the comprehensive spatial average:

$$\langle\phi\rangle(z) = \frac{1}{S_c}\int\int_{(x\in(a,b),y\in(-6H,6H))\cap S_f} \phi(x,y,z)\mathrm{d}x\mathrm{d}y, \tag{2.30}$$

where $\langle\rangle$ denotes spatial average, ϕ denotes the quantity to be spatially-averaged, S_f denotes the fluid area at height z. For the periodic boundary condition (PBC) case, S_c denotes the total area at height z for the entire horizontal plane, i.e. $x \in (0, 12H), y \in (-6H, 6H)$ (see Fig .2.6a). For the synthetic turbulence inflow (STI) cases, S_c denotes the area at height z for a horizontal plane across the entire span $(y \in (-6H, 6H))$, and between two x coordinates a and b separated by $2H$ (see Fig .2.6b).

When applying the comprehensive spatial averaging to the Navier stokes equations can be written as (Xie and Fuka, 2018),

$$-\frac{\partial\langle P\rangle}{\rho\partial x_i} - \langle\frac{\partial\tilde{p}}{\rho\partial x_i}\rangle + \nu\frac{\partial^2\langle\overline{u_i}\rangle_c}{\partial x_k^2} + \nu\langle\frac{\partial^2\overline{u}_i}{\partial x_i^2}\rangle - \frac{\partial\langle\tilde{u}_i\tilde{u}_k\rangle}{\partial x_k} - \frac{\partial\langle\overline{u_i'u_k'} + \widehat{\overline{u_i''u_k''}}\rangle}{\partial x_k} = 0, \tag{2.31}$$

where the first term is the constant pressure gradient applied as a body force to the NS equation, the second term is the form or pressure drag force from the non-fluid regions, the fourth term is the viscous drag from the non-fluid regions, the third term is the viscous shear due to the gradient in the vertical direction of the time- and spatially- averaged velocity, the fifth term is the dispersive shear stress and the sixth term is the turbulent shear stress.

The comprehensive spatial average has the advantage of producing a smooth change of total momentum flux across the canopy interface . In comparison, the intrinsic spatial average, which only includes the fluid regions in the averaging, leads to a discontinuity in total momentum flux at the canopy height. The fact that the comprehensive spatial average gives a smooth change in momentum flux is potentially advantageous in developing a parametrisation of momentum flux, or other quantities, for a mesoscale model.

In accordance with (Xie and Fuka, 2018), a discontinuity is caused when using the intrinsic average. From (Xie and Fuka, 2018), "This is simply because the average area, which is used to calculate the stress with unit m^2s^2, changes by 33% at the cuboid height while the total shear force with unit m^4s^2 varies continuously across the entire height of the domain." The comprehensive averaging process allows the continuous momentum flux profile, as the total area being averaged does not change across the vertical extent. The time and spatial averages of the comprehensive spatial average data are about 30% less than for the intrinsic spatial average data which is due to the packing density of 33%, where the intrinsic method exclude the non-fluid regions.

2.1.4.1 Numerical schemes

The following numerical schemes define the chosen method for solving time $\partial/\partial t$, gradient, $\nabla\phi$, divergence, $\nabla \cdot \phi$, Laplacian, $\nabla^2\phi$, and interpolation schemes. Table 2.1 shows the applied numerical schemes for each category. These schemes are used throughout this research. The time scheme, backward, is a transient, second-order implicit discretisation scheme, which is potentially unbounded.

TABLE 2.1: Numerical schemes for all cases

Category	**Scheme**
time, $\partial/\partial t$	backward
Gradient, $\nabla\phi$	Gauss linear
divergence, $\nabla \cdot \phi$	Gauss linear
laplacian, $\nabla^2\phi$	Gauss linear corrected
Interpolation	linear

2.1.5 Particle Image Velocimetry Data

An essential part of the study was that basic simulations of the airflow around the Highfield Campus buildings on flat terrain could be validated against high-resolution experimental data. Experiments were conducted in the University of Southampton's $6.75m$ long re-circulating water tunnel using a 1:1000 scale 3D printed model. It should be noted that the model was a simplification in that:

- The buildings were placed on flat terrain;
- All the building roofs were made flat, whether they actually were or not.

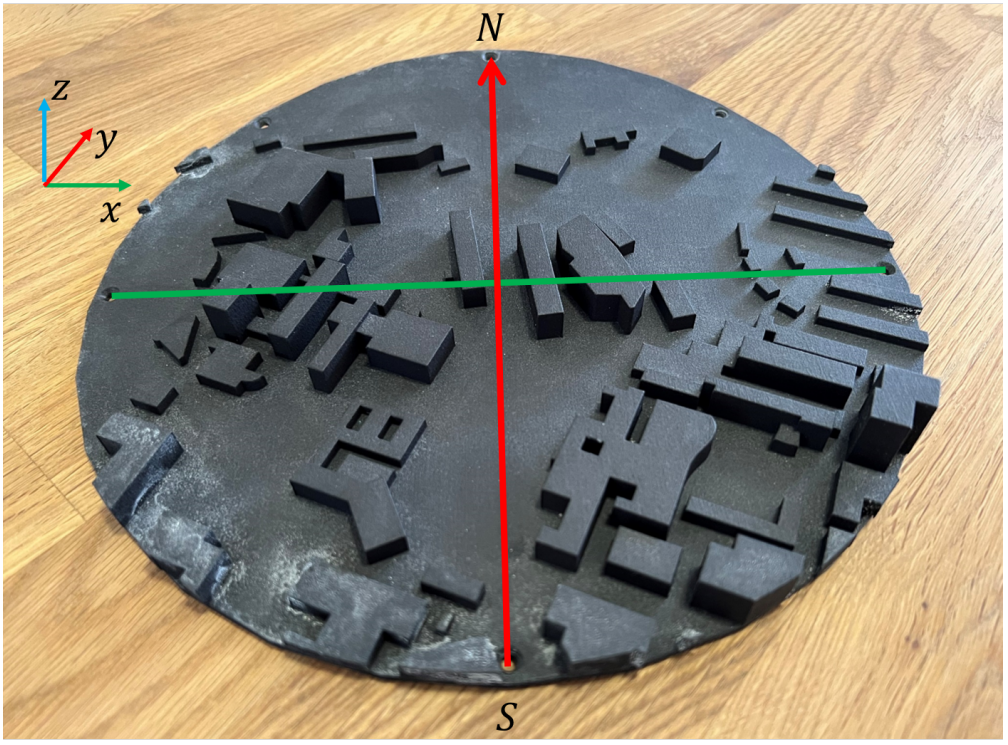

FIGURE 2.1: 3D print of the Highfield campus. The north-south is shown in red, west-east is shown in green. The coordinate system is also shown. The diameter of the 3D model or 'patch' is $25cm$

Fig. 2.2 from Lim et al. (2022) shows their experimental setup, which is the same for this study. The test section of the University of Southampton's water flume is $6.75m$ long and $1.20m$ wide. The measuring location is roughly $5.5m$ downstream of the leading edge of the test section. The water depth throughout the measurements was maintained at $600mm \pm 1mm$ and the $U_\infty = 0.45ms^{-1}$. The model was exposed to a naturally developed boundary layer which had a depth of $\delta = 83$ mm. The ratio $\delta/h = 12$ was close to that used in the LES simulation. Based on the model scale's average building height h=16 mm, the Reynolds number was $Re_h = 12,000$. The average

building height at full scale is 16 m. The experimental 'patch', the model shown in Fig. 2.1, is attached using screws. The test area encompasses around 450m in full scale and

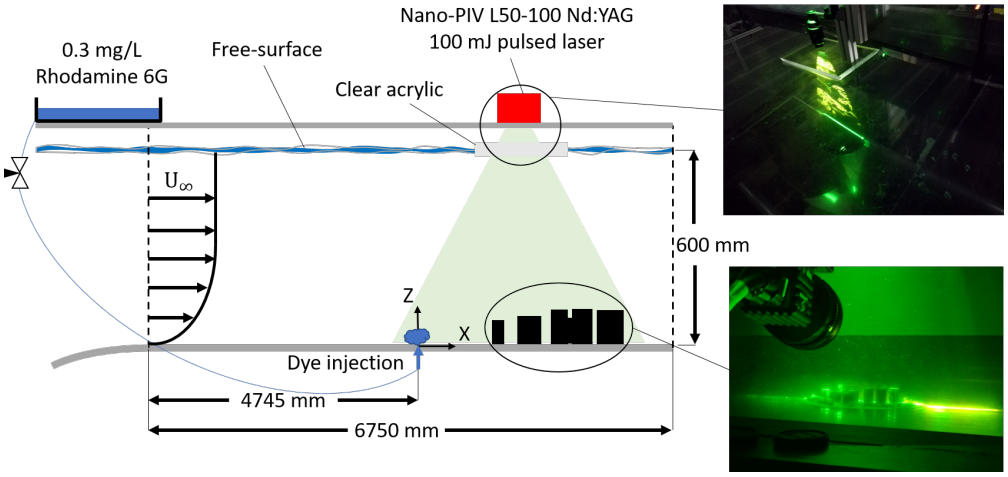

FIGURE 2.2: PIV setup showing laser plane and orientation and general setup within the flume experiment, from Lim et al. (2022)

The laser system used to illuminate the seeding particles was provided by $100mJNd:YAG$ double-pulsed laser. The emission wavelength was $532nm$ with a rate of $4Hz$. A total of 2000 image pairs, with a time of separation of $1200\mu s$ at a sampling rate of 2 Hz. Two CMOS cameras were used with a resolution of 4MP in a side-by-side configuration. This provided a field-of-view of $230mm$ in x and $135mm$ in z. LaVision's Davis software, version 8.4.0 was used to post-process the particle images to produce the vector maps. The laser is split into a sheet using sheet generation optics from LaVision. The laser sheet shines across the west-east direction, parallel to the direction of the flow.

The flow seeding was accomplished using $50\nu m$ polyamide particles, which were allowed to circulate throughout the flume before measurement. The errors in PIV measurement come from several sources. These include tracer dynamics, image mapping, interrogation, and resolution. The focus of the uncertainty analysis focuses on the errors from image mapping, from misalignment with the calibration plate due to the natural distortion of the image, known as pincushion distortion. In addition, errors in the magnification of the image as the magnification varies over the depth of the laser sheet (Adrian and Westerweel, 2011). Typically this produces an uncertainty of 0.3%. However, for the present work it was estimated at around 2%, taking into account only the refraction of the ray from air to water whilst neglecting the refraction through the glass; this error would decrease to around 1%.

For comparison with CFD data, a flat bare patch was placed in the sampling location. The same process was followed to measure the incoming naturally grown boundary layer's mean flow and turbulent statistics. This data was then applied at the inlet of

the Flume inflow case, FF8. This gives consistent boundary conditions between the cases to validate the CFD approach.

The PIV data used in the study consisted of that taken in the streamwise vertical plane equivalent to y=104 m in the computational domain (full scale, see Fig. 2.18). Vertical profiles were extracted at 14 locations given IDs 1–14, counting from upstream to downstream, starting from x = 220 m (13.3h) at 40 m intervals (Δx = 2.5h).

2.2 Idealised urban arrays with flat and pitched roof geometries

The idealised morphology studied here takes the form of a simplified urban-like geometry. Arrays of simple blocks, i.e. cuboids with either flat or pitched roofs, are studied. The baseline cuboid has dimensions $2H \times H \times H$, where $H = 1$ m. The Reynolds number based on the block width H and the velocity at height H in the upstream boundary layer is about 7400, or about 830 based on the friction velocity u_τ (Coceal et al., 2006; Cheng and Castro, 2002), estimated using an extrapolation from the linear turbulent shear stress profile above the canopy (e.g. Fig. 3.3). Given the different block heights and dimensionless domain heights in this work, it was chosen to use u_τ to non-dimensionalise quantities and to focus on the physics within and immediately above the canopy. Based on their research on arrays of cubes at a smaller Reynolds number, Xie and Castro (2006) state that "Reynolds number dependency (if it does exists) is very weak for such flows, except no doubt very close to solid walls. Turbulence generated by urban-like obstacles (with sharp edges) is large scale dominated and hardly at all dependent on the much-smaller-scale viscous dominated processes on the body surfaces". Flows over arrays of pitched-roof obstacles with sharp edges are expected to be very weakly dependent on the Reynolds number too.

Two different packing densities (i.e. λ_p= 33.3% and 16.7%) are simulated. The baseline flat roof cases of height H were validated against Castro et al. (2017). Further cases of height 1.5H with a flat roof or a 45° pitched roof were then compared with the baseline case. Fig. 2.3 shows the geometries of the three different blocks used and diagrams illustrating the packing densities.

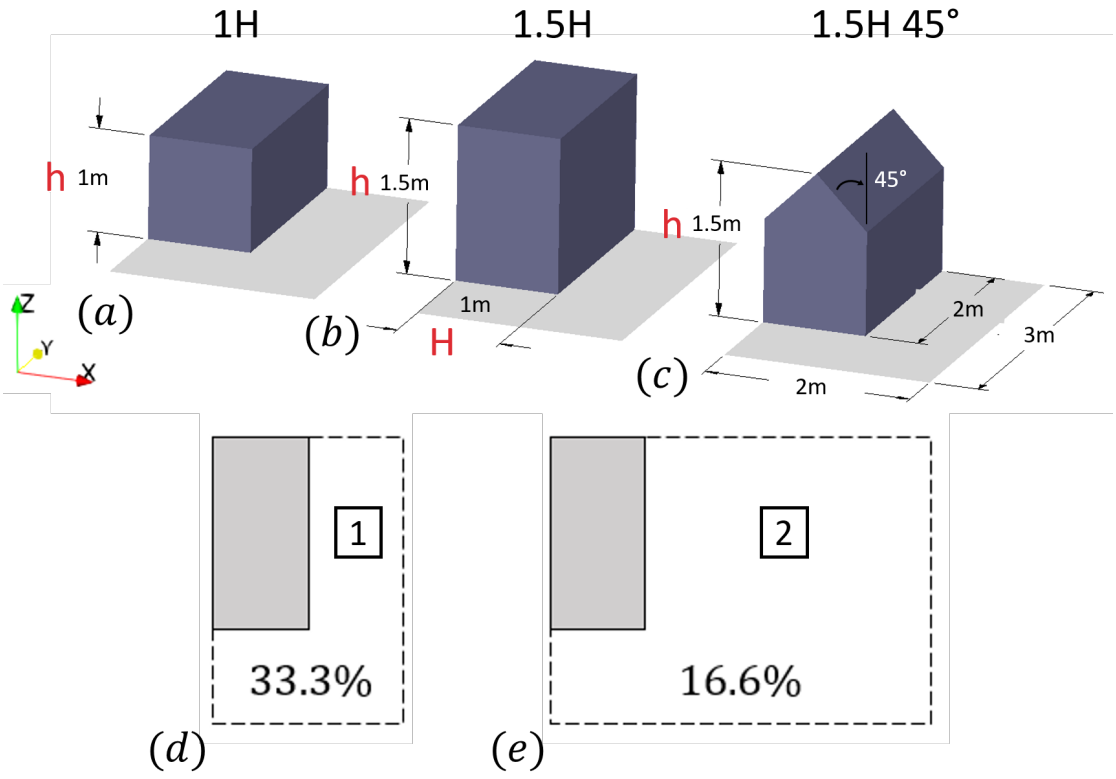

FIGURE 2.3: Diagram of the smallest repeat unit size for a) 1H, b) 1.5H, c) 1.5H 45° pitched roof, with the same plan view and packing density, λ_p= 33.3%. H, the block width. h, the block height. x coordinate is aligned with the flow direction and is perpendicular to the long side of the cuboid and the long street, and z coordinate is in the vertical direction, d) packing density λ_p= 33.3% (as in Fig.2.3), e) packing density λ_p= 16.7% where the width of the long street marked with "2" is tripled compared to "1" in d)

The meshes used in this study were created using snappyHexMesh, which is far more flexible and efficient than standard structured-mesh generators. It was primarily used here to assess its suitability for application to much larger domains in follow-on studies. Nevertheless, this study utilised the capability of snappyHexmesh to create uniform grids, grids with multiple levels of resolution and non-conformal and conformal meshes.

For the baseline flat-roof cases, uniform Cartesian grids (identified as (U), Table 2.9) were first created with a resolution of $H/16$. This was in accordance with the minimum level of resolution suggested in Xie and Castro (2006) and Coceal et al. (2006), which was adopted for all cases, except for those with specifically defined grids. Cartesian meshes with three levels of grid resolution (identified as (3R), Table 2.9) were created, as used in Xie and Castro (2006), for testing mesh sensitivity. These had a resolution $H/16$ up to $z = 2.5H$, a resolution $H/8$ between $z = 2.5H$ and $z = 8.5H$, and finally, a resolution $H/4$ from $8.5H$ up to the top of the domain at $12H$. The time step was chosen following the guidance that the maximum Courant number was less than unity. For the PBC cases (Table 2.9), the initialisation period was about

$600T_p$, and the averaging period was at least $700T_p$, where T_p was based on the block height and the freestream velocity. For the STI cases (Table 2.9), the initialisation period was $50T_p$, and the averaging period was $200T_p$. It took from 240 to 300 wall-clock hours on 200 cores to complete one simulation case.

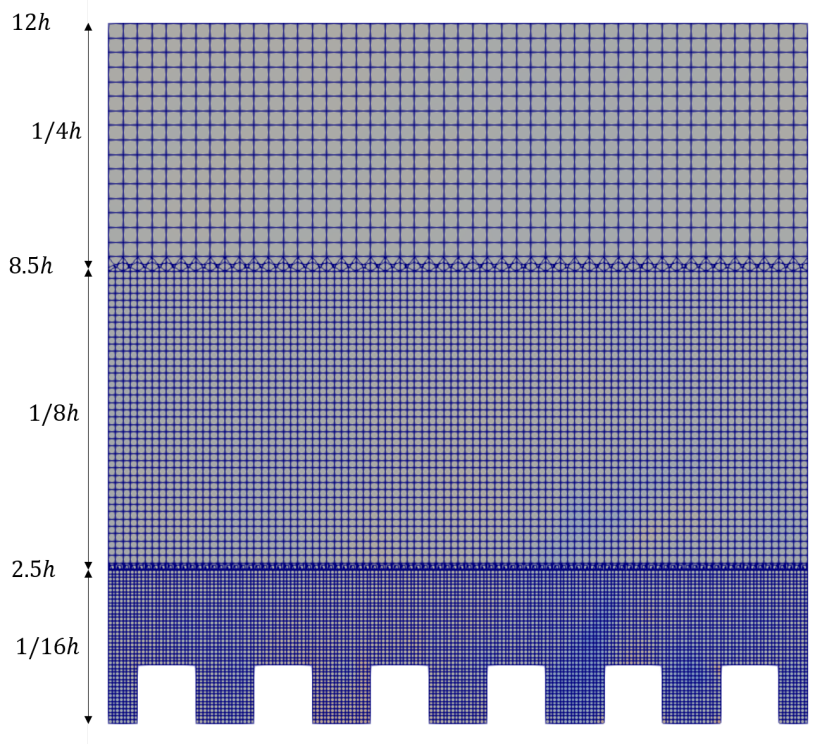

FIGURE 2.4: Grid for 1H(3R), refinement locations and local grid size given (Table 2.2).

All the Cartesian meshes created for the flat roof cases were conformal. However, if a simple Cartesian mesh is created for a pitched roof, the mesh is non-conformal, as shown in Fig. 2.5. To address the question of what impact this has, three meshing strategies were used for the pitched-roof cases: uniform conformal grids (UC), Uniform non-conformal grids (UNC) and a 3-level resolution-conformal grid (3RC).

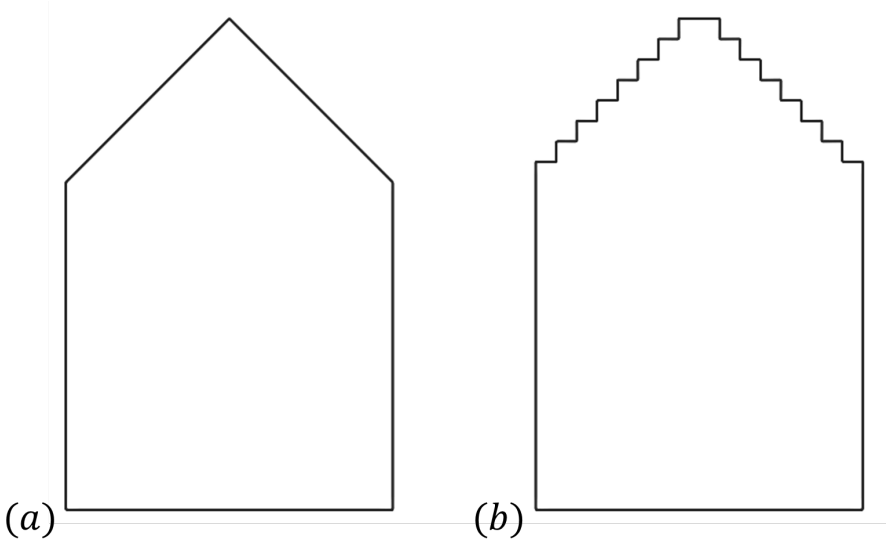

FIGURE 2.5: Side view of the surface meshes of pitched-roof cuboids of a) conformal mesh, 1.5H 45°(UC, 3RC) and b) non-conformal mesh, 1.5H 45°(UNC)

The majority of the cases were run at neutral stability conditions with PBC at the inflow and outflow (Table 2.9). For these cases, the domain had dimensions of $12H$x$12H$x$12H$, following Castro et al. (2017) as shown in Fig. 2.6a. The STI boundary condition was applied for the cases with thermally stratified inflows (Table 2.9). The domain was sized to match that used in Sessa et al. (2018, 2020), which was $29H$ x $12H$ x $12H$ shown in Fig. 2.6b. In both cases, periodic boundary conditions were applied to the spanwise boundaries, and a stress-free condition was set for the top boundary.

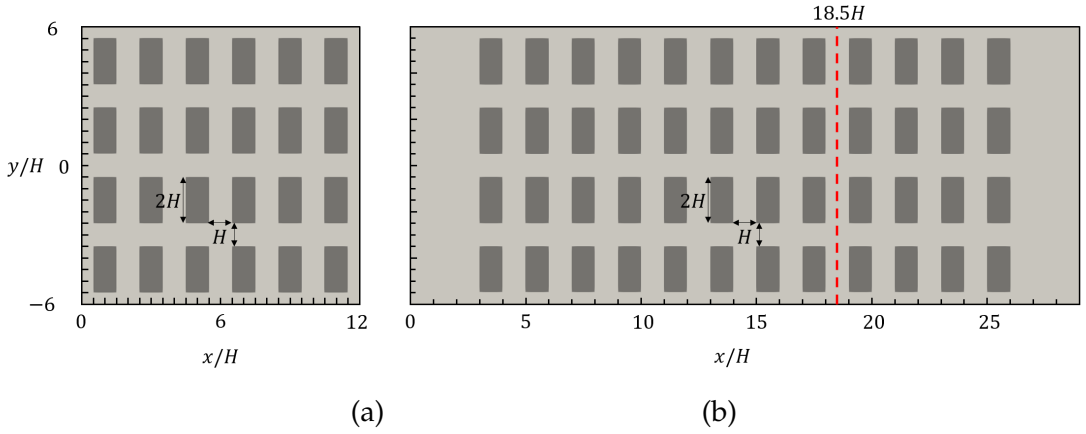

FIGURE 2.6: Plan view of the two domains with a packing density λ_p= 33.3%. (a) The PBC domain. (b) The STI domain. Removing every other column of cuboids in (a) results in λ_p= 16.7%. Red dashed line denotes where laterally averaged vertical profiles are presented. The flow direction is aligned with x

Table 2.9 summarises the neutral stability cases simulated with the baseline packing density of 33.3%, the neutral cases run to examine the effect of changing the packing

density from 33.3% to 16.7%, and the cases run to examine the impact of thermal stratification on the flow over arrays with a packing density 33.3%.

TABLE 2.2: A complete list of the simulated cases. H, block width (Fig.2.3). PBC, periodic boundary condition. STI, synthetic turbulence inflow boundary condition.

Case ID	λ_p(%)	Block height (H)	Ri	Roof type	Mesh type	In-outlet BCs
1H(**U**)	33.3	1	0	Flat	**U**niform	PBC
1H(**3R**)	33.3	1	0	Flat	**3**-level **R**esolutions	PBC
1.5H(**U**)	33.3	1.5	0	Flat	**U**niform	PBC
1.5H(**3R**)	33.3	1.5	0	Flat	**3**-level **R**esolutions	PBC
1.5H45°(**UC**)	33.3	1.5	0	Pitched	**U**niform **C**onformal	PBC
1.5H45°(**UNC**)	33.3	1.5	0	Pitched	**U**niform **N**on-**C**onformal	PBC
1.5H45°(**3RC**)	33.3	1.5	0	Pitched	**3**-level **R**esolution **C**onformal	PBC
1H(**U**)	16.7	1	0	Flat	**U**niform	PBC
1.5H(**U**)	16.7	1.5	0	Flat	**U**niform	PBC
1.5H45°(**3RC**)	16.7	1.5	0	Pitched	**3**-level **R**esolution **C**onformal	PBC
1.5H45°(**UCI**)	33.3	1.5	0, 0.2, 0.5, 1	Pitched	**U**niform **C**onformal	STI

2.2.1 Boundary and inflow conditions

The LES model must be used with boundary conditions appropriate to the problem. For urban flow simulations, the inflow and outflow faces typically have either periodic boundary conditions (PBCs) (e.g. Coceal et al., 2006) or synthetic turbulence inflow conditions (STI) (e.g. Xie and Castro, 2008). An LES simulation with PBCs is based on the assumption that the simulated domain is a repeat unit of a much greater region. This approach can substantially reduce the computational cost. However, when modelling a "real" urban geometry, the PBC approach could lead to an inaccurate representation of the flow in some scenarios, such as a change in roughness (Xie and Castro, 2009; Tomas et al., 2016, 2017; Sessa et al., 2018, 2020). Using the PBC

approach in non-neutral conditions requires additional precautions, such as adding additional forcing terms into the governing equations that should not influence the turbulence statistics (Boppana et al., 2014; Grylls et al., 2020).

Table 2.3 shows the boundary conditions applied for all simplified geometry cases. The inlet and outlet boundary conditions are included for both the periodic and STI cases. The top, Ground, $Side_1$ and $Side_2$ patches have the same boundary condition for all cases.

TABLE 2.3: Boundary conditions for the cuboid array cases

Boundary Patch Name	**Boundary Condition**
Inlet (PBC)	Periodic - Outlet
Outlet (PBC)	Periodic - Inlet
Inlet (STI)	Synthetic turbulent inflow
Outlet (STI)	Pressure Outlet
Top	Symmetry Plane
Ground	No-slip Wall
$Side_1$	Periodic - $Side_2$
$Side_2$	Periodic - $Side_1$

The STI method has been well documented (Xie and Castro, 2008; Sessa et al., 2018) and simulations using it have compared well to data from experiments (Marucci et al., 2018; Marucci and Carpentieri, 2020). As inputs, the STI approach requires vertical profiles of mean velocity, Reynolds stresses, and integral length scales. Furthermore, to apply thermal stratification at the inlet, STI requires, as additional inputs, vertical profiles of mean temperature and variance and the integral length of temperature fluctuations.

The PBC and STI boundary condition approaches are used for two different sets of simulation cases. The choice of boundary conditions was driven by the physics to be simulated, and so STI boundary conditions were used for examining the effect of thermal stratification. To enable the results to be compared with past work on block arrays with flat roofs, the same STI inputs were used for the neutral and stable stratification as in Sessa et al. (2018, 2020) (specifically Fig. 4 in Sessa et al. (2020)). This meant that the prescribed vertical profiles of mean velocity, Reynolds stresses, mean temperature and temperature fluctuations for simulating $Ri_b = 0,\ 0.2,\ 0.5$ and 1 were identical to those used in Sessa et al. (2018, 2020), which matched the experimental data in Marucci et al. (2018). Moreover, the same prescribed inflow data were used for $Ri_b = 0.2,\ 0.5$ and 1, because as stated in Sessa et al. (2020), using the same settings allows the effect of thermal stratification to be isolated.

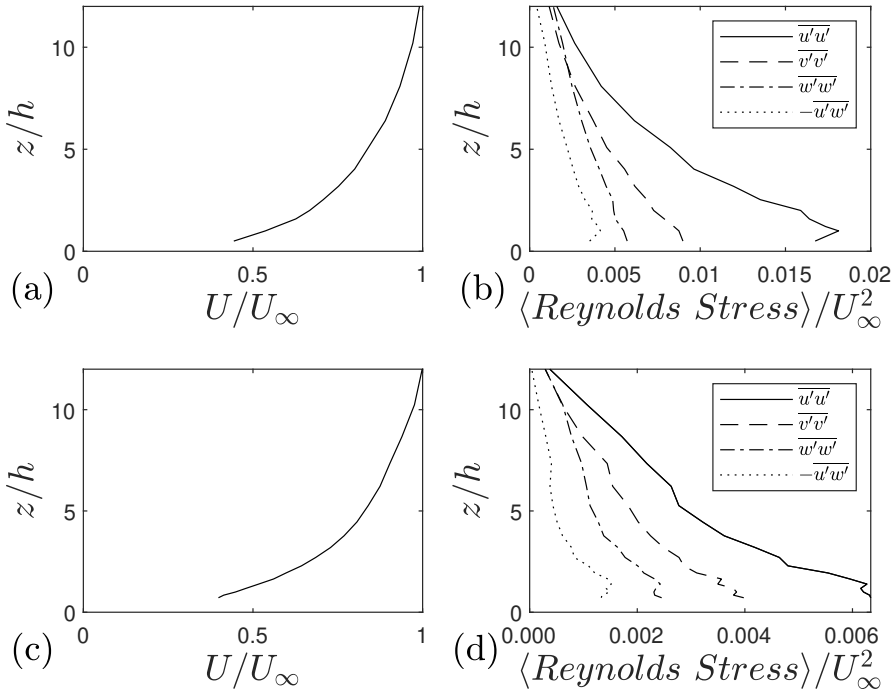

FIGURE 2.7: Vertical profiles prescribed at the inlet for a) mean streamwise velocity $Ri = 0$, b) turbulent statistics $Ri = 0$, c) mean streamwise velocity $Ri = 0.2, 0.5, 1$ and d) turbulent statistics $Ri = 0.2, 0.5, 1$

The integral length scales prescribed in the streamwise, spanwise and vertical directions are shown in Fig. 2.8. The accuracy of the prescribed length scales L_x, L_y, L_z were shown by Xie and Castro (2008) to not drastically affect the mean flow and turbulent statistics within or immediately above the canopy in sensitivity tests. The selected length scales match that prescribed by (Sessa et al., 2018, 2020), which are from the wind tunnel (Marucci et al., 2018; Marucci and Carpentieri, 2020).

The length scales shown in Castro et al. (2006) and Xie and Castro (2008) show that typical length scales of L_y and L_z do not change drastically over the depth of the boundary layer. On the other hand, the length scale Lx varies logarithmically over the depth of the boundary layer, reaching close to 1 at the boundary layer top.

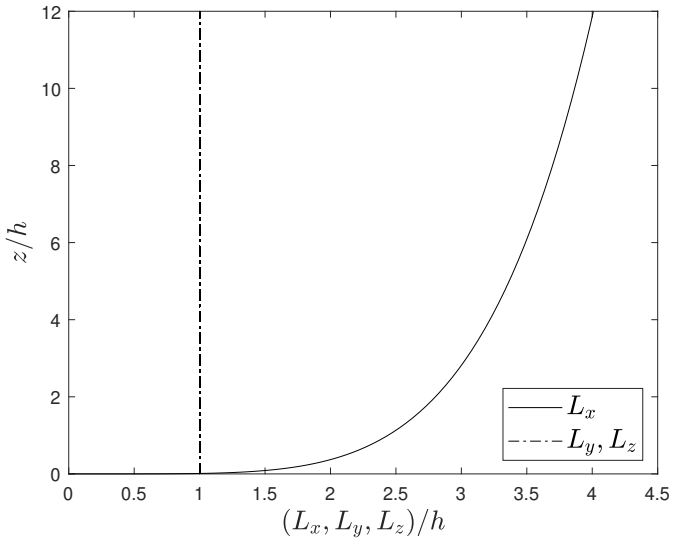

FIGURE 2.8: Vertical profiles prescribed at the inlet for integral length scale

For the stratified cases, the temperature and temperature fluctuation must also be prescribed. Profiles prescribed at the inlet match that prescribed by Sessa et al. (2020) matched with Marucci et al. (2018). The prescribed temperature and variance of temperature profiles are shown in Fig. 2.9.

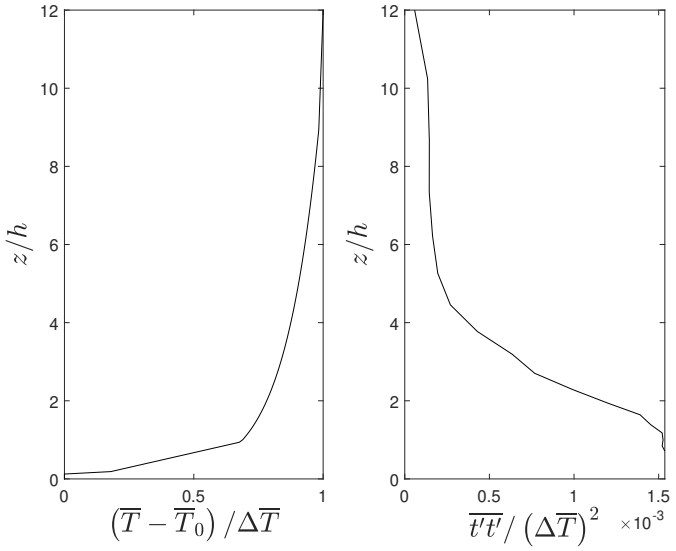

FIGURE 2.9: Vertical profiles prescribed at the inlet for a) mean temperature and b) temperature variance

The initialisation and averaging periods for the STI cases are shorter than that of the PBC cases. The initialisation period was $50T$, with an averaging period of $200T$, exceeding that in previous literature (Sessa et al., 2018, 2020). For the stratified cases, the gravity is altered to change the strength of stratification. Table 2.7 shows the gravity for each of the stratified cases.

TABLE 2.4: Change of gravity, g with the bulk Richardson number, Ri_b

Bulk Richardson number	g
$Ri_b = 0$	0.00
$Ri_b = 0.2$	0.74
$Ri_b = 0.5$	1.77
$Ri_b = 1$	3.54

2.3 Real urban geometries with flat and real terrain

In the course of generating the CAD files, the local building height was seen to be dependent on the terrain treatment. Building height data from the Ordnance Survey can be output in several ways. The height of a building is measured from the lowest point up to the selected height. This can be the top of the eaves or the lowest point the roof intersects the alignment of the external walls, AbsH2, or the absolute maximum height, AbsHMax, the building attains. Two other options exist for data export. These are RelHMax and RelH2. The relative height values give the building height relative to its lowest point. This setting was used for exporting the buildings for use with the flat ground. This is shown graphically in Fig. 2.10.

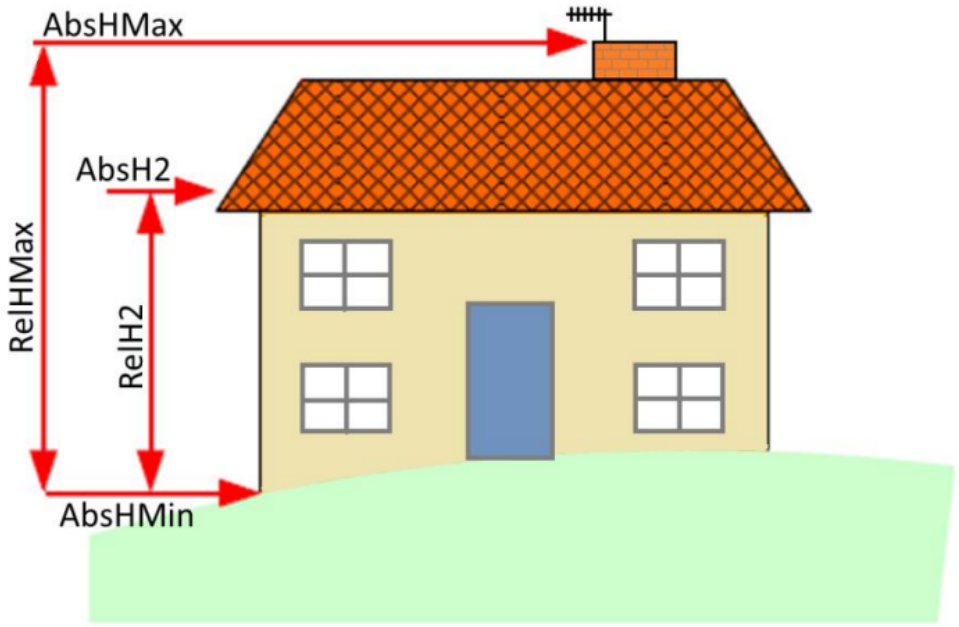

FIGURE 2.10: Building height attributes (BHA) export options from the Ordnance Survey

Therefore, if a location on the perimeter of a building is significantly lower than the majority of the perimeter, this building would have its reported height to be far greater than the height around most of its perimeter. If applying the building heights when using flat ground, the height of the building would not be representative of the vast majority of its local height above the ground.

Therefore the terrain treatment can affect local building height significantly. Fig. 2.17 shows rather drastic differences in local building height for a specific streamwise plane, $y = -104$m. Building height data is given as the distance of the roof to the lowest corner. Across the plane selected, the buildings generally have significantly shorter vertical extents locally for even slight variations in terrain height. For example, buildings labelled as 3, 4 and 5 have changes in local building height up to 1/4 of the total maximum local height across the perimeter of the building.

2.3.1 Settings for semi-realistic and realistic morphology cases

Southampton city lies at the primary confluence of the rivers Test and Itchen. There are also numerous small valleys across the urban area, such as in the Highfield campus, University of Southampton, as shown in Fig. 2.17. These challenge the numerical and physical modelling of wind field and dispersion. Therefore, it is necessary to tackle these issues with the University of Southampton's Highfield campus as a case study.

Complex (Campus)	**Canopy height average (m)**	**Resolution (in Canopy)**	**Domain size h(x,y,z)**
Flat terrain (SF8)	16.3	h/8	50, 56.25, 12
Flat terrain(SF12)	16.3	h/12	50, 56.25, 12
Flume flat terrain(FF8)	16.3	h/8	50, 56.25, 12
'Real' Terrain(ST8)	16.3	h/8	50, 56.25, 10

TABLE 2.5: Outline of Highfield Campus cases with different inflow and mesh-resolution settings.

Ordnance Survey data are used to generate CAD geometry of the Highfield campus terrain, including all buildings. In addition, the surrounding regions, up to 5h, have also been included in the CFD domain with the aim of taking account of their wake effects. The selected GIS data has a resolution of 5m (OS Terrain 5), and the buildings have been generated with the use of the Building Heights from Digimap, part of the OS MasterMap data set. The domain creation was achieved in Blender. Blender was chosen due to its exceptional handling of the .stl file type.

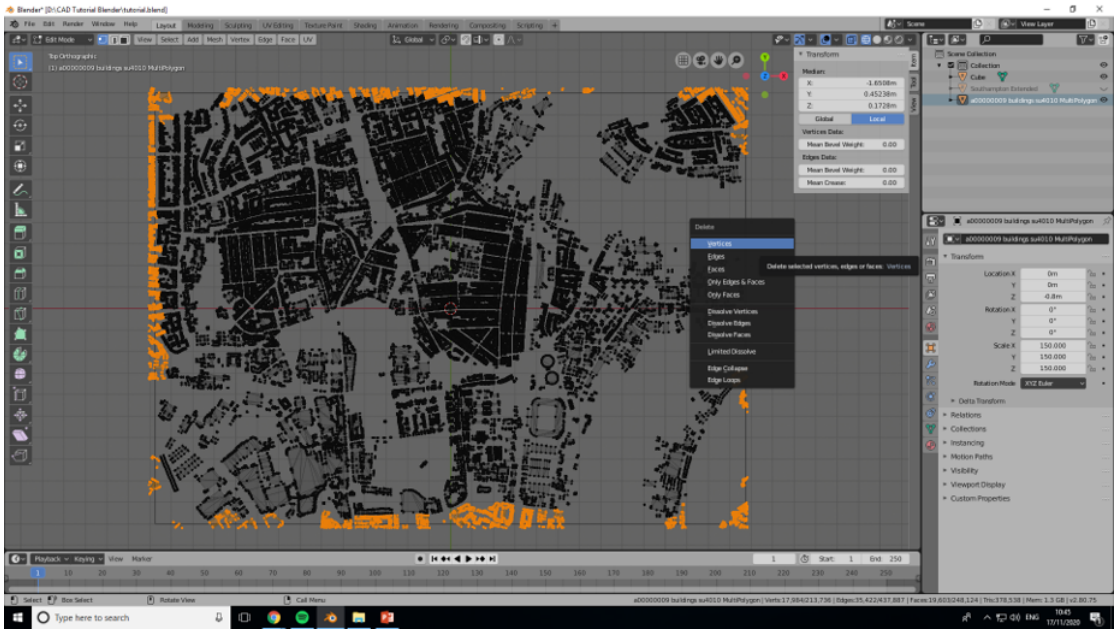

FIGURE 2.11: Blender screenshot of removal of buildings coincident with the vertical patches, inlet, outlet, side_1, side_2

Fig. 2.11 shows the removal process of all buildings that are coincident with the vertical domain patches, the inlet, outlet, side_1 and side_2. All buildings within $5h$ of the boundaries were removed to simplify any issues with boundary conditions, i.e. the side boundaries using symmetry boundary conditions.

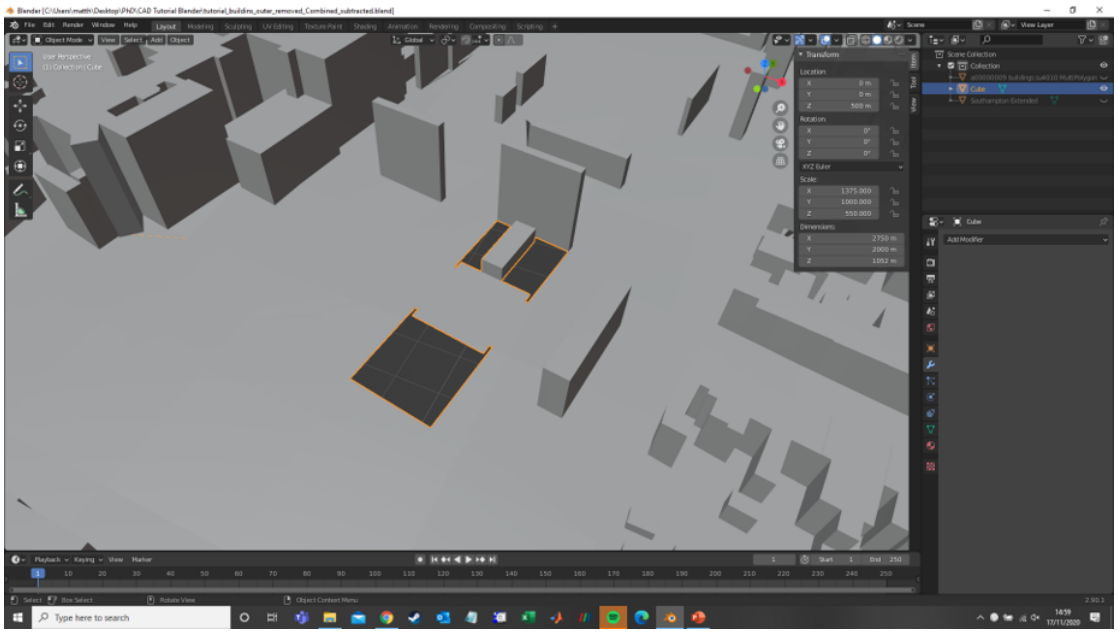

FIGURE 2.12: Blender screenshot of missing buildings from Ordinance Survey data

Fig. 2.12 shows one of the key issues with managing large cases. It is common to find buildings that are missing and thus leave a hole in the .stl surface. This issue must be

solved before running CFD on the domain. It is possible to fill the hole using Blender's simple create function, or it is possible to re-create the specific building. This can be done in Blender or within another CAD software package. This issue was found with most of the data output from the Ordinance Survey, and it needs to be dealt with. Data outputs take the form of $5km$ x $5km$ squares, and within this $25km^2$ area there were many buildings not present, as well as intersecting faces, among other issues. Other issues were not important due to the cell size. Being $2m$x$2m$x$2m$ means that non-coincident edges can be neglected as this process did not change the output mesh, whether it was solved or not.

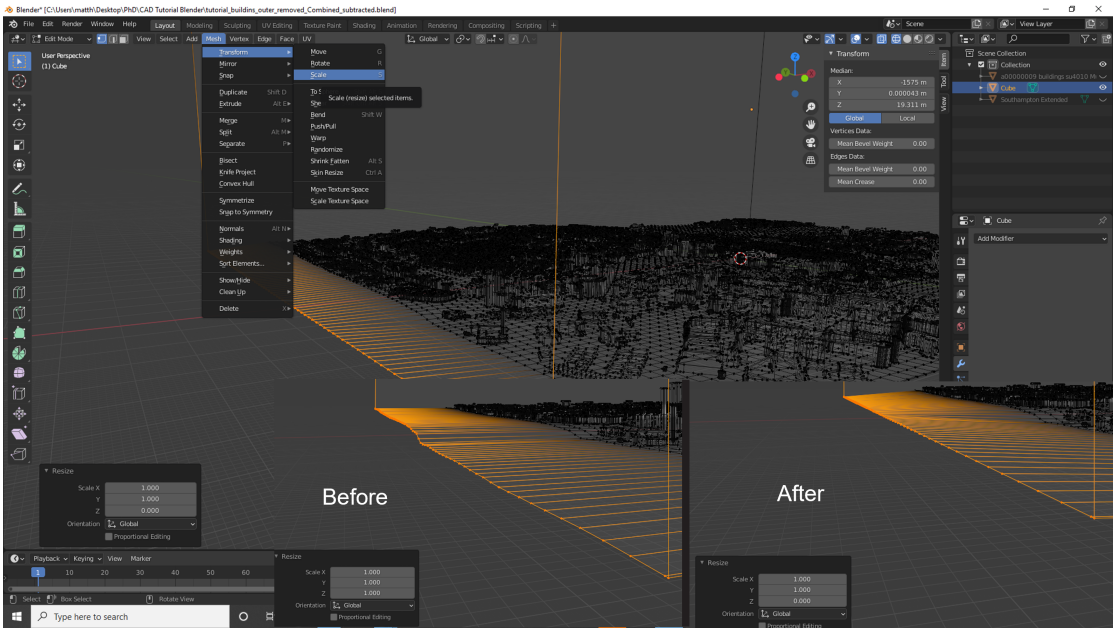

FIGURE 2.13: Blender screenshot of the vertex selection and translation for the inlet patch

Fig. 2.13 shows the inlet patch selected and having been translated upstream by $10h$. This allows the flow to develop, as occurs in the flat terrain case. The other main requirement is that the inlet patch be rectangular to use the synthetic turbulence generator at the inlet of Xie and Castro (2008). In order to have a smooth transition between the bottom side of the inlet and the real terrain, extra vertices are defined between the inlet patch and the first row of vertices in Fig. 2.13, using the subdivide command. These vertices are then constrained in the x, y horizontal directions and are 'smoothed' in the z wall-normal direction. This provides a smooth transition from the essentially flat ground plane of the inlet patch to the real terrain.

The turbulence inflow generation method (Xie and Castro (2008)) is used for a simplified model of the Highfield Campus with the real topology being replaced with a flat ground (Cases SF8 and SF12 in Table 2.5). This will be compared to a model with the real terrain (Case ST8 in Table 2.5) to understand and quantify the terrain effect. Two resolutions (e.g. 1/8H and 1/12H) for the flat ground cases (i.e. SF8 and SF12) are

compared with each other to verify the resolution, along with the validation against the experimental data over a flat ground.

Different inflow conditions are applied to test the sensitivity of inflow turbulence parameters, such as the turbulence intensities and Reynolds stresses. Fig. 2.14 a and b shows inflow conditions used for the DAPPLE site (Xie and Castro, 2009), which are originally obtained from wind tunnel experiments at EnFlo, University of Surrey. These vertical profiles are scaled for various building arrays so that the peaks of Reynolds stresses occur at the average canopy height. The mean velocity and Reynolds stresses obtained for the naturally grown turbulent boundary layer in the flume experiments are applied for comparison (Fig. 2.14 c and d). Cases SF8, SF12 and ST8 use the turbulent inflow quantities at the DAPPLE site, while FF8 use the flume inflow turbulent quantities.

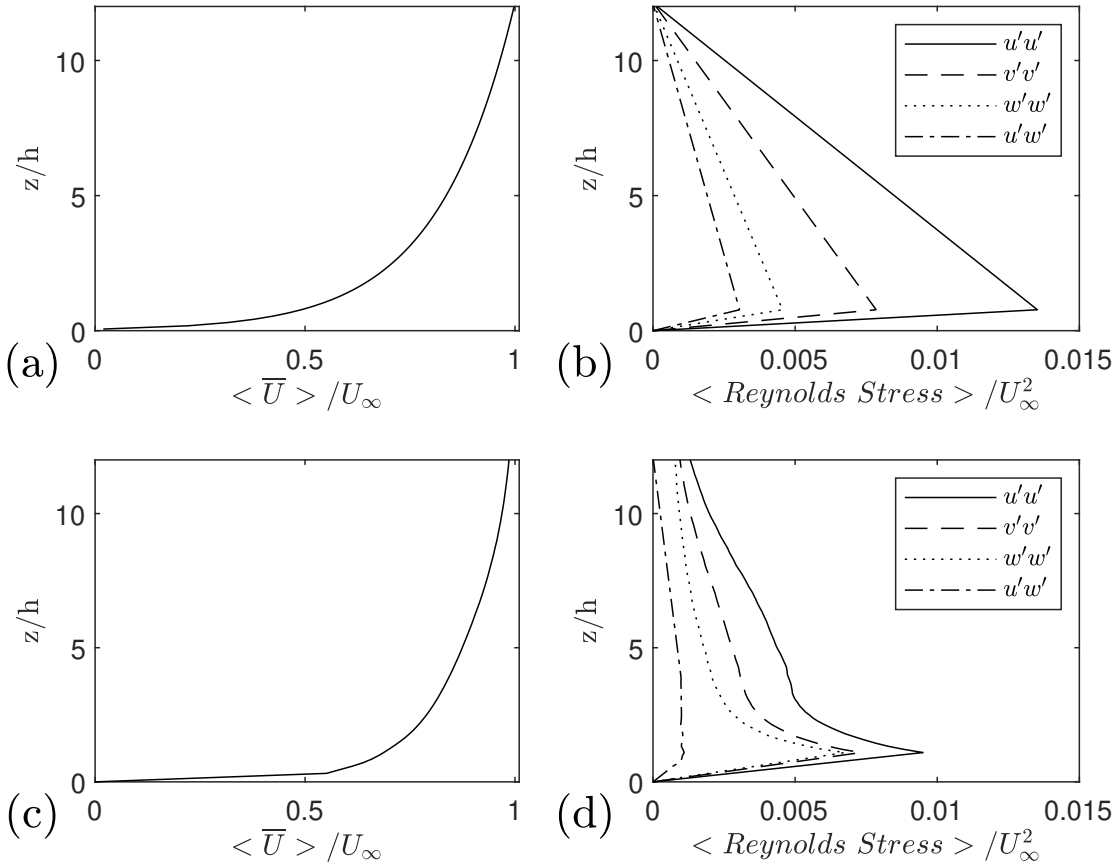

FIGURE 2.14: a) Inflow mean axial velocity and b) Reynolds stresses from the DAPPLE site wind tunnel data (Xie and Castro, 2009). c) Inflow mean axial velocity and d) the Reynolds stresses from the flume experiments.

Complex geometries	Boundary condition
Inlet	Synthetic turbulence Gen.
Outlet	Pressure Outlet
Top	Symmetry Plane
Ground	No-slip Wall
$Side_1$	Symmetry Plane
$Side_2$	Symmetry Plane

TABLE 2.6: Table outlining the Boundary conditions for the Cuboid array cases and complex geometry cases

The integral length scales prescribed in the streamwise, spanwise and vertical directions are shown in Fig. 2.15. The profiles here are the same as the ones given in Fig. 2.8.

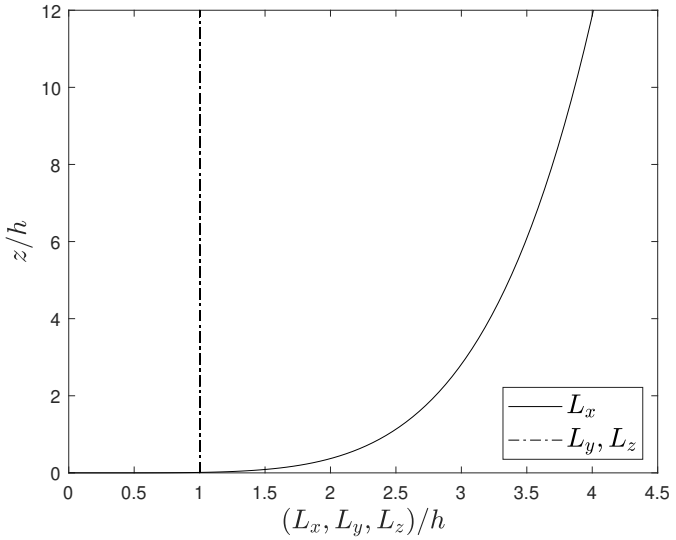

FIGURE 2.15: Vertical profiles prescribed at the inlet for integral length scale

For the stratified cases, temperature and temperature fluctuation must also be prescribed. Profiles prescribed at the inlet match that prescribed by Sessa et al. (2020) matched with Marucci et al. (2018). The prescribed temperature and variance of temperature profiles are shown in Fig. 2.16.

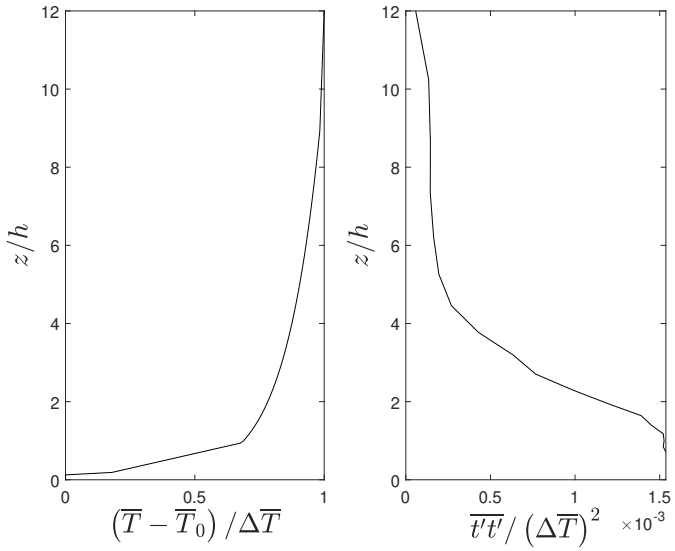

FIGURE 2.16: Vertical profiles prescribed at the inlet for a) mean temperature and b) temperature variance

The initialisation period was $50T$, with an averaging period of $200T$, exceeding that in previous literature (Sessa et al., 2018, 2020). For the stratified cases, the gravity is altered to change the strength of stratification. Table 2.7 shows the gravity for each of the stratified cases.

TABLE 2.7: Change of gravity, g with Bulk Richardson number, Ri

Bulk Richardson number	g
$Ri_b = 0$	0.00
$Ri_b = 0.2$	0.74
$Ri_b = 1$	3.54

2.3.2 Terrain elevation analysis

The area chosen for the study was centred on the University of Southampton's Highfield campus, which contains two significant valleys shown as the dark areas in Fig. 2.17 and the dark blue in Fig. 2.18. The domain was sized to include an area sufficient to capture the flow development over buildings upstream of the campus and the downstream evolution of the wakes created by the campus buildings. The final domain shown in Fig. 2.18a (the flat terrain case) is $900m$ (L_x^F) $\times$ $800m$ (L_y^F) and includes the Highfield campus plus the surrounding area out to a distance of $80m$ (equivalent to $5h$, where h is the average building height). Figure 2.18b shows the domain $1050m$ (L_x^T) $\times$ $800m$ (L_y^T) of the real terrain case, with a $150m$ extension upstream of $x = 0$ compared to Fig. 2.18a. The terrain elevation at location (x, y) in the region $-150m \leq x < 0$ was linearly interpolated between the real terrain elevation of

the corresponding interface ground ($x = 0, y$) and zero terrain elevation of the inlet ground ($x = -150$ m, y). The average elevation over the interface ($x = 0, y$) is zero. The first valley, which has a width of about 50 m and a depth of about $10m$ is shown at $x = 200m$ – $400m$ in Fig. 2.18b. The second deeper, narrower valley appears at $x = 800m$ – $900m$, was near the outlet of the CFD domain and was not the focus of this study.

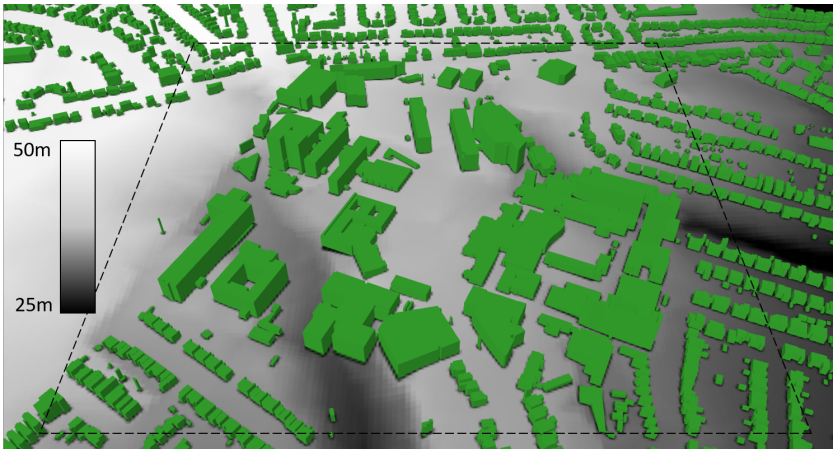

FIGURE 2.17: Three-dimensional geometry and terrain contours (above sea-level) of the Highfield campus, University of Southampton. The dashed frame shows extent of computational domain

This case is referred to as the realistic urban geometry (ST8 in Table 2.5). In order to understand the terrain effects on the urban flows, we generated one simplified flume model (FF8 in Table 2.5) and two simplified CFD models (SF8 and SF12 in Table 2.5) from ST8 replacing the realistic terrain by a flat surface. These are 'semi-realistic' cases.

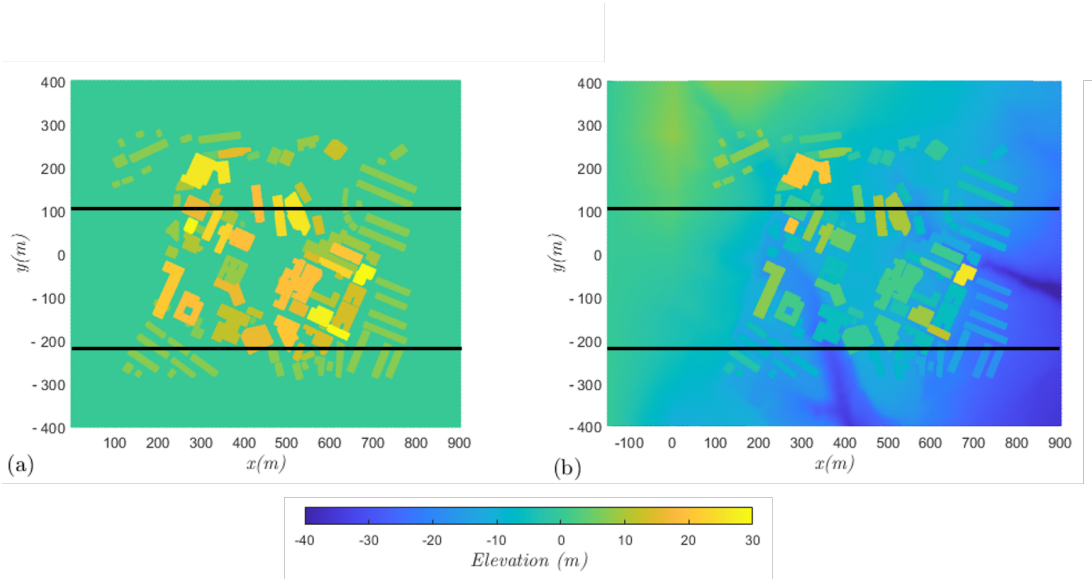

FIGURE 2.18: Contours of the terrain and building elevation for a) the flat terrain case with the ground placed at elevation $z = 0$, and b) the real terrain case with the inlet ground located at elevation $z = 0$. The positive x and y coordinates are west-to-east and south-to-north, respectively. The solid line at y=104 m indicates the streamwise-vertical $(x - z)$ plane in which the PIV data were taken. The solid line at $y = -210$ m indicates an example of $x - z$ plane for further data analysis (e.g. see Fig. 2.19)

Three-dimensional views of the ground elevation for both SF8 and ST8 are shown in figure 2.18. ST8 has a gentle downward slope across the spanwise extent of the domain.

To calculate the average slope (ignoring the building elevation) of each $x - z$ plane, firstly, the average ground elevation $E(y)$ for one $x - z$ plane at spanwise location y with a thickness of the resolution Δy was calculated. Linear interpolation was applied between the upstream and downstream building edges to fill in gaps left from removing building elevation. Secondly, the average gradient of the slope at y was estimated to be the ratio of $E(y)$ and the half length of the domain in the streamwise direction. Thirdly, an average linear slope (i.e. a linear function of x) for the slice starting from the inlet was calculated based on the average gradient. Four $x - z$ planes are shown in Fig. 2.19 for $y = -28m$, $-102m$, $-181m$ and $-210m$, respectively. The the spanwise-averaged slope gradient of the terrain elevation is approximately $-2.3°$.

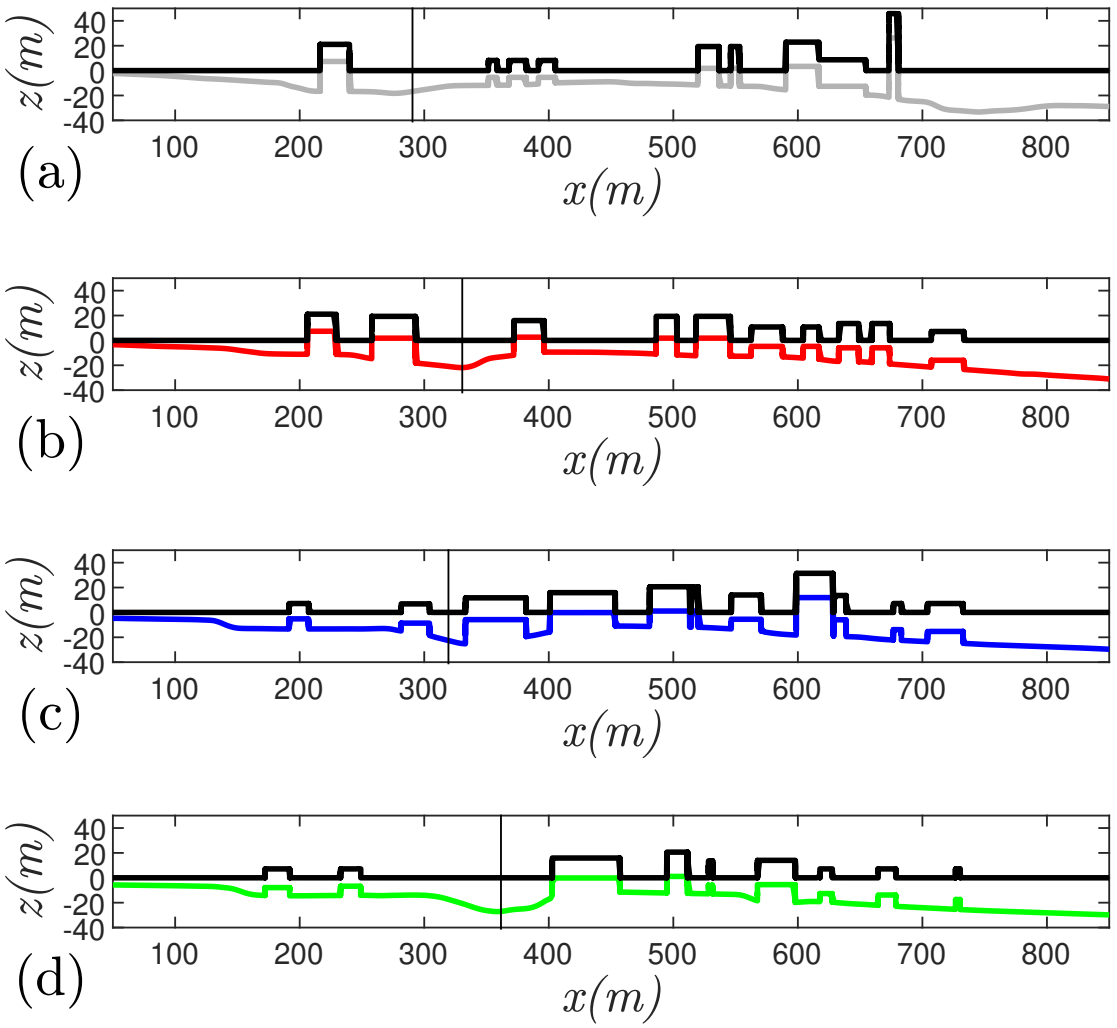

FIGURE 2.19: Terrain and building profiles different spanwise locations, a) $y = -28$ m, b) $y = -102$ m, c) $y = -181$ m and d) $y = -210$ m (see Fig. 2.18). The vertical solid line in each sub-figure marks the location of the valley crossing the $x - z$ plane. Station 1 at $(x, y) = (292$ m, -28 m), station 2 at $(x, y) = (336$ m, -102 m), station 3 at $(x, y) = (332$ m, -152 m) and station 4 at $(x, y) = (376$ m, -210 m)

The mean slope as a function of x is used as a moving average for the slope. The terrain elevation, buildings included, has the moving average slope subtracted from it to create a corrected elevation profile. Where the global slope is removed, the extremes remain, i.e. local hills and valleys. These corrected elevation profiles are shown with their respective locations with the flat ground (SF8) in figure 2.20. Deviations from the flat ground can be seen. The vertical line in each sub-figure marks the location of the valley closely aligned to the spanwise direction. The centre of the university campus, located at $x = 600m$, $y = 0$ is above the average slope in all locations.

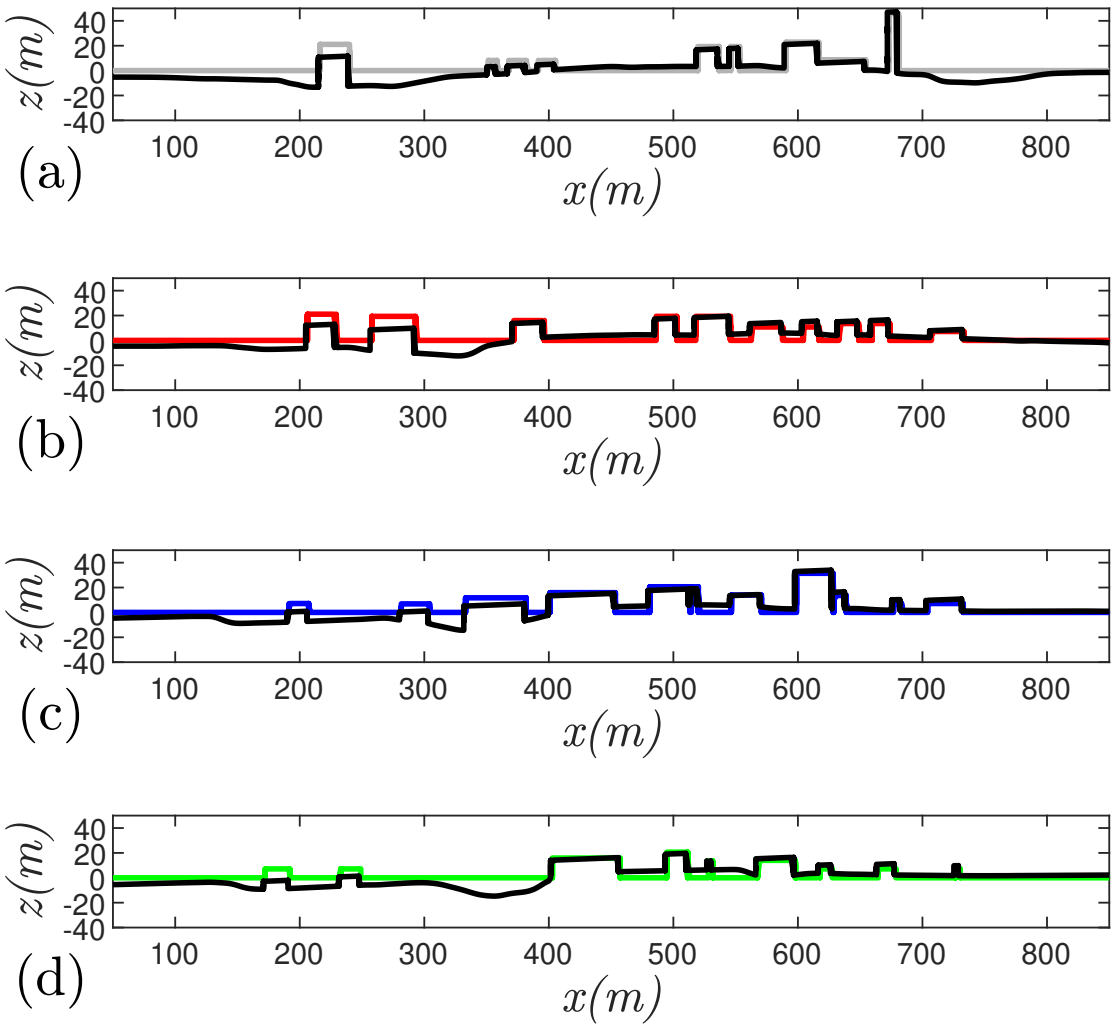

FIGURE 2.20: Corrected terrain and building profiles different spanwise locations, a) $y = 28m$, b) $y = 102m$, c) $y = 181m$ and d) $y = 210m$ from figure 2.18.

These new corrected elevation profiles calculated the statistics for the distribution of elevation height to give a more consistent comparison. The calculated quantities (mean, rms, skewness and kurtosis) for specific profiles and the average is given in Table 2.8.

Case	Slice Location y (m)	Mean Height (m)	RMS	Skewness	Kurtosis
SF8	28	5.893	9.895	2.006	6.929
ST8	28	7.128	11.196	1.689	6.571
SF8	102	5.270	7.112	0.969	2.416
ST8	102	8.276	8.284	0.243	2.000
SF8	180	5.928	8.014	1.372	4.275
ST8	180	9.505	9.607	0.937	3.949
SF8	210	3.372	5.567	1.540	4.178
ST8	210	7.008	8.035	0.306	2.483
SF8	Av.	4.092	6.118	1.177	3.560
ST8	Av.	6.384	7.424	0.635	3.001

TABLE 2.8: Raw data for the flat and terrain case elevation, buildings and terrain included for ST8

Table 2.8 shows that the elevation data for the flat terrain case SF8 is evidently more skewed than that of the terrain case ST8, as shown in Fig. 2.21. This is because the former has much more 0 elevation due to the flat terrain, whereas the latter has more randomly distributed terrain elevations. The elevation of the terrain and buildings is closer to Gaussian and more random. Buildings in the case ST8 are around 15% shorter on average compared to the flat case, SF8, when the building height is the vertical distance between the roof and the average ground level around the perimeter of the building. We would speculate that a 15%difference should not alone produce significant differences in the flow quantities, compared to that by the much greater difference of the terrain.

Coburn et al. (2022); Xie and Castro (2009) emphasise that the distribution and the roof shape of the buildings play a more important role than a small change of the average building height. Comparing the statistics in Table 2.8 and Fig. 2.21 of the terrain and building elevation as a whole, one may argue that the real terrain case ST8 is less rough than the flat case SF8, which perhaps is opposite to intuition.

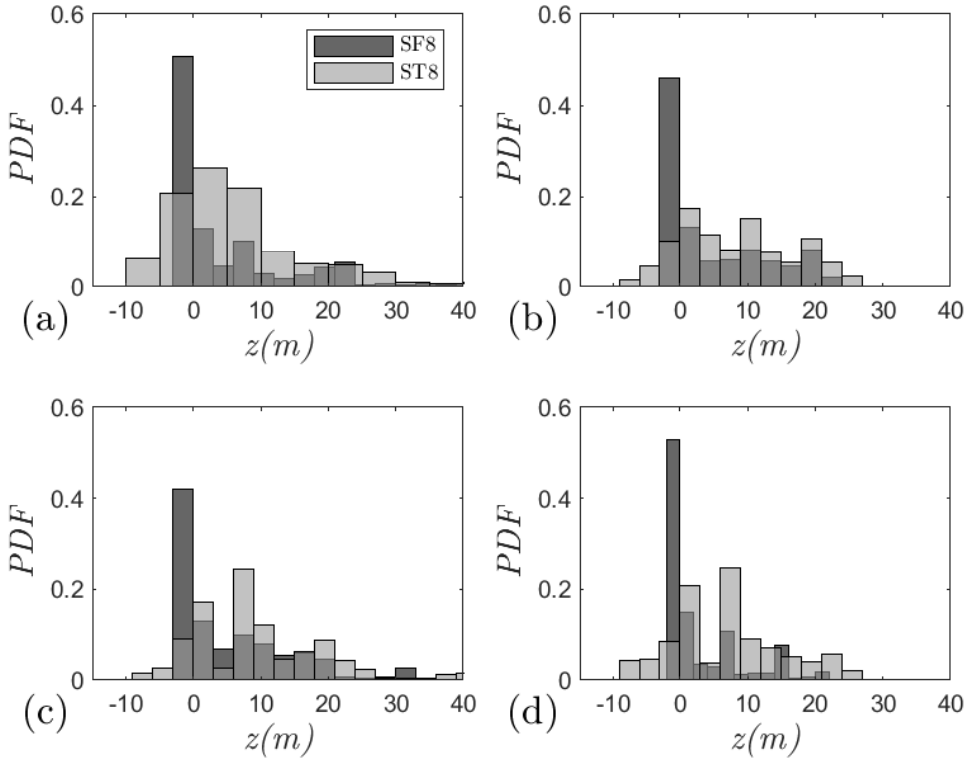

FIGURE 2.21: PDF of the elevation of the terrain and buildings with a spatial resolution of $2m$, which uses the elevation of the correct real terrain and building profile.

2.4 Case Summary

Table 2.9 outlines all the simulations presented here. With the case ID and a short description of the case itself. The first section is for the periodic cuboid array cases; the second is for the cuboid inflow cases with stable stratification. The third is the neutral inflow campus cases with flat and real terrain. The fourth is the inflow turbulence and stable stratification over flat and real terrain.

TABLE 2.9: A complete list of the simulated cases. *H*, block width (Fig.2.3). *PBC*, periodic boundary condition. *STI*, synthetic turbulence inflow boundary condition. The second half of the table outlines the cases of Complex geometry. *h*, average canopy height.

Case ID	λ_p (%)	Block height (H)	*Ri*	Roof type	Mesh type	In-out-BCs
1H(**U**)	33.3	1	0	Flat	**U**niform	PBC
1H(**3R**)	33.3	1	0	Flat	**3**-level **R**esolution	PBC
1.5H(**U**)	33.3	1.5	0	Flat	**U**niform	PBC
1.5H(**3R**)	33.3	1.5	0	Flat	**3**-level **R**esolution	PBC
1.5H45°(**UC**)	33.3	1.5	0	Pitch	**U**niform **C**onformal	PBC
1.5H45°(**UNC**)	33.3	1.5	0	Pitch	**U**niform **N**on-**C**onformal	PBC
1.5H45°(**3RC**)	33.3	1.5	0	Pitch	**3**-level **R**es. **C**onformal	PBC
1H(**U**)	16.7	1	0	Flat	**U**niform	PBC
1.5H(**U**)	16.7	1.5	0	Flat	**U**niform	PBC
1.5H45°(**3RC**)	16.7	1.5	0	Pitch	**3**-level **R**es. **C**onformal	PBC
1.5H(**UCI**)	33.3	1.5	0.2	Flat	**U**niform **C**onformal	STI
1.5H45°(**UCI**)	33.3	1.5	0,0.2, 0.5,1	Pitch	**U**niform **C**onformal	STI

Case ID	*h (m)*	Canopy res.	*Ri*	Terrain treatment	Inlet turb.
FF8	16	$1/8h$	0	Flat	Flume inflow
SF8	16	$1/8h$	0,0.2,1	Flat	Sim. UBL inflow
SF12	16	$1/12h$	0	Flat	Sim. UBL inflow
ST8	16	$1/8h$	0,0.2,1	Real	Sim. UBL inflow

Sim. UBL inflow describes the inflow conditions from Marucci et al. (2018); Marucci and Carpentieri (2020) and Sessa et al. (2018, 2020). Flume inflow describes the incoming flow conditions from the water tank experiment used for case FF8.

Chapter 3

Simplified arrays: Flat vs pitched roofs

3.1 Validation and Verification

3.1.1 Validation of flow simulation around cuboid array

Fig. 3.1 suggests that the domain height was sufficient as there are no effects on the profiles close to the top boundary.

To validate the methodology, simulations were first made of cases 1H(U) and 1H(3R) with PBC at $\lambda_p = 33.3\%$. Fig. 3.1 show vertical profiles of the mean streamwise velocity component U, streamwise normal stress $\overline{u'u'}$, vertical normal stress $\overline{w'w'}$, and Reynolds shear stress $-\overline{u'w'}$ at the centre of the long street marked "1" in Fig. 2.3d. Overall, the differences in these turbulent statistics between the cases 1H(U), 1H(3R) and the LES data in Castro et al. (2017) are negligible within the canopy.

The mean streamwise velocity profiles sampled at typical locations (not shown) also agree well with those in Castro et al. (2017). The two cases 1H(U) and 1H(3R) yield accurate mean flow fields within the street canyon. The turbulent stress profiles of the case 1H(U) are in agreement with those in Castro et al. (2017) over the entire vertical extent. Within the street canyon, the turbulent stresses for case 1H(3R) are in reasonable agreement with those in Castro et al. (2017). Nevertheless, the discrepancy in the Reynolds stresses above $z = 2.5H$ between the case 1H(3R) and Castro et al. (2017) is visible, with its approximate maximum 5%. This difference is due to a greater proportion of the Reynolds stresses being modelled (unresolved) by the SGS model above $z = 2.5H$ due to the coarser resolution for the case 1H(3R). The modelled portion of the mixed time scale SGS model to the total Reynolds stress can be estimated (e.g. Xie et al., 2004). This is not of primary concern to this thesis. Despite

the difference, the mean streamwise velocity is accurately predicted for the case 1H(3R), again suggesting that the mixed time scale SGS model performs well for the coarser mesh.

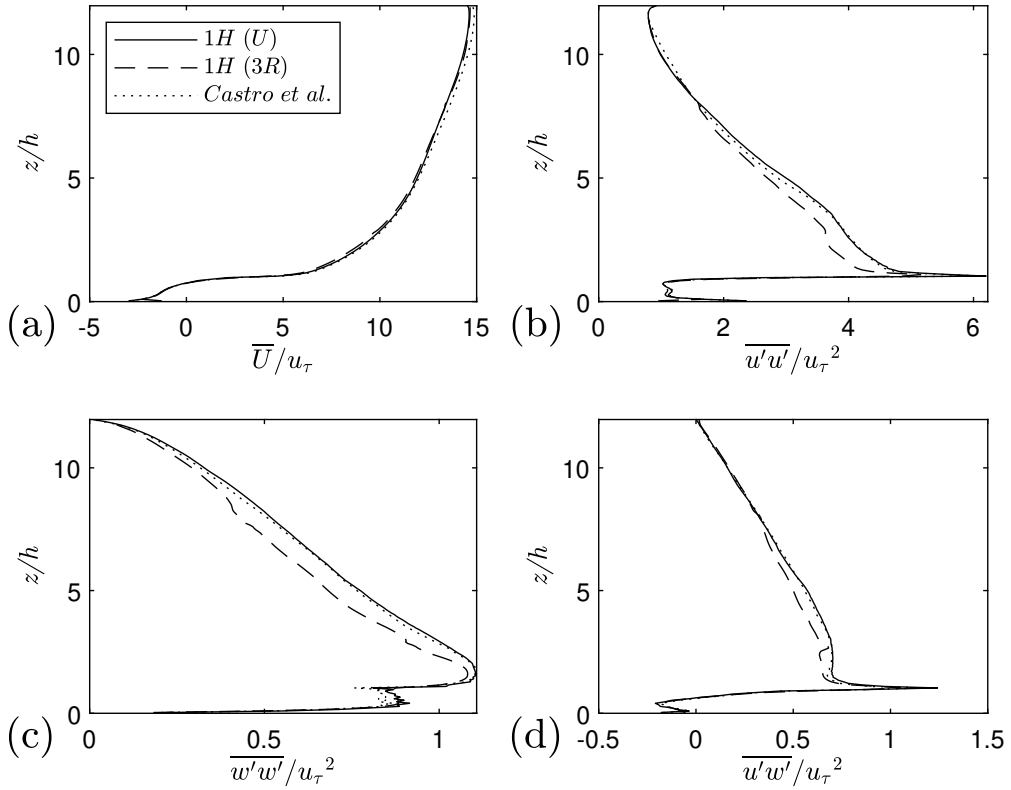

FIGURE 3.1: Comparison between cases 1H(U), 1H(3R) and Castro et al. (2017) data at long street location "1" marked in Fig. 2.3d. a) mean streamwise velocity U, b) streamwise normal stress $\overline{u'u'}$, c) vertical normal stress $\overline{w'w'}$, d) Reynolds shear stress $-\overline{u'w'}$

.

The Reynolds stress profile in Fig. 3.1d for the case 1H(3R) exhibits a slight disturbance at $z/h = 2.5$ and $z/h = 8$, due to the change of grid resolution. In summary, the results suggest that the two conformal (body-fitted) grids 1H(U) and 1H(3R) can produce satisfactory time-averaged velocities and turbulent statistics, e.g. Reynolds stresses. This provides the baseline of the mesh structure, from which the assessment of mesh sensitivity for the pitched-roof cases is carried out in Sect. 3.1.2.

3.1.2 Assessment of Conformal and Non-Conformal Meshes

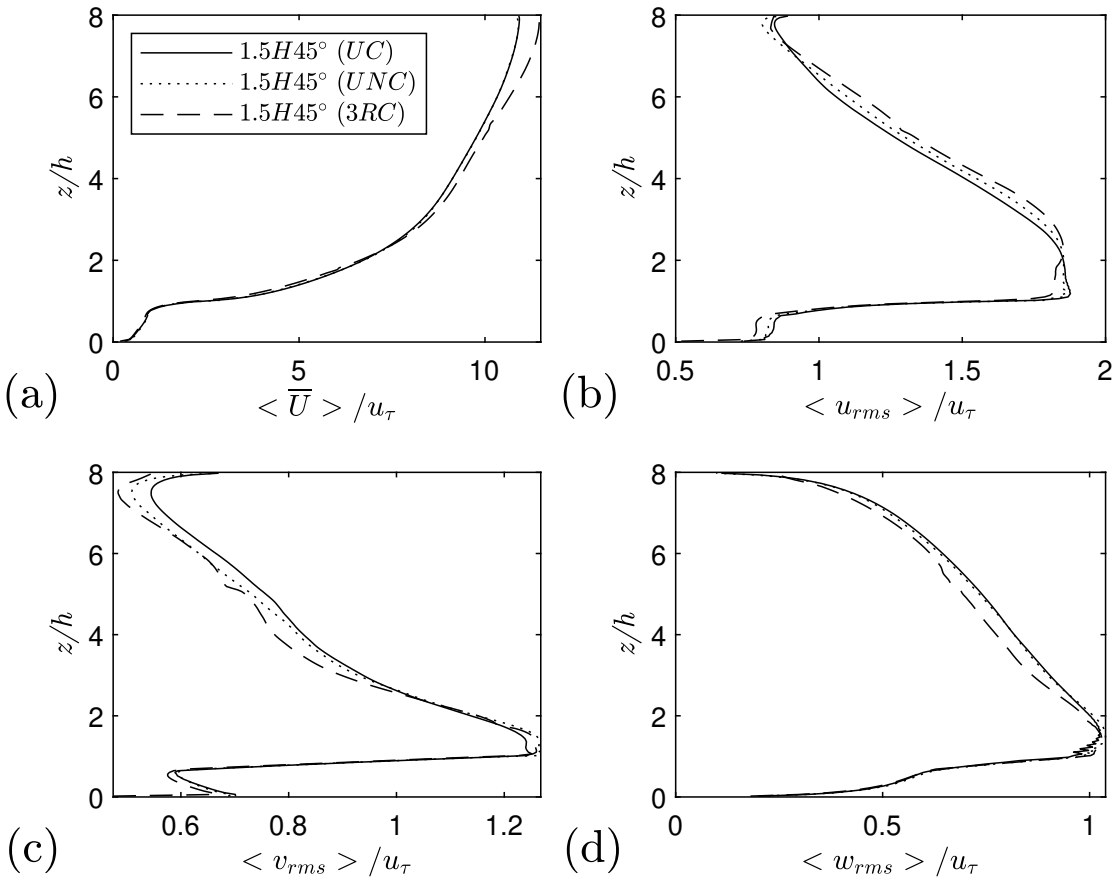

FIGURE 3.2: Grid and geometry effects on a) spatially averaged streamwise mean velocity, b) axial velocity fluctuation r.m.s. c) spanwise velocity fluctuation r.m.s. and d) vertical velocity fluctuation r.m.s.. All normalised by u_τ

This section examines the effect of having conformal or non-conformal grids on the flow predictions obtained for a block array with pitched roofs. This is done by comparing spatially averaged profiles for the 1.5H45° (UC), 1.5H45° (UNC) and 1.5H45° (3RC) cases at a packing density of 33.3% with PBC. Fig. 3.2 shows that all three cases produced consistent vertical profiles of mean streamwise velocity and root-mean-square velocity fluctuation components. Overall agreement between the three cases is satisfactory, especially for the mean velocity profile in Fig. 3.2a. All cases predict similar peak root-mean-square velocity fluctuations with differences of less than 5% within and above the canopy.

At the top of the domain, the increases in axial and particularly spanwise turbulence intensities are due to the so-called 'splatting' of the eddies on the top boundary, where the vertical velocity is constrained to be zero. However, this is not important because, as discussed in Xie et al. (2008), the domain height is great enough to avoid any top boundary condition effect on the regions of interest, i.e. within and immediately above the canopy. It can be seen that at $z/h = 2$ where the interface between the $H/16$

and $H/8$ grid regions occurs, the axial fluctuating velocity root-mean-square peak in Fig. 3.2b and a Reynolds shear stress peak in Fig. 3.3a are visible. These only have a very local effect and do not evidently impact the flow regions within and immediately above the canopy.

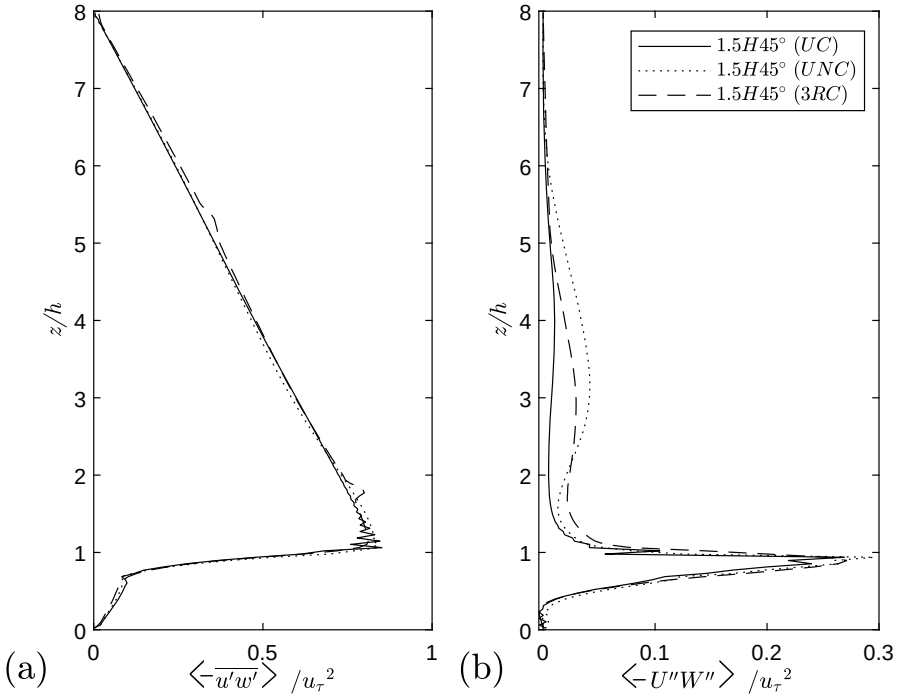

FIGURE 3.3: Grid effects for array of cuboids $\lambda_p = 33.3\%$ with 45° pitched roofs a) spatially averaged Reynolds stress and b) spatially averaged dispersive stress.

Fig. 3.3 shows spatially averaged vertical Reynolds shear stress $\overline{u'w'}$ and dispersive shear stress $\langle -U''W'' \rangle$. The dispersive stress is the vertical momentum flux across a horizontal slide (2.1.4) which is generated by spatial variations in the local time-averaged velocities calculated using spatial averaging over the horizontal slice (Xie and Fuka, 2018). There are negligible differences between the three cases within the canopy. The peak dispersive stress occurs just below the canopy top in all cases. The 1.5H45°(UNC) case with a non-conformal grid and 1.5H45°(3RC) case with coarse grid above the canopy produce a small but visible discrepancy (less than 2% of u_τ^2) from height $z/h = 2$ to $z/h = 5$, compared to the case 1.5H45°(UC). The discrepancy in the dispersive shear stress profile between the conformal and non-conformal grids is visible, with an approximate maximum of 3% of u_τ^2 at $z/h = 3$. This small discrepancy is more likely owing to the uncertainty of calculating the dispersive shear stress than grid conformity. Span-width size structures above the canopy require significant averaging time for obtaining a 'converged' dispersive shear stress. These data confirm the satisfactory accuracy of using the non-conformal grids for the global quantities and those far away from the obstacles. Nevertheless, the accuracy of the near-wall quantities, e.g. surface pressure, is still a question for the use of a

non-conformal grid, such as adopted by the PALM4U (Maronga et al., 2020) and uDALES (Heus et al., 2010; Suter et al., 2022) codes.

It is speculated that the inaccurate representation of the local flow details in the vicinity of the pitched roof in the non-body fitted grid case 1.5H45°(UNC) could affect the prediction of local skin friction and other flow parameters. Nevertheless, Figs. 3.2 and 3.3 suggest the overall discrepancy between the spatially averaged mean velocity, Reynolds stresses and dispersive stresses due to using a non-conformal rather than a conformal grid is small.

Fig. 3.3a shows a linear decrease in Reynolds shear stress from the canopy top, reducing to zero at the domain top. The three profiles of the non-dimensional total shear stress (not shown), including the drag due to the blocks, linearly increase within the canopy to almost unity at the ground, which is expected because a constant body force $\partial P/\partial x$ is set to drive the flow. This confirms the satisfactory accuracy of the simulations (see Xie and Fuka, 2018). The mesh resolution and numerical settings for the flat roof cases validated in Sect. 2.2, were kept the same for the pitched roof cases. All these ensure reliable results for the pitched roof cases.

3.2 Comparison of the turbulence statistics and aerodynamics of flat and 45° pitched roofs

This section compares flow fields, turbulence statistics, surface pressure coefficients and drag coefficients between arrays of cuboids with flat and 45° pitched roofs. It aims to provide an understanding of how having a pitched roof affects these quantities and thereby quantify the importance of accurately accounting for the impact of pitched roofs on the boundary-layer flow.

Two packing densities $\lambda_p = 16.7\%$ and 33.3% of uniform cuboid arrays with and without pitched roofs were simulated. Spatially-averaged mean velocities and Reynolds stress profiles were examined to understand the combined effects of a pitched roof and packing density.

3.2.1 Effect of pitched roof on urban canopy flows

It is known that the upper boundary conditions with a large ratio of the boundary-layer thickness to the building height, such as $\delta/h \approx 10$, yields a negligible effect on the flow and turbulence within and above the canopy (e.g. Coceal et al., 2006; Xie et al., 2008). It is worth identifying any differences of flow and turbulence over pitched-roof and flat-roof buildings in a thick boundary layer. Fig. 3.4a shows a comparison of the spatially averaged vertical profiles of mean axial velocity between the pitched roof case 1.5H45°(UC), and the flat roof cases 1.5H(U) and 1H(U), in which the vertical coordinate is normalised by the canopy height h, and the profiles of root-mean-square velocity fluctuation components are normalised by the friction velocity u_τ. Within the canopy, there are only small differences in the mean velocity between the three cases, as they are of the same packing density λp=33.3%. The two flat roof cases show a much greater inflexion of mean streamwise velocity at the canopy height (Fig. 3.4b), which is associated with an overall "smoother" canopy top resulting in a weaker shear immediately above the canopy, compared to the pitched roof case.

The pitched roof generates far more drag on the flow. This can be seen from the larger momentum deficit in Fig. 3.4a, and from the values of normalised friction velocity in Table 3.1, which show a significant increase for the pitched roof compared to the flat roof at $\lambda_p = 33.3\%$. Note a square of the normalised friction velocity (u_τ^2/U_{3h}^2) is denoted "drag coefficient" (Boppana et al., 2014). Here the mean streamwise velocity U_{3h} at $z = 3h$ is chosen as the reference velocity. Because the dimensionless domain height L_z/h is different for different cases (see Fig.3.12 3.12), the mean velocity at the domain top is not chosen as the reference velocity. Table 3.1 shows that the normalised friction velocity of the pitched-roof cuboid array is approximately 30% greater than

the 1.5H flat roof case and approximately 21% greater than the 1H flat roof case. This strongly suggests that an improved urban canopy model using more advanced parametrisations should take account of the pitched-roof effects.

TABLE 3.1: Normalised friction velocity for each case for packing densities, λ_p = 33.3% and λ_p = 16.7%. $U_{3h}$is the mean streamwise velocity at $z = 3h$

Case	λ_p	u_τ / U_{3h}
1H(UC)	33%	0.0995
1.5H(UC)	33%	0.0928
1.5H 45°(UC)	33%	0.1207
1H(3RC)	17%	0.133
1.5H(3RC)	17%	0.132
1.5H 45°(3RC)	17%	0.130

The flow-fields are now examined in detail to understand the reasons for the increase in friction velocity. Fig. 3.4d shows far higher vertical velocity fluctuations at the canopy height for the pitched roof in the same freestream wind; it is to be noted again that the friction velocity u_τ for the pitched roof case at $\lambda_p = 33.3\%$ is significantly greater than the flat roof cases. This could be considered similar to a random height array (Xie et al., 2008), which produces greater drag and turbulence mixing as well (i.e. than the uniform height blocks with flat roofs). The axial, spanwise and vertical velocity fluctuation root-mean-square data are shown in Fig. 3.4b, c and d, respectively. Within the canopy, the dimensionless root-mean-square velocity fluctuations are significantly different. The behaviour of the vertical profiles for the two flat roof cases is similar above the canopy. In contrast, the deeper canopy evidently suppresses the turbulent fluctuations of all three components within it. The pitched roof alters the behaviour of the vertical profiles significantly above the canopy.

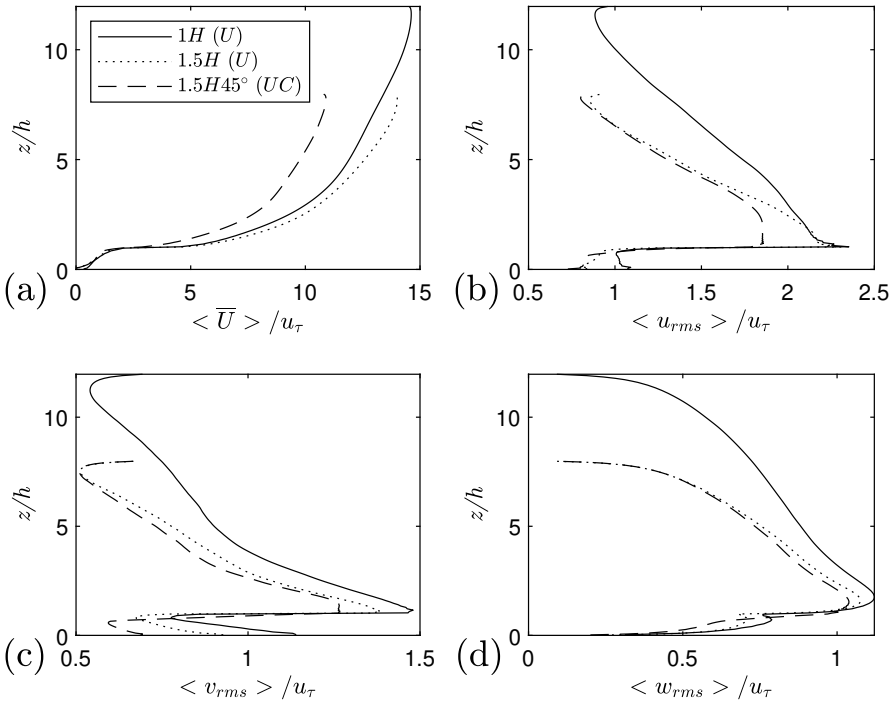

FIGURE 3.4: Comparison of the spatially averaged vertical profiles between flat roof and pitched roof. a) streamwise mean velocity $\overline{U}$, b) u_{rms}, c) v_{rms} and d) w_{rms}

Fig. 3.5a,b,c show mean ensemble average flow field vector plots of the street canyon in the $x-z$ plane up to a height of z/H=2 for the 1H(U), 1.5H(U) and 1.5H45°(UC) cases respectively. The differences in flow patterns are evident. Fig. 3.5a, b for the flat roof cases show skimming flow regimes (Oke, 1988), where the bulk of the flow does not enter the street canyon, and a stable circulation flow is formed in the canyon. A stagnation at $z/h = 0.94$ (Figs. 3.8c and 3.10a) confirms this. Fig. 3.5c for the pitched roof exhibits a flow in the wake interference regime (Oke, 1988), where the downward flows are deflected down the windward roof of the next block downstream, at the stagnation of $z = 0.85h$ (Figs. 3.8e and 3.10b). Dispersive stress within the canopy of the pitched-roof case $1.5H45°(UC)$ (Fig. 3.11) is much greater than that of the flat-roof case $1.5H(U)$ in the same incoming flow. Again, this suggests that the former generates a less stable circulation in the canyon and is in the wake interference regime, whereas the latter is in the skimming region (Oke, 1988).

Fig. 3.5c shows that the shear layer at the canopy top impinges on the windward pitched roof, which explains the greater vertical velocity fluctuations at the canopy height in the same freestream wind (Fig. 3.4d). Much greater vertical mean velocity magnitude (not shown) was also observed at the canopy height for the pitched roof case.

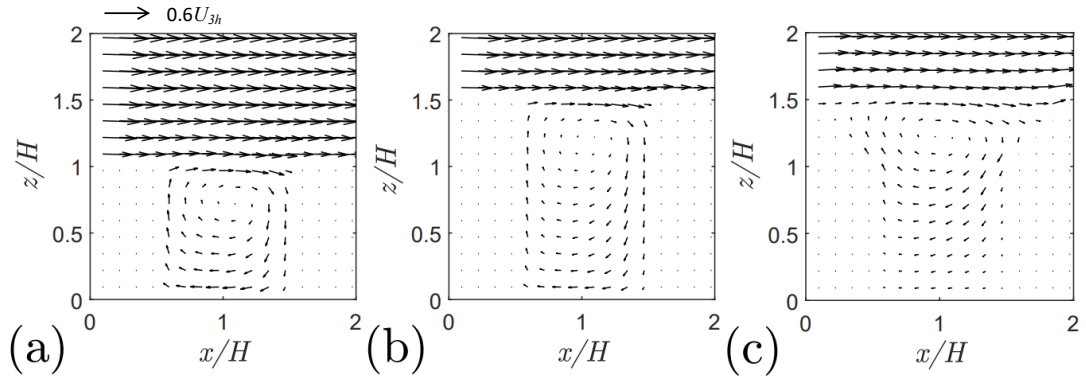

FIGURE 3.5: Vector plot of mean ensemble average velocity normalised by U_{3h} across the $x-z$ plane on the centre of the long street. a) 1H(U), b) 1.5H(U) and c) 1.5H45°(UC)

The observations above are reinforced by Fig. 3.6, showing different normalised instantaneous axial velocity contours for the 1.5H flat and pitched roof cases. The flat roof creates an obvious interface at the canopy top, where a thin shear layer forms, whereas the pitched roof generates a far thicker shear layer from the apex of the roof and a less visible interface. Vorticity contours (not shown) for both cases show the same phenomenon.

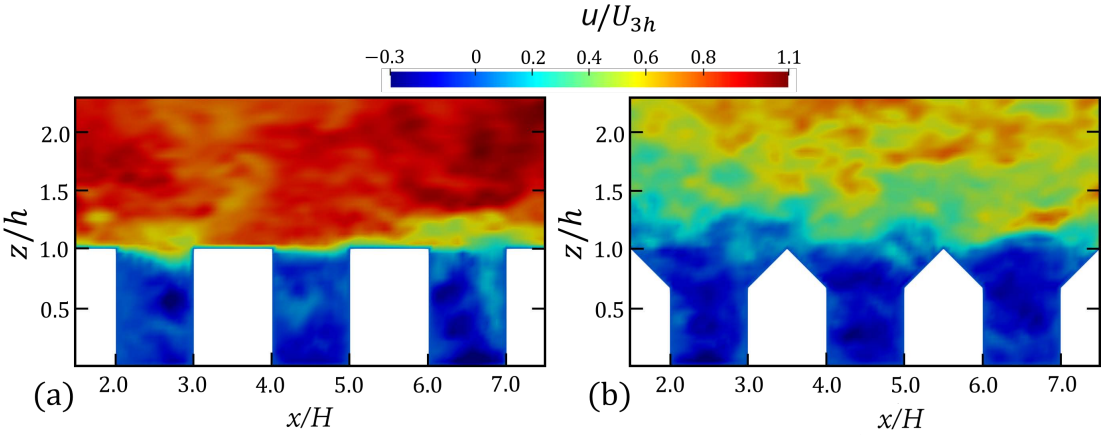

FIGURE 3.6: Normalised instantaneous streamwise axial velocity contour across $x-z$ plane on the centre of the long street for a) 1H(U), b) 1.5H(U) and c) 1.5H45°(UC)

Fig. 3.7 shows how the pitched roof changes the vertical/spanwise flow around the cuboid. The flow above the canopy evident in Fig. 3.7a,b has been documented for uniform height flat-roof cuboids with various aspect ratios (Willingham et al., 2014; Tomas et al., 2017). This vortex pair is present downstream, over the whole extent of the domain. However, the pitched roof effectively destroys these counter-rotating vortex pairs (Fig. 3.7c). This is due to the large mean upward flow at the apex of the roof, which is largely uniform across the span. The pitched roof also enhances the axial rotation seen at the corner of the apex.

The streamwise flow above the canopy of flat roof cuboids, not shown, has a higher velocity directly above the cuboids, being lower in between the cuboids, which corresponds to the high momentum pathway (HMP) and low momentum pathway (LMP), respectively (Yang and Anderson, 2018). The rotation above the flat roof cuboids is consistent with this (Barros and Christensen, 2014). This is opposite to the findings of Vanderwel and Ganapathisubramani (2015). However, their spanwise spacing was significantly larger, and the roughness was continuous along the streamwise direction.

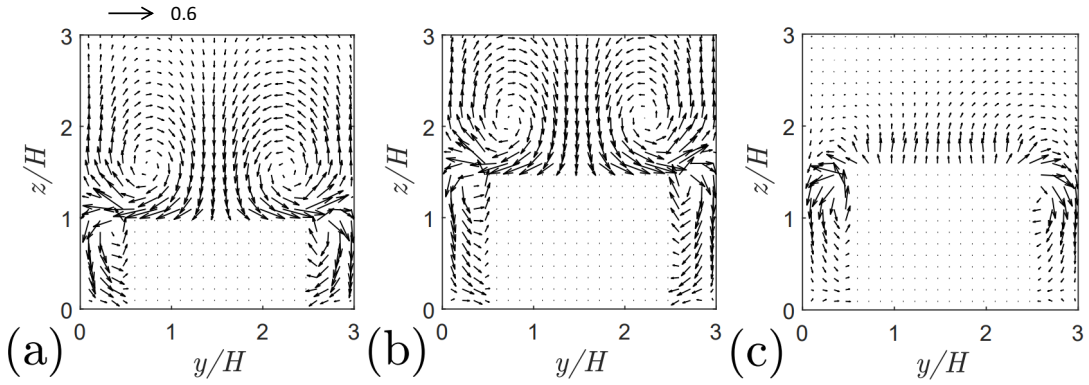

FIGURE 3.7: Vector plot of mean ensemble average velocity normalised by U_{3h} across the $y-z$ plane on the centre of the cuboid. a) 1H(U), b) 1.5H(U) and c) 1.5H45°(UC)

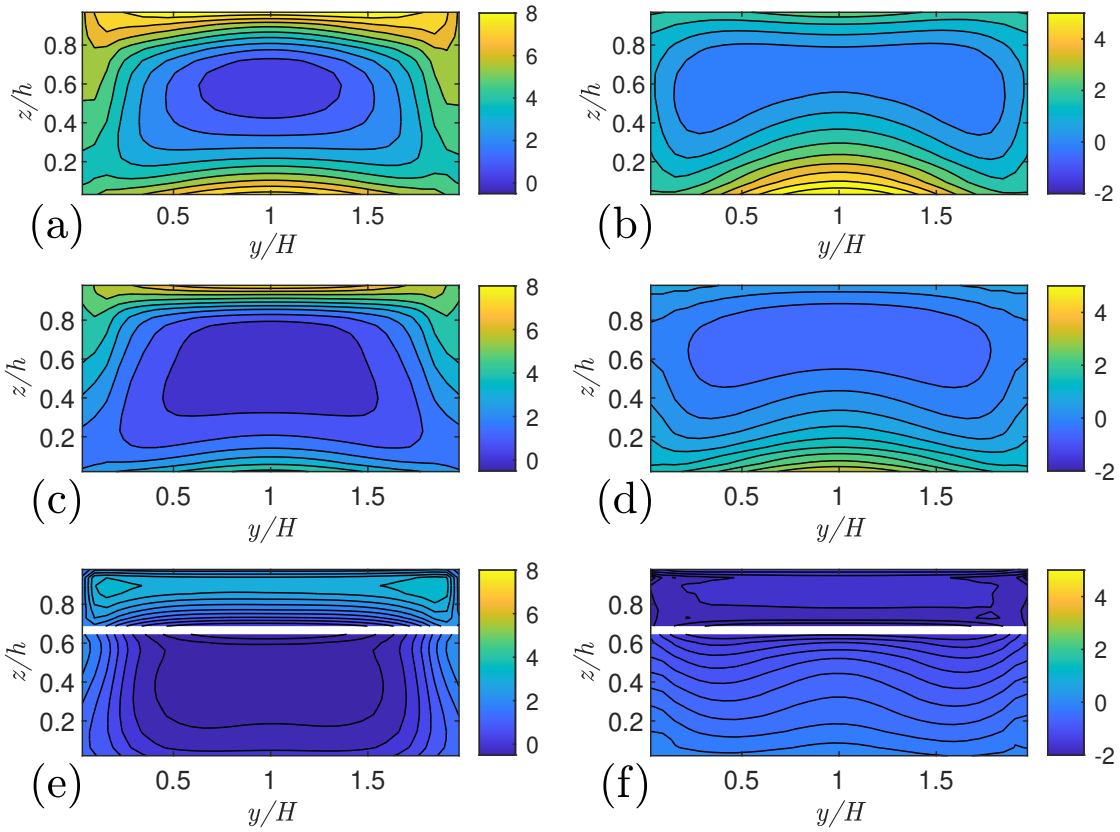

FIGURE 3.8: Surface pressure, P, contours normalised by ρu_τ^2. a) 1H(U) windward, b) 1H(U) leeward, c) 1.5H(U) windward, d) 1.5H(U) leeward, e) 1.5H45°(UC) windward, f) 1.5H45°(UC) leeward. White band denotes the roof-wall joint

Fig. 3.8 shows pronounced differences in the windward and leeward surface pressure distributions normalised by ρu_τ^2 on the three blocks. The windward side plots show similar pressure distributions for both the flat-roof cases, 1H(U) and 1.5H(U) (Fig. 3.8a, c respectively). The pitched-roof case, however, shows a considerably different surface pressure distribution. The vertical face from $z = 0$ to $2h/3$ shows a similar low-pressure region to the two flat roof cases but with a lower pressure which extends much deeper into the canopy and further across the span.

On the leeward side, similar distributions are again observed for the flat-roof cases (Fig. 3.8b, d). But the leeward side of the pitched roof case (Fig. 3.8e) displays a much more uniform distribution across the span due to the more uniform mean flow across the span shown in Fig. 3.7c.

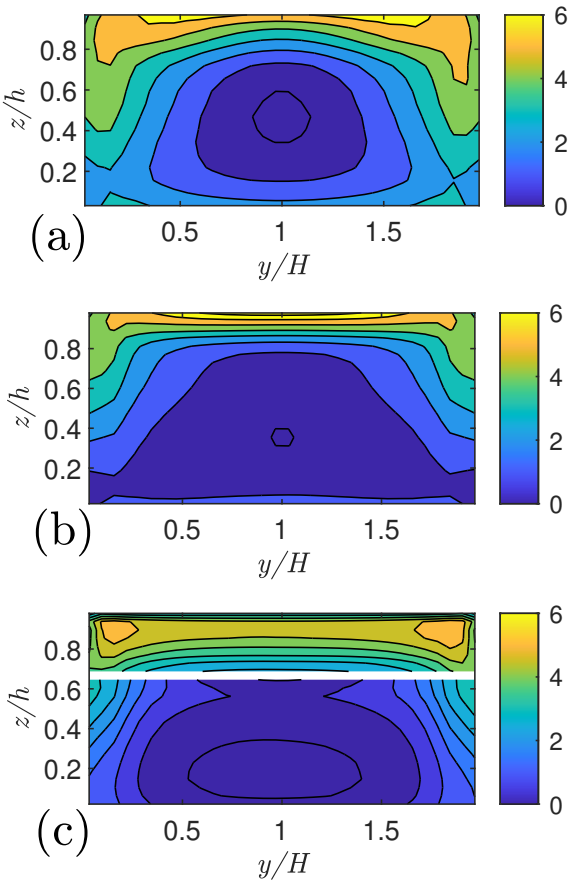

FIGURE 3.9: Contours of pressure difference, ΔP, between the windward and leeward sides normalised by ρu_τ^2. a) 1H(U), b) 1.5H(U), c) 1.5H45°(UC)

Fig. 3.9 shows contours of pressure difference between the windward and leeward sides for the three cases 1H(U), 1.5H(U), and 1.5H45°(UC). This figure shows a similar surface pressure difference distribution to that in Tsutsumi et al. (1992) with the highest volume ratio (packing density). The data collected also follows the same pattern: the surface pressure difference increases from low to high from the centre span to the cuboid edge. The pressure difference peak occurs at $y = 0$ and almost at the canopy top for the flat-roof block, whereas the pressure difference peaks on the pitched roof occurs at $y/H = 0.15$ and 1.85, and $z/h = 0.9$. The pressure difference on the pitched roof shows a high uniformity across the span, which probably results from a dominant flow along the roof surface towards the apex of the roof.

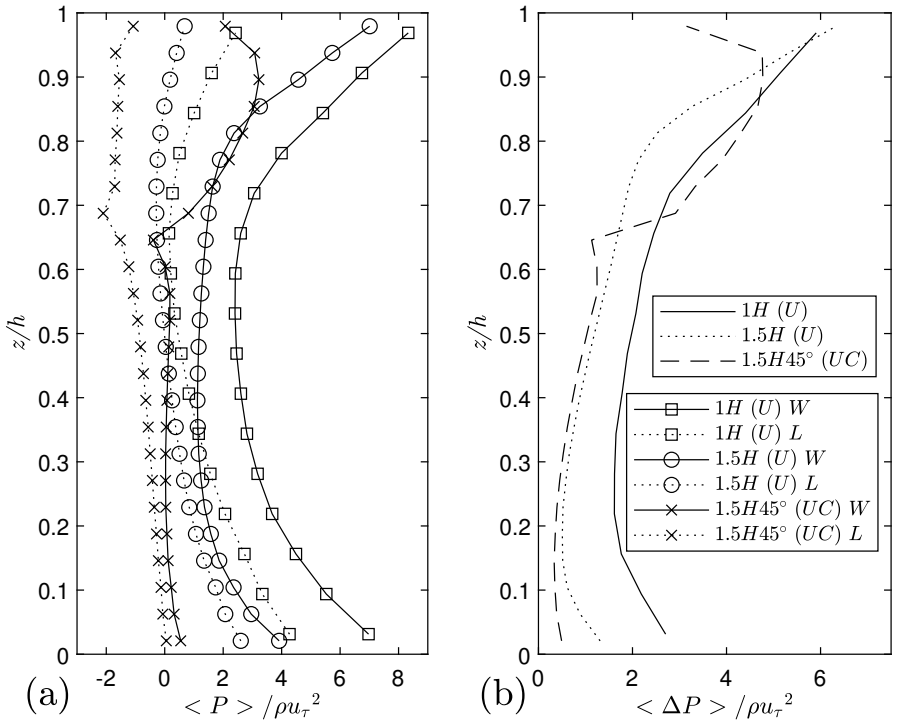

FIGURE 3.10: Comparison of vertical profiles of a) spanwise averaged surface pressure on windward (W) and leeward (L) sides, and b) pressure difference between windward and leeward sides

Fig. 3.10a shows vertical profiles of spanwise averaged surface pressure on windward and leeward sides. The profiles for two flat-roof cases are similar in shape, whereas the pitched roof creates significantly different shaped profiles above $z = 2h/3$. A noticeable inflexion is present in the pitched roof profiles at the transition between side and roof, which occurs at slightly different vertical locations on windward and leeward sides; this is likely due to not having data at the point of transition between the building's vertical and roof faces. The maximum surface pressure at $z/h = 0.9$ on the windward side denotes stagnation. Stagnation is not visible on the windward sides of the flat-roof cuboids, which occurs too close to the canopy top to be resolved in the current mesh. Fig. 3.10b shows normalised spanwise-averaged pressure difference. A considerable difference is evident between the flat-roof case 1.5H(U) and the pitched-roof case 1.5H45°(UC) above $z = 2h/3$.

The form drag due to the pressure difference between the windward and leeward faces is dominant. Xie and Castro (2006) show that the integrated pressure difference between the windward and leeward of an array of cubes is approximately 90% of the total body force imposed, which is equal to an integral of ρu_τ^2 over the ground surface. The pressure difference for the pitched-roof case exhibits an inflexion at $z = 2h/3$ as in Fig. 3.10a, accompanied by an abrupt increase in the pressure difference above $z = 2h/3$, which peaks at $0.9h$ and decreases towards the canopy top. The 1.5H(U) case exhibits a lower pressure difference across the depth of the canopy compared to

the shorter cuboid case 1H(U). A sharp increase occurs above $z = 0.8h$ for case 1.5H(U), and one occurs above $z = 0.7h$ for case 1H(U), which are consistent with the pressure profiles on the windward sides for the respective flat-roof cases in Fig. 3.10b. These changes in shape are likely associated with the heights of the recirculation centres within the long street shown in Fig. 3.7a, b. Again, these suggest that a one-dimensional urban canopy model that resolves the aerodynamic drag distribution within the canopy should take account of the pitched-roof effects.

Fig. 3.11a shows dimensionless spatially-averaged Reynolds shear stress profiles. Within the canopy, the pitched roof generates far less Reynolds shear stress. The profiles for the two flat roof cases are similar, with the lower cuboid case generating slightly more Reynolds shear stress within the canopy. When focusing on the flow immediately above and within the canopy, it is more appropriate to normalise quantities by the friction velocity. Table 3.1 shows more details of u_τ/U_{3h}, where U_{3h} is the mean streamwise velocity at $z = 3h$. When focusing on the flow far above the canopy, it is more appropriate to normalise the flow quantities by the free stream velocity U_∞, or the velocity high above the canopy, e.g. $z = 3h$. It was noticed that the peak Reynolds shear stress normalised by U_{3h} is about 100% higher for the pitched roof case (not shown), suggesting that the pitched roof vastly increases the drag, mixing and re-entrainment of the flow into the canopy. Within the canopy, Reynolds shear stress normalised by U_{3h} shows the same behaviour as that normalised by the friction velocity u_τ. Considering only the packing density $\lambda_p = 33.3\%$ against a flow region map based on flat-roof data, the flows fall into the skimming region. However, the entrainment into the street canyon is less-energetic due to the pitched roof because the mean flow in the shear layer has a non-negligible upwards component, and some portion of the flow is directed upwards instead of into the street canyon. Considering this, the flow over the pitched-roof array with $\lambda_p = 33.3\%$ falls into the wake interference regime.

The pitched roof creates a more uniform mean flow field across the span of the cuboid. The local peak Reynolds shear stress differs by less than 7% across the span of the cuboid at the long street location, i.e. station “1” in Fig. 2.3, with a maximum occurring at the centre of the span. The flat roof cuboid generates the maximum Reynolds shear stress at $0.1H$ from the spanwise edge of the cuboid.

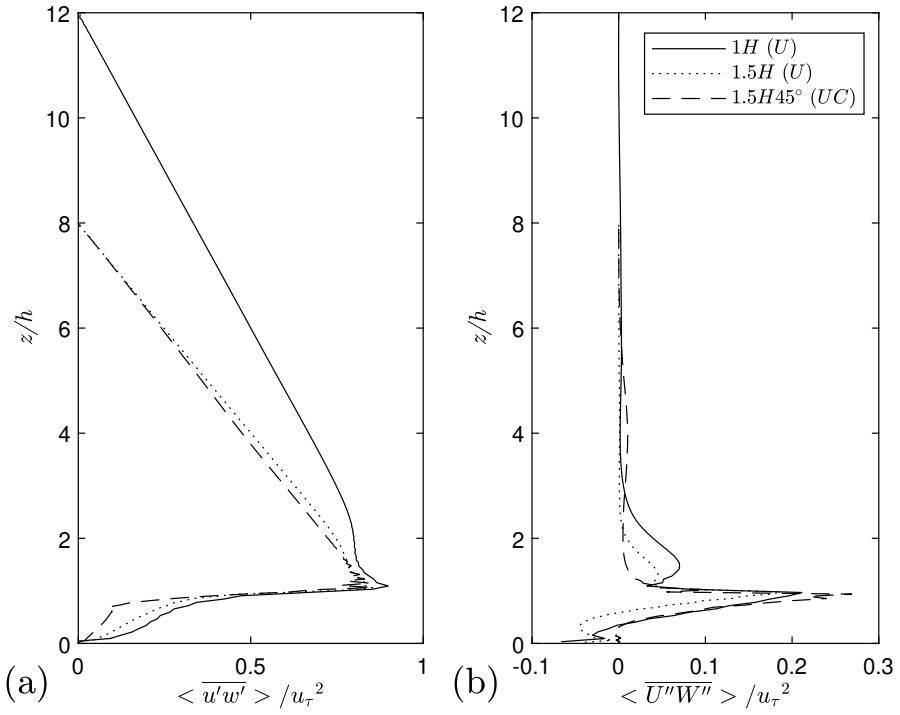

FIGURE 3.11: Spatially-averaged profiles of a) dimensionless Reynolds shear stress, b) dimensionless dispersive stress

Fig. 3.11b shows spatially-averaged vertical dispersive stress profiles, which are the mean flow contributions to vertical momentum flux. The pitched roof creates significantly larger dispersive stresses at the canopy height compared to the flat roof - it is to be noted the friction velocity u_τ is much greater for the pitched roof case. At $z = 2h$ and $1.5h$, the flat roof cuboids generate larger dispersive stresses, whereas the pitched roof generates negligible dispersive stress at the same height. It is speculated that the pitched roof generates more turbulent fluctuations and mixing at the canopy height resulting in less significant mean flow variations.

3.2.2 Packing density effects accounting for roof shape

Table 3.1 shows an evident increase of normalised friction velocity u_τ/U_{3h} for the pitched roof compared to the flat roof at packing density λ_p= 33.3%, suggesting a significant increase of drag coefficient u_τ^2/U_{3h}^2. Nevertheless, Table 3.1 shows no evident difference in u_τ/U_{3h} at packing density λ_p= 16.7%, suggesting that the impact of the pitched roof is highly dependent on the packing density.

Fig. 3.12 shows spatially-averaged mean streamwise velocity and Reynolds shear stress profiles for the three block geometries at packing densities of 33.3% and 16.7%. To emphasise the variation of the canopy drag for different blocks in a given wind, we deliberately use U_{3h} to scale the quantities. With the exception of the 1.5H45°(3RC) 16.7% case, the differences between the mean velocity profiles within and immediately

above the canopy are hard to discern. Oke (1988) suggests that a threshold line between the wake interference and skimming regimes is $h/W \approx 0.65$, where h/W is the canyon aspect ratio, and W is the canyon width. These data are based on a low ratio of building height to width, e.g. $h/W = 1$ (see Fig. 2.3, where $W = H$ for λ_p =33.3%). Oke (1988) also suggests being prudent when using such a threshold, given the uncertainties. As discussed in Sect. 3.2.1, the flow over the flat roofed arrays at λ_p =33.3% and h/W=1.5 is in the skimming regime, whereas at λ_p =16.7% and h/W=0.725 it is in the wake interference regime. Again, these are supported by the flow pattern, surface pressure and skin friction data.

The peak values of Reynolds shear stress for the higher packing density cases are all lower than the peaks for the lower packing density. It is crucial to note that the pitched roof increases the total drag coefficient substantially at the higher packing density $\lambda_p = 33.3\%$, whereas, at the lower packing density, $\lambda_p = 16.7\%$ the effect of the roof on the drag coefficient is small. This confirms the observation in Sect. 3.2.1 that the pitched roof alters the flow regime at λ_p =33.3%, but it does not at $\lambda_p = 16.7\%$. This suggests that the flow regime map against the canyon aspect ratio needs to take account of roof shape and requires a more systematic study of the issue, such as covering a certain range of λ_p and h/W, but as a starting point, a specific case is of interest. Given the significant effect of the pitched roof, the width W_r between one apex of the pitched roof to the next apex is used to calculate the canyon aspect ratio h/W_r. For the pitched roof at λ_p =33.3%, the aspect ratio $h/W_r = 0.725$ falls in the wake interference regime. This is consistent with the h/W=0.725 falling in the wake interference regime for flat-roof arrays at $\lambda_p = 16.7\%$.

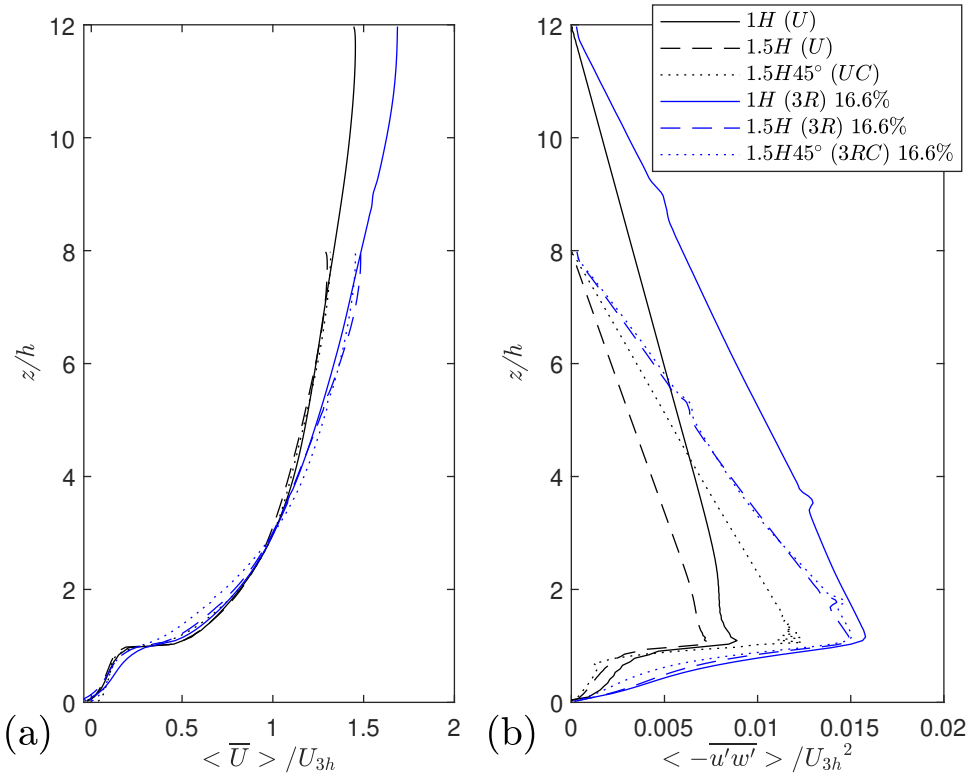

FIGURE 3.12: Effects of packing density and roof shape on a) spatial- and time-averaged axial velocity profile, and b) spatial- and time-averaged Reynolds shear stress

Fig. 3.13 shows spatially-averaged mean streamwise velocity and Reynolds shear stress within and immediately above the canopy. The spatially-averaged mean velocity profiles are similar in shape, but the arrays with the lower packing density produce a smoother transition in the mean flow at the canopy top. As with the values above the canopy shown in Fig. 3.12, there is a clear difference in the values of Reynolds shear stress within the canopy for the two packing densities. It is noticeable that the pitched roof reduces the Reynolds shear stress in most of the regions within the canopy for both packing densities, even though it substantially enhances the Reynolds shear stress at the canopy height when $\lambda_p = 33.3\%$. It is speculated that the 45° slope on the windward side of the block convects most of the turbulence upwards and downstream, whereas the straight vertical windward side of the flat-roof blocks convects a large fraction of the turbulence downwards into a large circulation within the long street canyon as shown in Fig. 3.5.

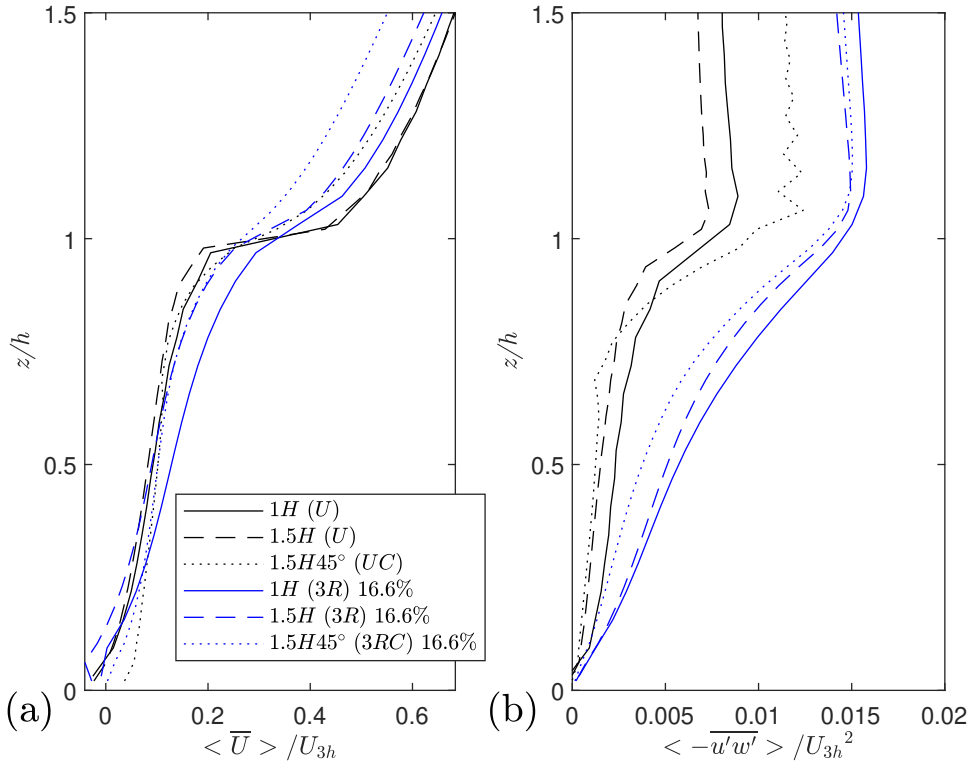

FIGURE 3.13: Effects of packing density and roof shape on a) spatial- and time-averaged axial velocity profile, and b) spatial- and time-averaged Reynolds shear stress

3.3 Discussion of surface pressure on pitched roofs

Holmes (2007) stated that surface loading is dependent on peak surface pressures. This suggests that the level of turbulence in the incoming flow is an essential factor in surface loading. Based on this, it is of interest to compare surface pressure coefficients calculated from the data produced here to values calculated from the Eurocode (En et al., 1991), which is used for estimating wind actions on structures, including pitched (gabled) roof buildings in urban or suburban environments.

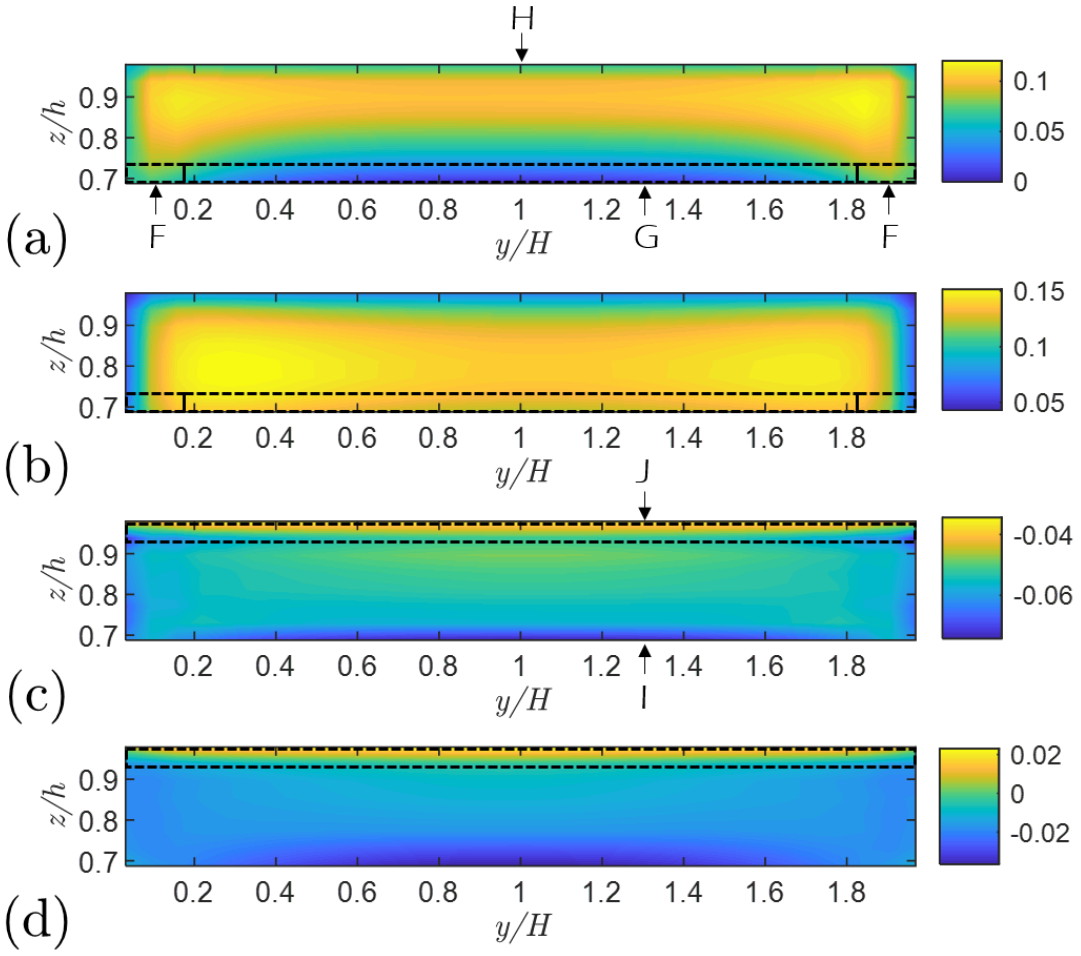

FIGURE 3.14: Surface pressure coefficient, C_p, for the windward side of (a) λ_p = 33.3% (b) λ_p = 16.7%, and the leeward side of (c) λ_p = 33.3% and (d) λ_p = 16.7%. Dashed lines demonstrate the regions for which wind loading can be calculated according to the Eurocode for wind actions, F, G, H for the windward side and J, I for the leeward side

The local surface pressure coefficient is calculated using Eq. 3.1,

$$Cp(t) = \frac{P(t) - P_0}{1/2\rho U_{\text{ref}}^2}, \tag{3.1}$$

where P_0 is the reference pressure, ρ is the density of air and U_{ref} is the time mean velocity, typically taken for low-rise buildings as the upstream velocity at the canopy top (Holmes, 2007). However, as PBC inflow conditions were used for these cases, U_{ref} was obtained following the method in Daniels et al. (2013) by fitting a power law with exponent 0.16, and a coefficient 2.675 to match the velocity profile with a freestream velocity U_∞ at the domain top. U_{ref} was then calculated at the canopy height $z = H$.

Fig. 3.14 shows contour plots of the surface pressure coefficient, as calculated using Eq. 3.1, for the two packing densities. To apply the Eurocode, the surface area is divided into regions F, G, H, I and J as indicated in Fig. 3.14. It is to be noted that the colour bar scales are different to highlight the regions.

Even though the block geometries are the same, there are obvious differences between the two surface pressure coefficient plots. Reducing the packing density and increasing the distance causes the stagnation point to migrate down the windward roof - around 10% of the overall building height. In addition, the pressure on regions F, G and H increases as the distance between buildings increases because the windward roof is more exposed.

Fig. 3.14c and d show a somewhat uniform pressure distribution on the leeward side roof, although slightly lower pressures are predicted on the leeward roof of the higher packing density case. This is likely due to a weakening of the street canyon type vortex, as it is 'stretched' further downstream, as confirmed in Bailey and Vincent (1943).

The Eurocode data (En et al., 1991) provided in Table 3.2 is for the most extreme load case of an isolated 45° pitched-roof building. It gives two sets of data for each of the 5 areas (see Fig. 3.14), and states "...four cases should be considered where the larges or smallest values of all areas F, G and H are combined with the largest or smallest values in areas I and J". Table 3.2 only lists the largest values from the first set data of F, G and H, and the smallest values from the second set data of I and J. Other data are all zero.

Table 3.2 shows that surface pressure coefficients from the two LES cases are very different from the predicted by the Eurocode. This is for two reasons: firstly, the Eurocode data represent the possible extreme of surface pressure coefficients, the estimation of which is outside the scope of this thesis; secondly, Eurocode does not take the effect of sheltering by surrounding buildings into account. Table 3.2 shows substantial differences in the LES predicted average mean surface pressure on every area for the two packing density cases. This questions the applicability of an isolated-building standard for use in suburban or urban environments.

TABLE 3.2: Average mean surface pressure coefficient on the F, G and H areas of windward roof, and the I and J areas of leeward roof, mandated in the Eurocode (En et al., 1991). The table lists the largest values from the first set data of F, G and H, and the smallest values from the second set data of I and J, provided by (En et al., 1991).

Case Description	**F**	**G**	**H**	**I**	**J**
Eurocode	0.7	0.7	0.6	-0.2	-0.3
$1.5H45°(3RC)$ $\lambda_p = 33\%$	0.064	0.025	0.089	-0.045	-0.056
$1.5H45°(3RC)$ $\lambda_p = 17\%$	0.092	0.133	0.121	0.0068	-0.018

3.4 Effects of stratification

3.4.1 Stratification effects on flow quantities around pitched roof buildings

As shown previously, the study of flow over pitched roofs in neutral conditions is a crucial stepping stone, albeit the occurrence of neutral atmospheric stability conditions is very rare. In this section, the effects of stable stratification are examined for pitched-roof cuboids. Again, it is to be noted that the same turbulent and temperature inflow statistics were used for the neutral and stable stratification as in the flat roof cases reported in Sessa et al. (2020). The imposed turbulent kinetic energy at the inlet in the neutrally stratified case is approximately twice that in the stably stratified cases.

Data from the STI domain is shown as spatially averaged between $a(17H) - b(19H)$ (Eq. 4.2). Fig. 3.15 shows laterally averaged time-mean vertical velocity and Reynolds stress profiles at $x = 18.5H$ for four stratified conditions. The mean velocity profile is negligibly affected by all the stratification conditions or the inflow turbulence level, whereas for flat-roof cuboids in Sessa et al. (2020) (i.e. Fig. 7) the effect was more evident.

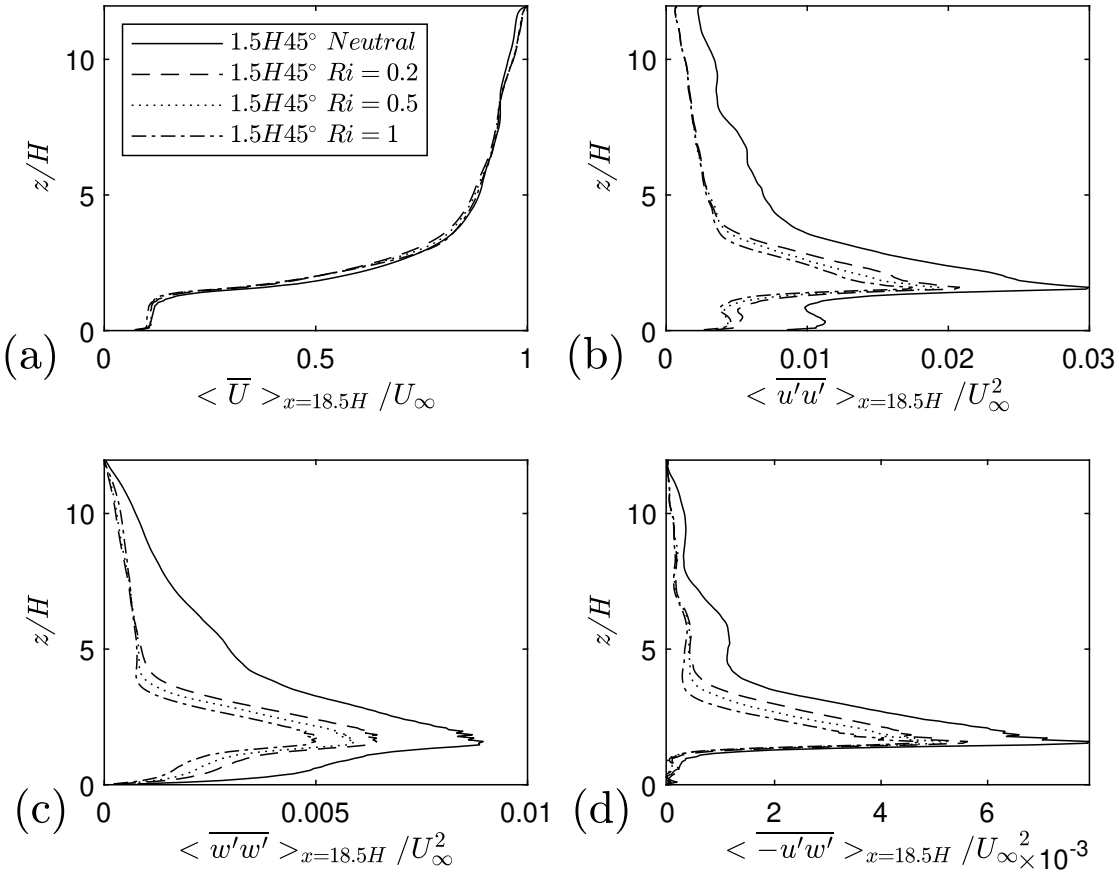

FIGURE 3.15: Spanwise averaged data at $x = 18.5H$ for neutral and stratified conditions, $Ri_b = 0.2, 0.5, 1$, (a) mean velocity, (b) streamwise stress, (c) vertical stress and (d) Reynolds stress, normalised by the freestream velocity

Fig. 3.15 shows an evident effect of stratification and inflow turbulence level on the turbulent statistics. The reduction of streamwise normal stress (Fig. 3.15b) in going from $Ri = 0.2$ to $Ri = 0.5$ for the pitched roof case is approximately 7%, in contrast to a reduction of 25% for the flat-roof case (Sessa et al., 2020). For $Ri_b = 0.2$ and $Ri_b = 1$, the differences are 16% and 50% for the pitched and flat roof cases, respectively. These suggest the effect of a pitched roof opposes typically associated with the stable stratification.

The evident differences in the streamwise and vertical stresses between the neutral and the case $Ri = 0.2$ (in Fig. 3.15) are mainly due to the large difference of the inflow turbulence level. Nevertheless, these differences for the pitched roof cuboids are far smaller than for the flat-roof cases shown in Fig. 8 in Sessa et al. (2020). This suggests that the flow created around pitched roof cuboids leads to an evident reduction in the effect of inflow turbulence level when compared to the flows over flat-roof cuboids for the same inflow conditions.

In neutral conditions, the flat roof generates around 10% stronger streamwise fluctuations than the pitched roof, whereas it generates around 10% less vertical fluctuations than the pitched roof (see Fig. 3.15, and Sessa et al. (2020)). This suggests that the pitched roof generates more three-dimensional turbulent eddies above the canopy, as opposed to the thin shear layers generated by the flat roof at the canopy height. Thermal stratification normally inhibits vertical momentum transport, while pitched roofs promote it by pushing flow upwards or downwards, so they have the opposite effect. The more energetic vertical turbulent fluctuations at the top of the pitched-roof cuboids reduce the effects of the stratification and the inflow turbulence level.

Through spanwise averaging across the entire region of the 8^{th} row, the flow quantities are shown in Fig. 3.16. This data is spanwise averaged, then averaged in the streamwise direction from the front of the building in row 8 up to the front of the buildings in row 9. The results are similar to the spanwise average at $x/h = 18.5$; however, the relative difference between the peak values for the different stratification strengths has decreased, and so have their peak values.

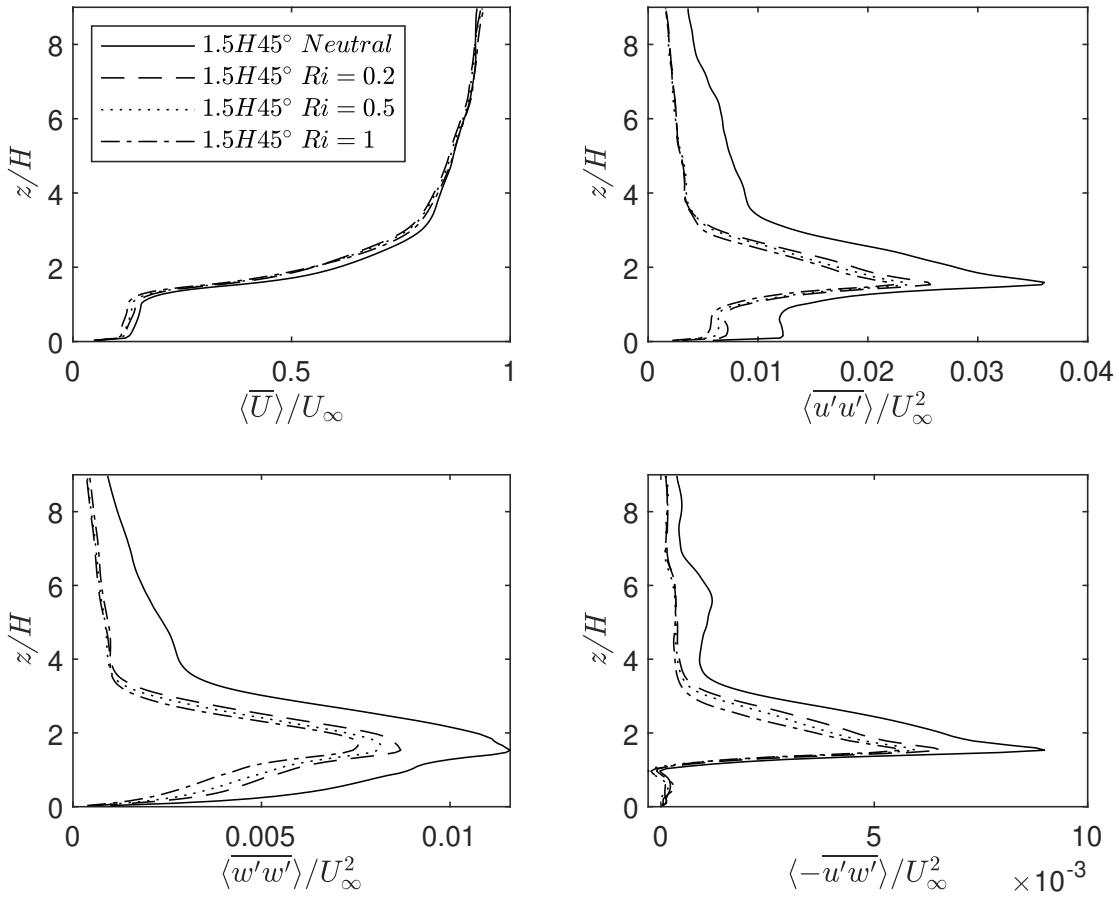

FIGURE 3.16: Spanwise averaged data for the 8^{th} **link to Fig. in methodology** row for neutral and stratified conditions, $Ri_b = 0.2, 0.5, 1$, (a) mean velocity, (b) streamwise stress, (c) vertical stress and (d) Reynolds stress, normalised by the freestream velocity

Fig. 3.17 shows contours of vertical stress $\overline{w'w'}$ across a vertical plane located at $y = -1.5H$ (see Fig. 2.6) for $Ri_b = 0$, 0.2, 0.5 and 1. It is evident that the stable stratification reduces the strength of fluctuations across the entire fetch of the domain. Fig. 3.17 also shows that the growth of the IBL is suppressed in the stratified flow. However, such a stratification effect is evidently less effective in suppressing the IBL when compared to its effect on the flow over flat-roof cuboids (Sessa et al., 2020), as discussed in 3.5.1.

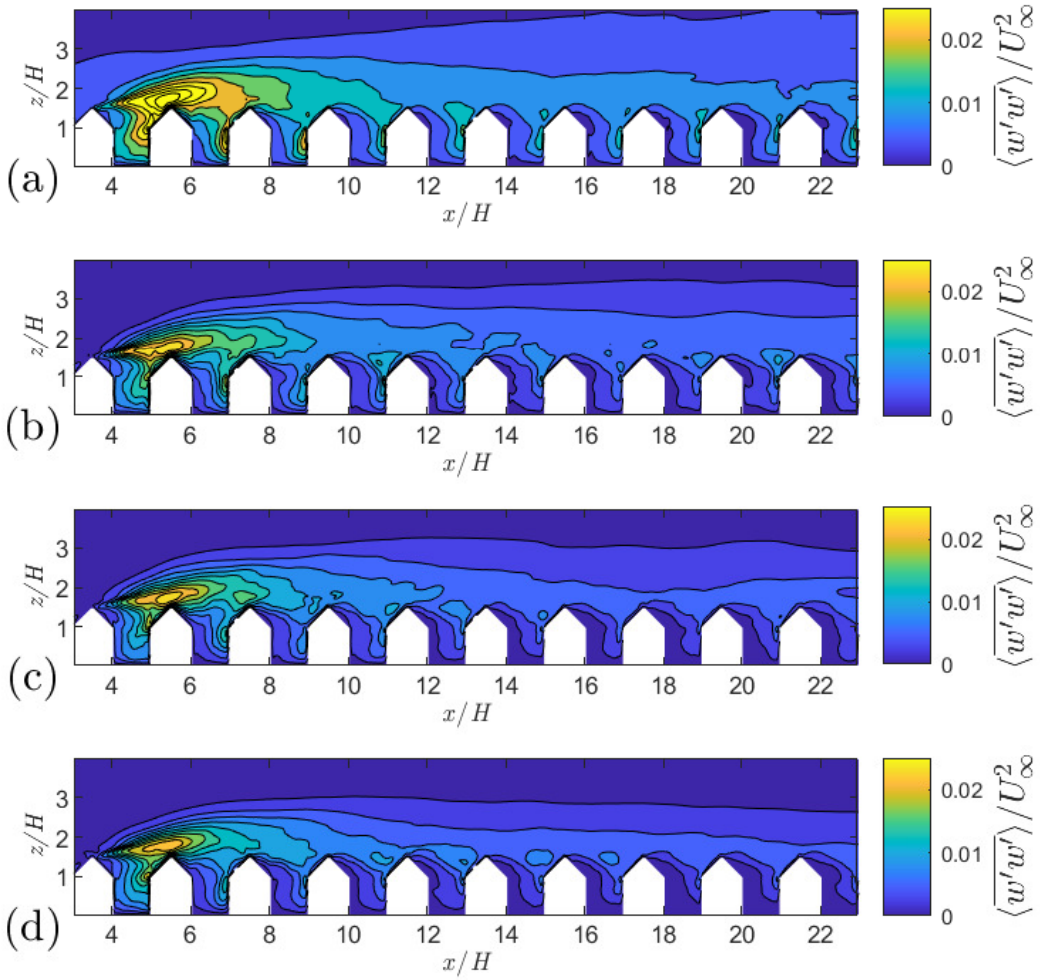

FIGURE 3.17: Variance of vertical turbulent fluctuations normalised by freestream velocity for a) $Ri_b = 0$, b) $Ri_b = 0.2$, c) $Ri_b = 0.5$ and b) $Ri_b = 1$, along the longstreet location

The spanwise averaged data from the leading edge of the array is shown in Figs. 3.18 and 3.19 for the normalised streamwise and vertical velocity respectively, and Figs. 3.20 and 3.21 show the normalised streamwise vertical stress and Fig. 3.22 shows the normalised Reynolds shear stress.

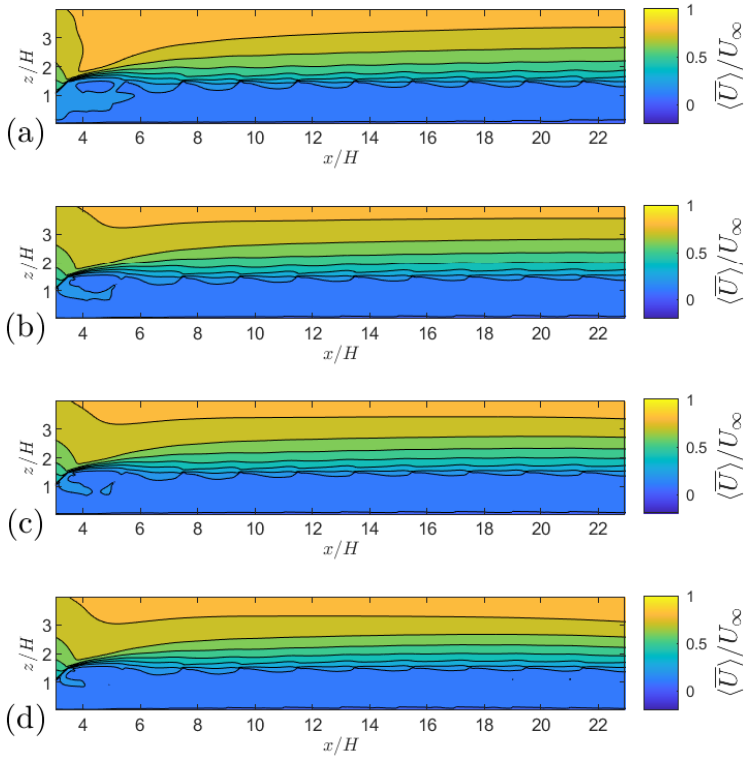

FIGURE 3.18: Contours of spanwise averaged mean streamwise velocity. For a) Neutral, b) $Ri_b = 0.2$, c) $Ri_b = 0.5$ and d) $Ri_b = 1$

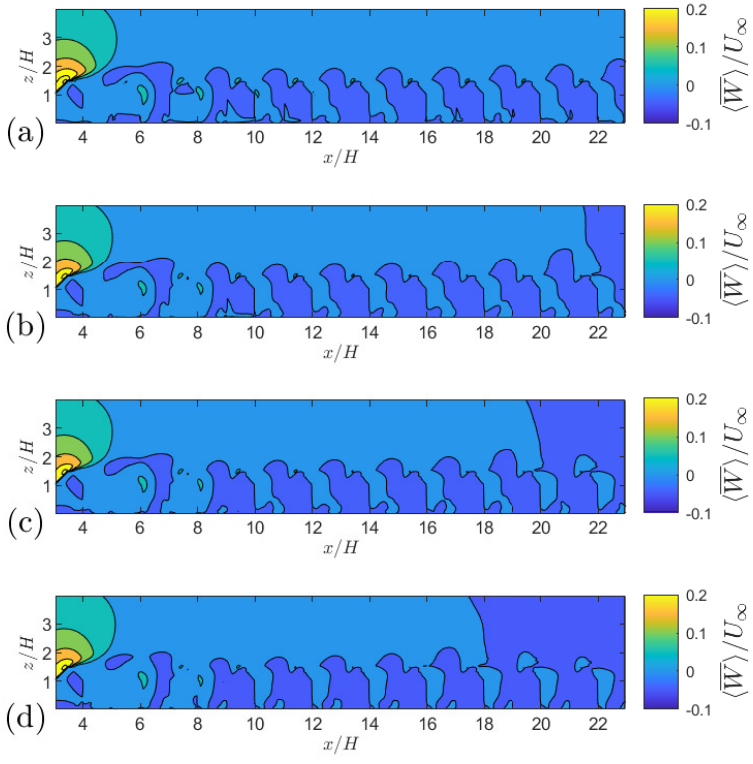

FIGURE 3.19: Contours of spanwise averaged mean vertical velocity. For a) Neutral, b) $Ri_b = 0.2$, c) $Ri_b = 0.5$ and d) $Ri_b = 1$

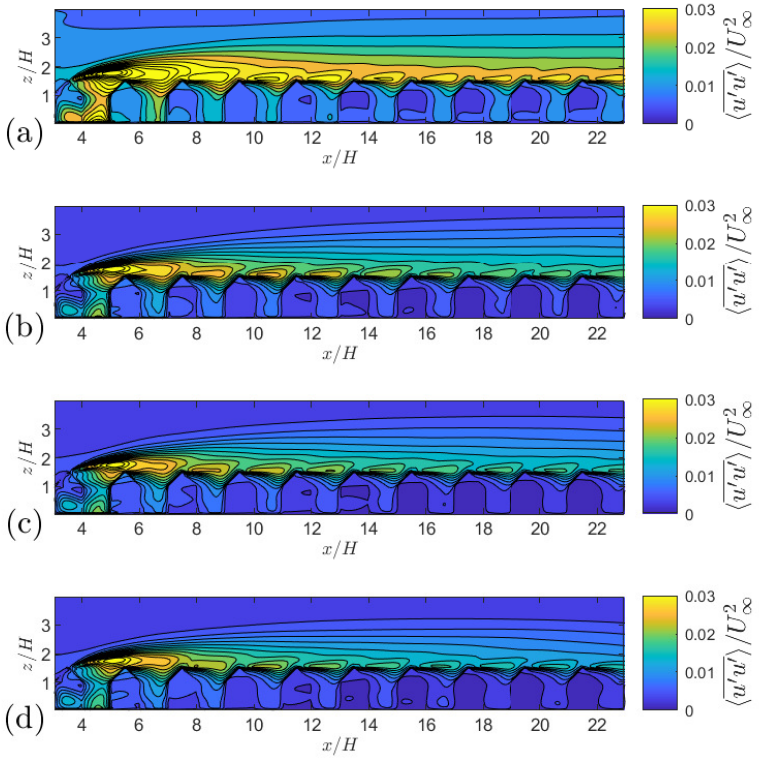

FIGURE 3.20: Contours of spanwise averaged streamwise velocity variance. For a) Neutral, b) $Ri_b = 0.2$, c) $Ri_b = 0.5$ and d) $Ri_b = 1$

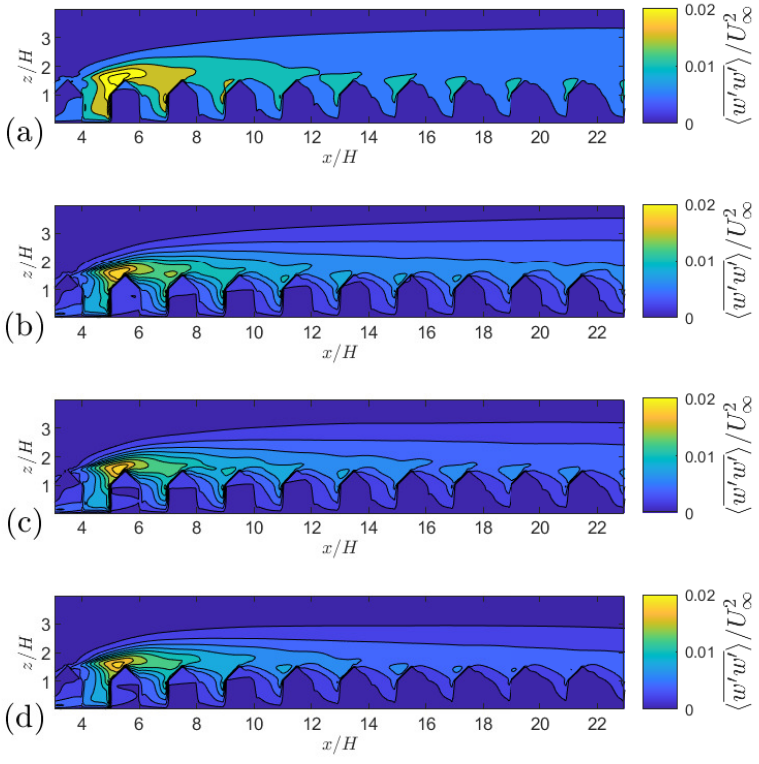

FIGURE 3.21: Contours of spanwise averaged vertical velocity variance. For a) Neutral, b) $Ri_b = 0.2$, c) $Ri_b = 0.5$ and d) $Ri_b = 1$

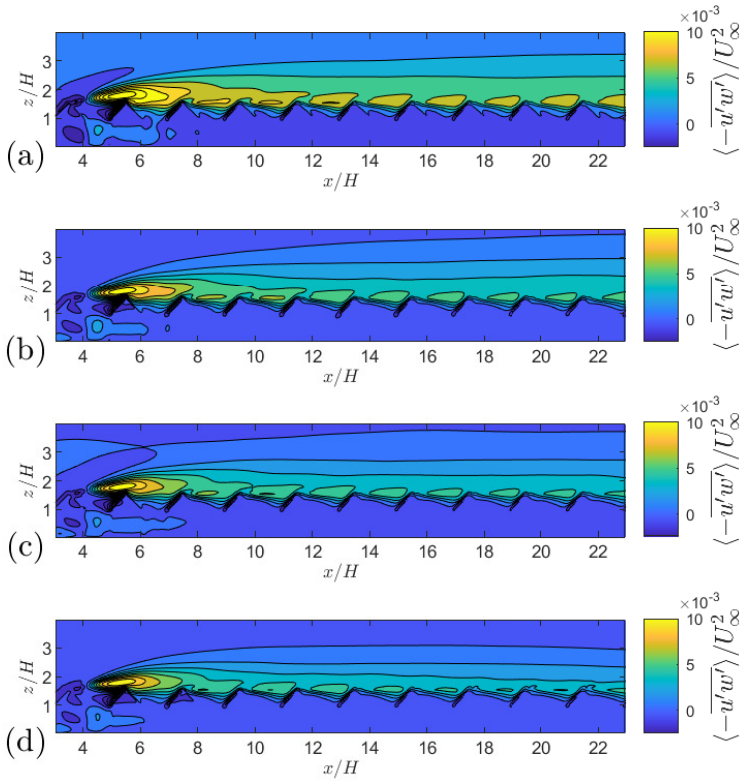

FIGURE 3.22: Contours of spanwise averaged Reynolds shear stress. For a) Neutral, b) $Ri_b = 0.2$, c) $Ri_b = 0.5$ and d) $Ri_b = 1$

The stratification decreases the strength of the fluctuations as expected, but it is downstream that is surprising. The stratification damps the turbulence and affects the mean flow fields. The 'wavey' nature of the contour of mean streamwise velocity (Fig. 3.18) is reduced by the stratification. The mean vertical velocity is also reduced with increasing stratification strengths (Fig. 3.19).

The turbulent normal stresses (Fig. 3.20 and 3.21) show weaker peaks and more greatly reduced values at the canopy top downstream. The Reynolds shear stress (3.22) is significantly reduced, the peak value downstream of every roof apex is drastically lower, but the overall shape of the contours is similar. Towards the tail end of the space shown, there is a visible reduction in the height of the border between Reynolds shear stress values for the neutral case and $Ri_b = 0.2$; this outermost border is still increasing in height at $x/H = 23$.

Spatially averaged vertical stress profiles are shown in Fig. 3.23. Row three has the highest peak vertical fluctuations. As expected, there is a decrease in the vertical velocity variance from the neutral case to $Ri_b = 0.2$, and then subsequent decreases as the Richardson number increases. The decrease between each of the stratified cases increases further downstream. In row three, the decrease of the peak value between $Ri_b = 0.2$ to $Ri_b = 1$ is 4.8%, in row 6, the decrease is 7.4%, and in row 9, the decrease

is 15.8%, Even at row 10 the decrease is still increasing, at 16.6%, but the rate of increase is slowing.

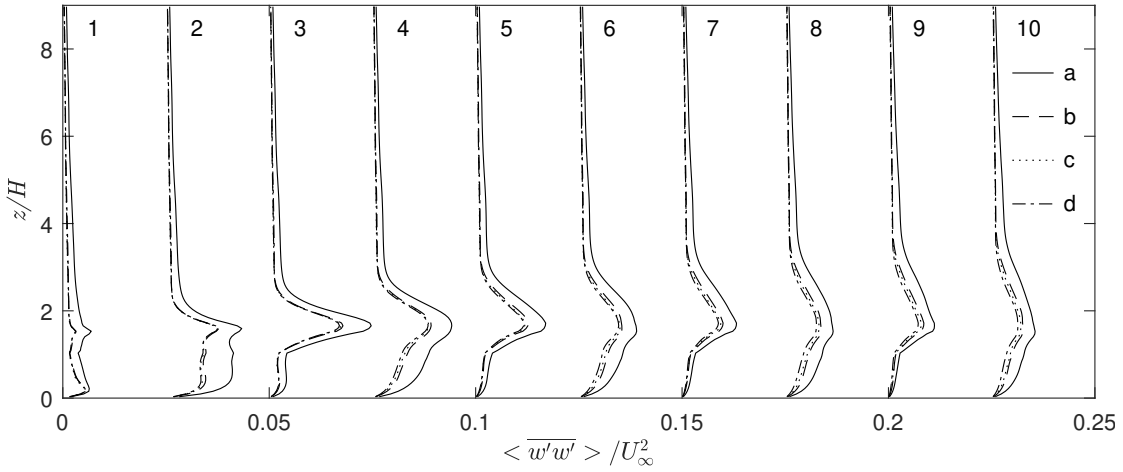

FIGURE 3.23: Pitched roof spatially averaged vertical profiles of vertical velocity variance. Each profile is averaged across the entire domain span and a $2h$ streamwise region starting at the front of each building, representing the building row. a) Neutral, b) $Ri = 0.2$, c) $Ri = 0.5$ and d) $Ri = 1$

3.4.2 Stratified flow around flat and pitched roof buildings

Comparing the effects of flat-roofed and pitched-roofed cuboids for neutrally stratified, fully developed urban boundary layers was shown at the beginning of Chapter 3. This section 3.4.2 compares the differences in the flow field and turbulence statistics for the roughness step change, where the leading edge of the array and subsequent building rows are simulated. This is shown for a stratified flow at $Ri_b = 0.2$.

Fig. 3.24 shows the streamwise mean velocity, streamwise and vertical normal stresses and Reynolds stress for the 8^{th} row of buildings, $x = 17H - 19H$ in Fig. 2.6. The peak values for both of the normal stresses are around 40% greater in the case of the pitched roof at the canopy top. The Reynolds shear stress peak for the pitched roof case is around 56% greater than that of the flat roof case.

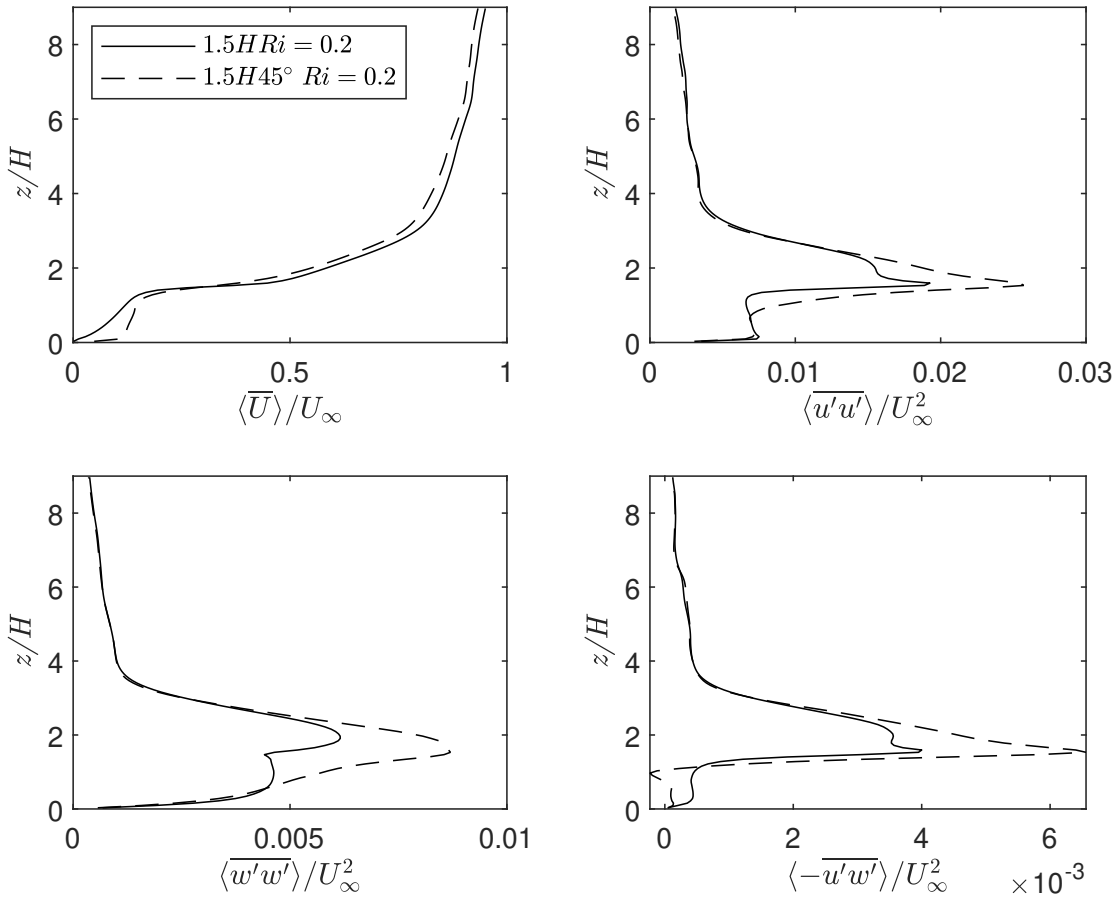

FIGURE 3.24: Spatially averaged data across the 8^{th} row for stratified flow around flat and pitched roof cuboids with a stratification strength of $Ri = 0.2$ for normalised a) mean streamwise velocity, b) streamwise velocity variance, c) vertical velocity variance and d) Reynolds shear stress

Comparatively, the spanwise averaged contour of vertical normal stress shown, in Fig. 3.25 shows a substantial peak in the vertical normal stress for the flat roof cuboid at the start of the array. The roof shape of the pitched roof case essentially makes the roughness step change not as aggressive. The wall normal cross-sectional area, above $2/3h$, reduces linearly to zero, as discussed previously. The roof shape helps the roughness step change to be less severe. The greatest peak value comes around the apex of the second row of buildings, impinging on the roof of the second-row buildings.

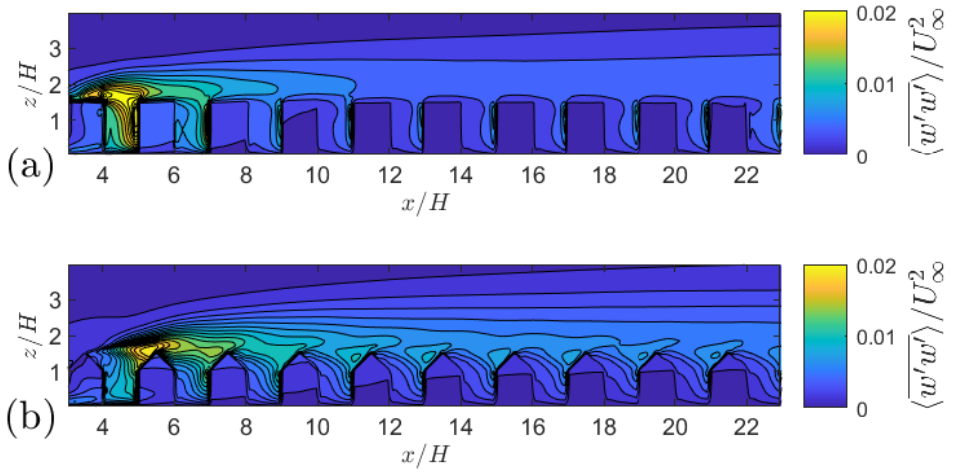

FIGURE 3.25: Stratified flow around flat and pitched roof spanwise averaged vertical velocity variance with a stratification strength of $Ri_b = 0.2$ for a) flat, b) pitched cases.

The same can be said for the Reynolds shear stress. The peak value occurs over the second row of buildings in the pitched roof case, compared to above the first row of buildings for the flat roof cuboids. However, downstream, as shown in Fig. 3.24, the pitched roof cuboids generate greater Reynolds shear stress at and just above the top of the canopy than that generated by the flat roof cuboids.

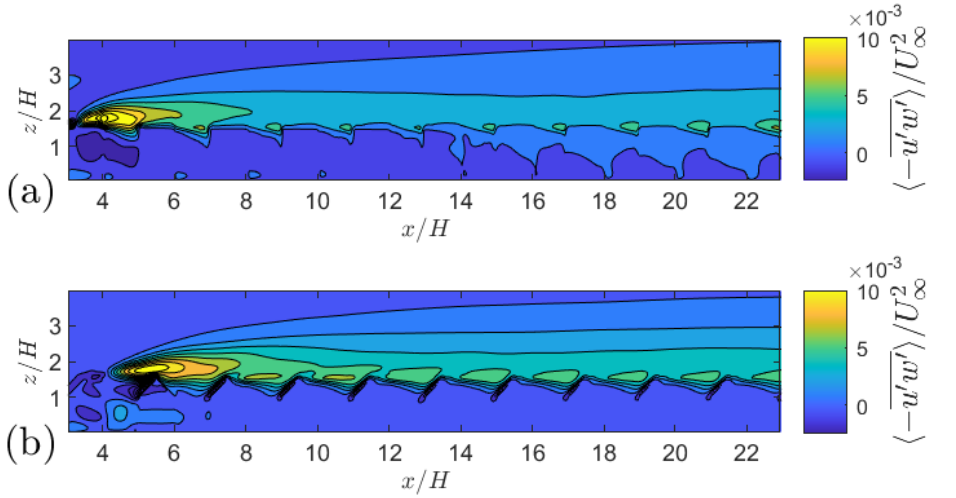

FIGURE 3.26: Stratified flow around flat and pitched roof spanwise averaged Reynolds shear stress with a stratification strength of $Ri_b = 0.2$ for a) flat, b) pitched cases.

This is further confirmed by the spatially averaged vertical profiles for each row as shown in Fig. 3.27 for the vertical normal stress and Fig. 3.28 for the Reynolds shear stress. The pitched roof generates greater vertical normal stress and Reynolds shear stress in every row downstream of row 2. The pitched roof, as shown previously, generates larger vertical momentum flux at the canopy height in developed boundary

layers, here it is shown that even in developing boundary layers, after two rows of buildings, the peak Reynolds shear stress is far greater.

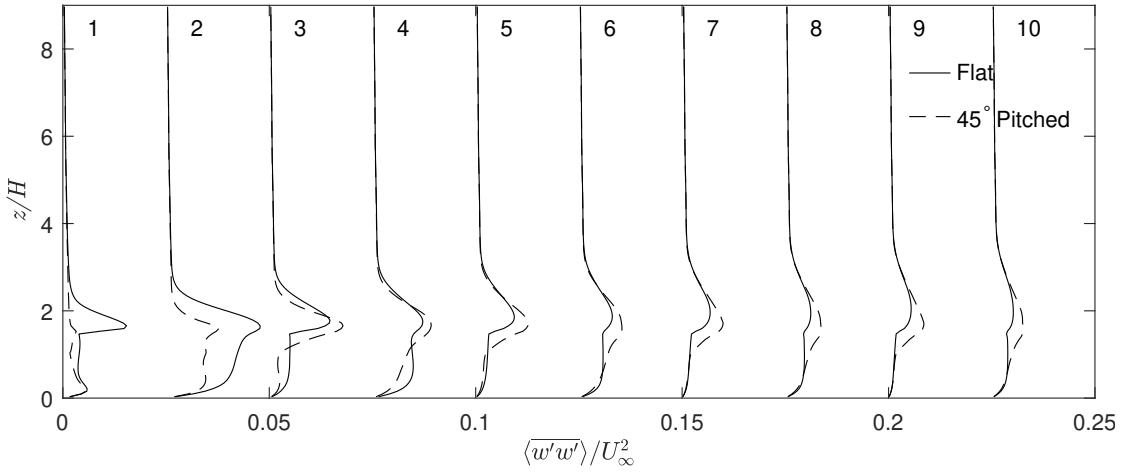

FIGURE 3.27: Flat and Pitched roof spatially averaged vertical profiles of vertical velocity variance for $Ri_b = 0.2$. Each profile is averaged across the entire domain span and a $2h$ streamwise region starting at the front of each building, representing the building row. Numbers indicate the building row. $0.025\langle\overline{w'w'}\rangle / U_\infty^2$ is added to each subsequent profile to plot all profiles on the same graph.

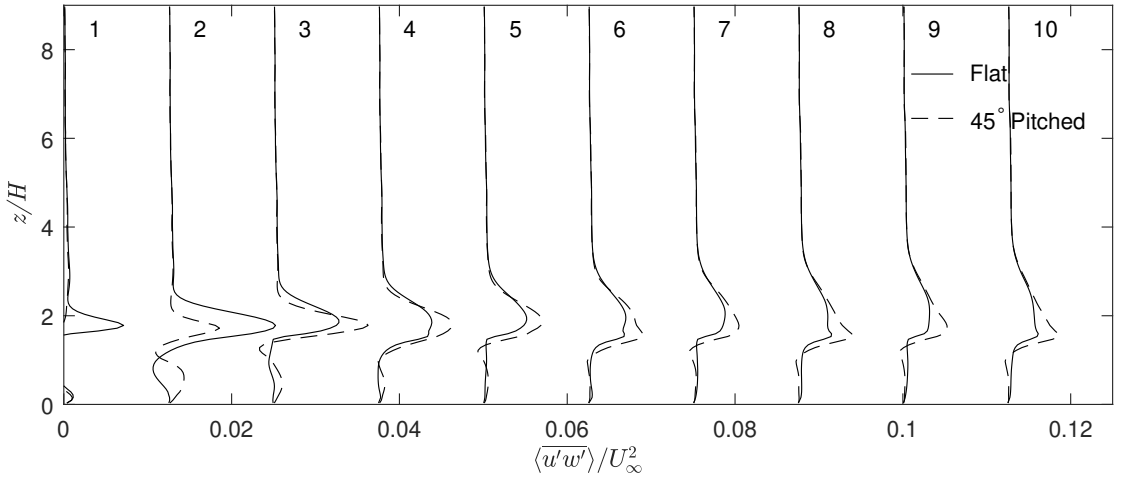

FIGURE 3.28: Flat and Pitched roof spatially averaged vertical profiles of Reynolds shear stress for $Ri_b = 0.2$. Each profile is averaged across the entire domain span and a $2h$ streamwise region starting at the front of each building, representing the building row. Numbers indicate the building row. $0.0125\langle\overline{u'w'}\rangle / U_\infty^2$ is added to each subsequent profile to plot all profiles on the same graph.

3.5 Internal Boundary Layers over Simplified Arrays

3.5.1 IBL depth methodology

Sessa et al. (2018) developed an approach to defining the IBL interface by identifying the abrupt change in gradient of the vertical Reynolds stress profiles. Following the methodology of Sessa et al. (2018), the IBL depth for the pitched-roof array can be estimated. Fig. 3.33 shows spatially-averaged vertical normal stress profiles over an area of $2H$(streamwise) $\times$ $12H$(lateral) centred at $x_{le} = 4H$, $6H$, ..., and $22H$, marked with 1, 2, ..., and 10, respectively. The spatial average is defined in Eq. 4.2, where $a = x_{lee} - H$, and $b = x_{lee} + H$.

The colour lines with symbols denote the IBL interfaces. It is evident that the thermal stratification suppresses the IBL growth. The IBL depth in Fig. 3.33 is evidently greater than that over a flat-roof array with the same input settings, including stratification condition Sessa et al. (2020). This confirms our early concluding remarks that compared to the flat roof, the pitched roof enhances the mixing, significantly increases the aerodynamic drag, and reduces the thermal stratification effect.

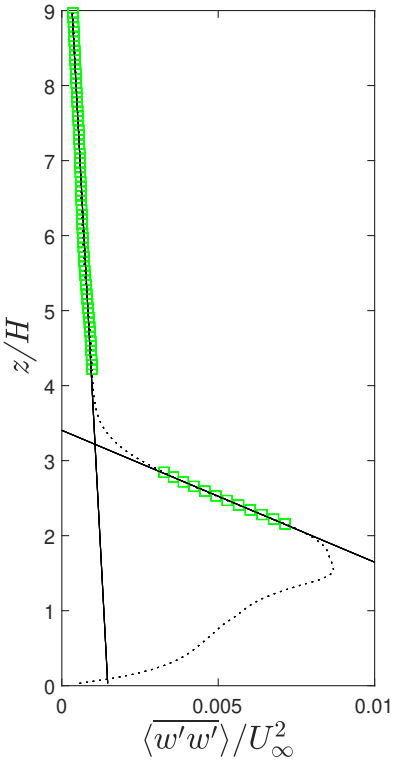

FIGURE 3.29: Spanwise- streamwise ($x/h = 2$) averaged vertical velocity variance for determining the IBL depth according to Sessa et al. (2018, 2020). Lines were constructed using the two set of data, one within the IBL and one above the IBL. vertical extent of the intersection defines the IBL depth.

One difference between the method shown here and that of Sessa et al. (2020) is the use here of the comprehensive average across the whole of the repeat unit. Sessa et al. (2020) uses laterally or spanwise averages made up of 60 points across the midpoint in the streamwise direction between rows of buildings. This should not alter the results too drastically, as the data specifically for the IBL depth prediction is above the canopy height.

Fig. 3.29 shows the spatially averaged normalised vertical normal stress for the $2H$ region between $x/H = 17 - 19$ for the pitched roof cuboid, with a strength of stratification of $Ri = 0.2$.

This figure shows the formulation of the best-fit lines drawn from the two approximately linear regions on the vertical profile of vertical normal stress. The two solid black lines are the linear lines of best fit for each of the data given in hollow green squares. The lines were constructed using a linear best fit. For example, in Fig. 3.29 the error of the fitting is as follows. For the data above $z/H = 4$, the error was less than 1%, with a residual value of $R = 0.993$. For the data between $z/H = 2 - 3$, the error was less than 2%, with a value of $R = 0.985$.

The intersection of the lines of best fit provides the approximation of the IBL depth at that location, or as is the case here using spatial average data, the average depth across the $2H$ streamwise region or repeat unit.

3.5.2 Simplified arrays - Roughness change

For the cases using the synthetic inflow generation, the IBL depth will grow from the lead row of buildings due to this roughness change. Fig. 3.30 shows the IBL depth taking into consideration the cuboid depth, then normalised by the cuboid depth. Fig. 3.31 shows the IBL depth considering the building height, normalised by the building height. These two Figs. essentially tell the same story, which is easier understood by looking at Fig. 3.31 for the buildings are all the same height. Compared to the data generated by Sessa et al. (2020), it is easier to discuss the difference with Fig. 3.30 as this is the normalisation method used in that paper.

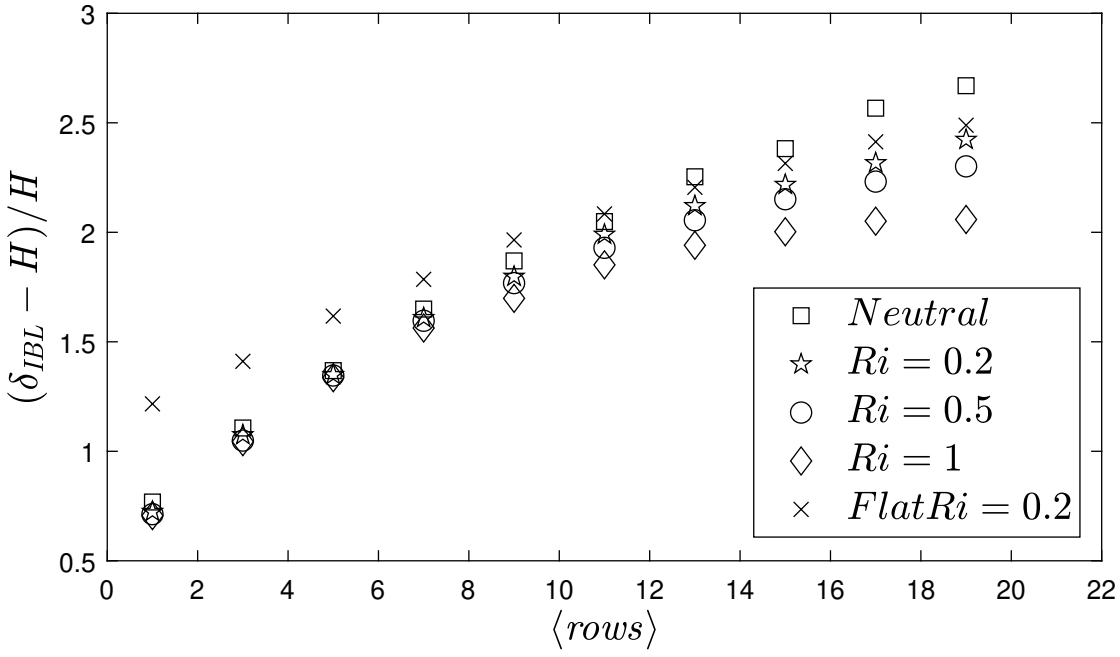

FIGURE 3.30: Internal boundary layer depths, using the method of Sessa et al. (2018, 2020), along the inflow domain for the simplified arrays, for neutral (pitched roof) and Stratified (flat and pitched roofs) inflow conditions, normalised by the local building height. Data is spatially averaged across each row, beginning at the front of the first building and averaged across the span and $2H$ in the streamwise, Ri given in the figure is the bulk Richardson number Ri_b

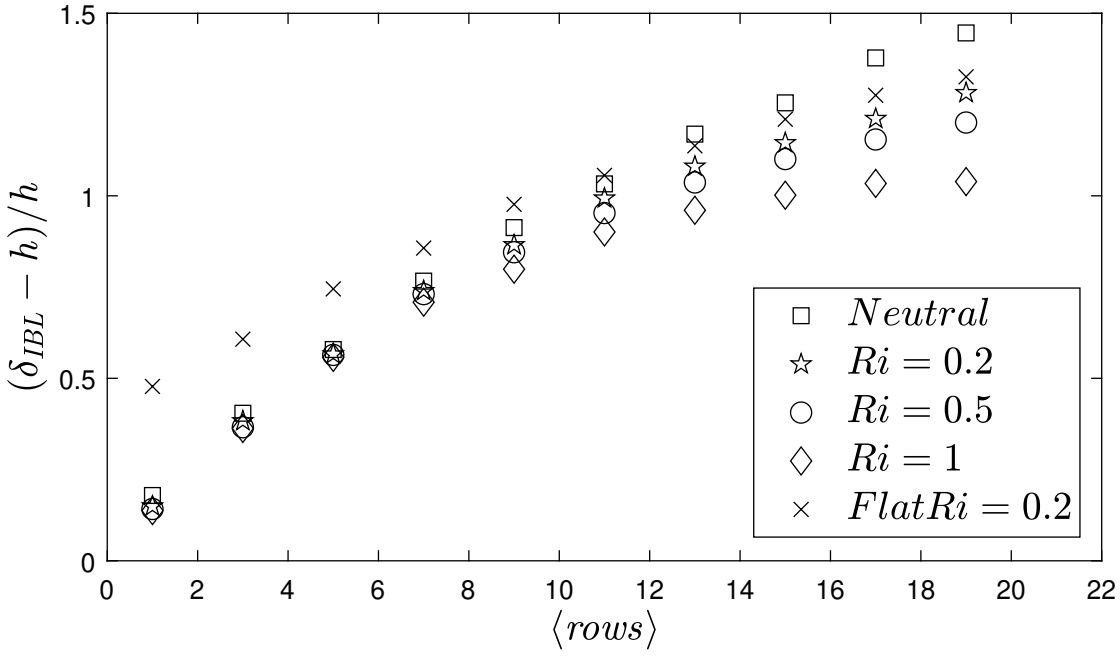

FIGURE 3.31: Internal boundary layer depths, using the method of Sessa et al. (2018, 2020), along the inflow domain for the simplified arrays, for neutral (pitched roof) and Stratified (flat and pitched roofs) inflow conditions, normalised by the local building's streamwise extent. Data is spatially averaged across each row, beginning at the front of the first building and averaged across the span and $2H$ in the streamwise direction, Ri given in the figure is the bulk Richardson number Ri_b

Comparing the Neutral case firstly to the stratified flows for the pitched roof in Fig. 3.31, the stronger stratification does indeed limit the growth of the IBL; this was shown previously by Sessa et al. (2020). Interestingly, the IBL for $Ri_b = 1$ seems to have mostly stopped developing compared to the more weakly stratified flows, which are obviously still growing in depth. Compared to the data shown by Sessa et al. (2020) in which the IBL seems to stop developing for flat roofs after $x/H = 17.5$.

Flat roof data is provided here for the flat roof case of equal total height to that of the pitched roof cases with a stratification strength of $Ri_b = 0.2$. The IBL depth in the flat roof case shows quite different behaviour. The extreme-ness of the flat roof cuboid's flat front produces a very thick IBL near the leading edge. At row 1, the IBL thickness for the flat roof case is almost 3 times that of any of the pitched roof cases when taken from the height of the canopy top 3.31. The growth rate of the IBL for the flat roof case decreases more rapidly than that of the pitched roof case.

Fig. 3.32 visualises the IBL depth by plotting the IBL depth from Fig. 3.31 on top of the spatially average vertical normal stress profiles, $\langle \overline{w'w'} \rangle$, for both flat and pitched roof cases. Given a longer fetch, the IBL depth over the pitched roof array would be thicker than that over the array of flat roof buildings assuming the same inflow conditions for the stable stratification of $Ri_b = 0.2$. From this figure, qualitatively, it is very obvious that the growth rate of the IBL between the two cases is quite different.

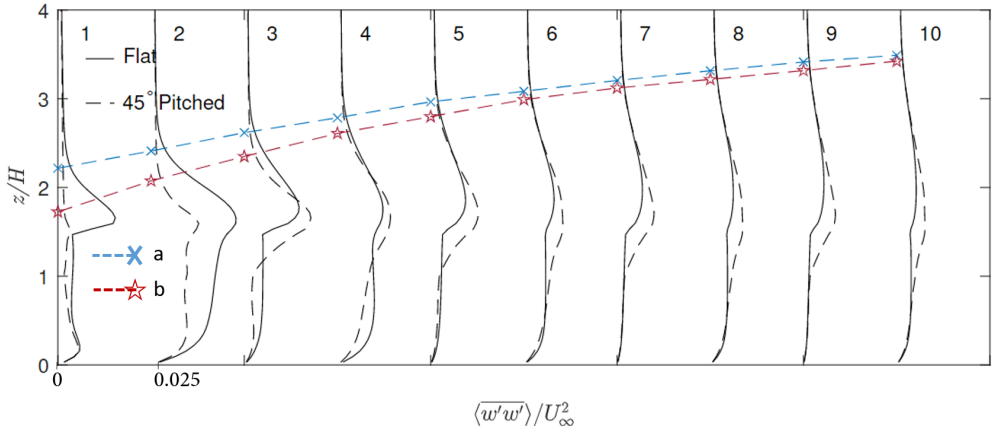

FIGURE 3.32: Spatially-averaged vertical normal stress profiles over an area of $2H$ (streamwise) $\times$ $12H$ (lateral) centred at $x_{lee} = 4H$, $6H$, ..., and $22H$, marked with 1, 2, ...,and 10, respectively. The colour lines with symbols denote the internal boundary layer interfaces for $Ri_b = 0.2$ for a) Flat and b) pitched cases

The effect of stratification on the IBL depth is shown visually in Fig. 3.33. The IBL data overlaid on the spatially average vertical normal stress profiles for the pitched roof cases with increasing stratification strength of $Ri_b = 0, 0.2, 0.5, 1$. The first three rows all have a quite similar IBL depth; at location 4, they begin to split. The IBL depth in the strongest stratification case, $Ri_b = 1$, could, given a longer fetch, begin to decrease in height.

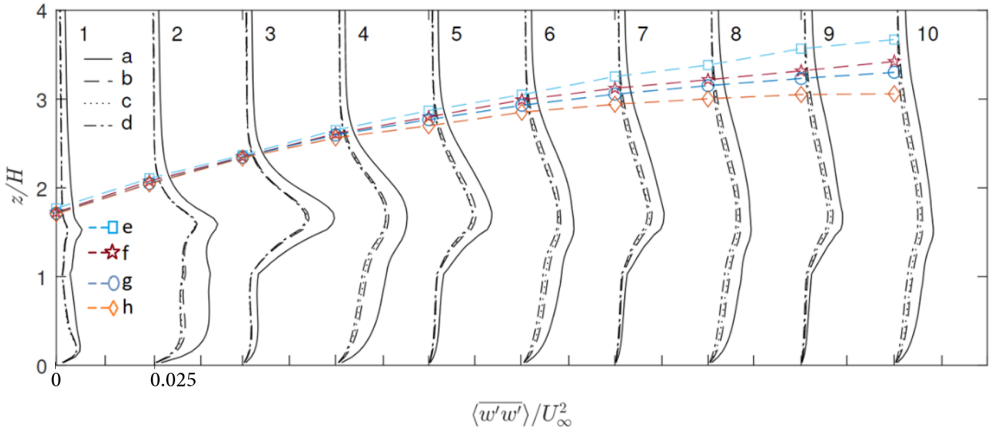

FIGURE 3.33: Spatially-averaged vertical normal stress profiles over an area of $2H$ (streamwise) $\times$ $12H$ (lateral) centred at $x_{lee} = 4H$, $6H$, ..., and $22H$, marked with 1, 2, ...,and 10, respectively. The colour lines with symbols denote the internal boundary layer interfaces. a, e) $Ri_b = 0$, b, f) $Ri_b = 0.2$, c, g) $Ri_b = 0.5$ and d, h) $Ri_b = 1$

Fig. 3.34 demonstrates the method's robustness to determine the IBL depth (Sessa et al., 2018). Sessa et al. (2018) discusses that the step change and uniform height cuboids provide a more obvious interface. The pitched roof array, for which the proportion of solid to fluid volume linearly decreases to zero above $2/3h$, still has a clearly visible interface. This could be assisted by the stratification damping the TKE above the IBL and the pitched roof generating greater TKE than the flat roof case.

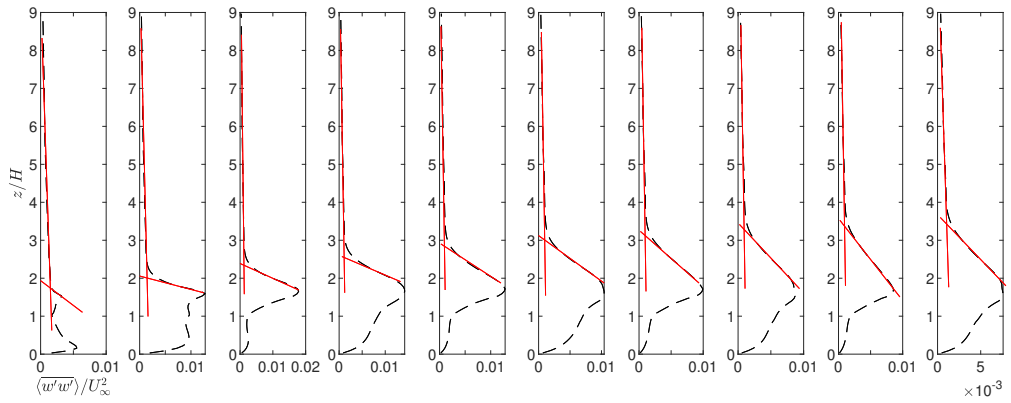

FIGURE 3.34: Spanwise, $2H$ (streamwise) averaged dimensionless vertical normal stress for the pitched roof case, 1.5H45°, with a thermal stratification of $Ri_b = 0.2$. Red lines are linear fittings to determine the IBL depth for each streamwise $2H$ strip

3.6 Summary

LES has been used to carry out simulations of the flow within urban boundary layers over idealized arrays of cuboids with and without pitched roofs under neutral and stable stratification conditions. The use of non-conformal Cartesian grids was shown to produce similar spatially-averaged quantities (mean velocities, second-order

turbulent statistics and dispersive stresses) compared to those from conformal (body-fitted) meshes.

Results from PBC simulations with arrays of flat roof cuboids (with two different overall heights) and pitched roof cuboids showed significant changes in the mean flow and Reynolds stresses produced by the pitched roof cuboids, including increases in turbulent momentum flux and drag for the three-dimensional pitched roof array compared to both three-dimensional flat roof arrays. The packing density altered the results considerably. With looser packing densities (16%), the pitched roof contributed a similar total drag to the flat roof, irrespective of overall total height. The flow regime for the tighter packing density (33%) differs substantially between the pitched and flat roof cuboid, being wake-interference and skimming flow, respectively. For $\lambda_p = 16\%$, both cases exhibit wake-interference flow patterns.

Results from the STI simulations show that the internal boundary layer generated by an array of pitched roof cuboids is quite different to that of the flat roof cuboid, generating a shallower IBL. The effect of stable stratification was reduced by the pitched roof cuboid, compared to that of the flat roof cuboid, with smaller differences of turbulent momentum flux between subsequent increases in the strength of the stable stratification.

Chapter 4

Effects of complex geometry, terrain and stratification

This chapter discusses the validation of the CFD data to the experimental PIV-captured flow field data. The sensitivity to the inflow conditions will be shown, comparing the differences between a simulated urban boundary layer (Counihan, 1969) and a naturally grown turbulent boundary layer. Mesh sensitivity will also be shown comparing cases given in Table 2.5.

In order to fully understand the terrain effect on the flow within the urban canopy, it was decided to focus on comparing the flat case (SF8) to a case with the same building array with the real terrain (ST8). The effect of stratification is also shown; this is applied to both the flat and terrain cases.

4.1 Validation

4.1.1 Validation of flow simulation around Semi-realistic array, CFD and PIV

The meshing strategy developed in Section 2.3.1 is used for the SF8 and ST8 cases, using the realistic urban geometries of the Highfield campus, University of Southampton. Firstly, validation against the flume data is carried out.

All roofs within the domain are simplified to flat roofs for the CFD and water tunnel models. From the previous discussion, section 3.2, 45° pitched roofs will impact the flow field. However, within the campus, most roofs are industrial-style flat roofs. Outlying suburban housing was also simplified to have flat roofs, but this region is not of interest within the scope of this study.

Experimental velocity measurements were captured using PIV. PIV data was sampled for $600s$, creating image pairs at a rate of $2Hz$ with $1.2ms$ time separation between particle images. The CFD was sampled at $\Delta t = 1.2s$ and averaged for $100,000s$. The CFD is simulated at full length scale, and the kinematic viscosity, $\nu = 0.00045m^2s^{-1}$, was scaled to match the Reynolds number between FF8 and SF8, $Re_h = 16,000$. The Reynolds number for the PIV was $Re_h = 5,000$, which is suitable to achieve Reynolds number independence given the current geometry (Xie and Castro, 2006). The averaging period, velocity and characteristic length give the turn-over time. The turn-over time is defined as the number of times flow passes a certain distance, $cycles = (UT)/h$. Here, the distance is defined as the average building height h, the averaging time is given by T, and U is the mean freestream velocity. This gives $192,500$ cycles for the PIV and $2,360$ cycles for FF8. This study uses the same measurement setup and technique used by Lim et al. (2022).

The uncertainty in the experimental results due to measurement techniques is estimated to be roughly 1.5% for the velocity measurements. This is visually represented as the width of the markers in the following figures and corresponds to the maximum uncertainty. It should be noted that for the CFD data, the data across the entire plane is available, but the PIV data can have a reduced field-of-view due to the angle between upstream and downstream buildings shielding the laser sheet. This is somewhat reduced by using multiple cameras.

Figs. 4.1 and 4.3 show a comparison between the naturally grown turbulent boundary layer in the flume and the LES case FF8 (Table 2.5). Vertical profiles of mean streamwise and vertical velocity are shown (Fig. 4.1), and u_{rms}, w_{rms} and $\overline{u'w'}$ are shown (Fig. 4.3) at 14 locations (Fig. 4.1) with spacing $\Delta x = 2.5h$ and starting at $x = 13.3h$.

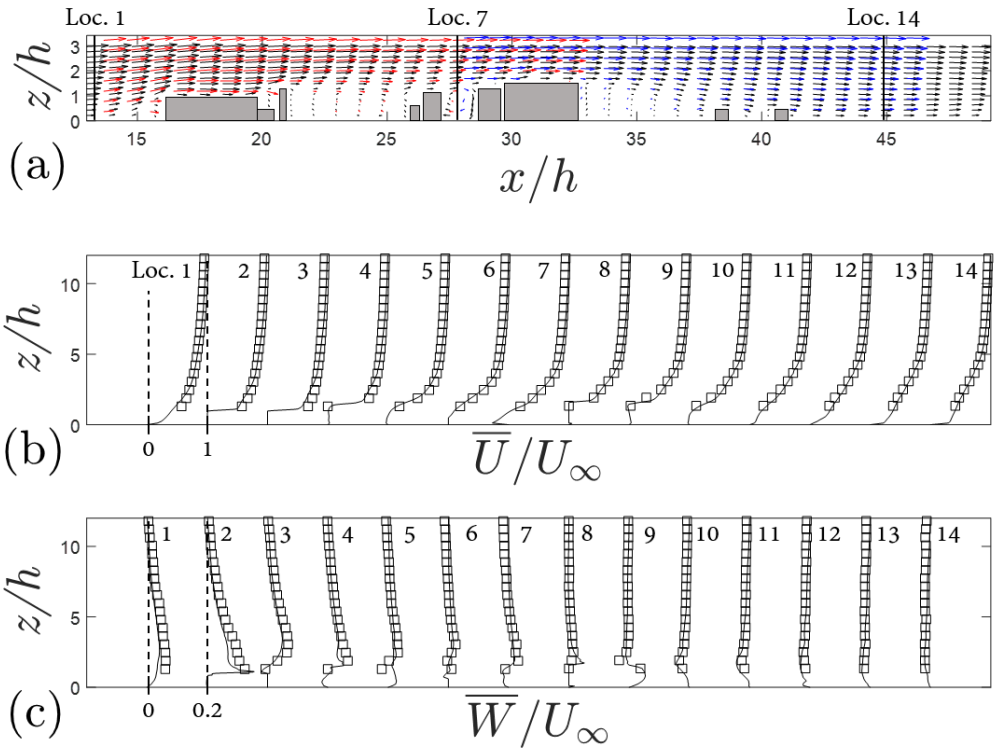

FIGURE 4.1: 14 vertical profiles (locations detailed in Fig. 2.17, location 7 is given and spacing between locations is 2.5h) of mean velocity at streamwise locations, squares - PIV data showing every fifth data point, solid line - LES data. Showing a) PIV (camera 1 -red, camera 2 -blue) and LES (black)(FF8 in Table 2.5) vectors on a vertical across plane at y=104m detailed in Fig. 2.17, b) Mean normalised streamwise velocity and c) mean normalised vertical velocity at different streamwise locations.

Fig. 4.1 shows that there are slight under-predictions at some locations, but all the LES mean axial velocity data are within 5% of the experimental values. The vertical velocity differs slightly more, but agreement between the mean velocity profiles in Fig. 4.1 appears as good as might can be expected when comparing to PIV data from a 1:1000 scale model.

Fig. 4.2 shows the in-plane mean normalised velocity contours for the PIV and CFD cases. The agreement qualitatively is very good. There is little visible difference between the streamwise mean velocity contours. The vertical velocity contour for the PIV (Fig. 4.2c) is noisier than the streamwise velocity, as is expected, being one order in magnitude smaller. The vertical velocity peaks are well captured by the CFD, and even the street-canyon style flow can be seen in both cases at $x/h = 27 - 29$. The stitching of the data from each camera to form a single contour was achieved through linearly weighting within the overlap region.

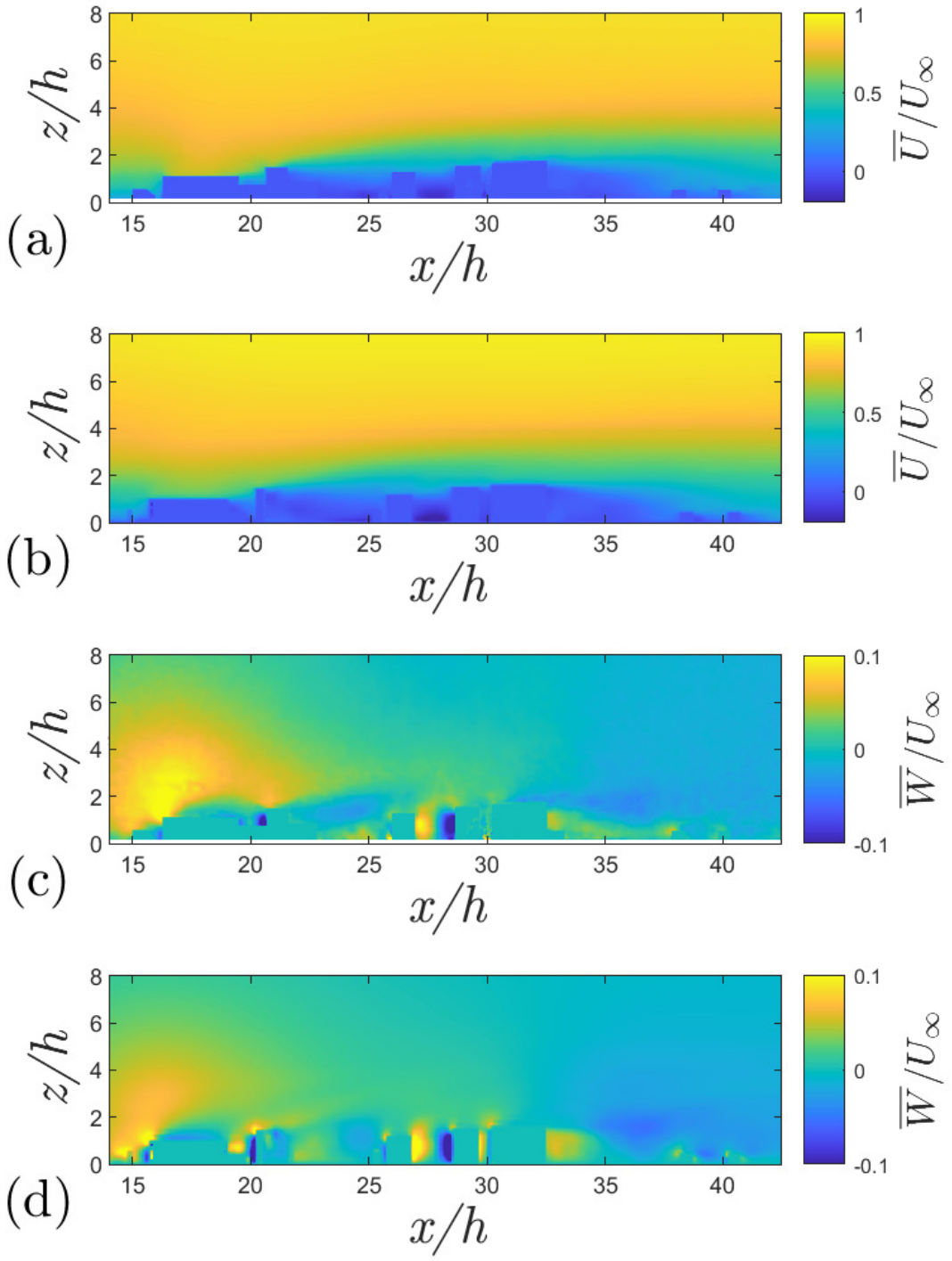

FIGURE 4.2: Streamwise and vertical velocity contours for CFD and PIV data. For PIV (a,c) and CFD (b,d)

Agreement of the mean velocity profiles is as good as can be expected from the small-scale PIV testing carried out; there are slight under-predictions at some locations. However, all the CFD data falls within 5% of the experimental values for the mean axial velocity. The vertical velocity differs slightly more, but the agreement is deemed acceptable.

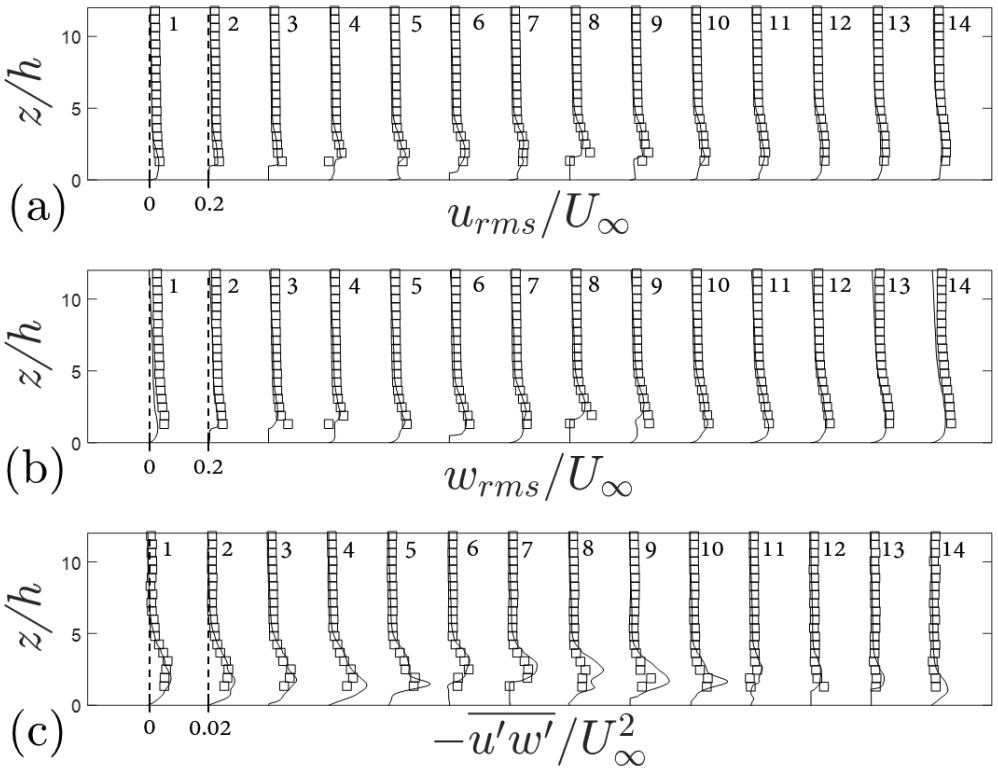

FIGURE 4.3: a) normalised axial velocity fluctuation r.m.s, b) normalised vertical velocity fluctuation r.m.s. and c) normalised vertical Reynolds shear stress. Symbols and lines are the same as in Fig. 4.1b.

Fig. 4.3 shows profiles of the r.m.s. axial and vertical velocity fluctuations and the mean vertical Reynolds shear stress. The agreement for both of the normal stresses is generally very good. There is a small under-prediction of the peak values which occur close to the ground and building surfaces, for example, in the fourth profile in Fig. 4.3, but also an over-prediction of vertical turbulent momentum flux between profiles 6-8, again close to building surfaces (apart from location 7 which will be discussed in the following section).

It should be noted that in the near wall regions, the PIV data is affected by the high-intensity reflections from the model's surface, which makes gathering high-quality data in this region essentially impossible using this particular setup Lim et al. (2022). Away from the wall, the agreement is very good in regions dominated by free shear layers downstream of the elements, which create free shear layers devoid of reflections of the laser sheet. Overall, the LES data with the flume inflow turbulent quantities are in promising agreement with the experimental data.

A double peak can be seen in the Reynolds shear stress at location 8 within Fig. 4.3 for the LES and experimental data. It is less clear in the PIV data, but it is still visible

when plotting all data points. A recirculation formed in this typical long street canyon creates a negative streamwise velocity at the ground (Fig. 4.1b). The Reynolds shear stress's upper peak is around $z/h = 2.5$. This is caused by the free shear layer from the upstream building, which has convected downstream but forced upwards. The lower peak is generated by the building directly upstream.

Fig. 4.4 shows the in-plane normal stress components along with the Reynolds shear stress for both the PIV data and FF8 with the inflow prescribed from just upstream of the PIV array. It is possible to see, close to the wall, where values for the stresses in the PIV data are very high. As noted previously, gaining high-quality data in the near-wall region is almost impossible. Away from the wall, the peak locations are well represented in the CFD. Both normal stresses have similar distributions, and the peak values are close, within 15%. The Reynolds shear stress is slightly over-predicted in the CFD results, but the prediction of the locations of the peak values are in good agreement.

The noise seen in the PIV contours is likely due to the averaging period compared to that of the CFD. The averages for the PIV and FF8 are made up of 2000 and $83,000$ time steps, respectively. The relatively low number of data points included within the averaging period for the PIV is the most likely cause for the noisy/grainy look of the PIV contours in Fig. 4.4.

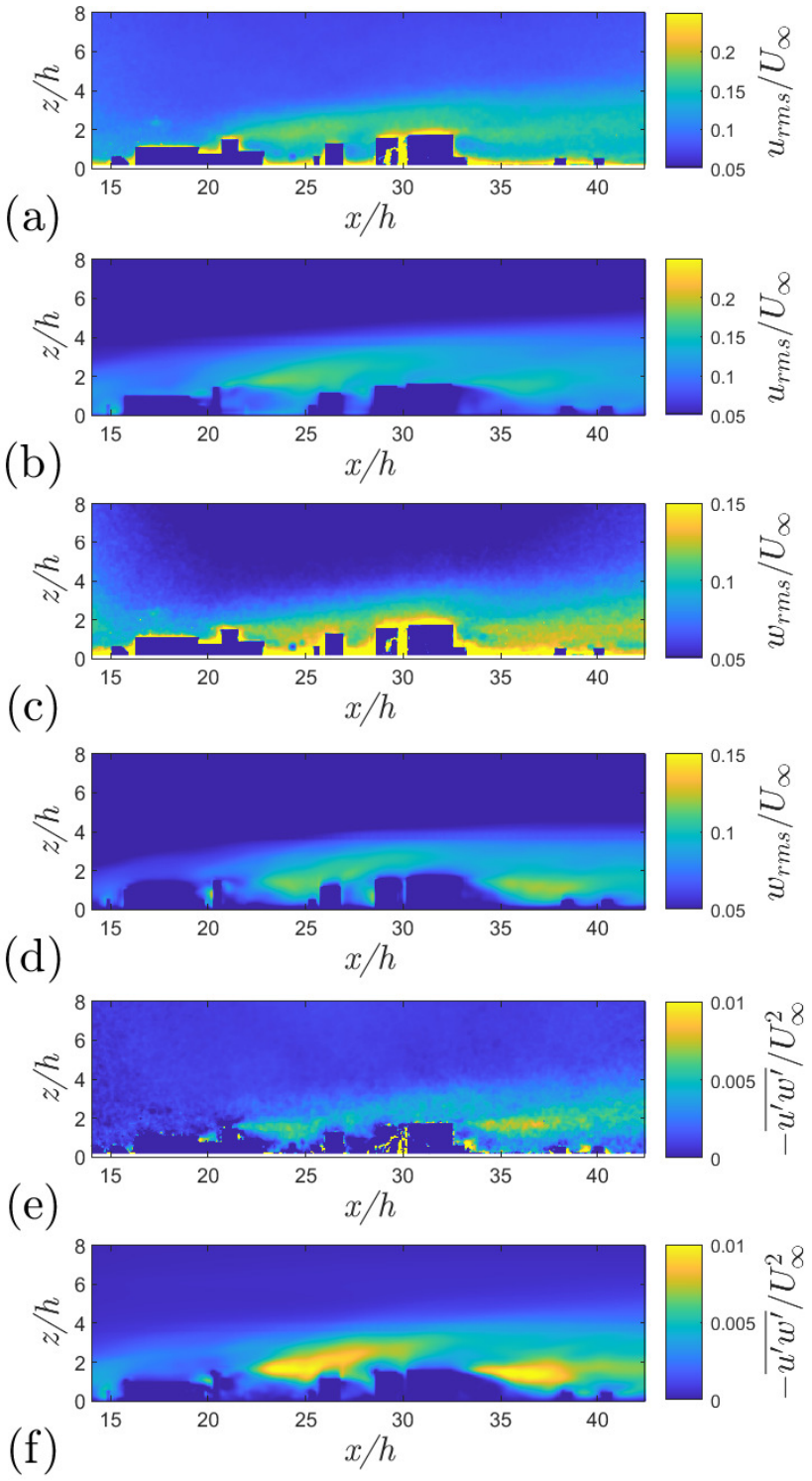

FIGURE 4.4: Streamwise and vertical r.m.s. velocity and Reynolds shear stress contours for CFD and PIV data. Prescribed turbulent inflow data for CFD taken from PIV flat plate data, inflow profiles are given in Fig. 4.5. For PIV (a,c,e) and CFD (b,d,f)

To summarise, as noted previously, the data for the PIV case near the ground ($z/h \lesssim 0.25$) is unusable. Due to reflections from the laser sheet and the reduced number of seeding particles compared to the flow away from the wall. Overall the agreement is sufficient. Peak locations seem to match well. There is under-predication in the normal stresses. It is argued that due to the Reynolds shear stress being only slightly over-predicted that the CFD is sufficiently accurate. This study uses the same measurement setup and technique used by Lim et al. (2022), and the agreement here is similar to that was shown, which was deemed acceptable considering the challenges of small-scale PIV discussed previously.

4.1.2 Sensitivity to incoming turbulence

In order to test the sensitivity to incoming turbulence, FF8 will be compared to a case using the same geometry but different turbulence intensity inflow conditions. These new inflow conditions (Fig. 4.5) are from what is called a simulated urban boundary layer from the EnFlo wind tunnel at surrey university. The wind tunnel inflow data prescribed at the inlet is taken from Xie and Castro (2009), used for the DAPPLE project (Arnold et al., 2004). Wind tunnel measurements of the primary stresses and vertical Reynolds shear stress were taken upstream of the measurement domain, within a simulated urban boundary layer (Counihan, 1969). The simulated urban boundary layer is a term defined by Counihan (1969) to describe a boundary layer created in the wind tunnel, which uses large spires and two-dimensional roughness elements to generate turbulence with appropriate length scales upstream of the measuring location. The turbulence was generated through the use of spires far upstream and two-dimensional roughness elements leading to the experimental domain. This data was scaled to give the stress profile peak at the average canopy height, $h = 16m$. This was to simulate the effect of upstream roughness with a similar vertical extent. The profiles are typical of an urban area and will therefore be compared to the inflow conditions of the PIV data, which is a naturally grown smooth wall turbulent boundary layer. The inlet boundary condition prescribed mean streamwise velocity and inflow turbulence profiles are shown in Fig. 4.5. The inflow profiles for FF8 (Fig. 4.5c and Fig. 4.5d) were taken from the flat plate vertical profiles at the PIV measuring location, where The model was removed and replaced by a flat plate. The spanwise normal stress was approximated from $v_{rms}/u_\tau = 1.5$, (Xie et al., 2004).

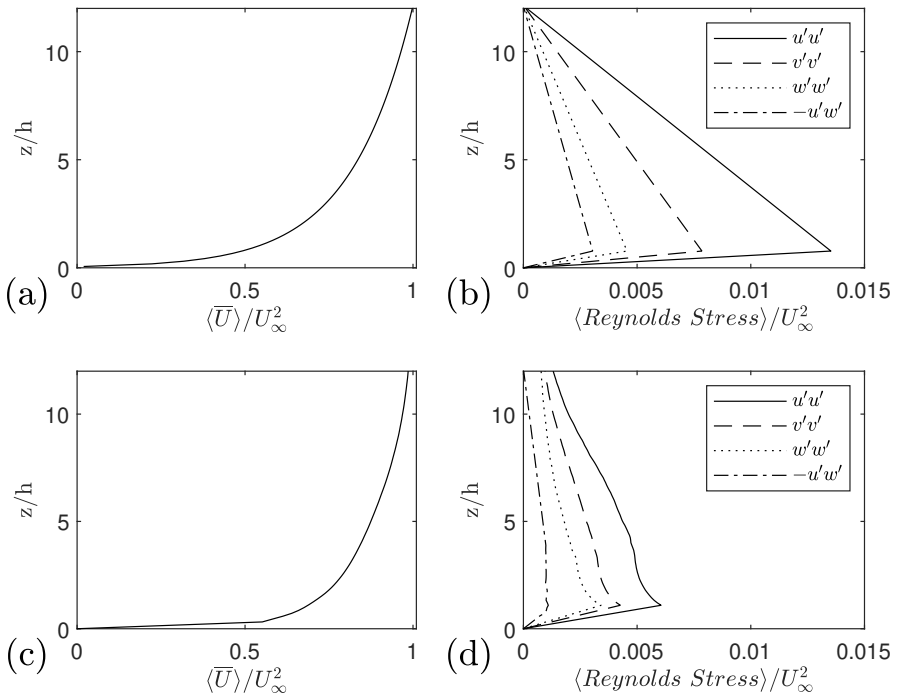

FIGURE 4.5: Prescribed mean streamwise velocity and inflow turbulence profiles. Normalised prescribed vertical profiles of a) mean streamwise velocity for SF8, b) normal and Reynolds stresses for SF8, c) mean streamwise velocity for FF8 and d) normal and Reynolds stresses for FF8

Figs. 4.6 and 4.7 show a comparison of mean velocities and turbulent statistics at location 7 ($x = 460m$, $y = 104m$ in Fig 2.17, and $x = 28.8h$ in Fig. 4.1a), between different inflow conditions and different resolutions. This location was chosen as it replicates a street-canyon type flow which has well-understood flow features.

Figs. 4.6 show that the difference in mean velocities, especially within the canopy, between FF8, SF8 and SF12 is very small. The effect of inflow turbulent quantities on mean flow is small within and just above the canopy, even for local results. This is due to the flow within and just above the canopy being within the IBL generated at the leading edge of the building array. The vertical velocity within and immediately above the canyon can be difficult to predict accurately, being more than one order of magnitude smaller than the streamwise velocity. It is also very sensitive to the location at which the data is sampled. As this location is the centre of a street-canyon like flow, moving slightly upstream or downstream would drastically change the vertical velocity, this cannot be said for the streamwise velocity. The overall shape is repeated for each of the vertical velocity profiles.

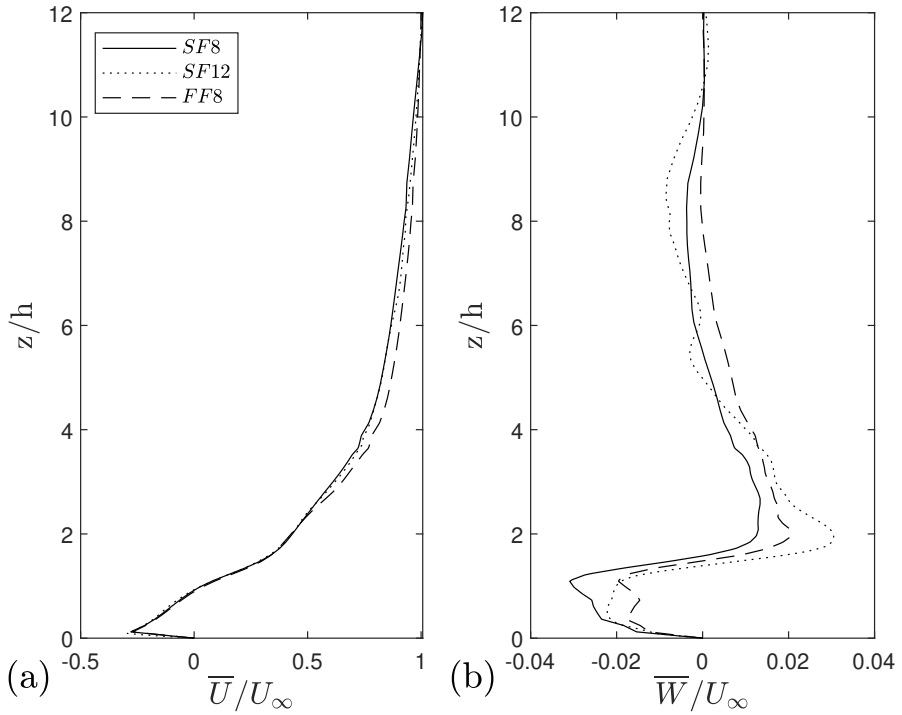

FIGURE 4.6: Vertical profiles of mean velocity at location 7 (x =460m, y = 104m in Fig. 2.17. x=28.8h in Fig. 4.1a). a) Mean normalised axial velocity, b) mean normalised vertical velocity.

Above the canopy, there is a slight difference caused by the different inflow conditions. In the less turbulent case, FF8 experiences less TKE. Therefore there is a slightly higher velocity, and this difference is roughly 5%.

All three cases closely agree on the peak of the streamwise and vertical r.m.s. with only a discrepancy of roughly 5%; the peak value of the vertical r.m.s. is very close. The Reynolds shear stress peak also shows a quite close between FF8 and SF12, where SF8 seems to predict a thicker shear layer, but the peak value is close to that of the other cases if located slightly deeper within the canopy. Below $z = 1.5h$, the difference is small. This again confirms that, as in Xie and Castro (2008), the LES results within and immediately above the canopy are not sensitive to the inflow turbulent quantities if they are not too unrealistic, and the distance of the sampling station from the inlet is large enough (e.g. larger than 14 times the canopy height).

There are clear differences above the canopy in the profiles of the 2^{nd} order velocity moments and turbulent statistics between the three cases (shown in Fig. 4.7). Particularly above $z = 1.5h$, which is the height of the building upstream of location 7. Above $z = 4h$, the difference is substantial due to the large difference in the turbulence prescribed between the two inflow conditions. The flow above the IBL would be representative of the roughness upstream or, in this case, the surface that generated the prescribed profiles.

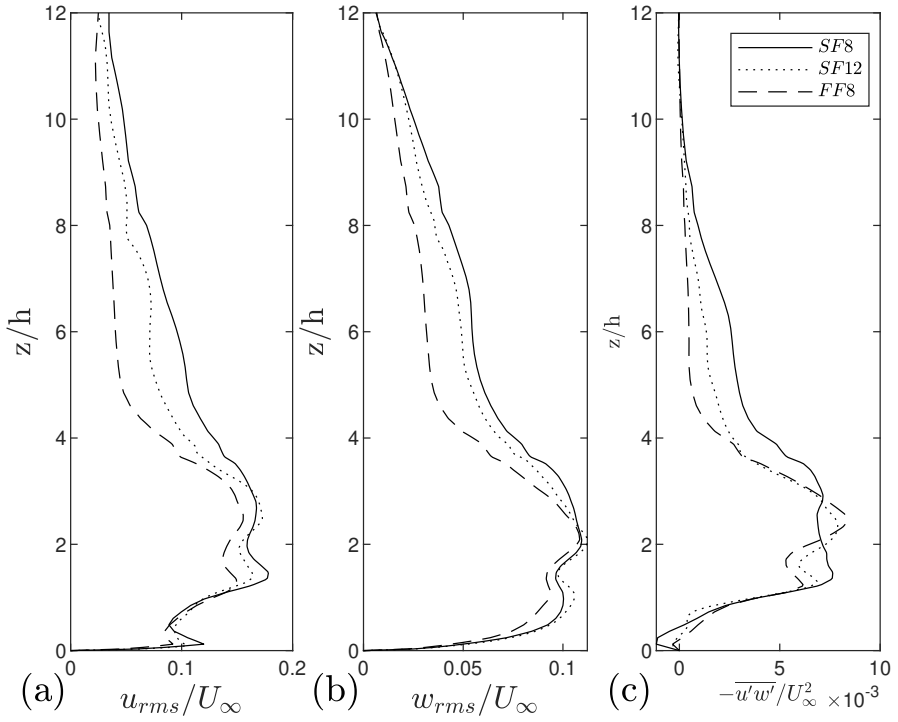

FIGURE 4.7: Same as in Fig. 4.6, but for a) normalised axial velocity fluctuation r.m.s, b) normalised vertical velocity fluctuation r.m.s. and c) normalised vertical Reynolds shear stress.

Spatial average data for the northern half ($+Y$) of the domain (see Fig. 2.18 for clarity) is shown for cases SF8 and FF8 in Fig. 4.8. The smaller spanwise extent of this region was chosen to focus on the region encompassing the buildings within the domain, without the regions of flat terrain surrounding the building group. The inflow conditions seem to have little effect on the velocity within and just above the canopy. Above the canopy, there is also little difference between FF8 and SF8. Averaging over the downstream half of the domain, from $h = 29h$ to $h = 56h$, a slight increase in the velocity profiles over the entire domain average. This is likely because this region includes a significant distance downstream that is devoid of buildings. The overall blockage of this area is less.

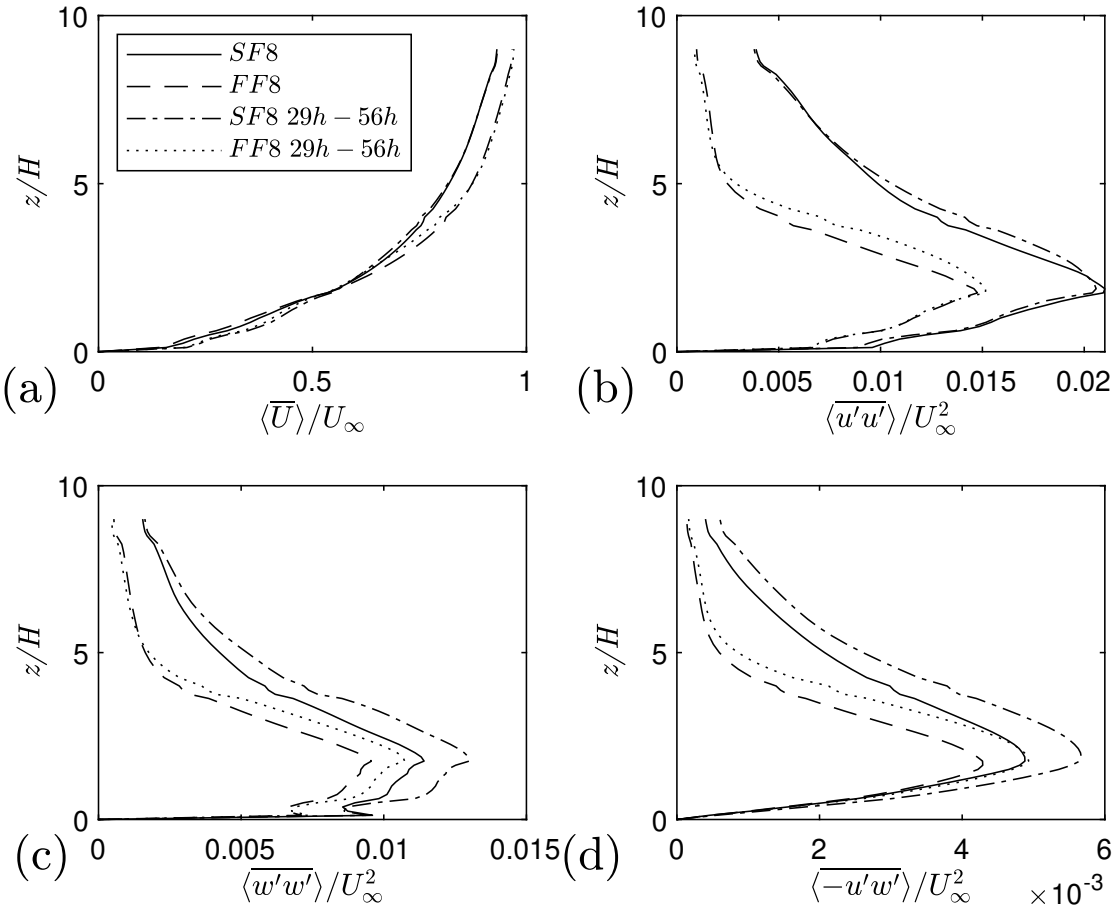

FIGURE 4.8: Spatial average data for the whole building region and downstream half for SF8 and FF8 showing the normalised a) Mean streamwise velocity, b) streamwise stress, c) vertical stress and d) Reynolds shear stress

Unlike the local results, the spatially averaged peak normal stresses are around 25% and 15% higher for the normal streamwise and vertical stress, respectively. The Reynolds shear stress is around 10% higher for the simulated urban turbulent boundary layer inflow (SF8). Considering the prescribed peak value of Reynolds shear stress was in the region of 2.5x higher, this result is quite satisfactory. Averaging over the downstream half of the domain, from $h = 29h$ to $h = 56h$, shows almost identical peak values and distribution for the normal streamwise stress to that of averaging the entire domain. The vertical stress has increased by around 10%, and the Reynolds shear stress is also 10% higher when compared with the total spatial average. This region, being further downstream from the leading edge of the building array has allowed the IBL to develop.

Spanwise averaged contours are shown for streamwise, spanwise, vertical stresses, and Reynolds stress in Figs. 4.9, 4.10, 4.11 and 4.12 respectively. The spanwise averaged streamwise stress (Fig. 4.9) shows a good qualitative agreement in the peak location and distribution, especially within the canopy. The main difference is the magnitude of the peaks, which for FF8 are around 2/3 of that for the SF8 case. The

difference between SF8 and FF8 is extremely clear above the canopy due to the different prescribed turbulent inflow profiles.

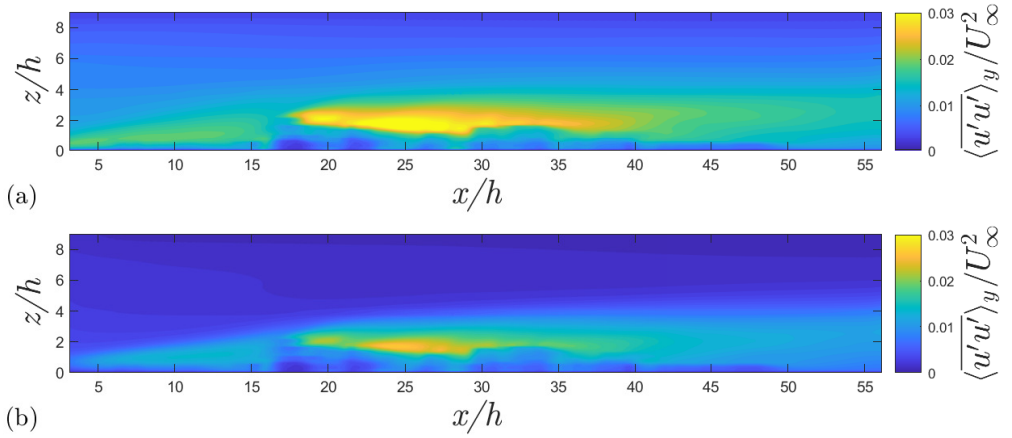

FIGURE 4.9: Spanwise averaged, normalised streamwise normal stress contours for a) SF8 and b) FF8

The spanwise averaged spanwise stress (Fig. 4.10) shows less sensitivity, within the canopy, to the change of incoming turbulence at the inlet than the streamwise stress. The peak values look to be quite similar, around a 15% decrease for FF8 compared to SF8. Again, qualitatively the agreement of the distribution looks to be similar between both cases.

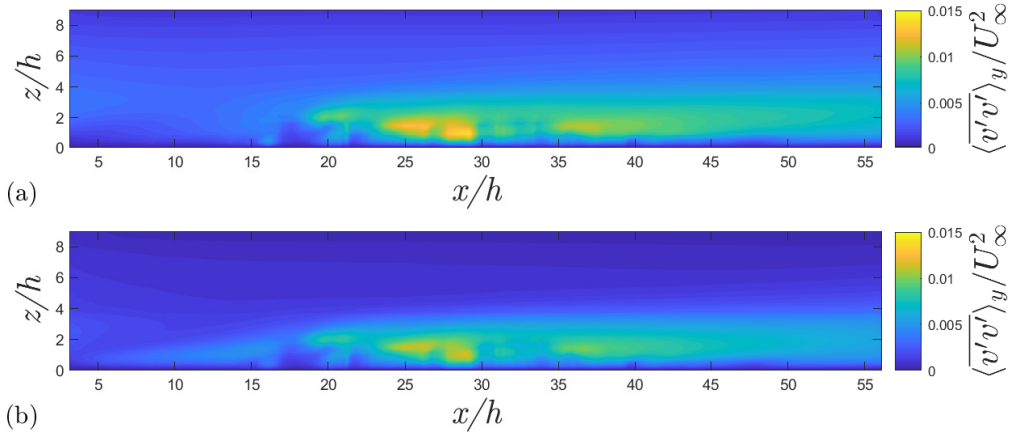

FIGURE 4.10: Spanwise averaged, normalised spanwise normal stress contours for a) SF8 and b) FF8

Shown in Fig. 4.11 is the spanwise averaged contour for vertical stress. The vertical stress is indicative of the internal boundary layer depth, as discussed previously and shown by Sessa et al. (2018). Qualitatively, it is possible to see the difference in average

thickness across the span of the building region. Using the updated method of Sessa et al. (2018) this can be quantified for this spanwise averaged data. This is discussed in section 4.4 for SF8. The interface of the IBL for FF8 should be significantly clearer than for SF8.

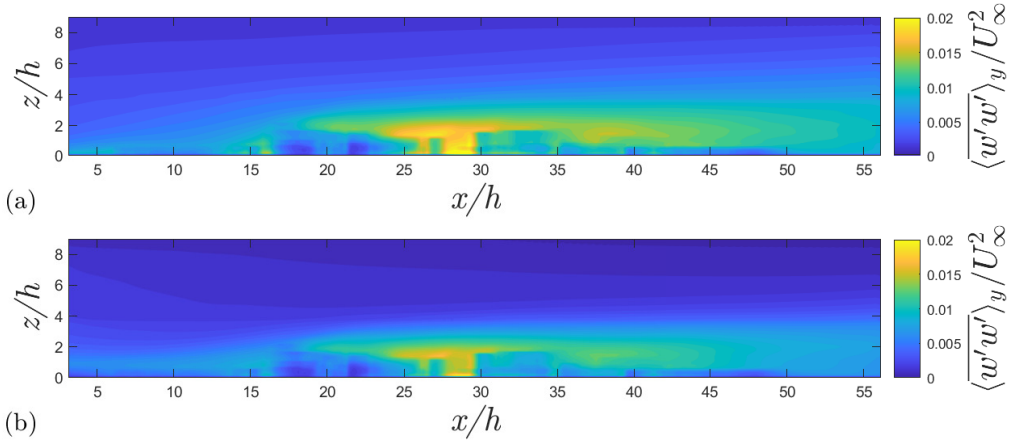

FIGURE 4.11: Spanwise averaged, normalised vertical normal stress contours for a) SF8 and b) FF8

The spanwise averaged Reynolds stress (Fig. 4.12) shows a similar sensitivity to the inflow conditions for the peak values. Again, the general shape and magnitude of the contours are similar in both cases. The magnitude of the first peak, $x/h = 25 - 27$ is around 30% larger for SF8. The peak downstream, beginning at $x/h = 36$ is much closer between the cases, with SF8 being only 13% larger, at $\langle -\overline{u'w'} \rangle / U_\infty^2 = 0.0076$ for SF8.

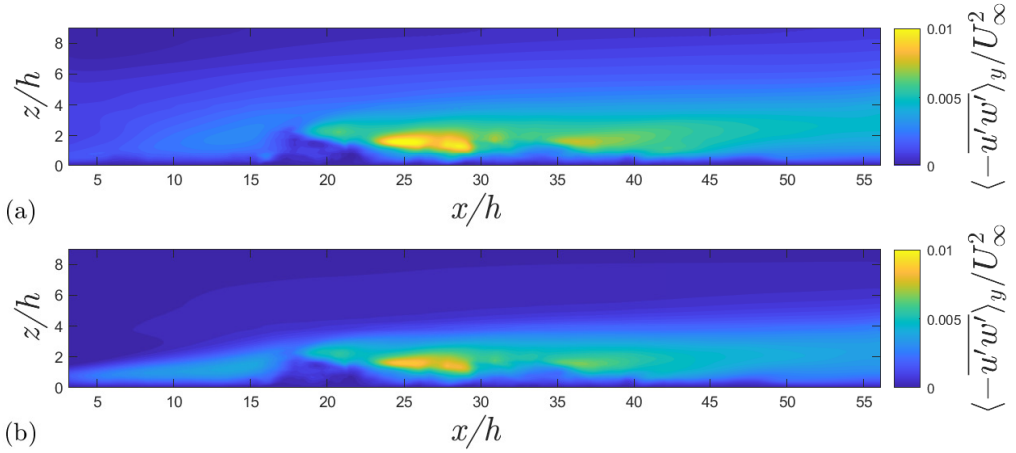

FIGURE 4.12: Spanwise averaged, normalised Reynolds stress contours for a) SF8 and b) FF8

As was discussed previously, the IBL depth is key to accurately predicting vertical spreading downstream of a scalar plume. Here, the IBL depth has been shown to be quite dependent on the turbulence upstream of the roughness step change. The different inflow conditions applied effectively creates a change in the ratio of roughness lengths for the two inflow conditions. The step change in roughness size gives rise to the growth of an IBL. The IBL height is estimated using the method of Sessa et al. (2018). The FF8 case exhibits a thinner IBL due to the effective change in roughness upstream, with the results shown in table 4.1. It should be noted that this IBL thickness is local to this location.

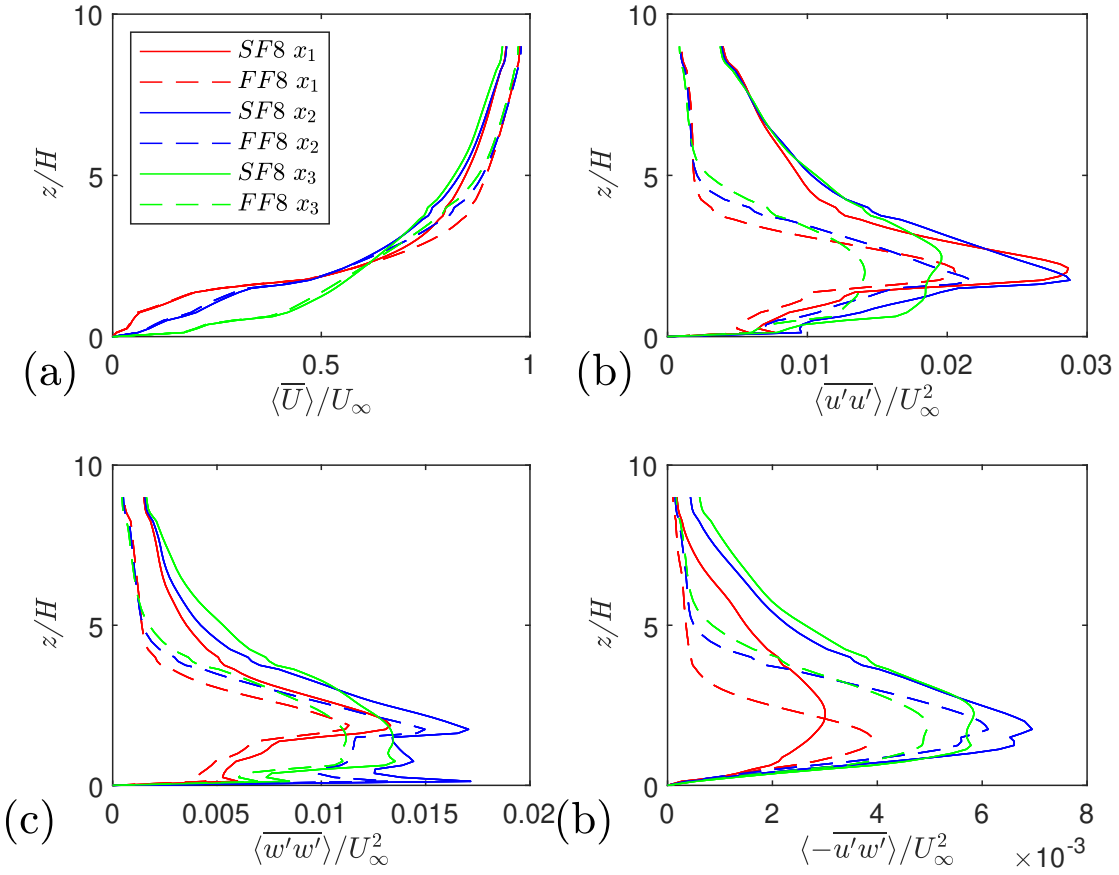

FIGURE 4.13: spanwise average flow quantities averaged across $x/h = 2$ streamwise strips for SF8 and FF8 showing normalised a) streamwise mean velocity b) streamwise normal stress, c) vertical normal stress and d) Reynolds shear stress. For the streamwise regions, where x_1, x_2, x_3 refer to the regions $4h - 6h$, $16h - 18h$, $28h - 30h$ respectively.

Fig. 4.13 shows the spanwise averaged normalised mean streamwise velocity, streamwise and vertical normal stresses and the Reynolds stress for different downstream regions. This is to help quantify the growth of the integral boundary layer with downstream distance. For the downstream regions: $4h - 6h$, $16h - 18h$, $28h - 30h$, the spanwise averaged internal boundary layer thickness is reported in table 4.1. The growth of the IBL is affected by the inflow conditions. However, given a

long enough fetch, it should be possible for the IBL of both SF8 and FF8 to attain the same depth.

Case	$4h{=}6h$	$16h{=}18h$	$28h{=}30h$
FF8	3.2	4.2	4.7
SF8	3.9	4.6	5.1

TABLE 4.1: Internal boundary layer depth according to the method of Sessa et al. (2018)

The normalised w_{rms} was used to estimate the IBL thickness (Sessa et al., 2018); the largest residual for the linear fitting was 7%, giving a maximum error of the thickness of the layer as $\pm 0.1h$. SF8 generates a far thicker IBL at the leading edge, but they are converging with downstream distance. In the centre of the building array, the IBL is roughly $1/2h$ thicker when typical turbulent stresses for urban areas were prescribed, when compared to the naturally grown smooth wall turbulent boundary layer for FF8.

In real situation, the incoming boundary layer can be quite different (more than the difference between SF8 and FF8). The results show the importance of inflow conditions on the local IBL thickness. As was shown by Sessa et al. (2020), the vertical spreading of scalar sources is driven by vertical turbulent motions within the IBL and canopy layers (Hertwig et al., 2018). Therefore, it would be sensible to suggest that correct prediction of the IBL depth would lead to more accurate ground-level concentrations, as it is not unreasonable to suggest this would have an impact on the downstream concentration of scalar sources near the ground downstream of a change in roughness, as the vertical spread of the scalar is mostly capped by the interface at the top of the IBL (Sessa et al., 2018). Given a long enough fetch, the IBL thickness would converge it seems; however, this is in excess of $30h$ downstream for this building array.

The Reynolds stress for the downstream regions is highly dependent on the buildings just upstream of the averaging region. The large peak value for SF8 at $16h - 18h$ is larger compared to the more uniformly vertically spread peak value downstream at $28h - 30h$, around $4/5$ of the centre region. The velocity field for SF8 and FF8 within the canopy (fig 4.15) shows the large buildings that take up a large spanwise extent of this region and are almost aligned perpendicular to the oncoming flow. These buildings lead to a large peak of Reynolds stress, as discussed previously, in location 7 (4.1). As can again be seen, the velocity field within the canopy is negligibly affected by the incoming turbulence prescribed at the inlet.

If the location of interest is far enough downstream, the IBL will become sufficiently developed, so the turbulent quantities within and just above the canopy will be indicative of the underlying surface. As is shown in Fig. 4.13 the difference between

each subsequent downstream region becomes smaller, especially for the Reynolds stress. The distance allowed for flow development should be set to be a minimum of $16h$ from the leading edge of the array for cases where the accuracy of the inflow conditions is unknown. This would provide an IBL depth with an error within 10%. For more appropriate prescribed inflow conditions, this distance could be lowered.

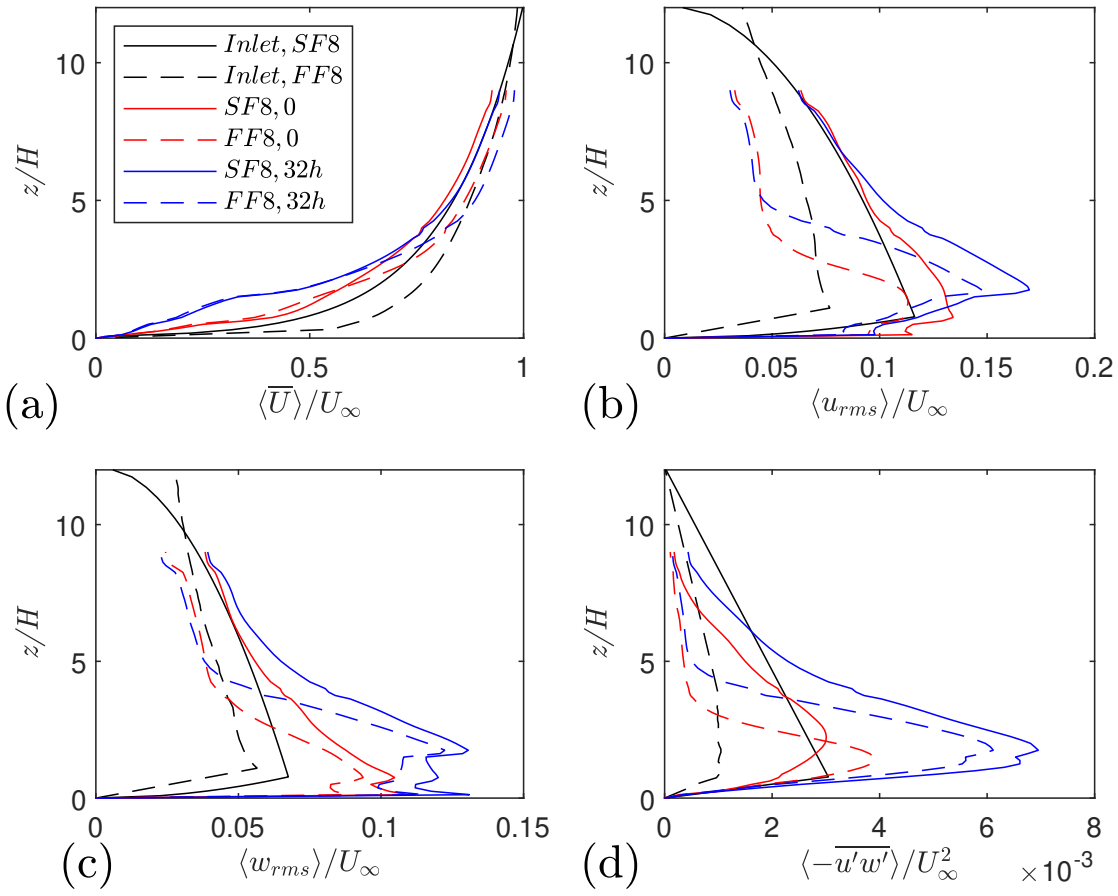

FIGURE 4.14: spanwise average flow quantities averaged across $x/h = 2$ streamwise strips for SF8 and FF8 showing normalised a) streamwise mean velocity b) streamwise r.m.s. velocity, c) vertical r.m.s. velocity and d) Reynolds shear stress. For the prescribed inlet values compared to the streamwise regions $0 = 0h - 2h$ and $32h = 32h - 34h$.

Fig. 4.14 compares the inlet prescribed vertical profiles to the spatially averaged quantities at the leading edge and mid fetch region $x = 32h - 34h$. The mean velocity profiles prescribed for FF8 and SF8 are given, compared to the spanwise averaged strips (Fig. 4.14a). The streamwise turbulence prescribed for SF8 and FF8 is shown in Fig. 4.14b.

The u_{rms} decays from the prescribed values to the leading edge for FF8. Between the leading edge and the centre of the streamwise fetch u_{rms} changes very little above the internal boundary layer. It does not decay above the IBL from the prescribed values at

the inlet for SF8. The peak values of u_{rms} are considerably smaller at both averaging regions compared to the difference between the inlet profiles.

The w_{rms} is shown in Fig. 4.14c along the fetch of the domain for both FF8 and SF8. Decaying very slightly for FF8 and growing very slightly for SF8. The peak values of w_{rms} are quite similar between FF8 and SF8 for the two spatial averages. This difference is smaller than that of the difference at the inlet at $z/h = 1$. The Reynolds shear stress is shown in Fig. 4.14d. The prescribed peak Reynolds shear stress for SF8 is 3x that prescribed in FF8. However, in the strip from $x/h = 0 - 2$, the peak Reynolds shear stress generated in FF8 is approximately 20% higher than SF8.

Within the canopy, the velocity, qualitatively, is shown to have little difference between inflow conditions (Fig. 4.15). It is useful to look at contours as they show the full flow field across the $x - y$ plane, as local peaks may be differ significantly while spatially averaged data can show good quantitative agreement.

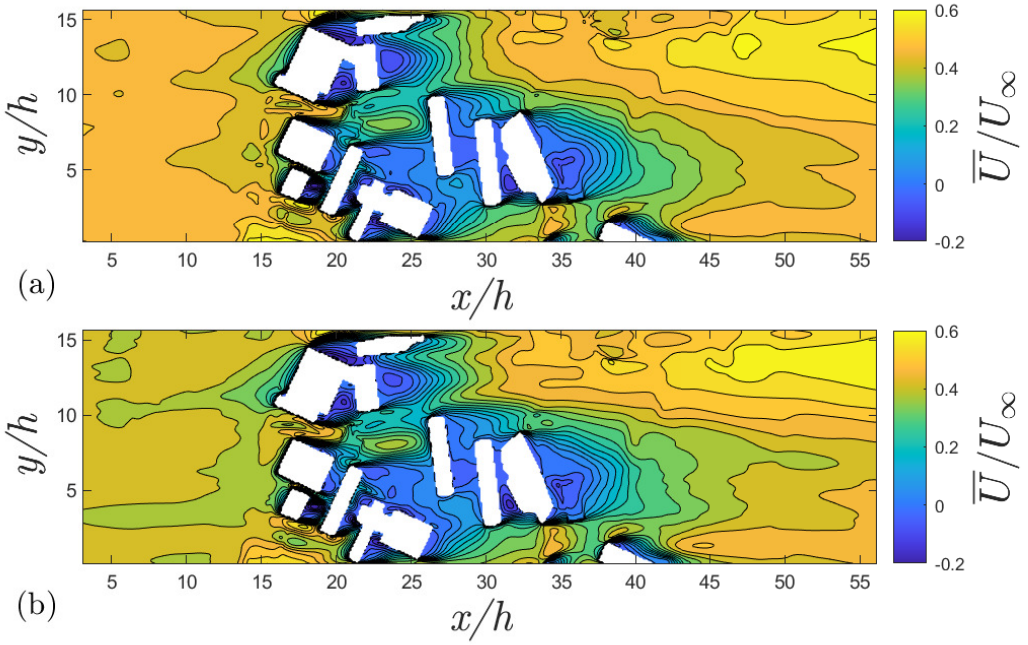

FIGURE 4.15: Streamwise mean velocity within the canopy at $z/h = 1$ for a) SF8 and b) FF8

It can be suggested that as long as appropriate boundary conditions are used, the velocity field generated will be more than adequate. The results show that the difference between inflow turbulence levels is small within the canopy, given sufficient time to develop. In the region just above the canopy, the difference is also small. For wind loading use cases applying approximate inflow profiles would be sufficient. Prediction of the turbulence profiles within the domain, especially local profiles, will also not be drastically affected by the prescribed turbulent profiles at the

inlet. Spatial averages within the domain have shown some sensitivity to inflow conditions both above and within the canopy. The greatest effect inflow conditions have is on the vertical extent of the internal boundary layer thickness. If the vertical spreading of a ground-level source is of particular importance, appropriate prescribed profiles or incoming turbulence from a precursor simulation should be used.

4.2 Comparing flat and real terrain

4.2.1 Effects of terrain treatment on flow quantities

Fig. 4.16 shows the mean axial velocity and Reynolds shear stress profiles at the same 14 locations as shown in Fig. 4.1.

The terrain effect is visible on the velocity profiles; there is clearly a higher velocity within the canopy in locations 5,6,7. Further downstream, the difference is much less. Locally the building height can be different, which is visible at location 8, as the local ground height makes this building shorter in this location. The effect on the Reynolds shear stress is visible but difficult to generalise from vertical profiles.

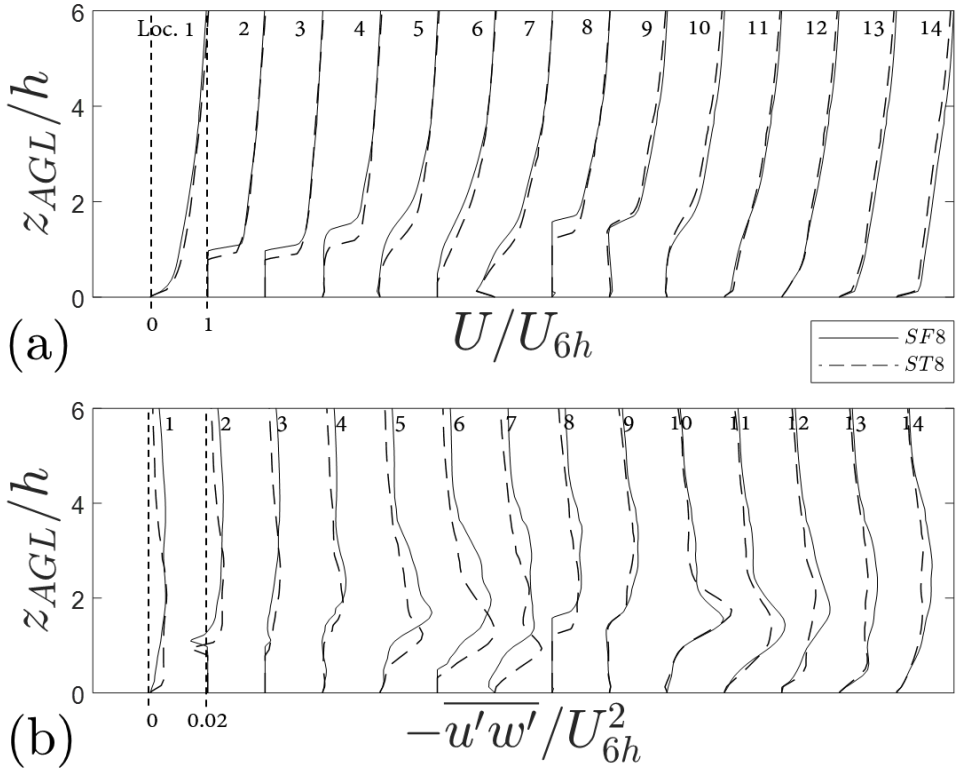

FIGURE 4.16: Vertical profiles of a) mean axial velocity, and b) Reynolds shear stress at the 14 locations shown in (4.1).

The campus has a somewhat clustered nature to the layout of the buildings. As shown in Fig. 4.17. Significant Reynolds shear stress can be seen at locations 5, 6 and 7 in Fig. 4.16. These locations are within an open area (a car park) and are downstream of a clustered group of buildings. These buildings are labelled as buildings 2 and 3 in Fig. 4.17 and a building just off the south of this (building 4 in fig 4.17). Channelling occurs between buildings 2 and 3, forcing the fluid into the open region. This region is

dominated by the faster moving fluid on the north side of the dashed line and the slower region in the wake of buildings 2 and 3.

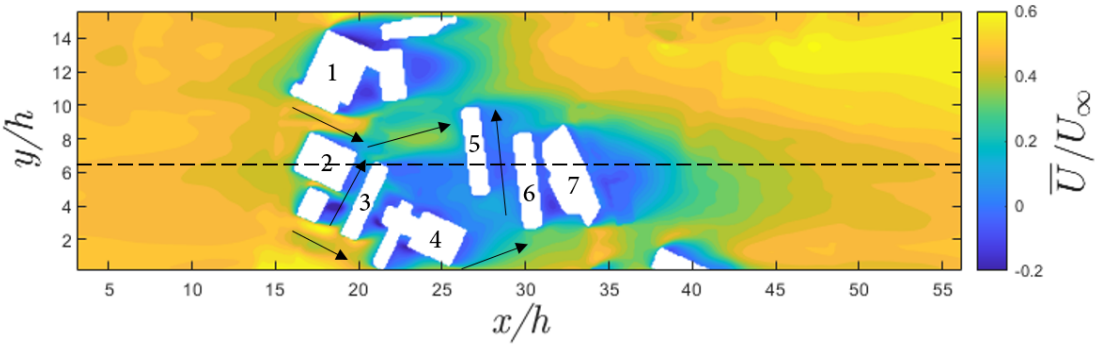

FIGURE 4.17: Contour of time mean streamwise velocity of the north half of the building array across a plane at $z/h = 1$. Building label ID's and dotted line showing plane location.

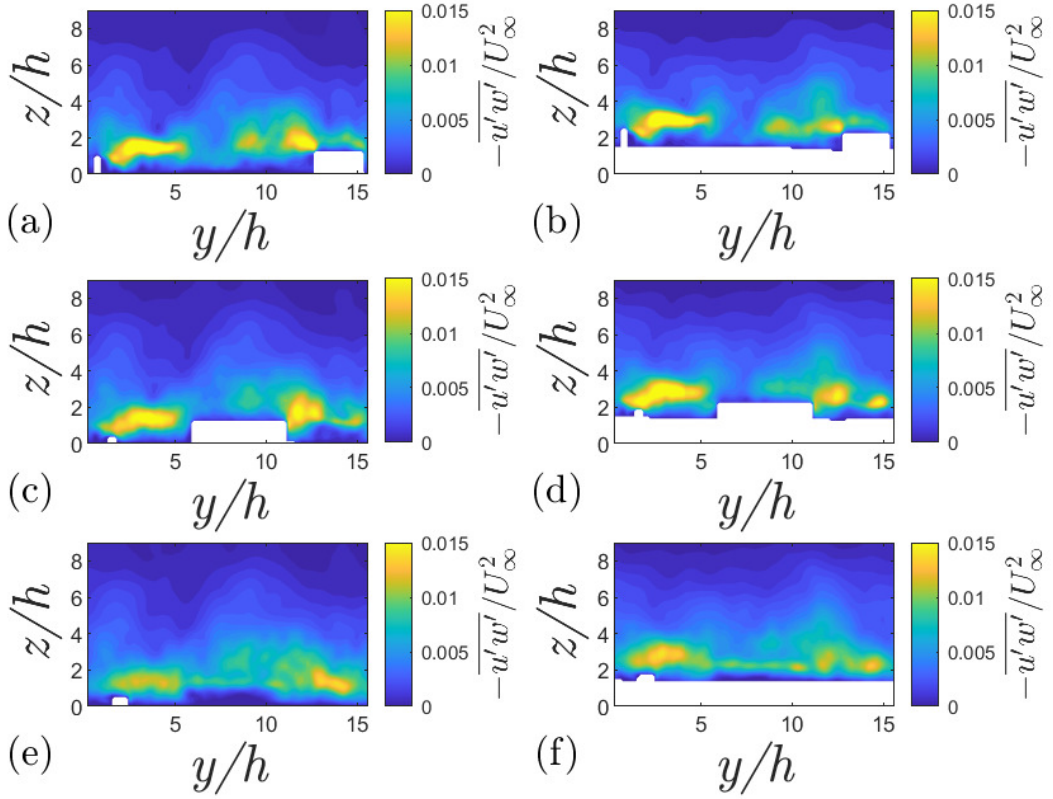

FIGURE 4.18: Contour of normalised Reynolds stress at a&b) $x/h = 25.5$, c&d) $x/h = 27$ and e&f) $x/h = 28.5$ for SF8 (a,c,e) and ST8 (b,d,f) Y values need changing

It was expected to 'see' large Reynolds shear stress at the building top in the street canyon between buildings 5 and 6, as found in typical canyon flows. However, as shown in Fig. 4.18 the surrounding buildings cause lower Reynolds stress around building 5 at the canopy top and for the leftmost half of its spanwise extent, it is much

reduced due to the surrounding buildings. This is caused by the funnelling between buildings 1 and 2. The flow within the gap between building 5 and 6 goes towards the north (positive y direction) even though the buildings are aligned a few degrees counter-clockwise away from the perpendicular. Due to the placement of building 5 and 6 and the orientation of buildings encompassing them, the flow direction in the canyon is approximately 80 degrees to the free-stream flow direction. Small amounts of Reynolds shear stress are visible at the building top in Figs. 4.18ef; this is the shear layer from the building top, the peak of which approximately 1/2 of that of the peaks from the surrounding buildings.

The terrain seems to reduce the Reynolds shear stress peaks slightly in Fig. 4.18. The peaks on the right-hand side, around $y/h = 10 - 15$, are closer to the ground due to the terrain roll-off in this region.

The domain height for ST8 is slightly shorter at the inlet, around 24% less. There is an expansion of around 20m in the vertical direction at the inlet. This accounts for a slowdown in the freestream velocity of 3% for ST8 compared to SF8. This accounts for the mean flows looking somewhat similar overall, but ST8 having a slightly lower velocity towards the end of the domain in Fig. 4.19.

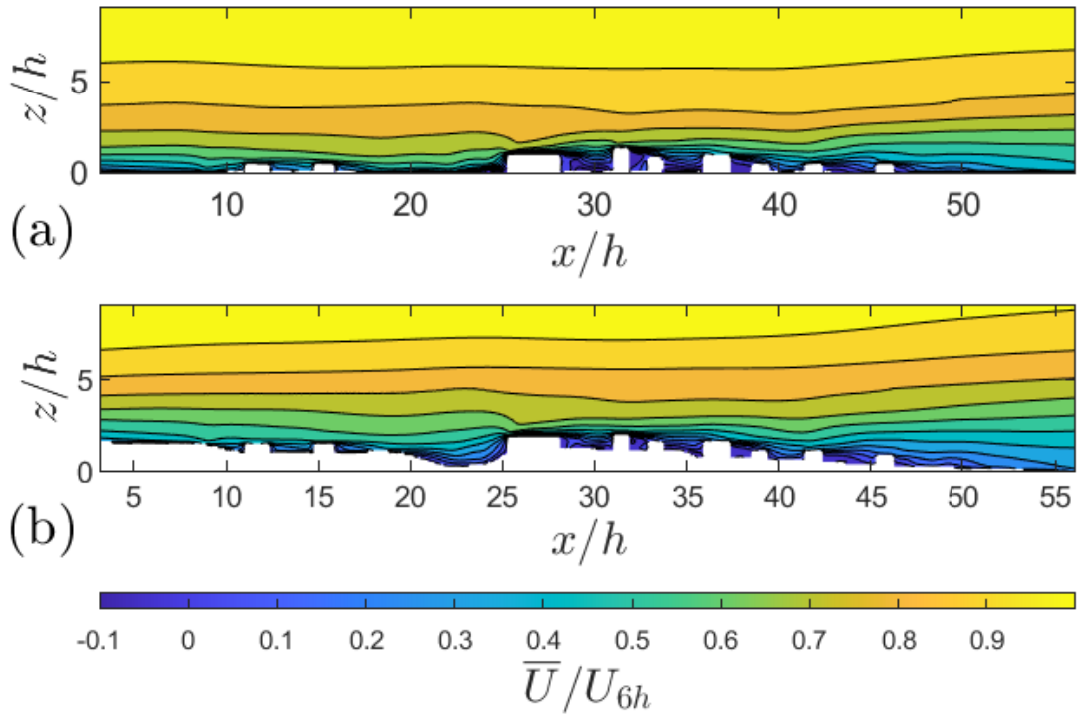

FIGURE 4.19: Mean streamwise velocity across an x, z plane at $y = -210m$ shown in (Fig.2.18) for a) SF8 and b) ST8.

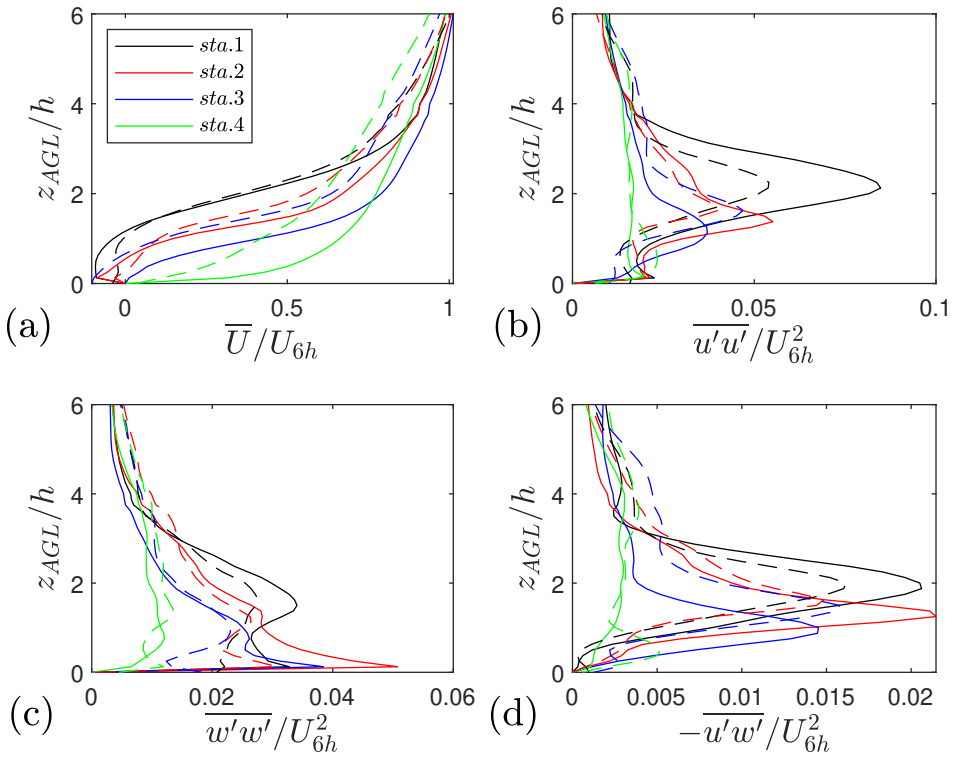

FIGURE 4.20: Vertical profiles of a) streamwise mean velocity, b) streamwise normal stress, c) vertical normal stress and d) Reynolds shear stress for each of the four measuring stations, station 1 at $x/h, y/h = 18.25, -4$, station 2 at $x/h, y/h = 21, -6.5$, station 3 at $x/h, y/h = 20.75, -9.5$ and station 4 at $x/h, y/h = 23.5, -14$ (See Fig. 2.19)

Perhaps not surprisingly, the terrain effect on the local flow and turbulent quantities differs substantially from place to place. We focused on four typical stations which were located in the valley (see Fig. 2.19). Fig. 4.20 shows vertical profiles of mean streamwise velocity at the four stations for the flat and real terrains. At station 4 the mean streamwise velocity is significantly affected by the deep and wide valley at $y = -210$ m. At station 3, the effect of the valley is still evident. At stations 1 and 2, the terrain effect on the mean streamwise velocity is much less; this is because of the shallow valley at $y = -28$ m and -102 m and the tall building immediately upstream of them.

Fig. 4.20b, c and d show the normal stresses $\overline{u'u'}$, $\overline{w'w'}$ and Reynolds shear stress $\overline{u'w'}$, respectively. These second-order turbulent statistics are highly dependent on the local terrain and the upstream buildings. It would be extremely challenging to set up a simple method to account for the terrain effect and, therefore, to correct the turbulent stresses obtained from a flat terrain model.

Locally, the flow velocity can differ from the effects of terrain quite substantially. The time-mean of the streamwise velocity component is given in Fig. 4.20. At stations 3 and 4 the mean streamwise velocity is affected substantially. All four stations show

smaller flow velocities above the canopy for ST8. At the average canopy height, the streamwise velocity is roughly half for (ST8).

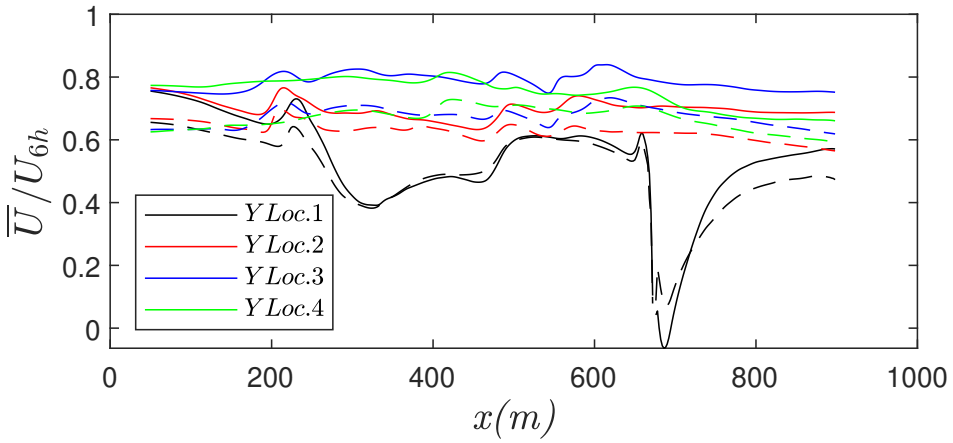

FIGURE 4.21: Dimensionless axial velocity at 4 spanwise locations (given in Fig. 4.20) at $3h$ above the average ground level

Fig. 4.21 shows four streamwise mean velocity profiles respectively at $y = -28$ m, -102 m, -152 m, and -210 m, and $z_{AGL} = 48$ m ($3h$) (see Fig. 2.19). of which the spanwise coordinates y ($Y\ Loc.1$, $Y\ Loc.2$, $Y\ Loc.3$ and $Y\ Loc.4$) are, respectively, as the same as the 4 stations ($sta.1$, $sta.2$, $sta.3$, and $sta.4$) in Fig. 4.20. Overall, the mean streamwise velocity at z_{AGL}= $3h$ is higher over the flat terrain (SF8) than over the real terrain (ST8). This confirms the early concluding remark (e.g. from Fig. 4.30). For the $Y\ Loc.1$ profile, there is a peak negative velocity at approximately $x = 700$ m, which is close to the tallest building in the array and is lower than that building.

The streamwise velocity above the canopy is greater within the flat domain across a large portion of the domain, as shown in Fig. 4.22. The velocity was sampled at 36m AGL for every location, the local ground height. In the case where the terrain is included, Fig. 4.22b, the low-velocity region extending in the spanwise direction follows quite closely the valley in that region. The buildings shown in this figure show the building locations; however, most of these buildings are not present at this height AGL. It is to purely represent their location and to remove any discontinuities in the contour. Still far away from the ground, the effects of the terrain can still be seen in the streamwise velocity contours. At this height, the effect of singular buildings is difficult to discern. The effect of the terrain, however, is still clearly visible. Even though the terrain height change is a similar order to that of the buildings, and smaller in some regions.

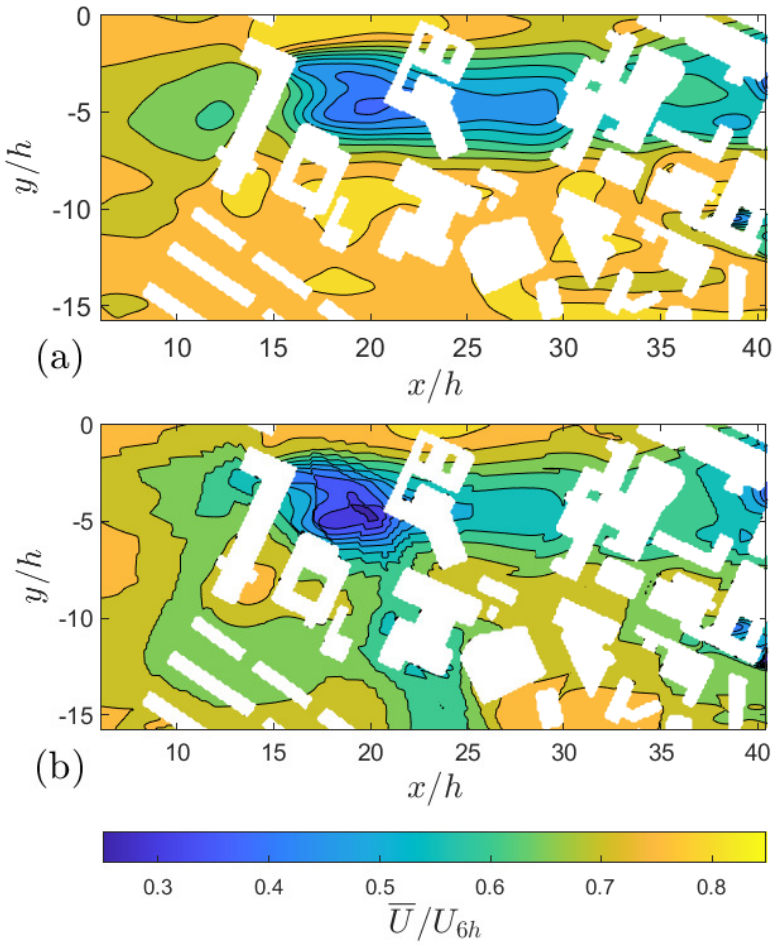

FIGURE 4.22: Dimensionless streamwise velocity at $z_{AGL}/h = 3$ for a) SF8 and b) ST8.

Due to the terrain effects, there is greater streamwise flow velocity within the canopy at $1/2h$ AGL (Fig. 4.23). Buildings upstream can be 'hidden' due to terrain roll-off. Downstream buildings are then more exposed to higher flow velocities deeper within the canopy. At the southwest corner of Figs. 4.23a and 4.23b, the channelling effect is reduced between the large building (with extent from $x/h, y/h = 12, -9$ to $x/h, y/h = 16, -2.5$, and the 3 smaller elongated buildings, located between $x/h, y/h = 11, -10$ to $x/h, y/h = 19, -15.5$. Upstream of $x/h = 10$, the terrain is roughly at the roof line of the smaller buildings, thus shielding these buildings.

However, ST8 exhibits stronger channeling downstream between $x/h = 25$ and $x/h = 35$. This region of the domain has a higher elevation than the upstream region. Upstream buildings are shielded by the terrain, reducing effective exposure. The deep valley that runs almost spanwise through the domain reduces the absolute height of the buildings, which further reduces the effective frontal area seen by the flow of the upstream buildings. This, coupled with the higher elevation in this region, produces a higher streamwise convection through this region of the canopy.

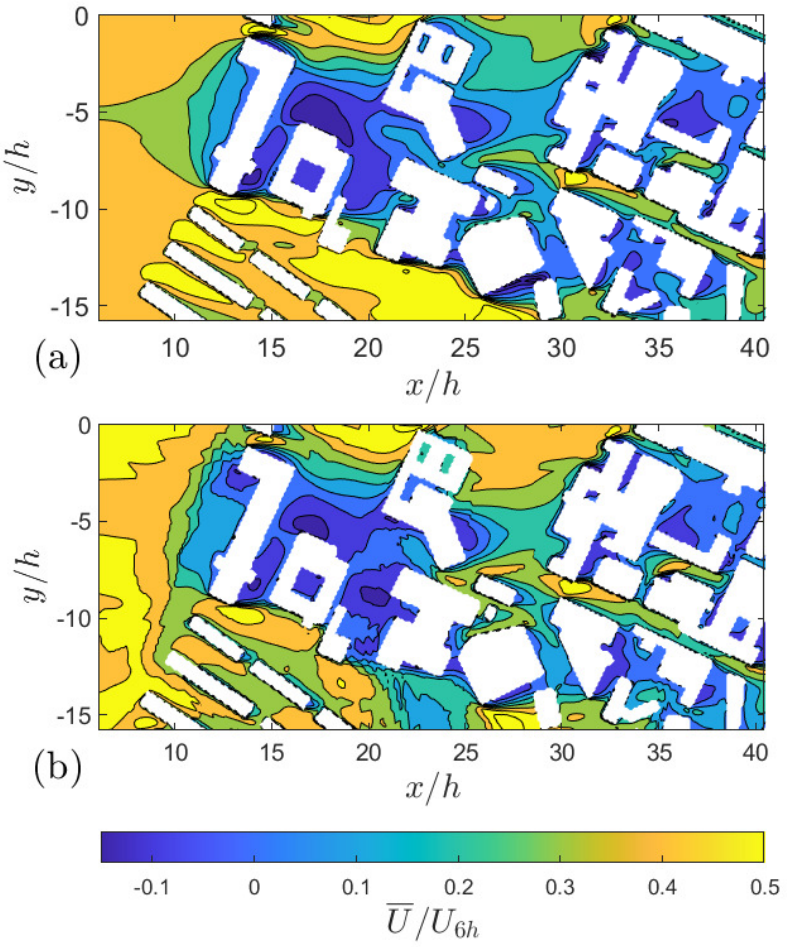

FIGURE 4.23: Dimensionless streamwise velocity at $z_{AGL}/h = 0.5$ for a) SF8 and b) ST8.

To quantify the terrain effect on the local mean velocity, the ratio of mean streamwise velocity is defined,

$$\overline{U}_{ST8}/\overline{U}_{SF8} = \frac{\|\overline{U}_T(x,y,z_{AGL})\|}{\|\overline{U}_F(x,y,z_{AGL})\|}, \tag{4.1}$$

where $\|\overline{U}_T(x,y,z_{AGL})\|$ and $\|\overline{U}_T(x,y,z_{AGL})\|$ are the absolute values of the mean streamwise velocity for the real terrain case ST8, and the flat terrain case SF8, respectively. Changes in the ratio of velocity magnitude coincide with the elevation within ST8. The elevation through the domain is shown, along with the ratio of velocity magnitude at $z_{AGL}/h = 3$ in Fig. 4.24c.

Fig. 4.24a shows the elevation contours of the real terrain in the valley region ($0 \leq x/h \leq 40$, $-15 \leq y/h \leq 0$). Over this region, the ratio $\overline{U}_{ST8}/\overline{U}_{SF8}$ of the mean-streamwise velocity at $z_{AGL} = 9$ m is shown in Fig. 4.24b. It is to be noted that the fluid regions above buildings are not shown. Changes in the ratio contours of the

streamwise velocity correlate positively with the elevation contours in Fig. 4.24a. Usually, a high elevation on a location in Fig. 4.24a is associated with a high ratio $\overline{U}_{ST8}/\overline{U}_{SF8}$ on the same location in Fig. 4.24b. Such correlation is also visible at z_{AGL} =36 m shown in Fig. 4.24c. This correlation is certainly due to local variation of elevation, suggesting that some corrections for the wind velocity within and immediately above the canopy must be carried out to take into account the local terrain variation as well as the global slope (see Fig. 4.30a-b), when a flat terrain has to be used in experiments or numerical simulations. The ratio $\overline{U}_{ST8}/\overline{U}_{SF8}$ of the mean-streamwise velocity is less than unity across most of the domain, as shown in Fig. 4.24, which is consistent with that in Fig. 4.30.

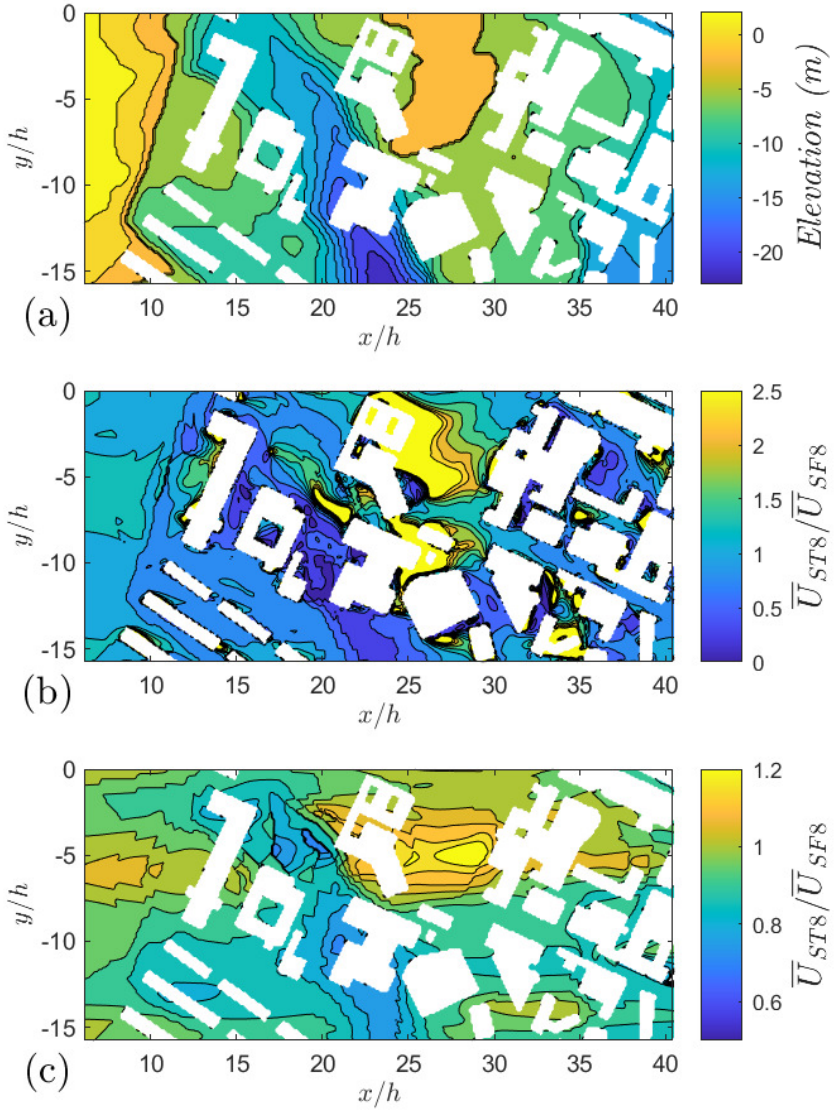

FIGURE 4.24: a) elevation of the ground in ST8, b) the ratio of the mean-streamwise velocity for ST8 and SF8 at points $z_{AGL}/h = 0.5$ and c) also shows the ratio of mean velocities at $z_{AGL}/h = 3$.

The up-slope and down-slope boundary layer effects are similar to that for the boundary layer within a half-diffuser or the boundary layer over a wing without separation. There exists a negative or favourable pressure gradient for the up-slope condition, and the opposite is true for the down-slope, where a positive pressure gradient occurs. Approaching the top of the hill, there is a speed-up within the boundary layer close to the surface (Taylor, 1998). Cindori et al. (2020) reviewed the effects, including the mean speed up at the crest of a simple sinusoidal hill, where the mean speed up is shown to be present for flows over both smooth and rough hills (Safaei Pirooz and Flay, 2018).

The effect of terrain can still be seen high above the canopy, Fig. 4.22, even when the effects of single buildings are difficult to distinguish. The mean speed up is still visible even at $z/h = 3$ above the ground level. Fig. 4.25 shows the elevation of the terrain and buildings. The elevation across line *a* (Fig. 4.25) goes from $-3m$ down to a minimum of $-17m$ up to $-7m$. Across line *b* (same figure), the terrain elevation goes from $-5m$ down to a minimum of $-25m$ up to $-9m$. The overall slope here is present, but the terrain change is significant; the terrain decreases in height by $20m$ and increases again by $16m$. The change in the height of the terrain occurs over much larger distances, taking roughly $16h$ to descend $1h$ (slope of roughly -1 in 16) between $x/h = 7.5$ *to* 23. From $x/h = 23$ *to* 30, the change in height is roughly $1h$ over a downstream distance of $7h$. The buildings typically have downstream extents averaging about $3h$. The greater extent over which the terrain height change occurs could be the reason why the flow high above the canopy is still directly affected by the terrain elevation.

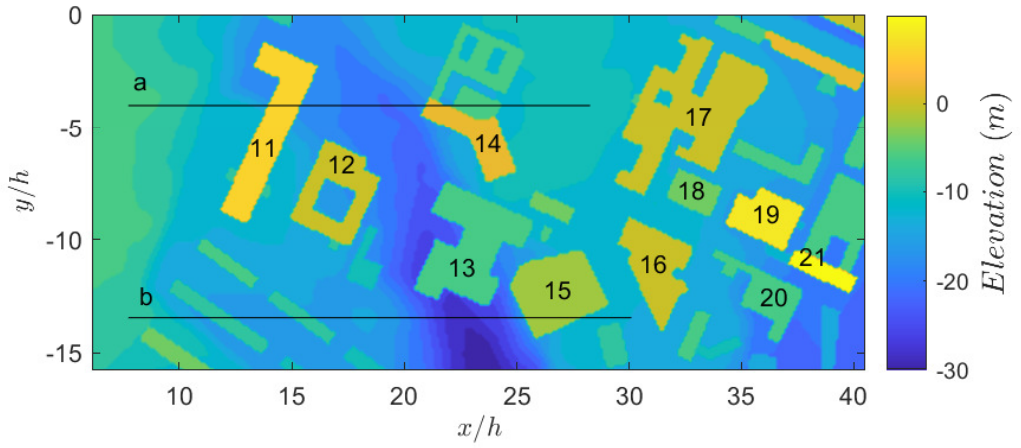

FIGURE 4.25: Terrain and building elevation contour with buildings labelled, lines are defined for terrain height comparison.

A secondary effect of the terrain is to shelter buildings from the upstream flow or increase the exposure of downstream buildings. The relative building heights are

quite different when the terrain is included, ST8, compared to the flat domain, ST8.

From analysing the data, the flow seems to follow the terrain. This is shown as the higher speed region seen in front of the building at $x/h, y/h = 12, -4.5$ in Fig. 4.23. Further downstream, the terrain which leads to the building centred at $x/h, y/h = 23, -12.5$, is significantly reduced in elevation compared to the buildings downstream. The relative differences between the buildings labelled in Fig. 4.25 are shown in Table 4.3. The average building height of each building labelled in Fig. 4.25 for ST8 was calculated by averaging the height of the building around its perimeter.

Building Height (m)

Case	**11**	**12**	**13**	**14**	**15**	**16**	**17**	**18**	**19**	**20**	**21**
SF8	21.1	19.3	11.3	15.9	15.9	20.6	19.3	15.5	28.4	14.0	31.4
ST8	17.3	11.8	4.2	12.6	8.0	9.8	11.1	11.8	4.0	18.8	21.9
ST8(av)	21.5	17.1	13.6	15.4	14.3	12.7	10.2	8.3	24.2	11.0	30.7

TABLE 4.2: Building height relative to the campus centre location ($x/h, y/h = 27.5, -5$), ST8(av) gives the average building height around the building perimeter.

The effective height of each of the buildings compared to the fixed point ($x/h, y/h = 27.5, -5$) is shorter for almost every building due to the terrain height changes. This demonstrates the shielding that occurs due to the terrain changes. This location was chosen as it is close to the geometric centre of the array, and sits upon a high point within the campus, the most exposed region. The table shows that the average height of a building around its perimeter can be quite different to its maximum height (SF8 data in 4.3 is essentially the maximum height of a building around its perimeter and also the height relative to the campus centre location).

The dimensionless turbulent kinetic energy at $z_{AGL} = 9$ m is shown in Fig. 4.26. In most of the area, the TKE over the real terrain within the canopy is evidently reduced due in part to the global down-slope (or diffuser) effect. This is consistent with Fig. 4.30c. Such global diffuser effect on the TKE is so great that the effect due to the local elevation variation is only visible just downstream of the valley (e.g. $21 \leq x/h \leq 25$, $-15 \leq y/h \leq 0$), where the TKE for ST8 is greater than that for SF8. Shielding of a building by the terrain also plays a part. The inclusion of terrain in this case makes the surface effectively less rough. the increased velocity through the canopy show there is a smaller drag contribution provided by the buildings. In the case where inclusion of the terrain is neglected, local turbulence generated within the canopy will be over-predicted.

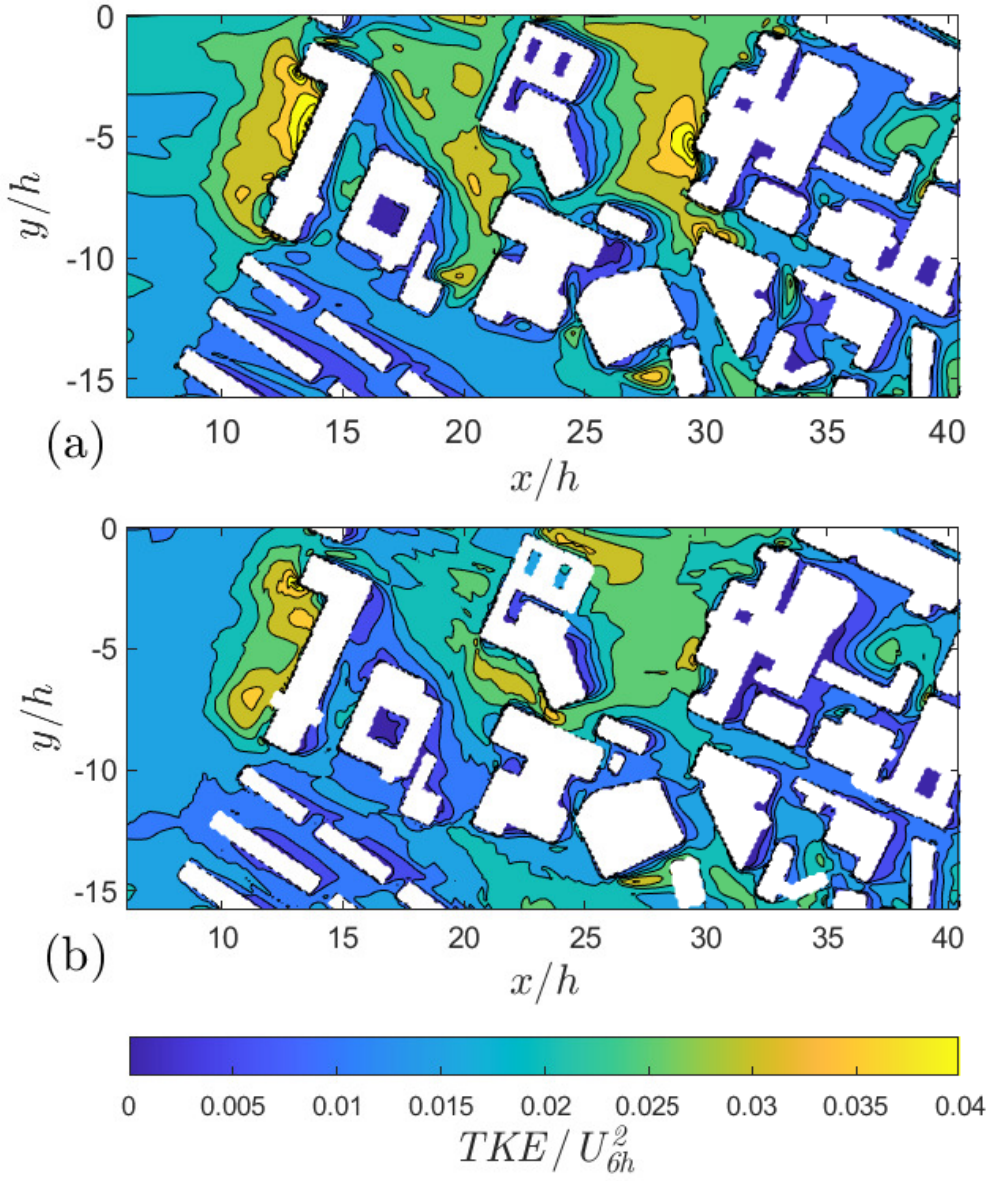

FIGURE 4.26: Dimensionless turbulent kinetic energy at $z_{AGL} = 9m$ across the domain for a) SF8 and b) ST8.

The local effect of terrain is to increase the velocity within parts of the canopy with a sudden increased exposure. There is a reduction in the strength of the turbulence within the canopy, and the vertical momentum flux is also reduced within the canopy (Fig. 4.27). Re-entrainment into the canopy is stronger when the effective roughness is greater.

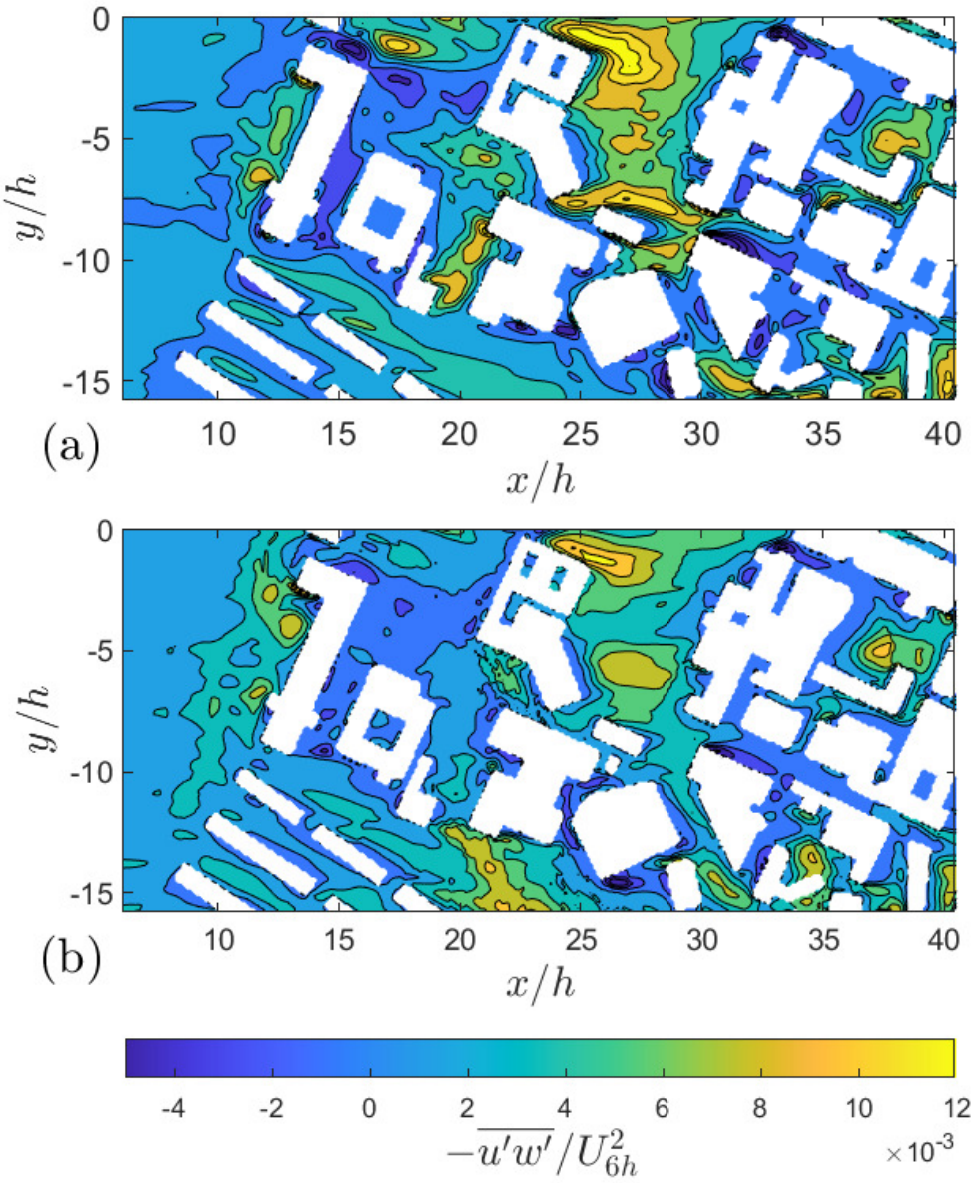

FIGURE 4.27: Dimensionless vertical turbulent momentum flux within the canopy, at $z_{AGL} = 9m$ across the domain for a) SF8 and b) ST8.

The x, z plane across the dashed line in Fig. 4.17 is shown for both SF8 and ST8 in Fig. 4.28. The effective shielding of the buildings downstream (from $x/h = 25$ *to* 35) is greater for SF8 than ST8 as the building upstream (from $x/h = 15$ *to* 22) is within a valley. In ST8, this increases the streamwise velocity within the canopy as the upstream buildings are visibly hidden. The terrain roll-off also reduces the magnitude of the vertical velocity across the canopy, as seen in Fig. 4.28c&d, except downstream of the last building. As the terrain roll-off increases, the building's absolute height compared to those downstream would be far higher. Even for the Southampton University Highfield campus, with its relatively flat terrain.

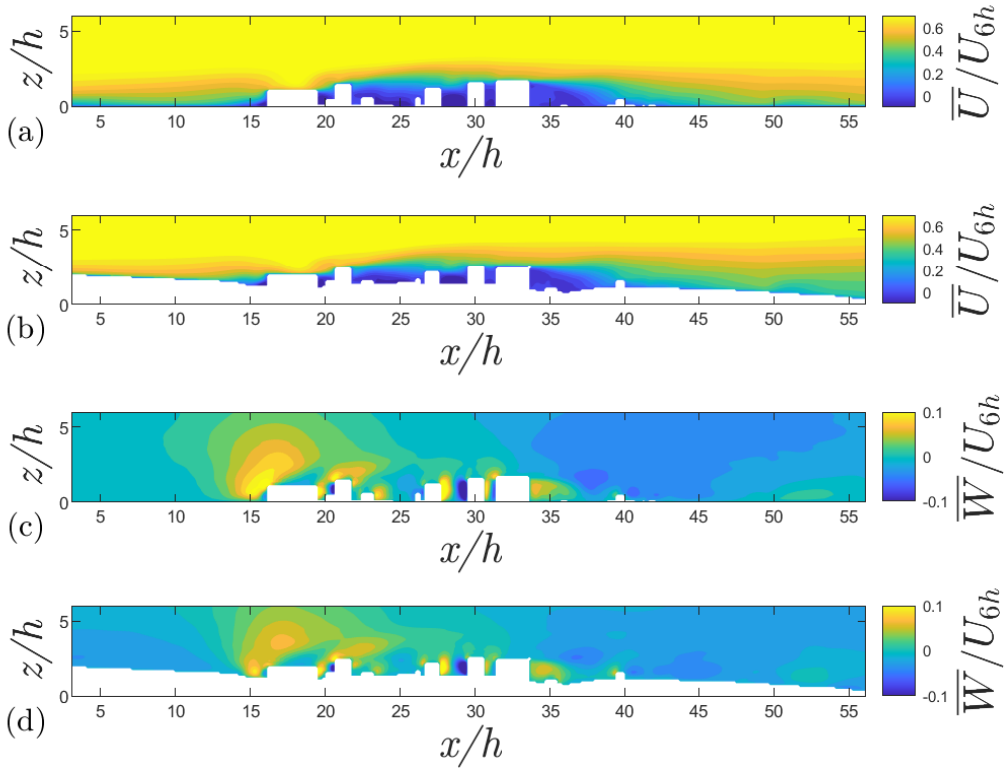

FIGURE 4.28: x, z planes located at $y/h = 6.25$ (fig 4.17). Showing contours time mean streamwise velocity (a&b) for SF8 and ST8 respectively and contours of time mean vertical velocity (c&d) for SF8 and ST8 respectively

The terrain effect on the mean velocities is visible at $y/h = 0$, shown in Fig. 4.29. The wake region extends further downstream of the large building located at $x/h = 40$ to 45. The wake is also deeper due to the terrain roll-off downstream of this building. Buildings downstream would experience the wake of a much taller building upstream.

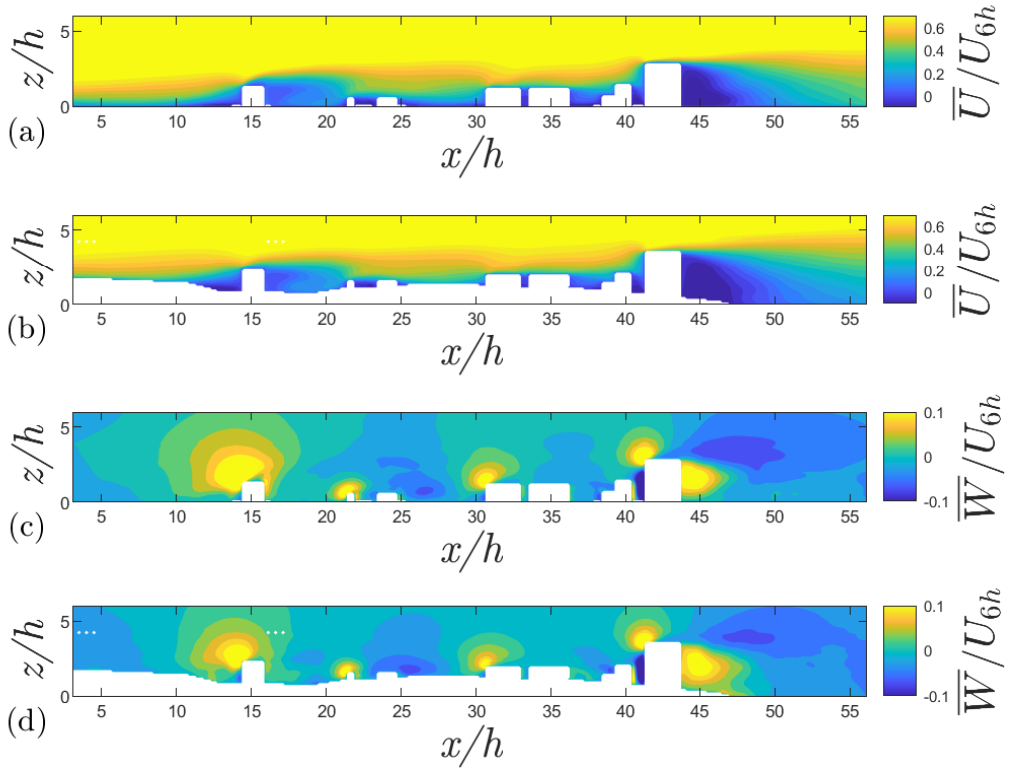

FIGURE 4.29: x,z planes located at $y/h = 0$. Showing contours of time mean streamwise velocity (a&b) for SF8 and ST8 respectively and contours of time mean vertical velocity (c&d) for SF8 and ST8 respectively.

4.2.2 Spatially averaged data

Spatially averaging over the domain with real topology is challenging. Two methods are used here. The first method is to average data at the same above ground level (AGL) height, defined in Equation 4.2,

$$\langle \phi \rangle_t(z_{AGL}) = \frac{1}{S_t} \int_{(S_t)} \phi(x, y, z_{AGL}) dxdy, \tag{4.2}$$

where $\langle\rangle_t$ denotes the spatial average over the area not covered by buildings, which accounts for approximately 71% of the entire bottom surface area). ϕ denotes the quantity to be spatially-averaged, S_t denotes the total area not covered by buildings and is constant over the entire AGL height z_{AGL}. In other words, this average does not take into account the fluid region which is above a building, and of which the coordinates (x, y) are within the ground perimeter of the buildings. Otherwise, this could introduce inconsistencies when using Eq. 4.2.

The second method computes the averages separately for the northern (between $y/h = 0$ *to* 15) and southern (between $y/h = 0$ *to* -15) halves. For this method, $z/h = 0$ is set at the average ground $z/h = 0$ location of all points within the

averaging region. This method is a comprehensive average, taking into account the building regions (as fluid regions with 0 velocities, see 4.2).

The domain height for the ST8 case is slightly shorter at the inlet, around 20% less (Table 2.5) compared to the SF8 case. Both cases maintain the same inflow conditions in the region $0 \leq z \leq 10h$. This ratio of boundary layer to average building height is close to those of wind and water tunnel experiments (e.g. Xie and Castro (2009)). To have a comparison between the flat and real terrain case, all quantities are normalised by the spatially-averaged mean streamwise velocity U_{6h} at $z_{AGL} = 6h$.

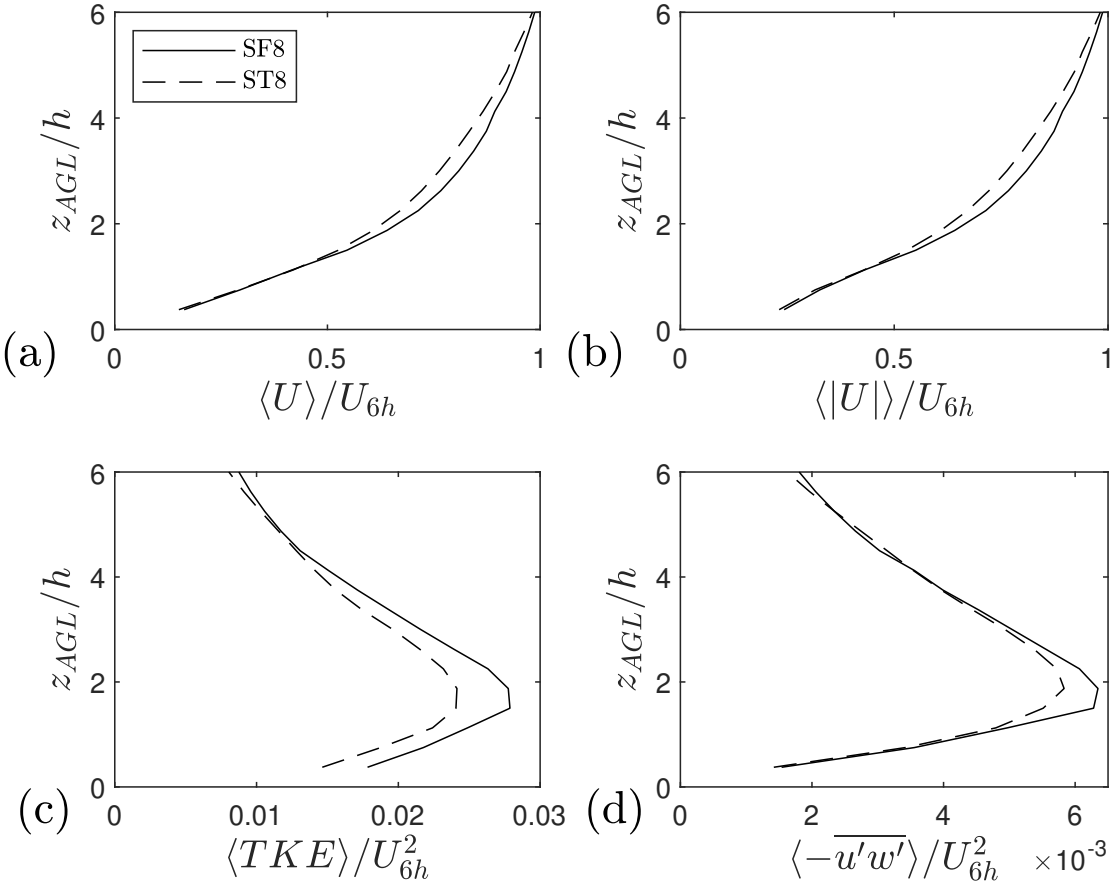

FIGURE 4.30: Spatially averaged data for SF8 and ST8, for the following normalised quantities: a) mean-streamwise velocity, b) mean velocity magnitude, c) turbulent kinetic energy and d) vertical turbulent momentum flux. All quantities are normalised by the spatially-averaged mean streamwise velocity U_{6h} at $6h$.

The spatially-averaged mean velocities and turbulent statistics are shown in Fig. 4.30. Albeit the large local differences in the ratio of mean velocities (e.g. Fig.4.24), Fig. 4.30a and b show that the spatially averaged dimensionless streamwise velocity have a little difference between flat and real terrain cases. The peak spatially averaged Reynolds shear stress at z_{AGL} calculated from the flat terrain case SF8 is evidently greater than that from the real terrain case ST8, suggesting an evidently greater aerodynamic resistance in the flat terrain case for the same incoming flow. The

turbulent kinetic energy for SF8 is even greater than that for ST8, confirming that the flat terrain produces more turbulence resulting in more aerodynamic resistance. This supports the argument in Section 4.2.1 that the flat terrain case SF8 is rougher than the real terrain case ST8.

The turbulent boundary layer over the west-east down-slope (Fig. 2.18) is similar to the boundary layer on a diffuser wall, where the local boundary layer thickness grows faster than over a flat surface while it progresses downstream. Subsequently, the mean streamwise velocity slows down on the same elevation within the boundary layer. These are evidently shown in Fig. 4.30a. It is well known that a diffuser is designed to reduce the flow resistance within the diffuser. Again, Fig. 4.30d shows the peak Reynolds shear stress over the real terrain is evidently reduced compared to the flat terrain, resulting in reduced TKE (Fig. 4.30c). On the other hand, approaching the top of the hill, there is a speed up within the boundary layer close to the surface (Taylor, 1998; Safaei Pirooz and Flay, 2018; Cindori et al., 2020). This is because the up-slope suppresses the boundary layer and reduces its thickness while it progresses downstream. One can deduce that an east-west wind over the up-slope campus reduces the local boundary layer thickness and increases the local wind speed immediately above the canopy.

The following data shows the averaged flow quantities for the northern and southern halves, respectively. As apposed to the large differences in peak heights for the various normal and Reynolds stress profiles due to local terrain and building height effects, when averaged across this streamwise extent seems to collapse the terrain height effects to create similar vertical profiles. Especially the Reynolds stress, which now has a similar distribution and peak vertical location. The spanwise change in terrain is not as great as the streamwise terrain roll-off. As expected in the southern average, Fig. 4.32, there are larger differences than the northern region between SF8 and ST8, due to the greater terrain height changes, especially in the spanwise direction. Spanwise averaging of the flow quantities has the effect of smoothing the terrain effects as long as the terrain height change is minimal.

The average is done across the same level in the domain regardless of actual height from the local ground level. This maintains the height of, for example, the free shear layer downstream of a building so that the average is more representative of the flow features. The ground zero for the spatially averaged profiles is placed at the average ground location across the region to reduce any error from the averaging process.

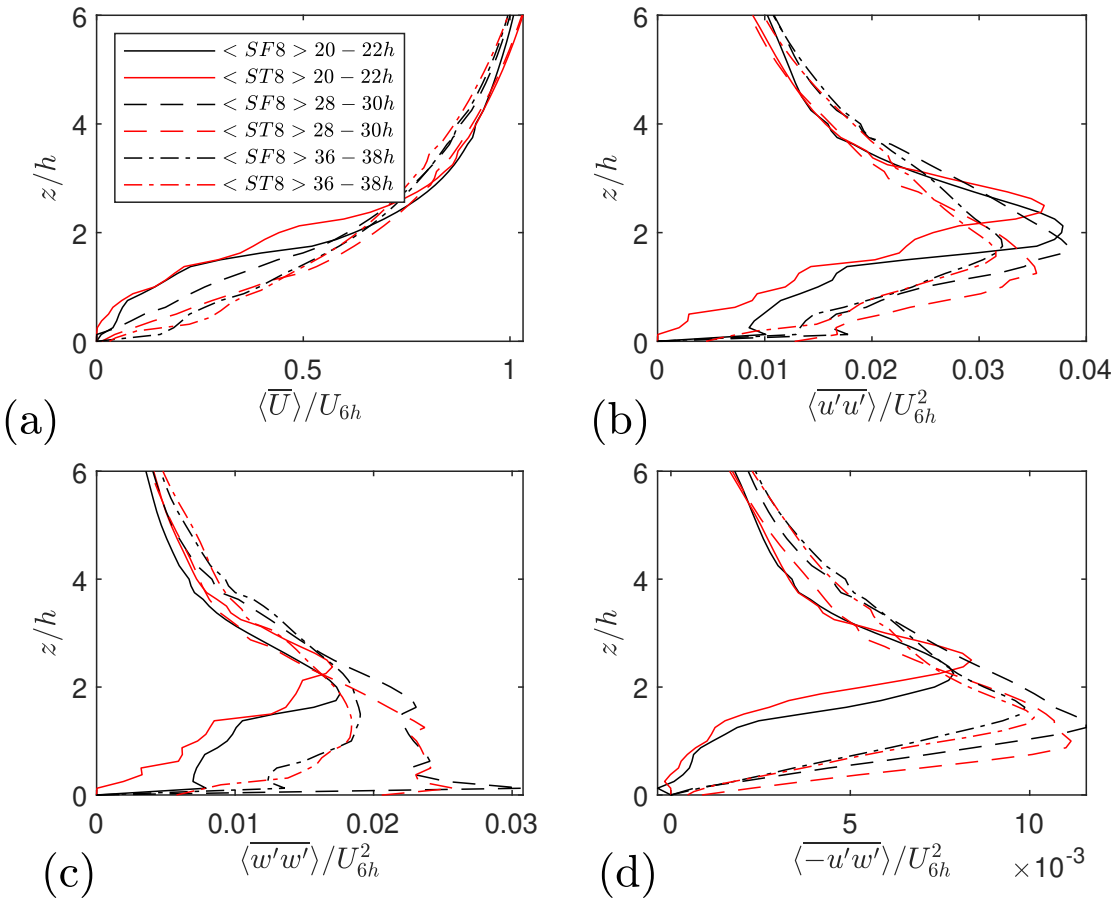

FIGURE 4.31: Spanwise averaged flow quantities, averaged across a streamwise regions of $x/h = 2$, for the northern region. Showing normalised a) mean streamwise velocity, b) streamwise stress, c) spanwise stress and d) Reynolds stress

Taking the terrain into account, there is a clear decrease in the Reynolds shear stress across all locations in the southern region in Fig. 4.32d the opposite is true in the northern region in Fig. 4.31d. It purely depends on whether the surrounding terrain shelters the building or effectively makes the building taller. Effectively reducing the frontal area of the canopy.

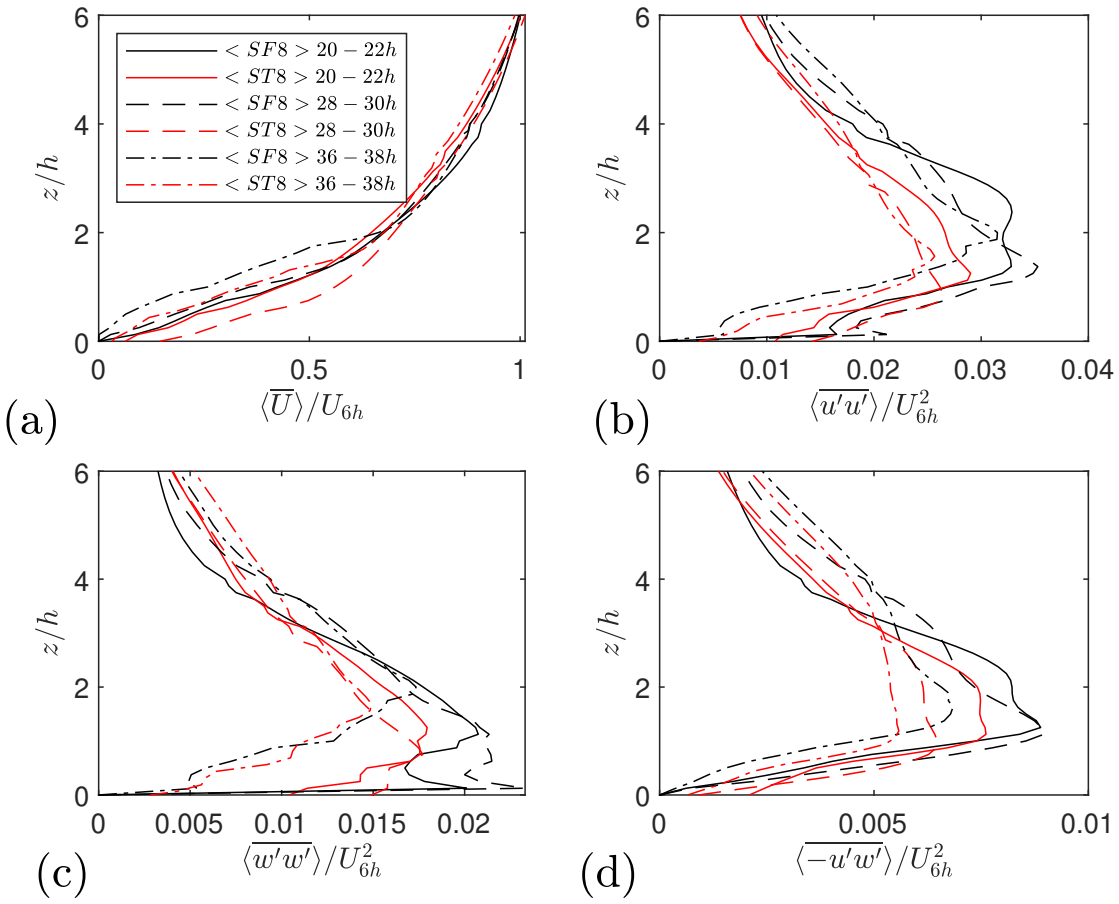

FIGURE 4.32: Spanwise averaged flow quantities, averaged across a streamwise regions of $x/h = 2$, for the southern region. Showing normalised a) mean streamwise velocity, b) streamwise stress, c) spanwise stress and d) Reynolds stress change normalisation label

Half	**Minimum elevation** z/h	**Mean Slope** %	**Terrain change** z/h	**Terrain change** x/h
North	1.56	-2.6	0.38	12.5
South	2.44	-3.55	1	7

TABLE 4.3: Terrain data for both the northern and southern half's of the domain. Minimum elevation within the array and slope is the average slope across the streamwise direction of the half. Terrain change slope is spanwise average of the up and down changes split into the magnitude of the elevation change and the downstream distance it occurs over

Both averaging methods agree for the southern region spatial average. Confirming both approaches are appropriate, showing the decrease in turbulence generated due to the terrain. The terrain change in this region averages to around $1h$, increasing towards the south ($-Y$, Fig. 2.18). The terrain change in the north region ($+Y$, Fig. 2.18) is much more gentle, and the average slope across its span is $1h$ less than that of

the Southern half. The terrain change in the streamwise direction has a sinusoidal shape with a decreasing mean, the amplitude of which is more than double in the southern region and occurs over a shorter distance. It can be suggested that using a metric such as the terrain change over x and the amplitude of this change could be used as a guideline for when to include the terrain in simulations.

Spanwise averaging the turbulent normal stress components is shown in Figs. 4.33, 4.34, 4.35 for the streamwise, spanwise and vertical normal components. Fig. 4.36 shows the spanwise averaged Reynolds stress. The peak values seen in the contours are slightly less for ST8. It is the vertical location of the peak that changes. The vertical normal stress is of particular importance. It can be used to approximate the edge of the IBL (Internal Boundary layer) and, therefore, the growth downstream. This will be discussed in more depth in section 4.4.

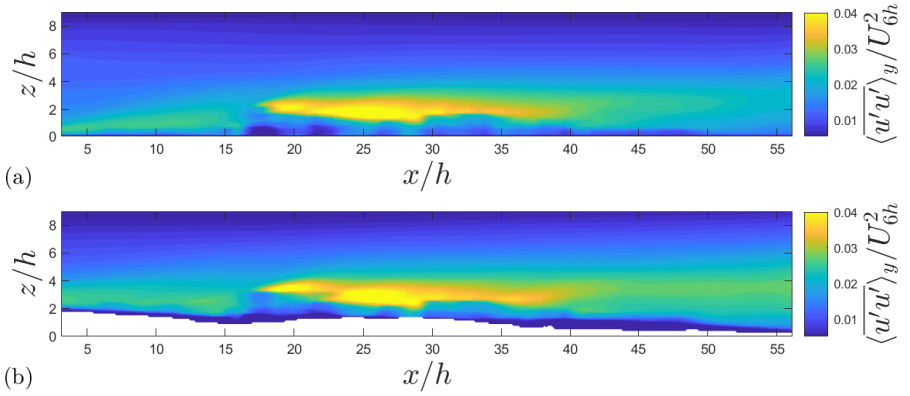

FIGURE 4.33: Spanwise averaged contours of normalised streamwise stress for a) SF8 and b) ST8

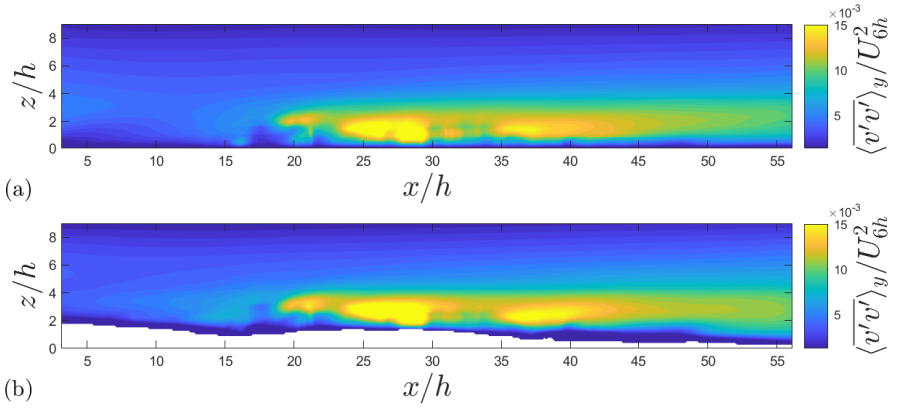

FIGURE 4.34: Spanwise averaged contours of normalised spanwise stress for a) SF8 and b) ST8

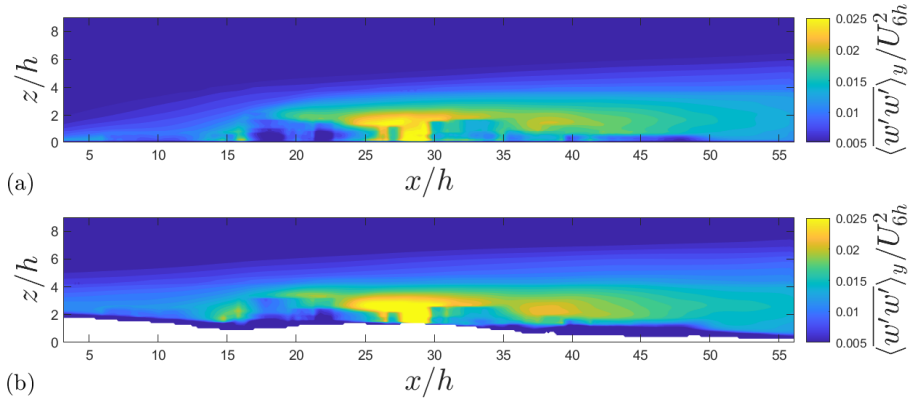

FIGURE 4.35: Spanwise averaged contours of normalised vertical stress for a) SF8 and b) ST8

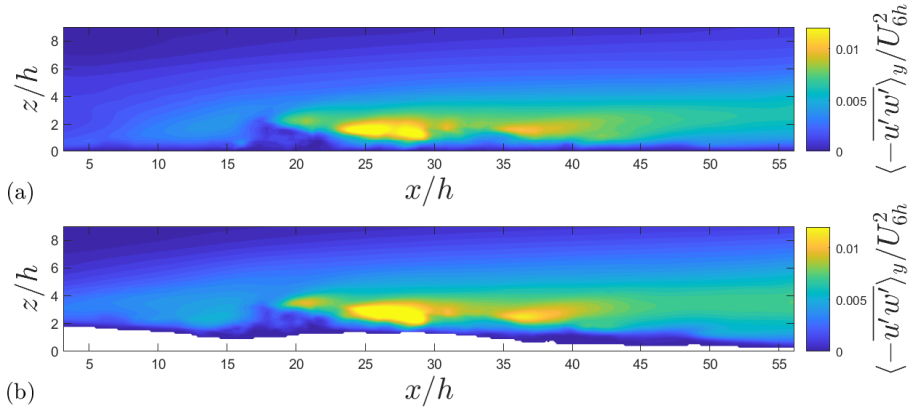

FIGURE 4.36: Spanwise averaged contours of normalised Reynolds shear stress for a) SF8 and b) ST8

4.3 Effects of incoming stratified flow on semi-realistic and complex geometry

4.3.1 Effects of stratification on flow quantities

The mean flow in and above the canopy is slightly affected by the strength of the stratification. Fig. 4.37a shows the vectors across the plane used for the PIV. There are little differences between the neutral and $Ri_b = 1$. The inflow turbulent quantities at various Ri_b numbers are the same as those in Sessa et al. (2020). Location 3 in Fig. 4.37b shows a slightly retarded streamwise velocity curve near the wall. The smaller velocity gradient near the building top is indicative of less turbulent mixing. This suggestion is supported by the decrease in the r.m.s. of both the streamwise and vertical velocity components and the Reynolds shear stress (Fig. 4.38) for the stratified cases and is largest for the highest stratification.

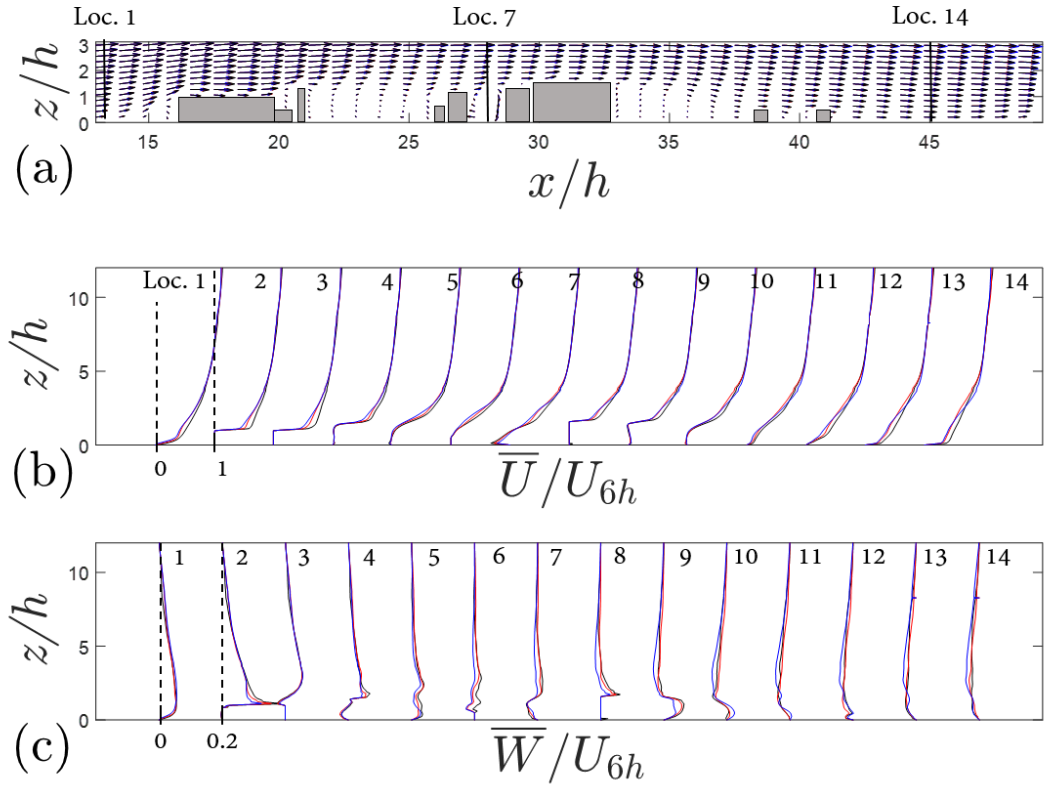

FIGURE 4.37: Comparison between different strengths of stable stratification for SF8. Neutral(Black), Richardson number $Ri_b = 0.2$(Red) and $Ri_b = 1$(Blue) cases for a) vector plots for each of the three cases and vertical profiles of b) mean streamwise velocity and c) mean vertical velocity. Across the Y = -104m plane (fig. 2.18).

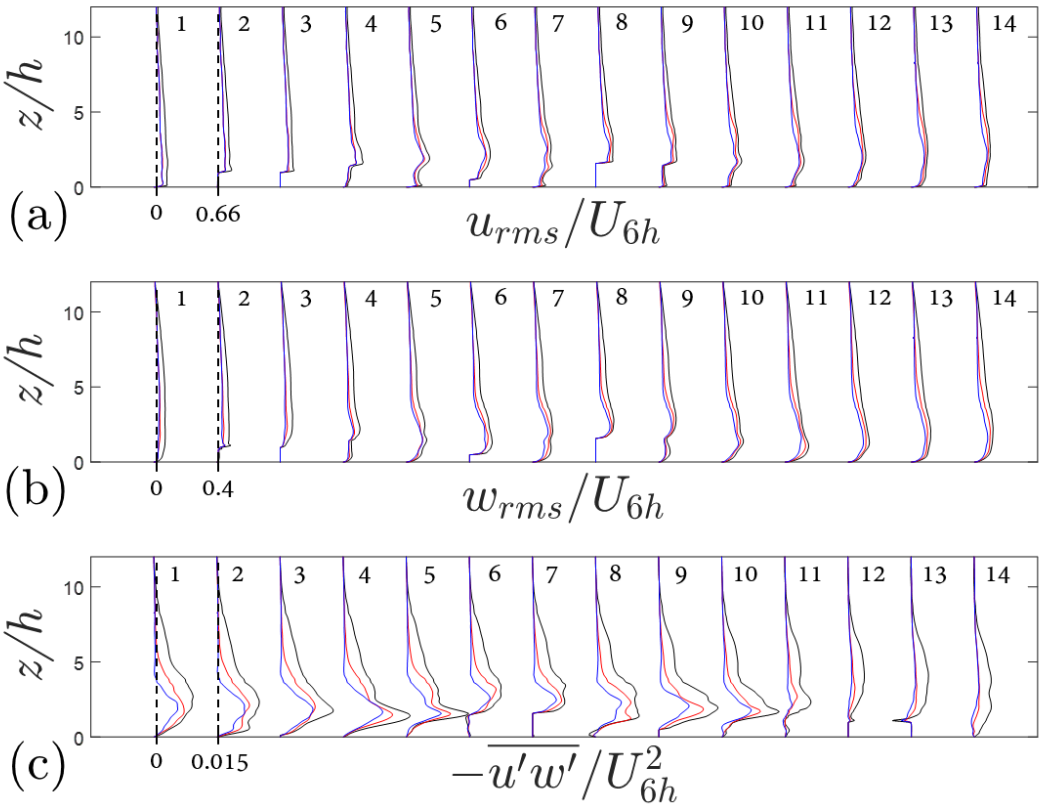

FIGURE 4.38: Comparison between different strengths of stable stratification for SF8. Neutral(Black), Richardson number $Ri_b = 0.2$(Red) and $Ri_b = 1$(Blue) cases for the vertical profiles of a) streamwise velocity r.m.s., b) vertical velocity r.m.s. and c) Reynolds shear stress. Across the Y = -104m plane (fig. 2.18).

It is useful to analyse a specific location to gain further insight into the effects of stratification. Location 7 (fig. 4.37) is more representative of a street canyon. The mean flow shown in Fig. 4.39a shows the typical street canyon-type flow, which is a smaller velocity above the canopy and weaker recirculation within the canyon. The strength of stratification seems to have the greatest effect on the Reynolds shear stress. The relative decrease between $Ri_b = 0.2$ and $Ri_b = 1$ for the r.m.s. of both in-plane velocity components is around 15%, depending on the height at which the decrease is measured. The Reynolds shear stress shows the greatest percentage decrease from $Ri_b = 0.2$ to $Ri_b = 1$ at approximately 30% decrease in the peak value. The lower peak, located at $z/h = 1$, seems to be largely dissipated in the two velocity component r.m.s. values and not visible in the Reynolds shear stress at this location. The lower peak for the neutral case is the stronger of the peaks in contradiction to $Ri_b = 1$.

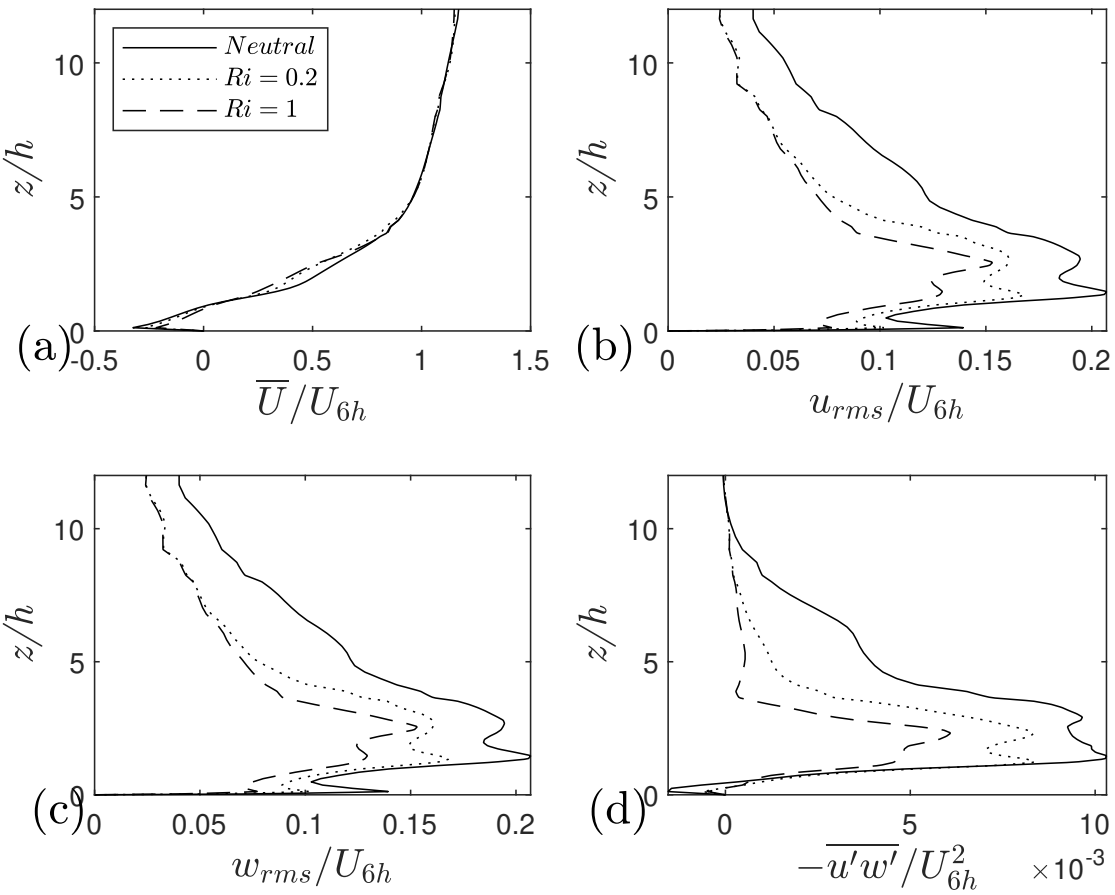

FIGURE 4.39: Effect of stratification on the flow quantities at the location 7 (fig. 4.37) for a) mean streamwise velocity, b) r.m.s. of streamwise velocity, c) r.m.s. of vertical velocity and d) Reynolds shear stress.

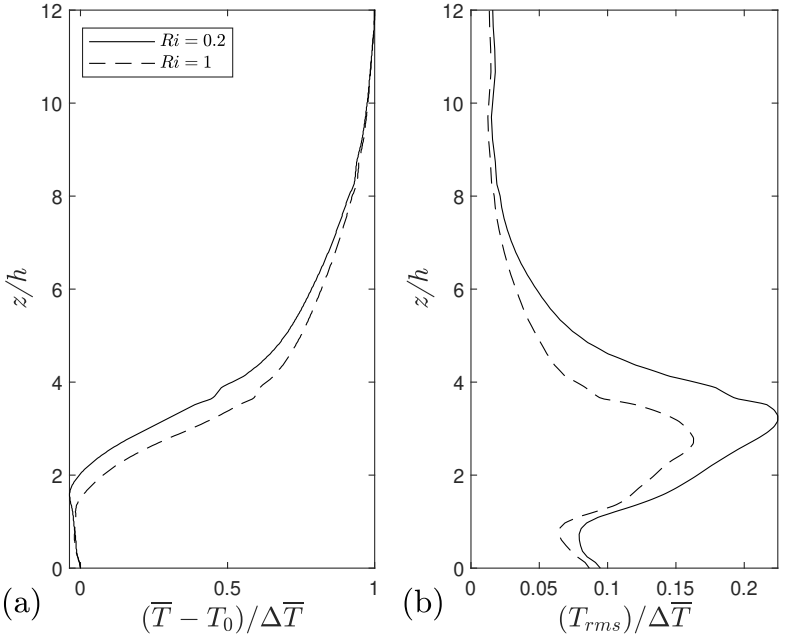

FIGURE 4.40: Effect of stratification on the vertical temperature profiles at the location 7 (fig. 4.37) for a) vertical profile of time mean temperature difference and b) r.m.s. of temperature.

The normalised vertical profiles of temperature at location 7 (fig. 4.37) do not quite collapse between $Ri = 0.2$ and $Ri = 1$ for the same inflow conditions. The temperature fluctuation is decayed for the stronger stable stratification condition.

Comparing the effects of stratification over SF8 is shown in Fig. 4.41. As was done for Fig. 4.30, the data here is averaged across the same local ground-level height. The mean flow and magnitude show similar behaviour between all cases. Fig. 4.41d shows the Reynolds shear stress is significantly decreased (-50%) between the neutral and $Ri = 0.2$. The decrease from $Ri_b = 0.2$ to $Ri_b = 1$ is less extreme, decreasing by around 25%. This change is reflected in the TKE (Fig. 4.41c). Above the canopy, the Reynolds shear stress for the case with $Ri_b = 1$ has significantly reduced above $4h$, compared to the case with $Ri_b = 0.2$. The stable stratification has been damped, significantly, the turbulence above the canopy (Fig. 4.41). Within and above the canopy, the damping of the stratification causes a decrease in normal and shear stresses.

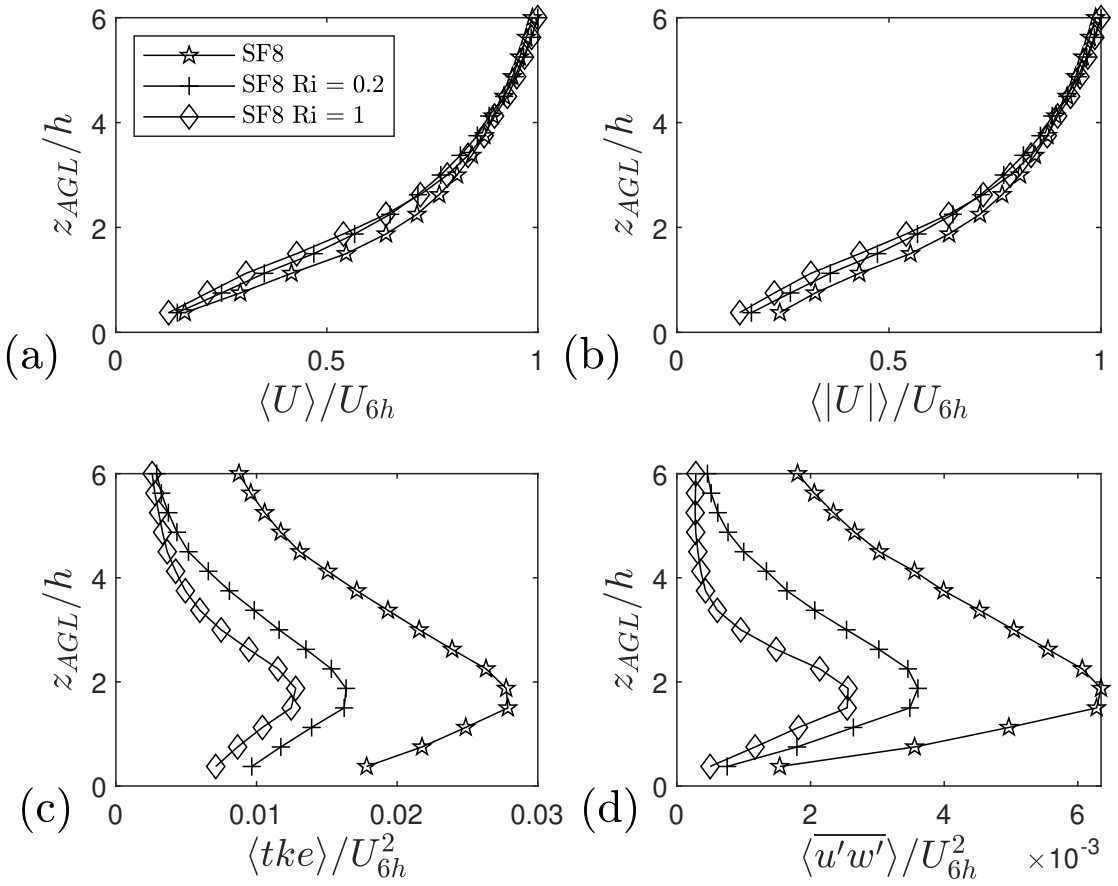

FIGURE 4.41: Spatially averaged data for SF8 comparing different Richardson numbers for the following normalised quantities: a) mean-streamwise velocity, b) mean velocity magnitude, c) turbulent kinetic energy and d) vertical turbulent momentum flux. All quantities are normalised by the spatially-averaged mean streamwise velocity U_{6h} at $6h$.

4.3.2 Effects of stratification and terrain on flow quantities

Fig. 4.42 compares the effect of terrain with the effect of stratification. The terrain and stratification combined have a significant effect on the TKE and Reynolds shear stress within and above the canopy, shown in Figs. 4.42c & 4.42d respectively. The decrease in the peak of the Reynolds shear stress between $SF8$ ($Ri_b = 1$) and $ST8$ ($Ri_b = 1$) is more than 50%. This is significant considering the decrease between the neutral conditions for SF8 and ST8 is only around 10%. The terrain drastically increases the damping produced by the stably stratified conditions. Above the canopy, the terrain also has a significant effect on the TKE and Reynolds shear stress. The shape of the profile for the TKE is much different to the other cases, being spread more vertically. This is somewhat unexpected and highlights the complexity of the urban canopy flows with real terrain.

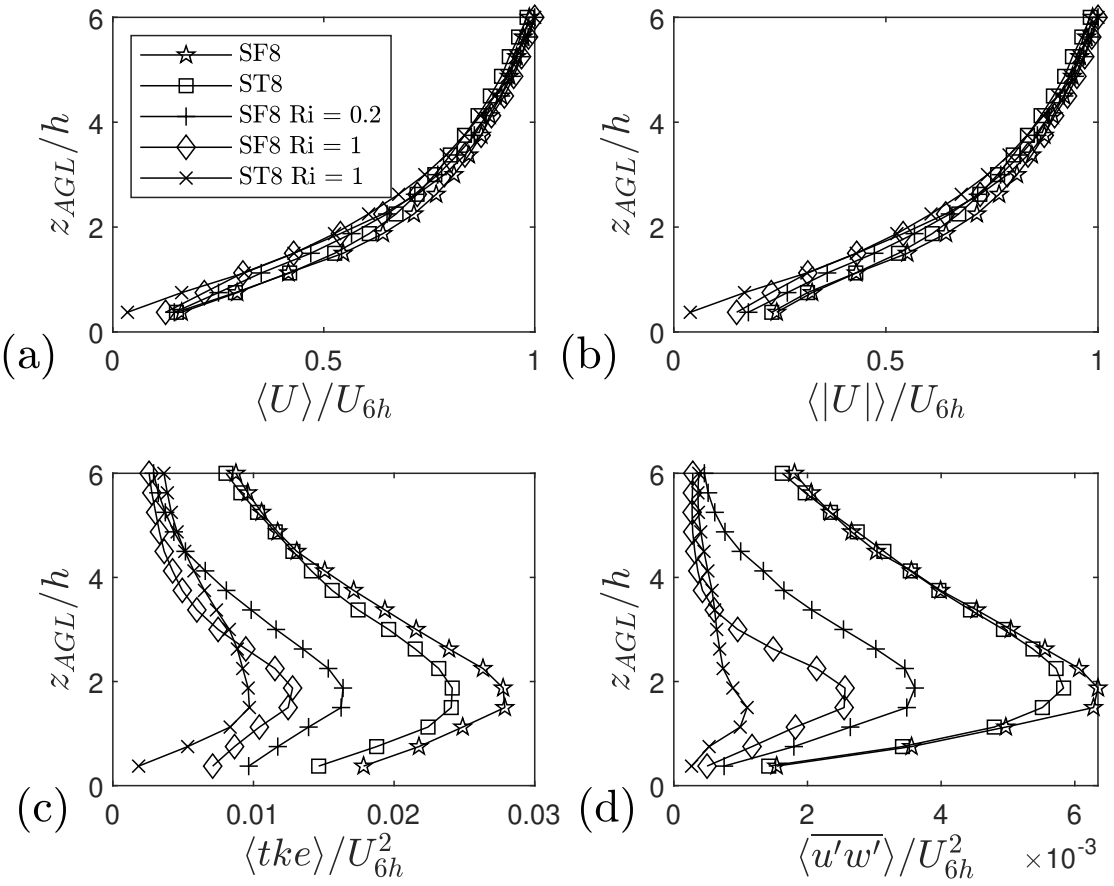

FIGURE 4.42: Spatially averaged data for SF8 and ST8 comparing different Richardson numbers for the following normalised quantities: a) mean-streamwise velocity, b) mean velocity magnitude, c) turbulent kinetic energy and d) vertical turbulent momentum flux. All quantities are normalised by the spatially-averaged mean streamwise velocity U_{6h} at $6h$.

Comparing the flow for FF8 for $Ri_b = 0.2$ and $Ri_b = 1$ is shown in Fig. 4.43 for the PIV sampling plane, $y = -104m$. As expected, the stronger stratification dampens the

fluctuations. Unexpectedly, in Fig. 4.43c, the second peak located between $x/h = 35 - 40$ is larger than that upstream, nearer the leading edge of the array. This is due to the large buildings located at $x/h = 26, 29, 30 - 32$, causing a large shear layer downstream of these buildings centred around $z/h = 2$. This stronger downstream peak is not seen in the $Ri_b = 1$ case; there is still a peak here, but weaker than the upstream one. The free shear layer between $x/h = 35 - 40$ is still visible and extends around $5h$ downstream.

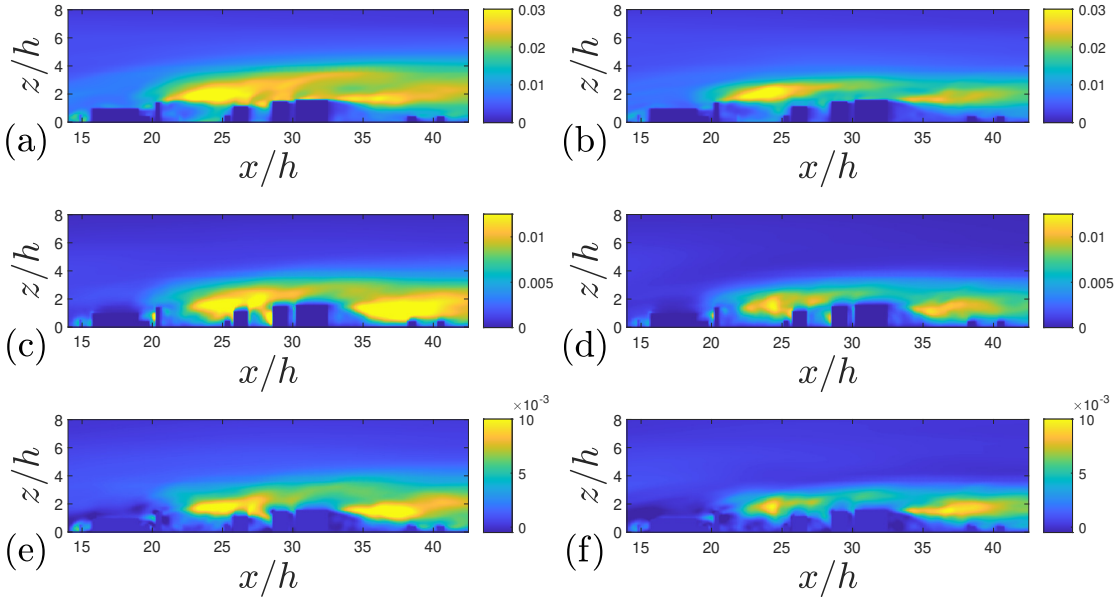

FIGURE 4.43: SF8 and ST8 comparing different Richardson numbers (0.2 and 1) for the following normalised quantities: a) streamwise normal stress ($Ri_b = 0.2$), b) Vertical normal stress ($Ri_b = 0.2$), c) vertical turbulent momentum flux ($Ri_b = 0.2$), d) streamwise normal stress ($Ri_b = 1$), e Vertical normal stress ($Ri_b = 1$) and f) vertical turbulent momentum flux ($Ri_b = 1$). All quantities are normalised by the spatially-averaged mean streamwise velocity U_{6h} at $6h$.

4.4 Internal Boundary Layers over Complex topography

Using the methodology proposed in Sessa et al. (2018) (3.5.1), the internal boundary layer (IBL) depth for both flat (SF8) and real terrain (ST8) cases was the estimated height of the critical slope-change point of spatially averaged vertical normal stress profiles $\overline{w'w'}$. The spatial average was defined below,

$$\langle \phi \rangle_s(x_m, z_{AGL}) = \frac{1}{2h \times Span} \int_{(x_m-h)}^{(x_m+h)} \left(\int_{(Span)} \phi(x, y, z_{AGL}) dy \right) dx, \tag{4.3}$$

where $\langle \rangle_s$ denotes the spatial average over a slice ($(x_m - h) \leq x \leq (x_m + h)$, -300 m $\leq y \leq 300$ m), which accounts for the span of the campus ($span$. ϕ denotes the quantity (i.e. $\overline{w'w'}$ to be spatially-averaged. Comprehensive spatial average method (Xie and Fuka, 2018) was used when the average slice crosses a building, in which all the solid regions within the average region at height z_{AGL} were included, but the value of the quantity within them was set to be zero.

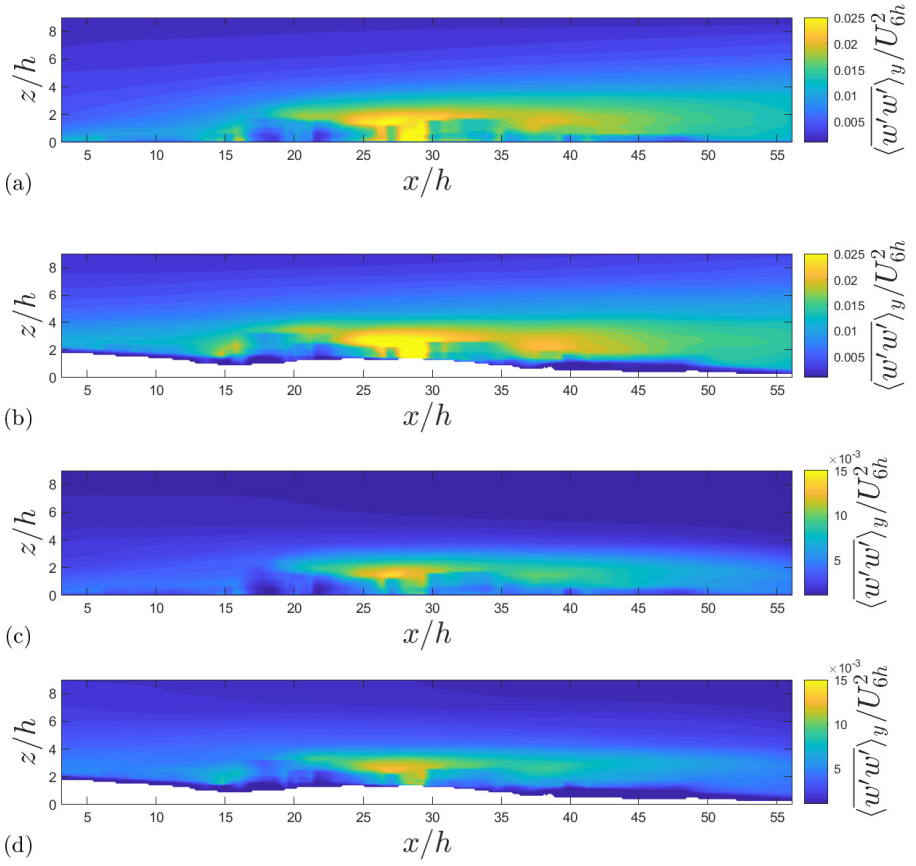

FIGURE 4.44: Spanwise averaged data for SF8 and ST8 comparing different Richardson numbers for the normalised vertical normal stress: a) SF8 ($Ri = 0$), b) ST8 ($Ri = 0$), c) SF8 ($Ri = 1$) and d) ST8 ($Ri = 1$). All quantities are normalised by the spatially-averaged mean streamwise velocity U_{6h} at $6h$.

Fig. 4.44 shows the normalised spanwise averaged vertical normal stress for cases SF8 and ST8. The overall contours look similar. Nevertheless, the distribution of the vertical normal stress $\overline{w'w'}$ from the real terrain case ST8 shows less spreading in the vertical direction while the IBL progresses downstream. Clearly, there is a drastic decrease in the vertical normal stress between neutral and stratified conditions for $Ri = 1$.

Fig. 4.45a and b respectively show the IBL depth (AGL) along the real urban canopy and the spanwise-averaged vertical normal stress $\overline{w'w'}$ over the real terrain, marked with the critical slope-change point (i.e. the intersection of the two straight lines). Overall, the IBL over the real terrain is evidently more shallow than that over the flat terrain. This is consistent with the early observation (e.g. Fig. 4.30) that the down-slope real terrain has less aerodynamic resistance and generates less TKE compared to the flat terrain, which is due to the so-called "diffuser" effect. It is to be noted that this does not conflict with another early observation (Sect. 4.2.2) that the external boundary layer (EBL), which is on the top of the IBL, is thicker over the down-slope real terrain compared to that over the flat terrain. Again, for an east-west wind passing over the up-slope of the campus, a thicker IBL (compared to a flat terrain) is expected given a greater aerodynamic resistance as discussed in (Sect. 4.2.2).

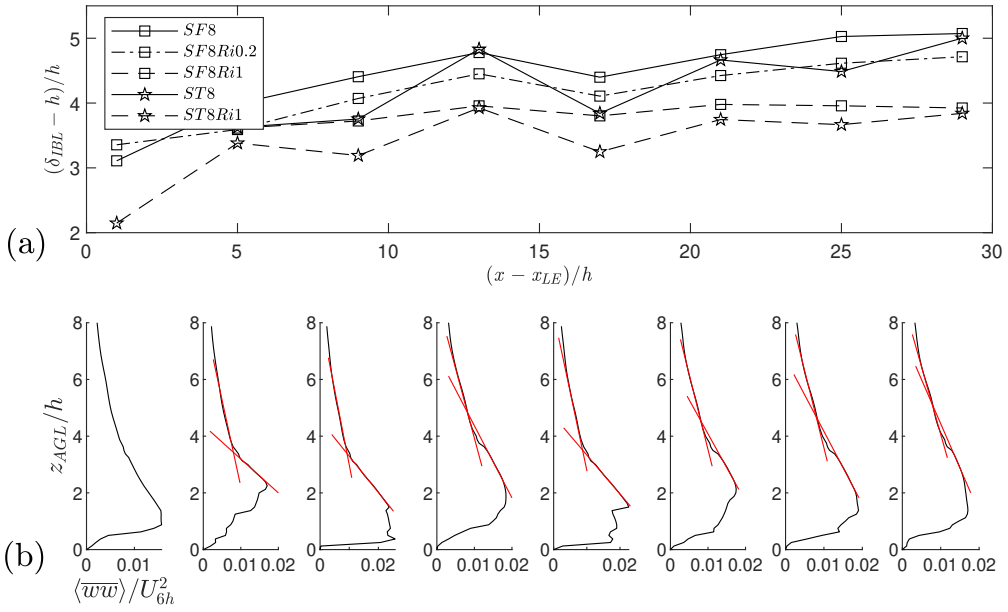

FIGURE 4.45: Internal boundary layer depths, using the method of Sessa et al. (2018, 2020), from the leading edge of the canopy for neutral and Stratified inflow conditions for flat and real terrain cases, normalised by the local building canopy height. Data is spatially averaged $2h$ in the streamwise direction, maintaining the method used in chapter 3. The leading edge of the canopy occurs at $14h$ in Fig. 4.44. Each location has it's zero set to the local average ground level

The IBL thickness, it seems, is a function of building height, terrain, and stratification strength. Obviously, a different wind direction over the building layout would have a

large impact and could completely change the IBL thickness over the same point for a different wind angle.

In this case, however the stratification has the largest impact on the IBL thickness. A decrease of approximately $1h$ in thickness is seen for ST8, reaching as much as $1.25h$, and around $0.75h$ for SF8, reaching as much as $1h$. The terrain has varying effects on the IBL thickness. At times producing an IBL to be similar height, averaged across the span, reaching a maximum difference of around $0.6h$. The terrain treatment affects the building height locally; however, as this data is spatially averaged, this is harder to ascertain for this, and the difference is most likely averaged out due to buildings being both smaller and taller than their flat case counterparts.

4.5 Summary

LES was used to simulate the UBL over the University of Southampton Highfield Campus using semi-realistic (flat terrain) and realistic (real terrain) urban geometries.

The semi-realistic geometry was validated using a water tunnel experiment with PIV. High-fidelity PIV data of the mean flow field and the Reynolds stresses were obtained to validate LES. The LES using water tunnel turbulent boundary layer quantities for the synthetic turbulent inflow generation showed satisfactory agreement with the experimental data.

The mean flow and turbulence quantities within the canopy were relatively insensitive to the use of different turbulence intensities prescribed at the inlet, given the same inflow integral length scale and almost the same mean streamwise velocity profile.

The comparison between flat and realistic terrain showed that the terrain effects produce significant differences, where the height change of a street-scale (O(0.1k m) topographic feature is of the same order of magnitude as the neighbourhood buildings. The ratio of the flow velocity of the real terrain to flat terrain case within and above the canopy was found to correlate well with the changes in ground-level elevation.

A global (average) gradient of the terrain is present throughout the real terrain case domain. The global downslope is significantly smaller than the changes in local terrain elevation which has a far smaller effect on the flow than the changes in local terrain elevation.

Simulations showed that the real terrain enhanced the effect of stable stratification conditions. For $Ri_b = 1$, the real terrain exhibits a decrease of around 60% in the spatially averaged vertical turbulent momentum flux (compared to SF8). For neutral conditions, the decrease is approximately 10%.

Chapter 5

Conclusions

This PhD study aimed to fill gaps in knowledge in two key areas of urban boundary layer research. The first was the effect of the suburban pitched roof on the flow and turbulence statistics for arrays of buildings. The second was to compare the effects of inflow conditions, small terrain features taking account of inflow turbulence level and thermal stratification. The conclusions drawn throughout this research are presented below.

5.1 Effect of pitched roofs

Large eddy simulations (LES) have been carried out to simulate the flow of urban boundary layers over idealized arrays of cuboids with and without pitched roofs under neutral and stable stratification conditions. The reliability and accuracy of the results have been ensured by conducting rigorous evaluation tests, including examining mesh sensitivity and body conformity.

The results for a baseline flat roof cuboid array were first validated against previous data. The same mesh and numerical settings were then preserved as far as possible to ensure the reliability of flow simulations made for the 45° pitched roof cases.

The non-conformal Cartesian meshes used in some CFD codes, such as PALM4U and uDALES, provide high computational efficiency, but their users might have doubts with regard to the accuracy, such as in the near wall regions. This study has examined their accuracy of the global quantities, such as the spatially averaged mean velocities, second-order turbulent statistics and dispersive stresses. It is concluded that these meshes produce accurate spatially-averaged quantities compared to those from conformal (body-fitted) meshes.

Compared to that produced by an array of flat roof cuboids, introducing an array with 45° pitched roofs leads to significant changes in the mean flow field, the Reynolds stresses, and drag and increases the turbulent momentum flux at the canopy height by approximately 50%. The magnitude of these changes strongly suggests that it is important to account for the effect of roof shape in urban arrays. In other words, the pitched roof array enhances the turbulent mixing and aerodynamic drag in a manner similar to having a random height array of flat-roofed cuboids (Xie et al., 2008). It has also been shown that the pitched roof reduces the Reynolds shear stress in most of the regions within the canopy for both packing densities, even though it substantially enhances the Reynolds shear stress at the canopy height when $\lambda_p = 33.3\%$.

The results have shown that the pitched roof case exhibits a different flow regime to that of the flat roof cases at packing density $\lambda_p = 33.3\%$. The pitched roof, due to decreased packing density in the top third of the canopy, is in the wake-interference regime, as opposed to the skimming flow regime experienced by the flat roof cuboids. At $\lambda_p = 16.7\%$ both the flat-roof and pitched roof cases are in the wake-interference regime. The normalised spatially averaged profiles of Reynolds stress over the flat- and pitched-roof buildings show a significantly smaller difference compared to $\lambda_p = 33.3\%$. This suggests that the pitched roof only plays a crucial role within a certain range of packing densities.

Although the pitched roof and random height arrays are more common than flat-roofed buildings of uniform height in urban areas, current parametrizations are typically based on arrays of uniform-height cuboids with flat roofs. The need for taking the effect of pitched roofs into account is given more importance by the fact that the results showed a much stronger effect for a packing density of around $\lambda_p = 33.3\%$, which is more common in suburban regions than $\lambda_p = 16.7\%$. The results suggest that omitting these effects in high-resolution mesoscale models may introduce non-negligible errors into boundary-layer predictions over typical suburban and urban regions where there are a high proportion of pitched roof or non-uniform height buildings. Frontal solidity and packing density provide adequate descriptions of arrays for developing parametrizations for the effects of flat-roofed buildings in mesoscale models, adding a further parameter to differentiate between arrays with different roof geometries would improve the performance of these models.

It is also to be noted that the LES predictions showed considerable differences in mean surface pressure coefficient compared to values derived from using the Eurocode standard/method. While some of that was due to the Eurocode considering peak values, a substantial fraction is also attributable to the Eurocode not considering the shielding effect of surrounding buildings which suggests that there is a need to consider for a more refined Eurocode to address this aspect.

Simulations showed that having pitched roofs meant that the effect of increasing stable stratification conditions ($0 \leq Ri_b \leq 1$) was very much reduced in comparison to the same incoming flow for flat roof cuboids. The relative difference in the vertical fluctuations between two weak stratification conditions $Ri_b = 0.2$ and $Ri_b = 1$ was around 16% less for the pitched roof cases, while a reduction of 50% was found for flat roof ones (Sessa et al., 2020). It is concluded that pitched roofs may greatly enhance the turbulent mixing in stable stratification conditions and so improve the urban ventilation in the local environment. Consequently, pollution models which ignore the effects of pitched roofs may be overly pessimistic.

5.2 Complex geometry and terrain

Large eddy simulations (LES) were carried out to simulate atmospheric airflows over the Highfield Campus of the University of Southampton using semi-realistic (flat terrain) and realistic (real terrain) urban geometries, aiming to quantify and understand the impact of the urban terrain variation at street scale (O(0.1 km)) on the aerodynamics and turbulent boundary layer.

Water tunnel experiments were carried out using a 1:1000 scale 3D-printed model of the university buildings placed on a flat (semi-realistic) terrain in a naturally developed turbulent boundary layer. The Reynolds number was $Re_h = 12,000$ based on the average building height h and freestream velocity. High-fidelity PIV data of the mean flow field and the Reynolds stresses were obtained for the validation of LES. Allowing for the uncertainties introduced by the small scale of the model and the limitations of PIV measurement close to its surface, data from an LES simulation with STI showed good agreement with the PIV data.

To assess the sensitivity of the results to uncertainties in defining the appropriate turbulence quantities to apply to the inflow, one set of "simulated atmospheric boundary layer" data generated from the University of Surrey EnFlo wind tunnel (e.g. Xie and Castro (2009)) were used for synthetic turbulence inflow (STI) boundary conditions, against the other set of naturally generated boundary layer data from the water tunnel at the University of Southampton. The turbulence statistics sampled at sufficient distance (e.g. more than 10 average building heights) from the inlet and within and immediately above the urban canopy predicted by the large-eddy simulations were relatively insensitive to the precise inflow Reynolds stresses, given the same inflow integral length scale and similar mean streamwise velocity profile. This does not undermine the importance that street and city scales of airflow are coupled.

A systematic comparison of large-eddy simulations of atmospheric airflows over the flat and real terrains showed that the terrain effects are crucial, where the elevation

change of street-scale (O(0.1k m)) topographic features is of the same order of magnitude of the neighbourhood buildings. While the atmospheric boundary layer (ABL) progresses over a downslope terrain, it experiences less aerodynamic resistance compared to flat terrain, and produces less turbulent kinetic energy, resulting in a faster-growing total boundary layer thickness (AGL) and a slow-growing internal boundary layer thickness (AGL). This is due to the so-called "diffuser" effect. On the other hand, while the ABL progresses over an upslope terrain, it is expected to experience greater aerodynamic resistance compared to flat terrain, resulting in a reduced total boundary layer thickness.

It is even more crucial to quantify and understand how street-scale terrain variations modulate the local mean velocity and turbulent statistics field at an above-ground-level height. This can help to correct the experimental and numerical data from the widely used flat terrain models. The study has shown the ratio of the real-terrain streamwise velocity to the flat-terrain data on the same horizontal coordinates and at the same AGL height correlates positively very well with the real terrain elevation, with a maximum ratio greater than 2 and a minimum less than 0.5. This is because the local boundary layer cannot adjust itself immediately in response to street-scale terrain variations. Subsequently, a high streamwise mean velocity is expected on the same AGL height over a region with high terrain elevation, vise versa.

Given the global (average) gradient of the west-east downslope is much smaller than the local terrain gradients, the former should have little contribution on this strong modulation on the local mean velocity field. In other words, this real terrain's modulation on the mean streamwise velocity field is in a similar manner and strength in an east-west wind passing the upslope. At a height immediately above the urban canopy (e.g. $z_{AGL} = 2.3h$), a similar modulation on the local mean velocity is weaker but still evident.

Simulations showed that the real terrain enhanced the effect of stable stratification conditions. For $Ri_b = 1$, the real terrain exhibits a decrease of around 60% in the spatially averaged vertical turbulent momentum flux (compared to SF8). For neutral conditions, the decrease is approximately 10%. This study showed that a thinner IBL was generated in the real terrain case, but also that the thickness of the IBL was affected by the stratification in a similar manner for both terrain and flat cases.

5.3 Final comments and future work

This PhD study aimed to improve the understanding of the effects of pitched roofs in an urban canopy, the inflow turbulence intensity, terrain and thermal stratification effects on the flow and turbulence statistics over a real urban area.

To achieve a more accurate CFD predictions for real urban scenarios, future works should consider the outcomes of this work in order to closely represent the urban surface. This includes variations in roof shape, small topographic features and thermal stratification.

For three-dimensional arrays, the pitched roof (compared to a flat roof of the same overall height) was shown to generate 30% greater drag for tighter packing densities (33%) with a flow direction perpendicular to the axis of the roof apex line. For looser packing densities (16%) the total drag was similar for flat and pitched roofs. However, the wind direction within the urban boundary layer is rarely constant. Wind directions change with various time scales. Therefore, analysis of different wind directions (from perpendicular to parallel to the roof line) should be undertaken in order to map out the overall effect of pitched roofs.

The effect of weakly stable thermal stratification was shown to be significant; the pitched roof was able to reduce the damping effect on the turbulence generated by the array of buildings compared to the flat roof array. Weakly stable stratified boundary layers are only the start of the story. The effect of stronger stable stratification and unstable thermal stratification has yet to be examined for an array of pitched roof buildings. This is of great importance to improve predictions from mesoscale models for urban areas.

The inclusion of real terrain combined with the building layout of a real urban area showed non-negligible effects on the flow field compared to the same building layout with a simplified flat ground. Local changes in terrain elevation $(O(0.1km))$ correlated well with the changes in the mean velocity. The global terrain change or mean downward slope present throughout the domain had a somewhat smaller effect on the flow, given its magnitude $(O(h/1km))$, compared to the local terrain variation. It is far more important to include smaller topographic features than larger domain-scale features, albeit it is missing in the mesoscale models and is very challenging to CFD codes and experiments. It is to be noted that local results may be heavily dependent on the wind direction. A wind angle opposite and perpendicular to that shown would be the first step in quantifying the local effects of the terrain for a real urban area.

5.4 Appendix A

Boundary-Layer Meteorology (2022) 185:415–442
https://doi.org/10.1007/s10546-022-00738-1

RESEARCH ARTICLE

Numerical Simulations of Boundary-Layer Airflow Over Pitched-Roof Buildings

Matthew Coburn[1] · Zheng-Tong Xie[1] · Steven J. Herring[1]

Received: 15 November 2021 / Accepted: 26 July 2022 / Published online: 23 August 2022

Abstract
Arrays of buildings with pitched roofs are common in urban and suburban areas of European cities. Large-eddy simulations are performed to predict the boundary-layer flows over flat and pitched-roof cuboids to gain a greater understanding of the impact of pitched roofs on urban boundary layers. The simulation methodology is validated for an array of flat roof cuboids. Further simulations show that changes in the type of grid conformity have a negligible effect on the mean flow field and turbulent stresses, while having a visible, but small, effect on the dispersive stresses for a given packing density. Comparisons are made for flat and 45° pitched roof cuboid arrays at packing densities of 16.7% and 33.3%. The interactions between pitched-roof buildings and their effect on the urban boundary layer are considerably different to those of flat-roof buildings. The pitched roofs at a packing density of 33.3% leads to significant changes in the mean flow field, the Reynolds stresses, and the aerodynamic drag. Further work investigates the effects of changes in turbulence level and atmospheric thermal stratification in the approaching flow. Importantly, in comparison to a flat-roof array, the pitched-roof one at a packing density of 33.3% evidently increase the friction velocity and greatly reduces the effects of stable stratification conditions and changes in inflow turbulence level.

Keywords Atmospheric thermal stratification · Cartesian mesh · Drag coefficient · Packing density · Pitched roof · Spatial-average

1 Introduction

Past research in urban atmospheric problems has shown that coupling may exist between atmospheric airflow at the city scale (O(10 km)), neighbourhood scale (O(1 km)), and street scale (O(0.1 km)) (Barlow et al. 2017; Fernando 2010). This spatial coupling effect is par-

Zheng-Tong Xie
z.xie@soton.ac.uk

Matthew Coburn
mc6g16@soton.ac.uk

Steven J. Herring
sjhbac@gmail.com

[1] University of Southampton, Southampton SO17 1BJ, UK

ticularly strong around urban forms such as groups of tall buildings (Han et al. 2017; Fuka et al. 2018; Hertwig et al. 2019), or around steep topographic changes. To understand the importance of coupling effects we require a mapping between urban morphology and flow-field characteristics, such as mean velocity, turbulent statistics, momentum and heat fluxes. Acquiring such data for the varied range of geometries encountered in urban areas challenges both numerical and experimental simulations in many ways.

1.1 Buildings with Pitched Roofs

Most of the published experimental and numerical studies of idealized buildings (e.g. Cheng and Castro 2002; Stoesser et al. 2003; Coceal et al. 2006; Xie and Castro 2006) have focused on arrays of cuboid blocks with flat roofs, placed in an aligned or staggered arrangement with uniform or non-uniform heights. Such studies are most relevant to urban flows over heavily populated urban areas where most of the building blocks are likely to be cuboid in shape. However, in the surrounding urban and suburban areas of cities (e.g. European cities) which experience regular heavy precipitation, whether in the form of rain or snow, most of the residential houses have pitched roofs. For example, in 2008 it was recorded that 93% of the dwellings in England had pitched roofs (Department for Communities and Local Government 2008). It is therefore of great interest to assess the effect of having pitched, rather than flat roofs, on the local flowfield and large-scale boundary-layer flow.

There are a small number of published papers (Barlow et al. 2004; Yassin 2011; Ferrari et al. 2016; Nosek et al. 2016, 2017; Llaguno-Munitxa et al. 2017; Badas et al. 2017; Woodward et al. 2021) in which different roof shapes and their effect on the flow field and dispersion has been investigated. Most of these studies (Barlow et al. 2004; Yassin 2011) have investigated two-dimensional street canyons. A few studies (Holmes 1994; Tominaga et al. 2015; Ozmen et al. 2016; Fouad et al. 2018; Woodward et al. 2021) have also examined a single isolated building with a pitched roof and these have provided an understanding of the mean surface pressure around the building (Ginger and Letchford 1995; Oliveira and Younis 2000; Tominaga et al. 2015) which has supported the development of building regulation codes.

Tominaga et al. (2015) investigated the flow field and surface pressure on an isolated building for one aspect ratio and three roof pitch angles using particle image velocimetry and computational fluid dynamics (CFD). They suggested that the flow pattern around a building with a pitched roof changes critically at a roof angle of around 20°. Holmes (1994) found that a 30° pitched roof on a single tropical house had a considerable effect on the mean roof pressures. The mean pressure coefficient on the upwind half of the roof was positive, while on the leeward side the flow did not re-attach on the roof, resulting in a near uniform surface pressure. On the other hand, Reardon and Holmes (1981) found that roof pitches up to 10° in winds normal to the ridge yielded a small separation bubble at the leading edge with high shear-layer curvatures, which were associated with high suction pressure, and rapid pressure recovery downwind to the flow reattachment position. They suggested these low pitch roofs to be called "aerodynamically flat". These papers suggest that modest changes in the angle of pitched roofs may have strong effects on the flowfield around the building and building surface pressures.

Fouad et al. (2018) investigated isolated pitched-roof buildings to explore the potential for obtaining useful design data using CFD methods by comparing their results to the Eurocode and ASCE10 standards. They concluded "the application of CFD techniques show great

potential to offer very good wind design data for structures with shapes not listed in the existing codes."

While building regulations are based on considering a single isolated building taking into account urban roughness, it is probable that the flow within the canopy of an array of pitched roof buildings will be considerably different to that around an isolated building, with some consequent effects on the surface pressure distribution. The limited studies on the effect of interference between buildings have focused on two buildings (e.g. Bailey and Vincent 1943; Holmes 2007). Bailey and Vincent (1943) suggested that having a maximum of two buildings upstream of the instrumented model was sufficient to be representative of built up areas. Holmes (2007) concluded that the building spacing was a key parameter. It is now well established that two building rows upstream of the measurement location is insufficient for a simulation of fully-developed internal boundary layer (IBL) over a very large array (e.g. Hanna et al. 2002; Xie and Castro 2008; Sessa et al. 2018). For arrays of building blocks placed in a fully developed turbulent boundary layer in the scenarios typically studied (e.g. low-rise buildings and small roughness length upstream of the array), it requires a fetch length of about ten average building heights (e.g. Hanna et al. 2002; Xie and Castro 2008). For arrays of buildings placed in a smooth laminar boundary layer, the required fetch length is much greater. It is to be noted that while generating near equilibrium and fully developed urban boundary layer flows is necessary for reducing the uncertainty of the research data, such conditions are not generally established in real urban atmospheric airflows.

Two parameters frequently used to characterise the morphology of urban areas are the frontal and plan solidities (e.g. Placidi and Ganapathisubramani (2015)). The latter is more often termed the 'packing density' λ_p. The effect of packing density in arrays of simplified buildings with flat roofs has been intensively studied (e.g. Cheng et al. 2007; Placidi and Ganapathisubramani 2015, 2018), and it has been shown that their total drag coefficient based on the freestream velocity is a function of the packing density. The drag coefficient function has minimums at $\lambda_p = 0$ or 100%, and a maximum in the lower half of the packing density range. Cheng et al. (2007) showed that the drag coefficient of a staggered array of cubes was greater than for an aligned one at both $\lambda_p = 6.25\%$ and 25%. The difference was greater at the smaller packing density. These results show that any study into the effect of pitched roofs should consider the effect of packing density.

1.2 Research Needs

The existing body of literature shows a clear need to investigate the effect of pitched roofs in building arrays at different frontal solidities, packing densities and aspect ratios with fetches sufficient to develop realistic urban boundary layers; to demonstrate improved methods for predicting the airflow and dispersion at neighbourhood scales; and to obtain spatially averaged momentum and scalar flux data which may be used to develop parametrizations for meso-scale models.

In addition to the above there is the question of thermal stratification effects in urban areas. These attracted little attention until one decade ago (Sessa et al. 2020). The studies published since then have focused on arrays of idealised cuboid-shape buildings (e.g. Boppana et al. 2014; Kanda and Yamao 2016; Tomas et al. 2016; Marucci et al. 2018; Marucci and Carpentieri 2020; Sessa et al. 2020), or real urban areas in which the building geometries have been simplified to have flat roofs (e.g. Xie et al. 2013). They have concluded that even weakly stable stratification conditions (i.e. the bulk Richardson number ≤ 1) have

a considerable impact on the urban boundary-layer turbulence and significantly impacted pollutant dispersion.

To our knowledge there has been no research into the nature of the flow over arrays of pitched-roof buildings in thermally stratified conditions. The sparse literature which exists though shows that a pitched roof generates a very different flows within and above the canopy top in neutral stratification, with more three-dimensional flow structures than flows over flat-roof buildings. The question arises as to whether the changes in thermal stratification lead to similar changes in the flow over pitched-roof buildings as those for flat roofs.

Rather than using conformal meshes to accurately capture the geometric details of buildings (such as pitched roofs), two widely used urban CFD codes PALM4U (Maronga et al. 2020; Krč et al. 2020) and uDALES (Heus et al. 2010; Grylls et al. 2020; Suter et al. 2021) use non-conformal Cartesian meshes. This simple treatment is attractive as it leads to significant improvements in computational efficiency, but raises the question of what the penalty in accuracy is compared to using conformal (body fitted) meshes? This question is also addressed by the study.

1.3 Outline of the Current Work

This study aims to address three knowledge gaps: (1) how the urban boundary layer is affected by having an array of buildings with pitched roofs, (2) how the effect of pitched roofs varies with the packing density of the array, and (3) how the effect of having pitched rather than flat roofs changes as the conditions vary from neutral to stable stratification.

Section 2 presents details of the numerical methods, Sect. 3 describes the cases and simulation settings. Section 4.1 details the verification and validation of the CFD model. Section 4.2 examines the effect of using conformal and non-conformal meshes, Sect. 5 presents a comparison between idealised block arrays with flat and pitched roofs, which includes spatially-averaged velocities, Reynolds stresses and surface pressures. Section 5.2 reports the effect of packing density in neutral stratification. Section 6 reports the atmospheric thermal stratification effects on airflow over pitched-roof buildings. Section 7 summarises the conclusions from the research undertaken.

2 Numerical Methods

2.1 Governing Equations

The flow which develops over arrays of blocks is innately unsteady and so is best resolved by adopting a large-eddy-simulation (LES) approach (e.g. Kanda et al. 2004; Xie and Castro 2006; Castro 2017). The LES models developed in this study were implemented was implemented within the open-source package OpenFOAM version 2.1.1. Eqs. 1 and 2 are respectively the filtered continuity and Navier–Stokes equations:

$$\frac{\partial u_i}{\partial x_i} = 0, \tag{1}$$

$$\frac{\partial u_i}{\partial t} + \frac{\partial u_i u_j}{\partial x_j} = -\frac{1}{\rho}\frac{\partial p}{\partial x_i} + \nu\frac{\partial^2 u_i}{\partial x_j \partial x_j} - \frac{\partial \tau_{ij}}{\rho \partial x_j} - \frac{1}{\rho}\frac{\partial P}{\partial x_i}\delta_{i1} + f\delta_{i3}, \tag{2}$$

where x_i and t are respectively spatial coordinate and time, u_i and p are respectively the resolved or filtered velocity and pressure, ρ is the density, ν is the kinematic viscosity, τ_{ij} is

the Subgrid-scale (SGS) stress. δ_{i1} is the Kronecker-delta and $\partial P/\partial x_i$ is the pressure gradient or body force term which drives the flow when periodic boundary conditions are used in LES. The term $f\delta_{i3}$ is the body force in the vertical direction due to applied thermal buoyancy and is calculated by using the Boussinesq approximation based on the estimated temperature from Eq. 3. The mixed time scale SGS model (Inagaki et al. 2005) was used to avoid using the near-wall damping functions as used in the Smagorinsky SGS model. Nevertheless, Xie and Castro (2006) suggested that the flow is very much building block-scale dependent and that the results are not sensitive to the precise nature of the SGS model, subject to a requirement that the grid sufficiently resolves the inertial range of the turbulent spectra.

The filtered transport equation of temperature is:

$$\frac{\partial T}{\partial t} + \frac{\partial u_j T}{\partial x_j} = \frac{\partial}{\partial x_j}\left[(D + D_r)\frac{\partial T}{\partial x_j}\right], \tag{3}$$

where T is the resolved-scale temperature, D is the molecular diffusivity of temperature, D_r is the SGS diffusivity given by ν_r/Pr_r, where ν_r is the SGS kinematic viscosity, Pr_r is the subgrid Prandtl number which is set to 0.9 (Xie et al. 2013).

2.2 Settings of Atmospheric Thermal Stratification

Atmospheric thermal stratification effects are set by using the bulk Richardson number. This offers a convenient approach for quantifying the strength of stratification due to the vertical temperature gradient in numerical simulations. The bulk Richardson number is defined as

$$Ri = \frac{g\delta(\overline{T}_\infty - \overline{T}_0)}{\overline{T}_0 U_\infty^2}, \tag{4}$$

where g is acceleration due to gravity, δ is the domain height, $\overline{T}_0$ is the mean ground temperature, $\overline{T}_\infty$ is the mean freestream temperature and U_∞ is the mean freestream wind speed.

2.3 Boundary Conditions

The LES model must be used with boundary conditions which are appropriate to the problem. For urban flow simulations the inflow and outflow faces typically have either periodic boundary conditions (PBCs) (e.g. Coceal et al. 2006) or synthetic turbulence inflow conditions (STI) (e.g. Xie and Castro 2008). The LES approach with PBCs is based on the assumption that the simulated domain is a repeat unit of a much greater region. This approach can substantially reduce the computational cost. However, when modelling a "real" urban geometry, the PBC approach could lead to an inaccurate representation of the flow in some scenarios, such as a change in roughness (Xie and Castro 2009; Tomas et al. 2016, 2017; Sessa et al. 2018, 2020). Using the PBC approach in non-neutral conditions requires additional precautions, such as adding additional forcing terms into the governing equations that should not influence the turbulence statistics (Boppana et al. 2014; Grylls et al. 2020).

The STI method has been well documented (Xie and Castro 2008; Sessa et al. 2018) and simulations using it have compared well to data from experiments (Marucci et al. 2018; Marucci and Carpentieri 2020). The STI approach requires vertical profiles of mean velocity, Reynolds stresses, and integral length scales as inputs. To apply thermal stratification at the inlet STI requires vertical profiles of mean temperature, and the variance and integral length of temperature fluctuations as additional inputs.

We use the PBC and STI approaches for two different sets of simulation cases. The choice of boundary conditions was driven by the physics to be simulated, and so STI boundary conditions were used for examining the effect of thermal stratification. To enable the results to be compared with past work on block arrays with flat roofs, the same STI inputs were used for the neutral and stable stratification as in Sessa et al. (2018, 2020) (specifically Fig. 4 in Sessa et al. 2020). This meant that the prescribed vertical profiles of mean velocity, Reynolds stresses, mean temperature and temperature fluctuations for simulating $Ri = 0,\ 0.2,\ 0.5$and1 were identical to those used in Sessa et al. (2018, 2020), which matched the experimental data in Marucci et al. (2018). Moreover, the same prescribed inflow data were used for $Ri = 0.2,\ 0.5$ and 1, because as stated in Sessa et al. (2020), using the same settings allows the effect of thermal stratification to be isolated.

2.4 Spatial Averaging

The spatial averaging method was adopted for processing the outputs from all simulations. Using spatially averaging over a whole $(x - y)$ plane (e.g. Fig. 3), a resolved instantaneous flow quantity ϕ in LES can be further decomposed into space-time average $\langle\overline{\phi}\rangle$ (Eq. 6), spatial variation of the time average Φ'', and resolved turbulence fluctuation ϕ' which is the deviation of the resolved instantaneous quantity ϕ from the time average $\overline{\phi}$,

$$\phi = \langle\overline{\phi}\rangle + \Phi'' + \phi', \tag{5a}$$

$$\text{and} \quad \overline{\phi} = \langle\overline{\phi}\rangle + \Phi'', \tag{5b}$$

where the time-averaged quantity $\overline{\phi}$ is equivalent to Φ for simplicity, such as $\bar{u_i}$ being equivalent to U_i. In particular, the comprehensive spatial average (Xie and Fuka 2018) was selected. This method includes the solid regions in the total volume, but ascribes zero values to the output quantities in them (i.e. the volume occupied by the building blocks shown as the grey area in Fig. 1d), while the solid regions within the domain are included in the total volume. Equation 6 defines the comprehensive spatial average:

$$\langle\phi\rangle(z) = \frac{1}{S_c}\int\int_{(x\in(a,b),y\in(-6H,6H))\cap S_f} \phi(x,\ y,\ z)\mathrm{d}x\mathrm{d}y, \tag{6}$$

where $\langle\rangle$ denotes spatial average, ϕ denotes the quantity to be spatially-averaged, S_f denotes the fluid area at height z. For the periodic boundary condition (PBC) case, S_c denotes the total area at height z for the entire horizontal plane, i.e. $x \in (0,\ 12H)$, $y \in (-6H, 6H)$ (see Fig. 3a). For the synthetic turbulence inflow (STI) cases, S_c denotes the area at height z for a horizontal plane across the entire span ($y \in (-6H, 6H)$), and between two x coordinates a and b separated by $2H$ (see Fig. 3b).

The comprehensive spatial average has the advantage that it produces a smooth change of total momentum flux across the canopy interface (Xie and Fuka 2018). In comparison, the intrinsic spatial average, which only includes the fluid regions in the averaging, leads to a discontinuity in total momentum flux at the canopy height. The fact that the comprehensive spatial average gives a smooth change in momentum flux is potentially advantageous in developing a parametrization of momentum flux, or other quantities, for a meso-scale model.

3 Details of Cases Studied

3.1 Array Geometries

The idealized-morphology studied here takes the form of a simplified urban-like geometry. Arrays of simple blocks, i.e. cuboids with either flat or pitched roofs, are studied. The baseline cuboid has dimensions $2H \times H \times H$, where $H = 1$ m. The Reynolds number based on the block width H and the velocity at height H in the upstream boundary layer is about 7400, or about 830 based on the friction velocity u_τ (Coceal et al. 2006; Cheng and Castro 2002), estimated using an extrapolation from the linear turbulent shear stress profile above the canopy (e.g. Figure 6). Given the different block heights, and dimensionless domain heights in the work, we choose to use u_τ to non-dimensionlise quantities, and to focus on the physics within and immediately above the canopy. Based on their research on arrays of cubes at a smaller Reynolds number, Xie and Castro (2006) state that "Reynolds number dependency (if it does exists) is very weak for such flows, except no doubt very close to solid walls. Turbulence generated by urban-like obstacles (with sharp edges) is large scale dominated and hardly at all dependent on the much-smaller-scale viscous dominated processes on the body surfaces". Flows over arrays of pitched-roof obstacles with sharp edges are expected very weakly dependent on the Reynolds number too.

Two different packing densities (i.e. $\lambda_p = 33.3\%$ and 16.7%) are simulated. The baseline flat roof cases of height H were validated against Castro et al. (2017). Further cases of height $1.5H$ with a flat roof or a 45° pitched roof, were then compared with the baseline case. Figure 1 shows the geometries of the three different blocks used and diagrams illustrating the packing densities.

3.2 Meshes and Test Cases

The meshes used in this study were created using SnappyHexMesh which is far more flexible and efficient than standard structured-mesh generators. It was primarily used here to assess its suitability for application to much larger domains in follow-on studies. Nevertheless, this study utilised the capability of SnappyHexmesh to create uniform grids, grids with multiple levels of resolution and non-conformal and conformal meshes.

For the baseline flat-roof cases uniform Cartesian grids (identified as (U), Table 1) were first created with a resolution of $H/16$. This was in accordance with the minimum level of resolution suggested in Xie and Castro (2006) and Coceal et al. (2006), which was adopted for all cases, except for those with specifically defined grids. Cartesian meshes with three levels of grid resolution (identified as (3R),Table 1) were created, as used in Xie and Castro (2006), for testing mesh sensitivity. These had a resolution $H/16$ up to $z = 2.5H$, a resolution $H/8$ between $z = 2.5\,H$ and $z = 8.5\,H$, and finally a resolution $H/4$ from $8.5H$ up to the top of the domain at $12H$. The time step was chosen following the guidance that the maximum Courant number was less than unit. For the PBC cases (Table 1), the initialisation period was about $600T_p$, and the averaging period was at least $700T_p$, where T_p was based on the block height and the freestream velocity. For the STI cases (Table 1), the initialisation period was $50T_p$, and the averaging period was $200T_p$. It took from 240 to 300 wall-clock hours on 200 cores to complete one simulation case.

All the Cartesian meshes created for the flat roof cases were conformal. However, if a simple Cartesian mesh is created for a pitched roof, the mesh is non-conformal as shown in Fig. 2. To address the question of what impact this has, three meshing strategies were used for

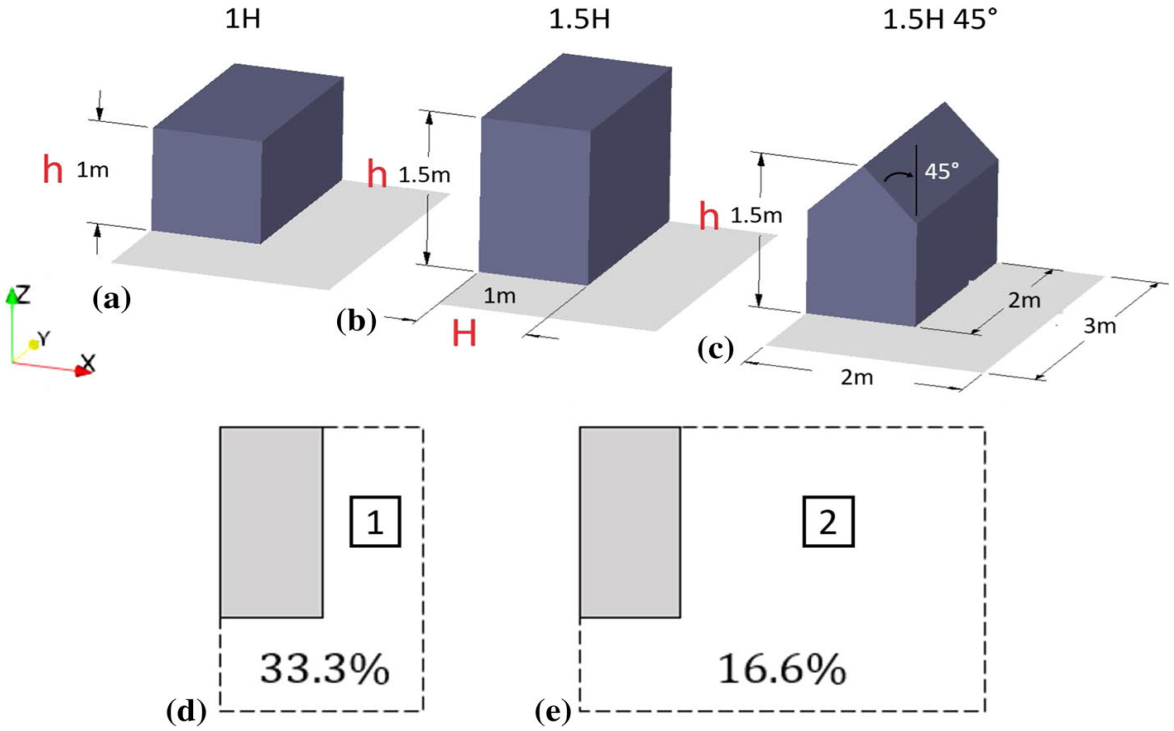

Fig. 1 Diagram of the smallest repeat unit size for **a** $1H$, **b** $1.5H$, **c** $1.5H45°$ pitched roof, with the same plan view and packing density, $\lambda_p = 33.3\%$. H, the block width. h, the block height. x coordinate is perpendicular to the long side of the cuboid and the long street, and z coordinate is in the vertical direction, **d** packing density $\lambda_p = 33.3\%$ (as in Fig. 1), **e** packing density $\lambda_p = 16.7\%$ where the width of the long street marked with "2" is tripled compared to "1" in (**d**)

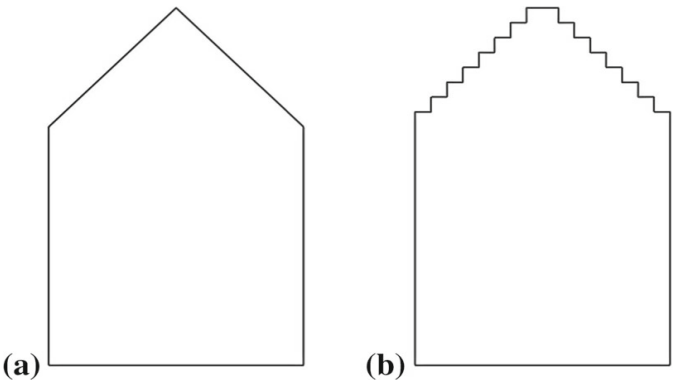

Fig. 2 Side view of the surface meshes of pitched-roof cuboids of **a** conformal mesh, $1.5H45°$(UC, 3RC) and **b** non-conformal mesh, $1.5H45°$ (UNC)

the pitched-roof cases: uniform conformal-grids (UC), Uniform non-conformal grids (UNC) and a 3-level resolution-conformal grid (3RC).

The majority of the cases were run at neutral stability conditions with PBC at the inflow and outflow (Table 1). For these cases the domain had dimensions of $12H \times 12H \times 12H$, following Castro et al. (2017) as shown in Fig. 3a. For the cases with thermally stratified inflows, the STI boundary condition was applied (Table 1). The domain was sized to match that used in Sessa et al. (2018, 2020), which was $29H \times 12H \times 12H$ shown in Fig. 3b. In both cases periodic boundary conditions were applied to the spanwise boundaries, and a stress free condition was set for the top boundary.

Table 1 summarises the neutral stability cases simulated with the baseline packing density of 33.3%, the neutral cases run to examine the effect of changing the packing density from

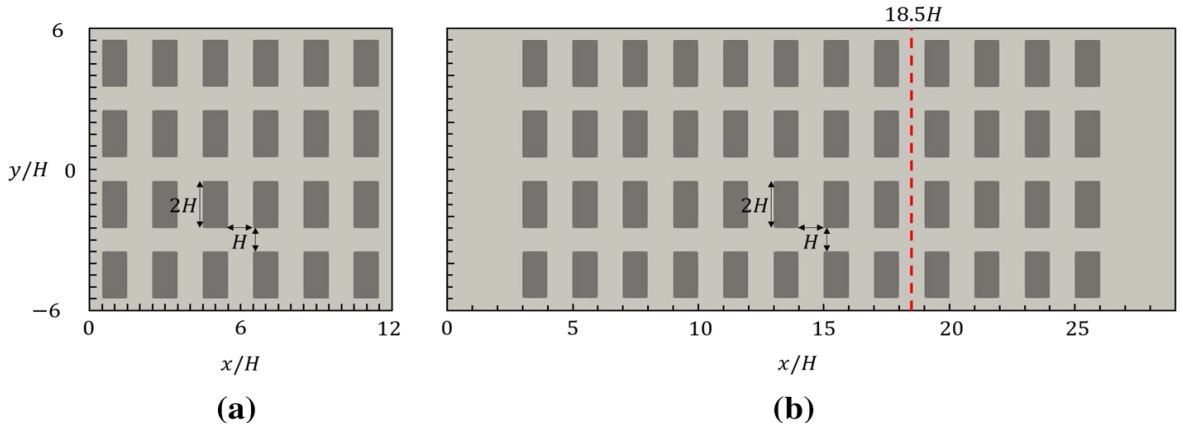

Fig. 3 Plan view of the two domains with a packing density $\lambda_p = 33.3\%$. **a** The PBC domain. **b** The STI domain. Removing every other column of cuboids in **a** results in $\lambda_p = 16.7\%$. The red dashed line denotes where the laterally averaged vertical profiles presented were determined

33.3 to 16.7%, and the cases run to examine the effect of thermal stratification on the flow over arrays with a packing density 33.3%.

4 Validation and Assessment of Mesh Sensitivity

4.1 Validation of Flow Simulation Around a Cuboid Array

To validate the methodology simulations were first made of cases 1 H(U) and 1 H(3R) with PBC at $\lambda_p = 33.3\%$. Figure 4 shows vertical profiles of the mean streamwise velocity component U, streamwise normal stress $\overline{u'u'}$, vertical normal stress $\overline{w'w'}$, and Reynolds shear stress $-\overline{u'w'}$ at the centre of the long street marked "1" in Fig. 1d. Overall, the differences in these turbulent statistics between the cases 1 H(U), 1 H(3R) and the LES data in Castro et al. (2017) are negligible within the canopy.

The mean streamwise velocity profiles sampled at typical locations (not shown) also agree well with those in Castro et al. (2017). The two cases 1 H(U) and 1 H(3R) yield accurate mean flow fields within the street canyon. The turbulent stress profiles of the case 1 H(U) are in agreement with those in Castro et al. (2017) over the entire vertical extent. Within the street canyon, the turbulent stresses for case 1 H(3R) are in reasonable agreement with those in Castro et al. (2017). Nevertheless, the discrepancy in the Reynolds stresses above $z = 2.5H$ between the case 1 H(3R) and Castro et al. (2017) is visible, with its approximate maximum 5%. This difference is due to a greater proportion of the Reynolds stresses being modelled (unresolved) by the SGS model above $z = 2.5H$ due to the coarser resolution for the case 1 H(3R). The modelled portion of the mixed time scale SGS model to the total Reynolds stress can be estimated (e.g. Xie et al. 2004). This is not of a primary concern of this paper. Despite the difference, the mean streamwise velocity is accurately predicted for the case 1 H(3R), again suggesting that the mixed time scale SGS model performs well for the coarser mesh.

In summary, the results suggest that the two conformal (body fitted) grids 1 H(U) and 1 H(3R) are able to produce satisfactory time-averaged velocities and turbulent statistics, e.g. Reynolds stresses. This provides the baseline of the mesh structure, from which the assessment of mesh sensitivity for the pitched-roof cases is carried out in Sect. 4.2.

Table 1 A complete list of the simulated cases

Case ID	$\lambda_p(\%)$	Block height (H)	Ri	Roof type	Mesh type	In-outlet BCs
1 H(**U**)	33.3	1	0	Flat	**U**niform	PBC
1 H(**3R**)	33.3	1	0	Flat	**3**-level **R**esolutions	PBC
1.5 H(**U**)	33.3	1.5	0	Flat	**U**niform	PBC
1.5 H(**3R**)	33.3	1.5	0	Flat	**3**-level **R**esolutions	PBC
1.5H45°(**UC**)	33.3	1.5	0	Pitched	**U**niform **C**onformal	PBC
1.5H45°(**UNC**)	33.3	1.5	0	Pitched	**U**niform **N**on-**C**onformal	PBC
1.5H45°(**3RC**)	33.3	1.5	0	Pitched	**3**-level **R**esolution **C**onformal	PBC
1 H(**U**)	16.7	1	0	Flat	**U**niform	PBC
1.5 H(**U**)	16.7	1.5	0	Flat	**U**niform	PBC
1.5H45°(**3RC**)	16.7	1.5	0	Pitched	**3**-level **R**esolution **C**onformal	PBC
1.5H45°(**UCI**)	33.3	1.5	0, 0.2, 0.5, 1	Pitched	**U**niform **C**onformal	STI

H block width (Fig. 1); *PBC* periodic boundary condition; *STI* synthetic turbulence inflow boundary condition

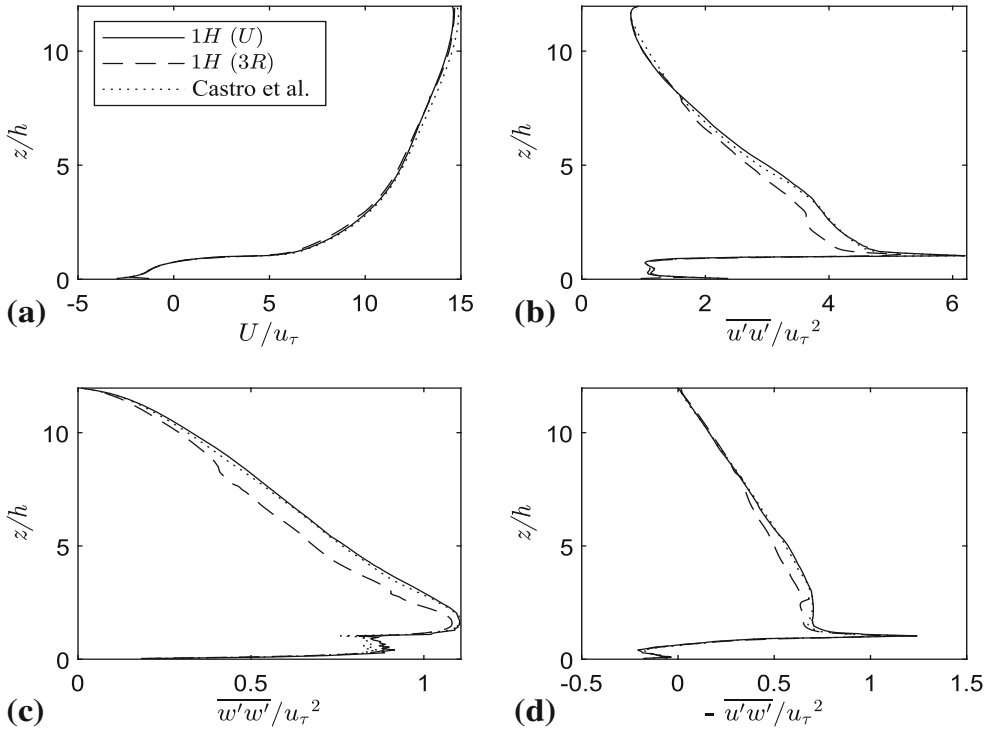

Fig. 4 Comparison between cases 1 H(U), 1 H(3R) and Castro et al. (2017) data at long street location "1" marked in Fig. 1d. **a** mean streamwise velocity U, **b** streamwise normal stress $\overline{u'u'}$, **c** vertical normal stress $\overline{w'w'}$, **d** Reynolds shear stress $-\overline{u'w'}$

4.2 Assessment of Conformal and Non-conformal Meshes

This section examines the effect of having conformal or non-conformal grids on the flow predictions obtained for a block array with pitched roofs. This is done by comparing spatially averaged profiles for the 1.5H45° (UC), 1.5H45° (UNC) and 1.5H45° (3RC) cases at a packing density of 33.3% with PBC. Figure 5 shows that all three cases produced consistent vertical profiles of mean streamwise velocity and root-mean-square velocity fluctuation components. Overall agreement between the three cases is satisfactory, especially for the mean velocity profile in Fig. 5a. All cases predict similar peak root-mean-square velocity fluctuations with differences of less than 5% within and above the canopy.

At the top of the domain, the increases in axial and particularly spanwise turbulence intensities are due to the so-called 'splatting' of the eddies on the top boundary, where the vertical velocity is constrained to be zero. This is not important, because as discussed in Xie et al. (2008) the domain height is great enough to avoid any top boundary condition effect on the regions of interest, i.e. within and immediately above the canopy. It can be seen that at $z/h = 2$ where the interface between the $H/16$ and $H/8$ grid regions occurs, the axial fluctuating velocity root-mean-square peak in Fig. 5b and a Reynolds shear stress peak in Fig. 6a are visible. These only have a very local effect and do not evidently impact the flow regions within and immediately above the canopy.

Figure 6 shows spatially averaged vertical Reynolds shear stress $\overline{u'w'}$ and dispersive shear stress $\langle -U''W'' \rangle$. There are negligible differences between the three cases within the canopy. The peak dispersive stress occurs just below the canopy top in all cases.

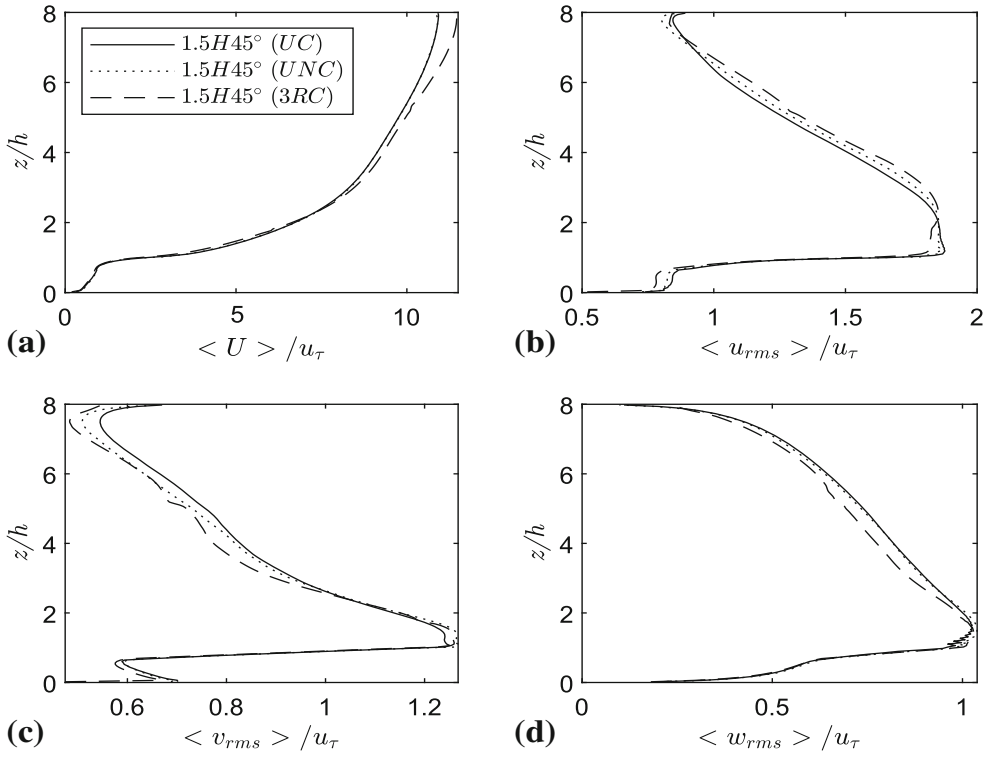

Fig. 5 Grid and geometry effects on **a** spatially averaged streamwise mean velocity, **b** axial velocity fluctuation root-mean square **c** spanwise velocity fluctuation root-mean square and **d** vertical velocity fluctuation root-mean square

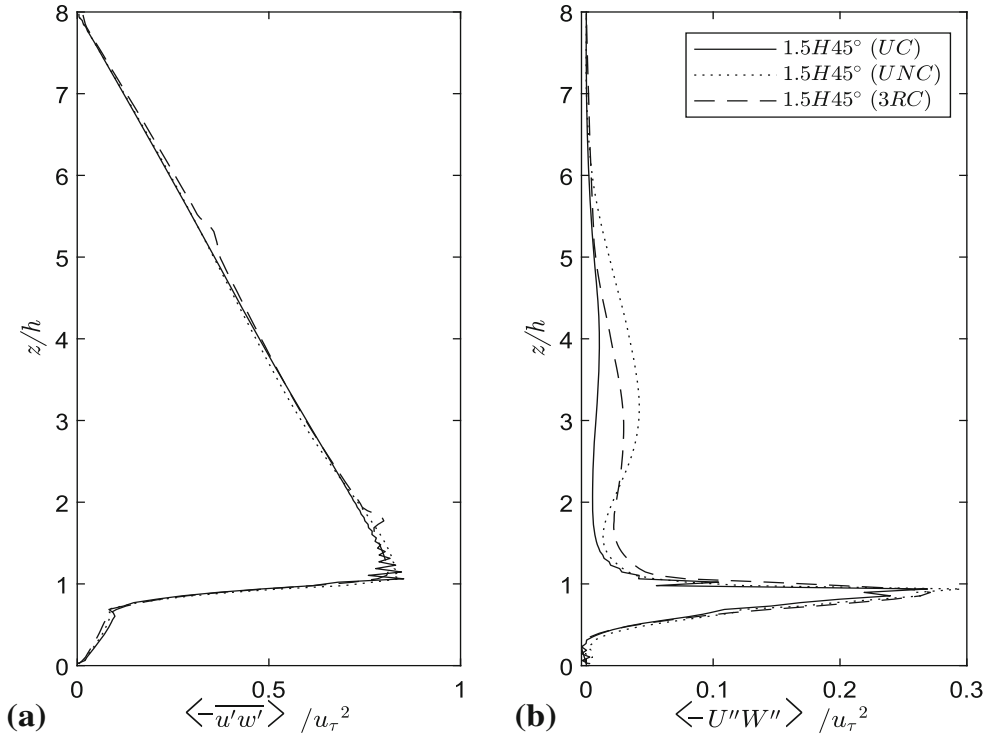

Fig. 6 Grid effects for array of cuboids $\lambda_p = 33.3\%$ with 45° pitched roofs **a** spatially averaged Reynolds stress and **b** spatially averaged dispersive stress

The 1.5H45°(UNC) case with non-conformal grid and 1.5H45°(3RC) case with coarse grid above the canopy produce a small but visible discrepancy (less than 2% of u_τ^2) from height $z/h = 2$ to $z/h = 5$, compared to the case 1.5H45°(UC).

The discrepancy in the dispersive shear stress profile between the conformal and non-conformal grids is visible, with an approximate maximum of 3% of u_τ^2 at $z/h = 3$. This small discrepancy is more likely owing to the uncertainty of the calculation of the dispersive shear stress than grid conformity. Span-width size structures above the canopy require significant averaging time for obtaining a 'converged' dispersive shear stress. These data confirm the satisfactory accuracy of using the non-conformal grids for the global quantities and those far away from the obstacles. Nevertheless, the accuracy of the near-wall quantities, e.g. surface pressure, is still a question for the use of a non-conformal grid, such as adopted by the PALM4U (Maronga et al. 2020) and uDALES (Heus et al. 2010; Suter et al. 2021) codes.

We speculate that the inaccurate representation of the local flow details in the vicinity of the pitched roof in the non-body fitted grid case 1.5H45°(UNC) could affect the prediction of local skin friction and other flow parameters. Nevertheless, Figs. 5 and 6 suggest that the overall discrepancy between the spatially averaged mean velocity, Reynolds stresses and dispersive stresses due to using a non-conformal rather than a conformal grid is small.

Figure 6a shows a linear decrease in Reynolds shear stress from the canopy top, reducing to zero at the domain top. The three profiles of the non-dimensional total shear stress (not shown) including the drag due to the blocks linearly increase within the canopy to almost 1 at the ground, which is expected because a constant body force $\partial P/\partial x$ is set to drive the flow. This confirms the satisfactory accuracy of the simulations (see Xie and Fuka 2018). The mesh resolution and numerical settings for the flat roof cases validated in Sect. 4.1, were kept the same for the pitched roof cases. All these ensure reliable results for the pitched roof cases.

5 Comparison of the Turbulence Statistics and Aerodynamics of Flat and 45° Pitched Roofs

This section compares flow fields, turbulence statistics, surface pressure coefficients and drag coefficients between arrays of cuboids with flat and 45° pitched roofs. It aims to provide an understanding of how having a pitched roof affects these quantities and to thereby quantify the importance of accurately accounting for the impact of pitched roofs on the boundary-layer flow.

Two packing densities $\lambda_p = 16.7$ and 33.3% of uniform cuboid arrays with and without pitched roofs were simulated. Spatially-averaged mean velocities and Reynolds stress profiles were examined to understand the combined effects of a pitched roof and packing density.

Table 2 Normalised friction velocity for each case for packing densities $\lambda_p = 33.3\%$ and $\lambda_p = 16.7\%$

Case	$\lambda_p(\%)$	u_τ/U_{3h}
1 H(UC)	33.3	0.100
1.5 H(UC)	33.3	0.093
1.5H45°(UC)	33.3	0.121
1 H(3RC)	16.7	0.133
1.5 H(3RC)	16.7	0.132
1.5H45°(3RC)	16.7	0.130

U_{3h} is the mean streamwise velocity at $z = 3h$

5.1 Effect of Pitched Roof on Urban Canopy Flows

It is known that the upper boundary conditions with a large ratio of the boundary-layer thickness to the building height, such as $\delta/h \approx 10$, yields a negligible effect on the flow and turbulence within and above the canopy (e.g. Coceal et al. 2006; Xie et al. 2008). It is worth identifying any differences of flow and turbulence over pitched-roof and flat-roof buildings in a thick boundary layer. Figure 7a shows a comparison of the spatially averaged vertical profiles of axial mean velocity between the pitched roof case 1.5H45°(UC), and the flat roof cases 1.5 H(U) and 1 H(U), in which the vertical coordinate is normalized by the canopy height h, and the profiles of root-mean-square velocity fluctuation components are normalised by the friction velocity u_τ. Within the canopy there are only small differences between the three cases, as they are of the same packing density $\lambda p = 33.3\%$. The two flat roof cases show a much greater inflection of mean streamwise velocity at the canopy height (Fig. 7b), which is associated with an overall "smoother" canopy top resulting a weaker shear immediately above the canopy, compared to the pitched roof case.

The pitched roof generates far more drag on the flow. This can be seen from the larger momentum deficit in Fig. 7a, and from the values of normalised friction velocity in Table 2, which show a significant increase for the pitched roof compared to the flat roof at $\lambda_p = 33.3\%$. Note a square of the normalised friction velocity (u_τ^2/U_{3h}^2) is denoted "drag coefficient" (Boppana et al. 2014). Here the mean streamwise velocity U_{3h} at $z = 3h$ is chosen as the reference velocity. Because the dimensionless domain height L_z/h is different for different cases (see Fig. 15), the mean velocity at the domain top is not chosen as the reference velocity. Table 2 shows that the normalised friction velocity of the pitched-roof cuboid array is approximately 30% greater than the $1.5H$ flat roof case, and approximately 21% greater than the the $1H$ flat roof case. This strongly suggests that an improved urban canopy model by using more advanced parametrizations should take account of the pitched-roof effects.

We now examine the flowfields in detail to understand the reasons for the increase in friction velocity. Figure 7d shows far higher vertical velocity fluctuations at the canopy height for the pitched roof in the same freestream wind; it is to be noted again that the friction velocity u_τ for the pitched roof case at $\lambda_p = 33.3\%$ is significantly greater than the flat roof cases. This could be considered similar to a random height array (Xie et al. 2008), which produces greater drag and turbulence mixing as well (i.e. than uniform height blocks with flat roof). The axial, spanwise and vertical velocity fluctuation root-mean-square data are shown in Fig. 7b, c and d respectively. Within the canopy, the dimensionless root-mean-square velocity fluctuations are significantly different. The behaviour of the vertical profiles for the two flat roof cases are similar above the canopy, whereas the deeper canopy evidently suppresses the turbulent

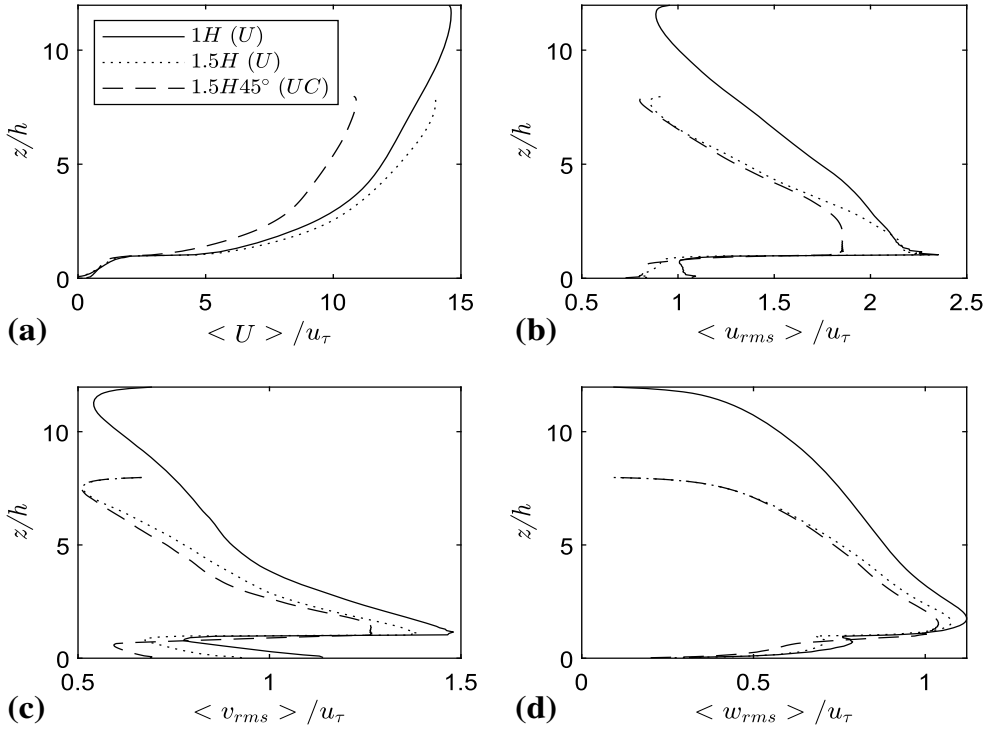

Fig. 7 Comparison of the spatially averaged vertical profiles between flat roof and pitched roof. **a** Streamwise mean velocity U, **b** u_{rms}, **c** v_{rms} and **d** w_{rms}

fluctuations of all three components within it. The pitched roof alters the behaviour of the vertical profiles significantly above the canopy.

Figure 8a, b, c show mean ensemble average flow field vector plots of the street canyon in the $x - z$ plane up to a height of $z/H = 2$ for the 1 H(U), 1.5 H(U) and 1.5H45°(UC) cases respectively. The differences in flow pattern are evident. Figure 8a, b for the flat roof cases show skimming flow regimes (Oke 1988), where the bulk of the flow does not enter the street canyon, and a stable circulation flow is formed in the canyon. A stagnation at $z/h = 0.94$ (Figs. 11c and 13a) confirms this. Fig. 8c for the pitched roof exhibits a flow in the wake interference regime (Oke 1988), where the downward flows is deflected down the windward roof of the next block downstream, at the stagnation of $z = 0.85h$ (Figs. 11e and 13b). Dispersive stress within the canopy of the pitched-roof case $1.5H45°$(UC) (Fig. 14) is much greater than that of the flat-roof case $1.5H(U)$ in the same incoming flow. Again, this suggests that the former generates a less stable circulation in the canyon, and is in the wake interference regime, whereas the latter is in the skimming region.

Figure 8c shows that the shear layer at the canopy top impinging on the windward pitched roof, which explains the greater vertical velocity fluctuations at the canopy height in the same freestream wind (Fig. 7d). Much greater vertical mean velocity magnitude (not shown) was also observed at the canopy height for the pitched roof case.

The observations above are reinforced by Fig. 9 which shows very different normalised instantaneous axial velocity contours for the 1.5 H flat and pitched roof cases. The flat roof creates an obvious interface at the canopy top, where a thin shear layer forms; whereas the pitched roof generates a far thicker shear layer from the apex of the roof, and a less visible interface. Vorticity contours (not shown) for both cases show the same phenomenon.

Figure 10 shows how the pitched roof changes the spanwise flow around the cuboid. The development of the secondary flows evident in Fig. 10a, b has been well documented

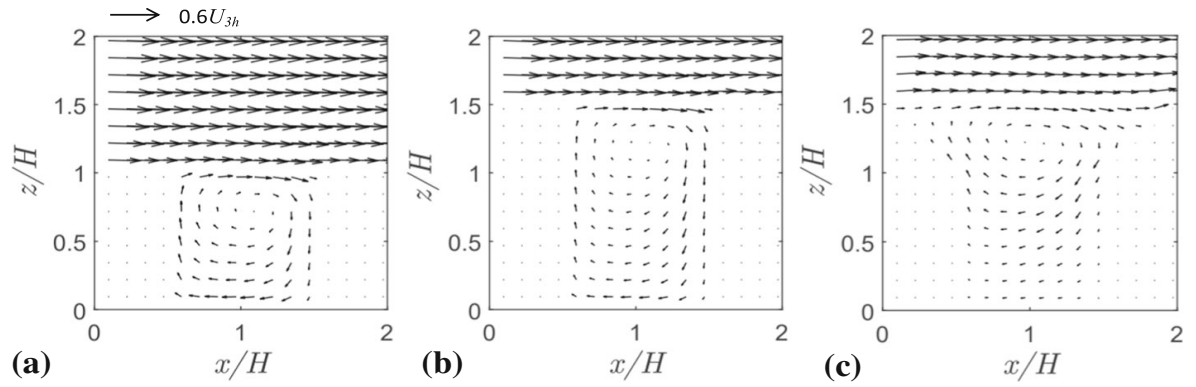

Fig. 8 Vector plot of mean ensemble average velocity normalised by U_{3h} across the $x - z$ plane on the centre of the long street. **a** 1 H(U), **b** 1.5 H(U) and **c** 1.5H45°(UC)

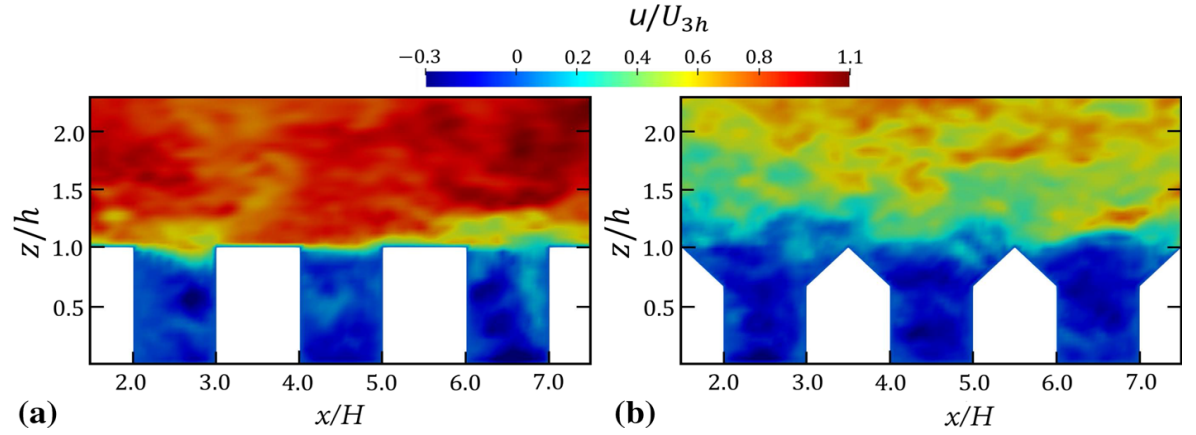

Fig. 9 Normalised instantaneous streamwise axial velocity contour across x-z plane on the centre of the long street for **a** 1.5H(U) and **b** 1.5H45°(UC)

for uniform height flat-roof cuboids with various aspect ratios (Willingham et al. 2014; Vanderwel and Ganapathisubramani 2015; Tomas et al. 2017). However, the pitched roof effectively destroys any secondary flow (Fig. 10c). This is due to the large mean upwards flow at the apex of the roof, which is largely uniform across the span. The pitched roof also greatly enhances the axial rotation seen at the corner of the apex.

Figure 11 shows pronounced differences in the windward and leeward surface pressure distributions normalised by ρu_τ^2 on the three blocks. The windward side plots show similar pressure distributions for both the flat-roof cases, 1 H(U) and 1.5 H(U) (Fig. 11a, c respectively). The pitched-roof case, however, shows a considerably different surface pressure distribution. The vertical face from $z = 0$ to $2h/3$ shows a similar low pressure region to the two flat roof cases, but with a lower pressure which extends much deeper into the canopy and further across the span.

On the leeward side similar distributions are again observed for the flat-roof cases (Fig. 11b, d). But the leeward side of the pitched roof case (Fig. 11e) displays a much more uniform distribution across the span, due to the more uniform mean flow across the span shown in Fig. 10c.

Figure 12 shows contours of pressure difference between the windward and leeward sides for the three cases 1 H(U), 1.5 H(U), and 1.5H45°(UC). This figure shows a similar surface pressure difference distribution to that in Tsutsumi et al. (1992) with the highest volume ratio (packing density). The data collected also follows the same pattern in that, the surface

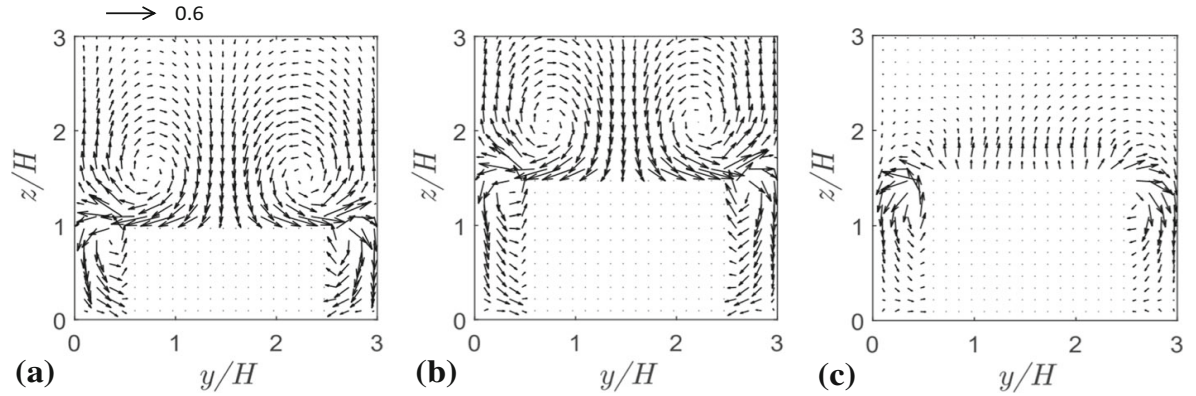

Fig. 10 Vector plot of mean ensemble average velocity normalised by U_{3h} across the $y-z$ plane on the centre of the cuboid. **a** 1 H(U), **b** 1.5 H(U) and **c** 1.5H45°(UC)

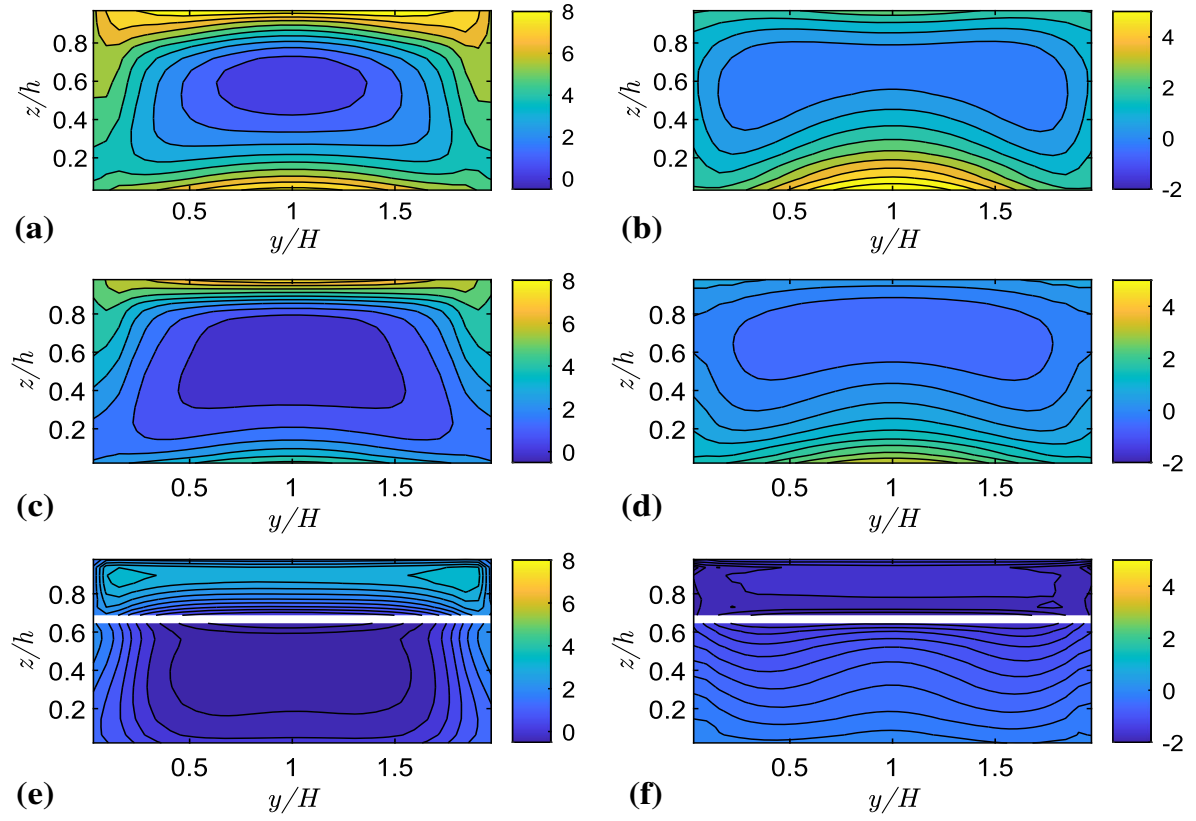

Fig. 11 Surface pressure contours normalised by ρu_τ^2. **a** 1 H(U) windward, **b** 1 H(U) leeward, **c** 1.5 H(U) windward, **d** 1.5 H(U) leeward, **e** 1.5H45°(UC) windward, **f** 1.5H45°(UC) leeward. White band denotes the roof-wall joint

pressure difference increases from low to high in going from the centre span to edge. The pressure difference peak occurs at $y = 0$ and almost the canopy top for the flat-roof block, whereas the pressure difference peaks on the pitched roof occurs at $y/H = 0.15$ and 1.85, and $z/h = 0.9$. The pressure difference on the pitched roof shows a high uniformity across the span, which probably results from a dominant flow along the roof surface towards the apex of the roof.

Figure 13a shows vertical profiles of spanwise averaged surface pressure on windward and leeward sides. The profiles for two flat-roof cases are similar in shape; whereas the

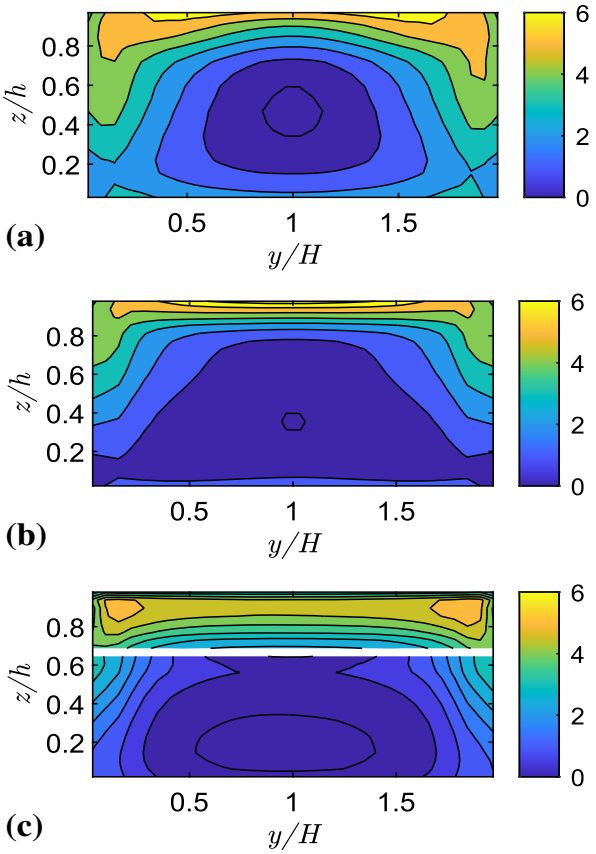

Fig. 12 Contours of pressure difference between the windward and leeward sides normalised by ρu_τ^2. **a** 1 H(U), **b** 1.5 H(U), **c** 1.5H45°(UC)

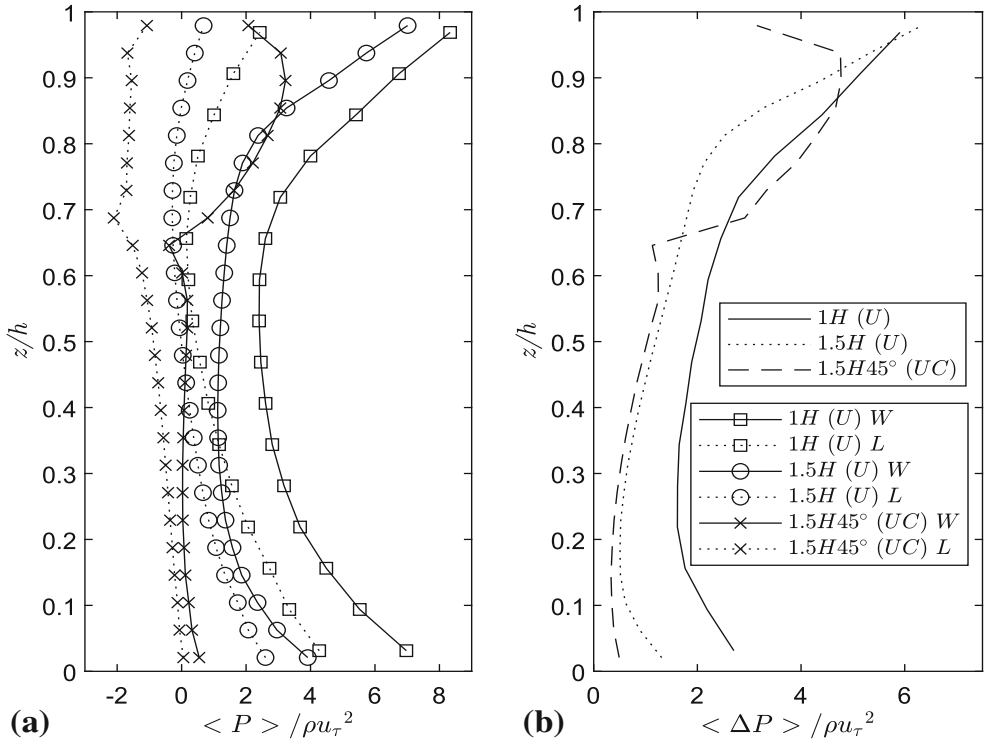

Fig. 13 Comparison of vertical profiles of **a** spanwise averaged surface pressure on windward (W) and leeward (L) sides, and **b** pressure difference between windward and leeward sides

pitched roof creates significantly different shaped profiles above $z = 2h/3$. A noticeable inflection is present in the pitched roof profiles at the transition between side and roof, which occurs at slightly different vertical locations on windward and leeward sides, this is likely due to not having data at the transition point. The maximum surface pressure at $z/h = 0.9$ on the windward side, denotes the stagnation. Stagnation is not visible on the windward sides of the flat-roof cuboids, which occurs too close to the canopy top to be resolved in the current mesh. Figure 13b shows normalised spanwise-averaged pressure difference. A considerable difference is evident between the flat-roof case 1.5 H(U) and the pitched-roof case 1.5H45°(UC) above $z = 2h/3$.

The form drag due to the pressure difference between the windward and leeward faces is dominant. Xie and Castro (2006) show that the integrated pressure difference between the windward and leeward of an array of cubes is approximately 90% of the total body force imposed, which is equal to an integral of ρu_τ^2 over the ground surface. The pressure difference for the pitched-roof case exhibits an inflection at $z = 2h/3$ as in Fig. 13a, accompanied by an abrupt increase in the pressure difference above $z = 2h/3$, which peaks at $0.9h$ and decreases towards the canopy top. The 1.5 H(U) case exhibits a lower pressure difference across the depth of the canopy, compared to the shorter cuboid case 1 H(U). A sharp increase occurs above $z = 0.8h$ for case 1.5 H(U), and one occurs above $z = 0.7h$ for case 1 H(U), which are consistent with the pressure profiles on the windward sides for the respective flat-roof cases in Fig. 13b. These changes in shape are likely associated with the heights of the recirculation centres within the long street shown in Fig. 10a, b. Again, these suggest that a one-dimensional urban canopy model that resolves the aerodynamic drag distribution within the canopy should take account of the pitched-roof effects.

Figure 14a shows dimensionless spatially-averaged Reynolds shear stress profiles. Within the canopy the pitched roof generates far less Reynolds shear stress. The profiles for the two flat roof cases are similar, with the lower cuboid case generating slightly more Reynolds shear stress within the canopy. When focusing on the flow immediately above and within the canopy, it is more appropriate to normalise quantities by the friction velocity. Table 2 shows more details of u_τ/U_{3h}, where U_{3h} is the mean streamwise velocity at $z = 3h$. When focusing on the flow far above the canopy, it is more appropriate to normalise the flow quantities by the free stream velocity U_∞, or the velocity high above the canopy e.g. $z = 3h$. We noticed that the peak Reynolds shear stress normalised by U_{3h} is about 100% higher for the pitched roof case (not shown), suggesting that the pitched roof vastly increases the drag, mixing and re-entrainment of the flow into the canopy. Within the canopy, Reynolds shear stress normalised by U_{3h} shows the same behaviour to that normalized by the friction velocity u_τ. Considering only the packing density $\lambda_p = 33.3\%$ against a flow region map based on flat-roof data, the flows fall into the the skimming region. However, the entrainment into the street canyon is less-energetic due to the pitched roof because the mean flow in the shear layer has a non-negligible upwards component and some portion of flow is directed upwards instead of into the street canyon. Taking account of this, the flow over the pitched-roof array with $\lambda_p = 33.3\%$ falls into the wake interference regime.

The pitched roof creates a more uniform mean flow field across the span of the cuboid. The local peak Reynolds shear stress differs by less than 7% across the span of the cuboid at the long street location, i.e. station "1" in Fig. 1, with a maximum occurring at the center of the span. The flat roof cuboid generates the maximum Reynolds shear stress at $0.1H$ from the spanwise edge of the cuboid.

Figure 14b shows spatially-averaged vertical dispersive stress profiles, which are the mean flow contributions to vertical momentum flux. The pitched roof creates significantly larger dispersive stresses at the canopy height compared to the flat roof - it is to be noted

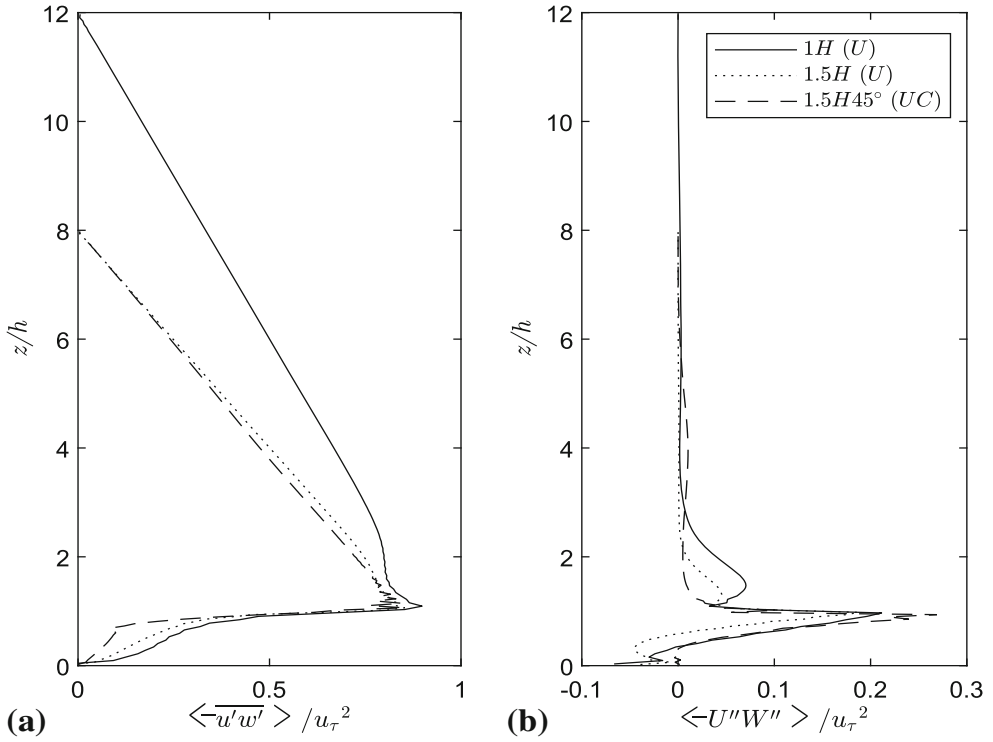

Fig. 14 Spatially-averaged profiles of **a** dimensionless Reynolds shear stress, **b** dimensionless dispersive stress

the friction velocity u_τ is much greater for the pitched roof case. At $z = 2\,h$ and $1.5\,h$, the flat roof cuboids generate larger dispersive stresses, whereas the pitched roof generate negligible dispersive stress at the same height. We speculate that the pitched roof generates more turbulent fluctuations and mixing at the canopy height resulting in less significant mean flow variations.

5.2 Packing Density Effects Accounting for Roof Shape

Table 2 shows an evident increase of normalised friction velocity u_τ/U_{3h} for the pitched roof compared to the flat roof at packing density $\lambda_p = 33.3\%$, suggesting a significant increase of drag coefficient u_τ^2/U_{3h}^2. Nevertheless, Table 2 shows no evident difference in u_τ/U_{3h} at packing density $\lambda_p = 16.7\%$, suggesting that the impact of the pitched roof is highly dependent on the packing density.

Figure 15 shows spatially-averaged mean streamwise velocity and Reynolds shear stress profiles for the three block geometries at packing densities of 33.3% and 16.7%. To emphasise the variation of the canopy drag for different blocks in a given wind, we deliberately use U_{3h} to scale the quantities. With the exception of the 1.5H45°(3RC) 16.7% case, the differences between the mean velocity profiles within and immediately above the canopy are hard to discern.

Oke (1988) suggests that a threshold line between the wake interference and skimming regimes is $h/W \approx 0.65$, where h/W is the canyon aspect ratio, and W is the canyon width. These data are based on a low ratio of building height to width, e.g. $h/W = 1$ (see Fig. 1, where $W = H$ for $\lambda_p = 33.3\%$). Oke (1988) also suggests being prudent when using such a threshold, given the uncertainties. As discussed in Sect. 5.1, the flow over the flat roofed arrays at $\lambda_p = 33.3\%$ and $h/W = 1.5$ is in the skimming regime, whereas at $\lambda_p = 16.7\%$

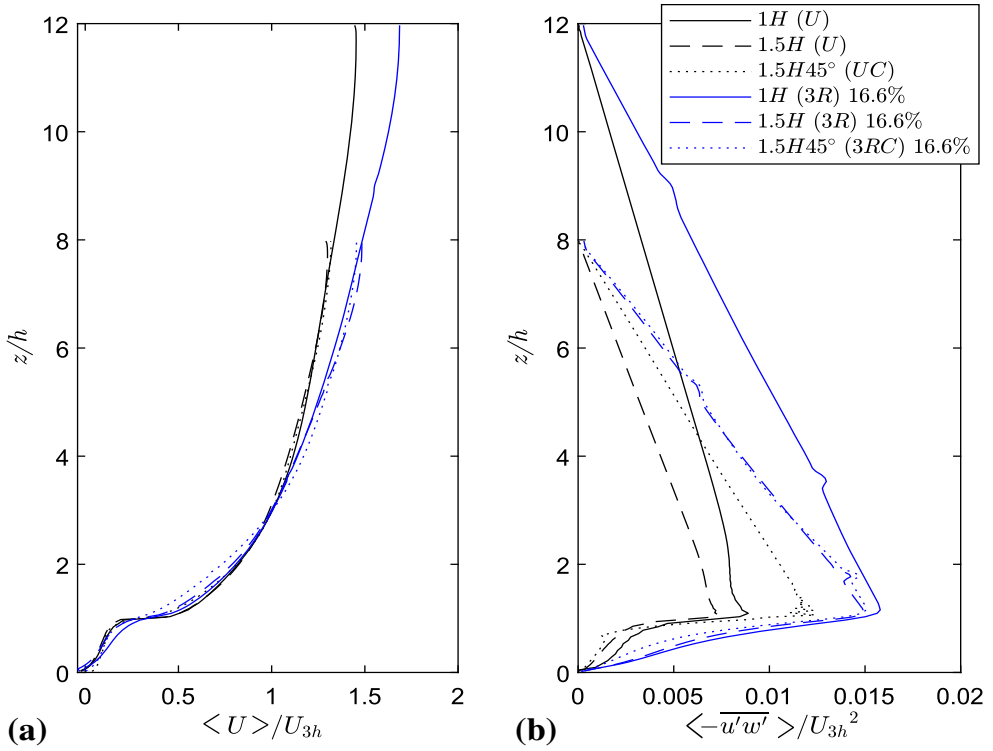

Fig. 15 Effects of packing density and roof shape on **a** spatial- and time-averaged axial velocity profile, and **b** spatial- and time-averaged Reynolds shear stress

and $h/W = 0.725$ it is in the wake interference regime. Again, these are supported by the flow pattern, surface pressure and skin friction data.

The peak values of Reynolds shear stress for the higher packing density cases are all lower than the peaks for the lower packing density.

It is crucial to note that the pitched roof increases the total drag coefficient substantially at the higher packing density $\lambda_p = 33.3\%$, whereas at the lower packing density $\lambda_p = 16.7\%$ the effect of the roof on the drag coefficient is small. This confirms the observation in Sect. 5.1 that the pitched roof alters the flow regime at $\lambda_p = 33.3\%$, but it does not at $\lambda_p = 16.7\%$. This suggests that the flow regime map against the canyon aspect ratio needs to take account of roof shape, and requires a more systematic study of the issue, such as covering a certain range of λ_p and h/W, but as a starting point, a specific case is of interest. Given the significant effect of the pitched roof, the width W_r between one apex of pitched roof to the next apex is used to calculate the canyon aspect ratio h/W_r. For the pitched roof at $\lambda_p = 33.3\%$, the aspect ratio $h/W_r = 0.725$ falls in the wake interference regime. This is consistent with the $h/W = 0.725$ falling in the wake interference regime for flat-roof arrays at $\lambda_p = 16.7\%$.

Figure 16 shows spatially-averaged mean streamwise velocity and Reynolds shear stress within and immediately above the canopy. The spatially-averaged mean velocity profiles are similar in shape, but the arrays with the lower packing density produce a smoother transition in the mean flow at the canopy top. As with the values above the canopy shown in Fig. 15, there is a clear difference in the values of Reynolds shear stress within the canopy for the two packing densities. It is noticeable though that the pitched roof reduces the Reynolds shear stress in most of the regions within the canopy, for both packing densities even though it substantially enhances the the Reynolds shear stress at the canopy height when $\lambda_p = 33.3\%$. We speculate that the 45° slope on the windward side of the block convects most of the

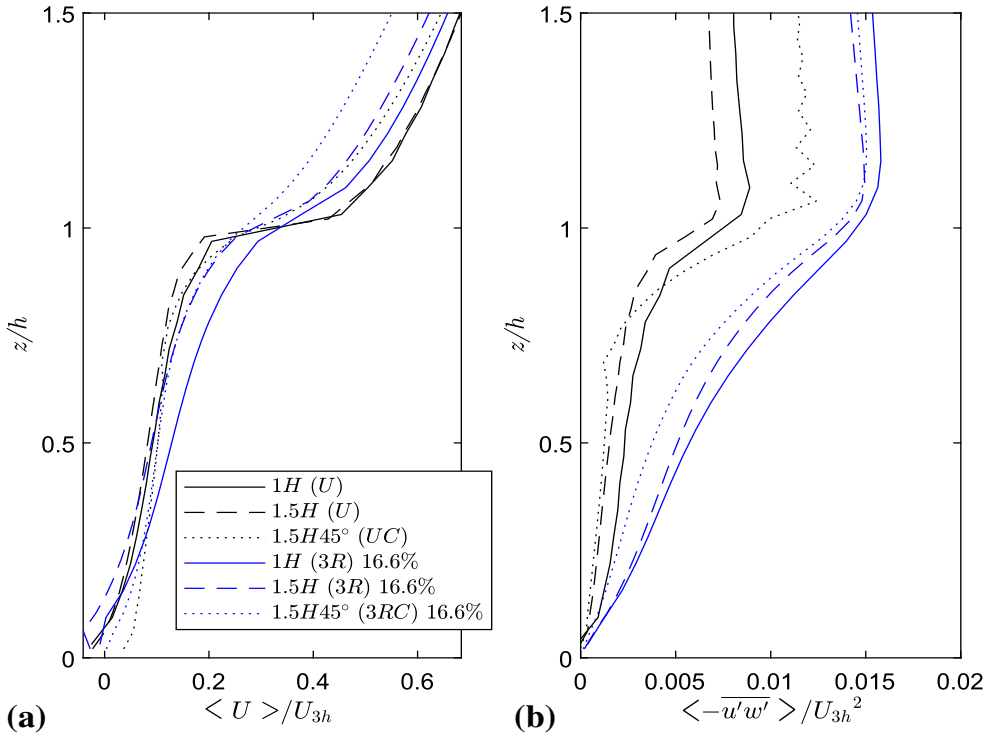

Fig. 16 Effects of packing density and and roof shape within the canopy on the **a** spatial- and time-averaged axial velocity profile and the **b** spatial- and time-averaged Reynolds shear stress

turbulence upwards and downstream, whereas the straight vertical windward side of the flat-roof blocks convects a large fraction of the turbulence downwards into a large circulation within the long street canyon as shown in Fig. 8.

6 Effects of Atmospheric Thermal Stratification

The study of flow over pitched roofs in neutral conditions as shown previously is a crucial stepping stone, albeit that the occurrence of neutral atmospheric stability conditions is very rare. In this section the effects of stable stratification are examined for pitched-roof cuboids. Again, it is to be noted that the same turbulent and temperature inflow statistics were used for the neutral and stable stratification as in the flat roof cases reported in Sessa et al. (2020). The imposed turbulent kinetic energy at the inlet in the neutrally stratified case is approximately twice that in the stably stratified cases.

Data from the STI domain is shown as spatially averaged between $a(17H) - b(19H)$ (Eq. 6). Figure 17 shows laterally averaged vertical mean velocity and Reynolds stress profiles at $x = 18.5H$ for four stratified conditions. The mean velocity profile is negligibly affected by all the stratification conditions or the inflow turbulence level, whereas for flat-roof cuboids in Sessa et al. (2020) (i.e. Fig. 7) the effect was more evident.

Figure 17 shows an evident effect of stratification and inflow turbulence level on the turbulent statistics. The reduction of streamwise normal stress (Fig. 17b) in going from $Ri = 0.2$ to $Ri = 0.5$ for the pitched roof case is approximately 7%, in contrast to a reduction of 25% for the flat-roof case (Sessa et al. 2020). For $Ri = 0.2$ and $Ri = 1$ the differences are 16% and 50% for the pitched and flat roof cases, respectively. These suggest the effect of a pitched roof opposes that typically associated with the stable stratification.

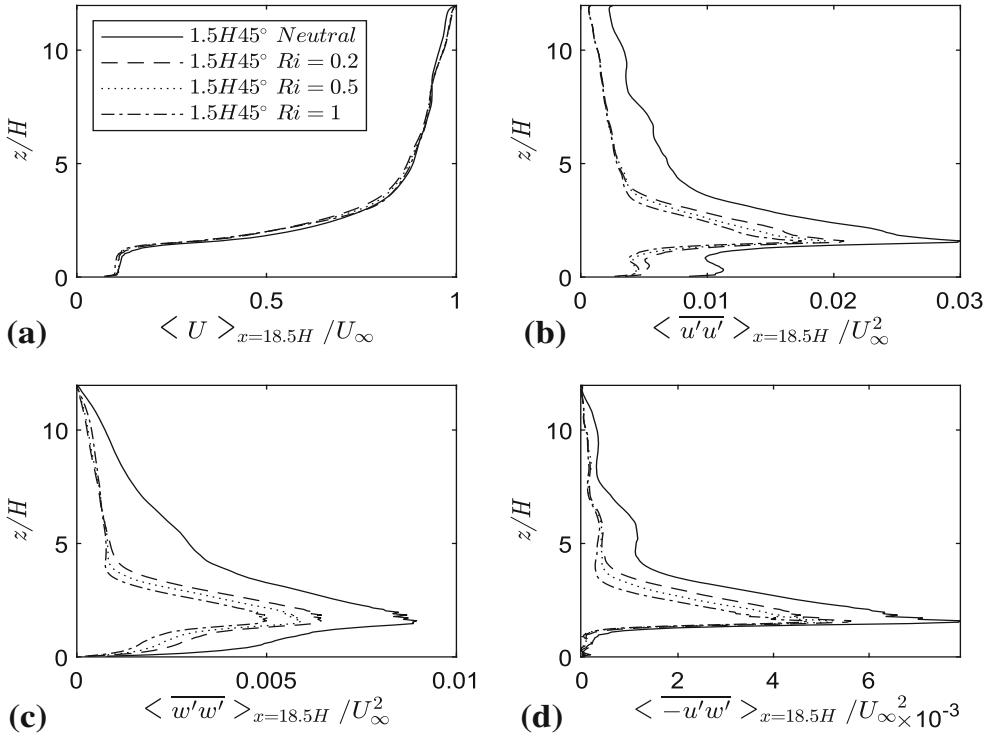

Fig. 17 Spanwise averaged data at $x = 18.5H$ for neutral and stratified conditions, $Ri = 0.2, 0.5, 1$, **a** mean velocity, **b** streamwise stress, **c** vertical stress and **d** Reynolds stress, normalised by the freestream velocity

The evident differences in the streamwise and vertical stresses between the neutral and the case $Ri = 0.2$ (in Fig. 17) are mainly due to the large difference of the inflow turbulence level. Nevertheless, these differences for the pitched roof cuboids are far smaller than for the flat-roof cases shown in Fig. 8 in Sessa et al. (2020). This suggests that the flow created around pitched roof cuboids leads to an evident reduction in the effect of inflow turbulence level, when compared to the flows over flat-roof cuboids for the same inflow conditions.

In neutral conditions the flat-roof generates around 10% stronger streamwise fluctuations than the pitched roof, whereas it generates around 10% less vertical fluctuations than the pitched roof (see Fig. 17, and Sessa et al. 2020). This suggests that the pitched roof generates more three-dimensional turbulent eddies above the canopy, as opposed to the thin shear layers generated by the flat roof at the canopy height. Thermal stratification normally inhibits vertical momentum transport while pitched roofs promote it by pushing flow upwards or downwards, so they have the opposite effect. The more energetic vertical turbulent fluctuations at the top of the pitched-roof cuboids reduce the effects of the stratification and the inflow turbulence level.

Figure 18 shows contours of vertical stress $\overline{w'w'}$ across a vertical plane located at $y = -1.5H$ (see Fig. 3) for $Ri = 0, 0.2, 0.5$ and 1. It is evident that the stable stratification reduces the strength of fluctuations across the entire fetch of the domain. Figure 18 also shows that the growth of the IBL is suppressed in the stratified flow. However, such a stratification effect is evidently less effective in suppressing the IBL when compared to its effect on the flow over flat-roof cuboids (Sessa et al. 2020), as we discussed in the preceding paragraphs.

Sessa et al. (2018) developed an approach to defining the IBL interface by identifying the abrupt change in gradient of the vertical Reynolds stress profiles. Following the methodology of Sessa et al. (2018), we estimated the IBL depth for the pitched-roof array. Figure 19 shows spatially-averaged vertical normal stress profiles over an area of $2H$(streamwise)

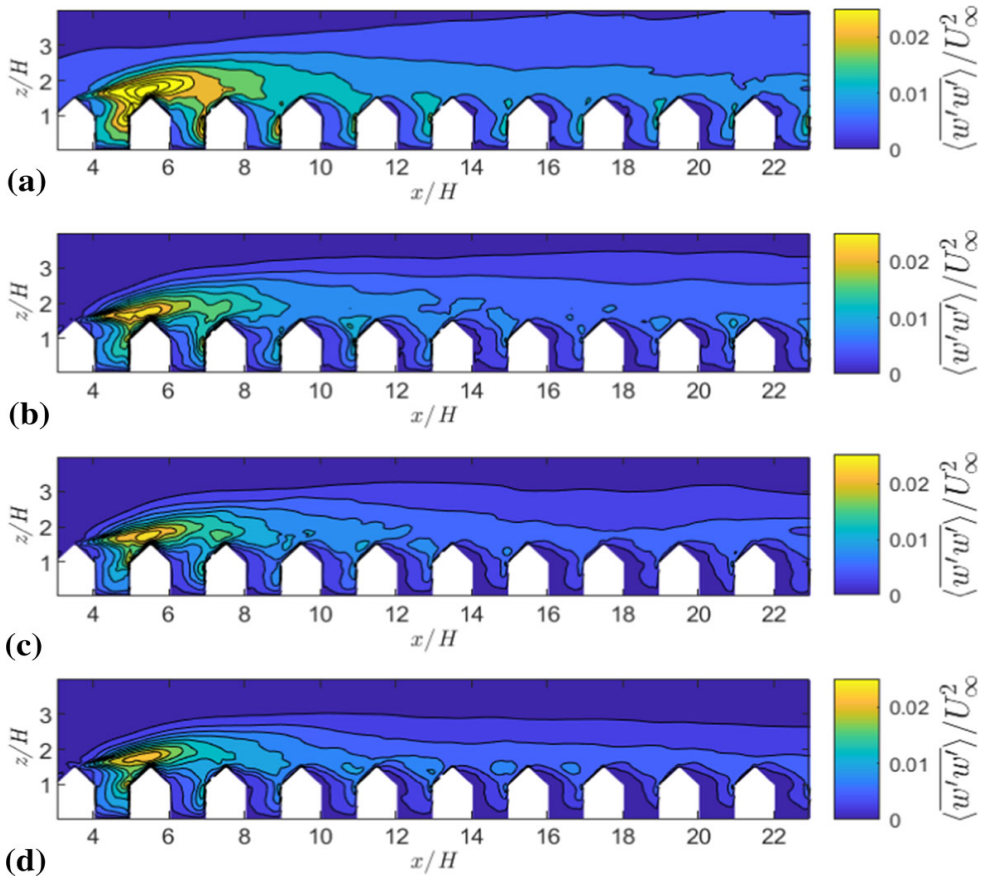

Fig. 18 Variance of vertical turbulent fluctuations normalised by freestream velocity for **a** $Ri = 0$, **b** $Ri = 0.2$, **c** $Ri = 0.5$ and **d** $Ri = 1$

$\times$ $12H$(lateral) centred at $x_{\text{lee}} = 4H$, $6H$, …, and $22H$, marked with 1, 2,…, and 10, respectively. The spatial average is defined in Eq. 6, where $a = x_{lee} - H$, and $b = x_{lee} + H$. The colour lines with symbols denote the IBL interfaces. It is evident that the thermal stratification suppresses the IBL growth. The IBL depth in Fig. 19 is evidently greater than that over a flat-roof array with the same input settings, including stratification condition Sessa et al. (2020). This confirms our early concluding remarks that compared to the flat roof, the pitched roof evidently enhances the mixing, significantly increases the aerodynamic drag, and reduces the thermal stratification effect.

7 Conclusions

Large-eddy simulations have been carried out to simulate the flow of urban boundary layers over idealized arrays of cuboids with and without pitched roofs, under neutral and stable stratification conditions. The reliability and accuracy of the results has been ensured by conducting rigorous evaluation tests, including examining mesh sensitivity and body conformity.

The results for a baseline flat roof cuboid array were first validated against previous data. The same mesh and numerical settings were then preserved as far as possible to ensure the reliability of flow simulations made for the 45° pitched roof cases.

The non-conformal Cartesian meshes used in some CFD codes, such as PALM4U and uDALES, provide high computational efficiency, but their users might have doubts with

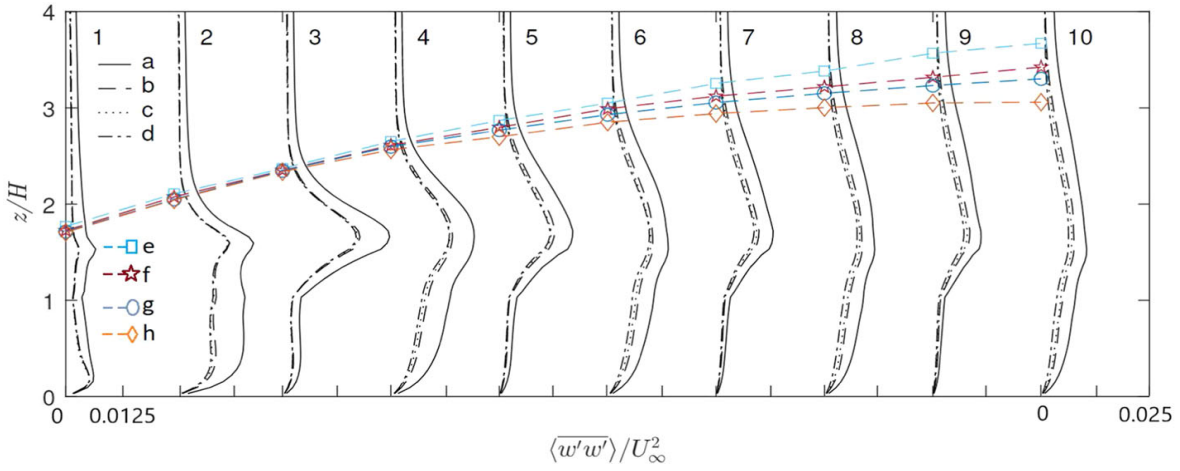

Fig. 19 Spatially-averaged vertical normal stress profiles over an area of $2H$(streamwise) $\times$ $12H$(lateral) centred at $x_{lee} = 4H$, $6H$,…, and $22H$, marked with 1, 2,…,and 10, respectively. The coloured lines with symbols denote the IBL interfaces. **a**, **e** $Ri = 0$, **b**, **f** $Ri = 0.2$, **c**, **g** $Ri = 0.5$ and **d**, **h** $Ri = 1$

regard to the accuracy, such as in the near wall regions. This study has examined their accuracy of the global quantities, such as the spatially averaged mean velocities, second order turbulent statistics and dispersive stresses. We conclude that these meshes produce accurate spatially-averaged quantities compared to those from conformal (body-fitted) meshes.

Compared to that produced by an array of flat roof cuboids, introducing an array with 45° pitched roofs leads to significant changes in the mean flow field, the Reynolds stresses, and drag, and increases the turbulent momentum flux at the canopy height by approximately 50%. The magnitude of these changes strongly suggests that it is important to account for the effect of roof shape in urban arrays.

The results have shown that the pitched roof case exhibits a different flow regime to that of the flat roof cases at packing density $\lambda_p = 33.3\%$. The pitched roof, due to decreased packing density in the top third of the canopy, is in the wake-interference regime, as opposed to the skimming flow regime experienced by the flat roof cuboids. At $\lambda_p = 16.7\%$ both the flat-roof and pitched roof cases are in the wake-interference regime. The normalised spatially averaged profiles of Reynolds stress over the flat- and pitched-roof buildings show a significantly smaller difference when compared to the results at $\lambda_p = 33.3\%$. This suggests that the pitched roof only plays a crucial role within a certain range of packing densities.

Although pitched roof and random height arrays are more common than flat-roofed buildings of uniform height in urban areas, current parametrizations are typically based on arrays of uniform-height cuboids with flat roofs. The need for taking the effect of pitched roofs into account is given more importance by the fact that the results showed a much stronger effect for a packing density of around $\lambda_p = 33.3\%$ which is more common in suburban regions than $\lambda_p = 16.7\%$. The results suggest that omitting these effects in a high-resolution meso-scale models may introduce non-negligible errors into boundary-layer predictions over typical suburban and urban regions, where there are a high proportion of pitched roof or non-uniform height buildings. Frontal solidity and packing density provide adequate descriptions of arrays for developing parametrizations for the effects of flat roofed buildings in meso-scale models, adding adding a further parameter to differentiate between arrays with different roof geometries would improve the performance of these models.

Simulations show that having pitched roofs means that the effect of increasing stable stratification conditions ($0 \leq Ri \leq 1$) is very much reduced in comparison to the same

incoming flow for flat roof cuboids. The relative difference in the vertical fluctuations between two weak stratification conditions ($Ri = 0.2$, and 1) is around 16% less for the pitched roof cases, while a reduction of 50% is found for flat roof ones (Sessa et al. 2020). We conclude that pitched roofs may greatly enhance the turbulent mixing in stable stratification conditions, and so improve the urban ventilation in the local environment. Consequently, pollution models which ignore the effects of pitched roofs may be overly pessimistic.

Acknowledgements This research is mainly funded by a studentship of the Faculty of Engineering and the Environment. MC thanks Dr Tim Foat from the Defence Science and Technology Laboratory (Dstl) for providing insight and support. The authors thank the three anonymous peer reviewers for their very valuable comments and suggestions. Computational work has been undertaken on Southampton University's Iridis systems. The datasets generated during and/or analysed during the current study are available from the corresponding author on reasonable request.

Declarations

Conflict of interest The authors declare that they have no conflict of interest.

References

Badas MG, Ferrari S, Garau M, Querzoli G (2017) On the effect of gable roof on natural ventilation in two-dimensional urban canyons. J Wind Eng Ind Aerodyn 162:24–34

Bailey A, Vincent N (1943) Wind-pressure on buildings including effects of adjacent buildings. J Inst Civil Eng 20(8):243–275

Barlow JF, Harman IN, Belcher SE (2004) Scalar fluxes from urban street canyons. part I: laboratory simulation. Boundary-Layer Meteorol 113(3):369–385

Barlow J, Best M, Bohnenstengel SI, Clark P, Grimmond S, Lean H, Christen A, Emeis S, Haeffelin M, Harman IN et al (2017) Developing a research strategy to better understand, observe, and simulate urban atmospheric processes at kilometer to subkilometer scales. Bul Am Meteorol Soc 98(10):ES261–ES264

Boppana V, Xie ZT, Castro I (2014) Thermal stratification effects on flow over a generic urban canopy. Boundary-Layer Meteorol 153(1):141–162

Castro IP (2017) Are urban-canopy velocity profiles exponential? Boundary-Layer Meteorol 164(3):337–351

Castro IP, Xie ZT, Fuka V, Robins AG, Carpentieri M, Hayden P, Hertwig D, Coceal O (2017) Measurements and computations of flow in an urban street system. Boundary-Layer Meteorol 162(2):207–230

Cheng H, Castro IP (2002) Near wall flow over urban-like roughness. Boundary-Layer Meteorol 104(2):229–259

Cheng H, Hayden P, Robins AG, Castro IP (2007) Flow over cube arrays of different packing densities. J Wind Eng Ind Aerodyn 95(8):715–740

Coceal O, Thomas TG, Castro IP, Belcher SE (2006) Mean flow and turbulence statistics over groups of urban-like cubical obstacles. Boundary-Layer Meteorol 121(3):491–519

Department for Communities and Local Government (2008) English Housing Survey. UK: Department for Communities and Local Government Publications, www.communities.gov.uk

Fernando HJS (2010) Urban atmospheres in complex terrain. Annu Rev Fluid Mech 42:365–89

Ferrari S, Badas MG, Garau M, Seoni A, Querzoli G (2016) The air quality in two-dimensional urban canyons with gable roof buildings: a numerical and laboratory investigation. In: 17th international conference harmonisation within atmospheric dispersion modelling for regulatory purposes, HARMO 2016, vol 2016, Hungarian Meteorological Service, pp 351–356

Fouad NS, Mahmoud GH, Nasr NE (2018) Comparative study of international codes wind loads and CFD results for low rise buildings. Alexandria Eng J 57(4):3623–3639
Fuka V, Xie ZT, Castro IP, Hayden P, Carpentieri M, Robins AG (2018) Scalar fluxes near a tall building in an aligned array of rectangular buildings. Boundary-Layer Meteorol 167(1):53–76
Ginger J, Letchford C (1995) Pressure factors for edge regions on low rise building roofs. J Wind Eng Ind Aerodyn 54:337–344
Grylls T, Suter I, van Reeuwijk M (2020) Steady-state large-eddy simulations of convective and stable urban boundary layers. Boundary-Layer Meteorol 175(3):309–341
Han BS, Park SB, Baik JJ, Park J, Kwak KH (2017) Large-eddy simulation of vortex streets and pollutant dispersion behind high-rise buildings. Q J R Meteorol Soc 143(708):2714–2726
Hanna S, Tehranian S, Carissimo B, Macdonald R, Lohner R (2002) Comparisons of model simulations with observations of mean flow and turbulence within simple obstacle arrays. Atmos Environ 36(32):5067–5079
Hertwig D, Gough HL, Grimmond S, Barlow JF, Kent CW, Lin WE, Robins AG, Hayden P (2019) Wake characteristics of tall buildings in a realistic urban canopy. Boundary-Layer Meteorol 172(2):239–270
Heus T, van Heerwaarden CC, Jonker HJJ, Pier Siebesma A, Axelsen S, van den Dries K, Geoffroy O, Moene AF, Pino D, de Roode SR, Vilà-Guerau de Arellano J (2010) Formulation of the Dutch Atmospheric Large-Eddy Simulation (DALES) and overview of its applications. Geosci Model Dev 3(2):415–444
Holmes J (1994) Wind pressures on tropical housing. J Wind Eng Ind Aerodyn 53(1–2):105–123
Holmes JD (2007) Wind loading of structures. CRC Press, Boca Raton
Inagaki M, Kondoh T, Nagano Y (2005) A mixed-time-scale SGS model with fixed model-parameters for practical LES. J Fluids Eng 127(1):1–13
Kanda I, Yamao Y (2016) Passive scalar diffusion in and above urban-like roughness under weakly stable and unstable thermal stratification conditions. J Wind Eng Ind Aerodyn 148:18–33
Kanda M, Moriwaki R, Kasamatsu F (2004) Large-eddy simulation of turbulent organized structures within and above explicitly resolved cube arrays. Boundary-Layer Meteorol 112(2):343–368
Krč P, Resler J, Sühring M, Schubert S, Salim MH, Fuka V (2020) Radiative transfer model 3.0 integrated into the PALM model system 6.0. Geosci Model Dev 14:3095–3120
Llaguno-Munitxa M, Bou-Zeid E, Hultmark M (2017) The influence of building geometry on street canyon air flow: validation of large eddy simulations against wind tunnel experiments. J Wind Eng Ind Aerodyn 165:115–130
Maronga B, Banzhaf S, Burmeister C, Esch T, Forkel R, Fröhlich D, Fuka V, Gehrke KF, Geletič J, Giersch S, Gronemeier T, Groß G, Heldens W, Hellsten A, Hoffmann F, Inagaki A, Kadasch E, Kanani-Sühring F, Ketelsen K, Khan BA, Knigge C, Knoop H, Krč P, Kurppa M, Maamari H, Matzarakis A, Mauder M, Pallasch M, Pavlik D, Pfafferott J, Resler J, Rissmann S, Russo E, Salim M, Schrempf M, Schwenkel J, Seckmeyer G, Schubert S, Sühring M, von Tils R, Vollmer L, Ward S, Witha B, Wurps H, Zeidler J, Raasch S (2020) Overview of the palm model system 6.0. Geosci Model Dev 13(3):1335–1372
Marucci D, Carpentieri M (2020) Dispersion in an array of buildings in stable and convective atmospheric conditions. Atmos Environ 222(117):100
Marucci D, Carpentieri M, Hayden P (2018) On the simulation of thick non-neutral boundary layers for urban studies in a wind tunnel. Int J Heat Fluid Flow 72:37–51
Nosek Š, Kukačka L, Kellnerová R, Jurčáková K, Jaňour Z (2016) Ventilation processes in a three-dimensional street canyon. Boundary-Layer Meteorol 159(2):259–284
Nosek Š, Kukačka L, Jurčáková K, Kellnerová R, Jaňour Z (2017) Impact of roof height non-uniformity on pollutant transport between a street canyon and intersections. Environ Pollut 227:125–138
Oke TR (1988) Street design and urban canopy layer climate. Energy Build 11(1–3):103–113
Oliveira PJ, Younis BA (2000) On the prediction of turbulent flows around full-scale buildings. J Wind Eng Ind Aerodyn 86(2–3):203–220
Ozmen Y, Baydar E, Van Beeck J (2016) Wind flow over the low-rise building models with gabled roofs having different pitch angles. Build Environ 95:63–74
Placidi M, Ganapathisubramani B (2015) Effects of frontal and plan solidities on aerodynamic parameters and the roughness sublayer in turbulent boundary layers. J Fluid Mech 782:541–566
Placidi M, Ganapathisubramani B (2018) Turbulent flow over large roughness elements: effect of frontal and plan solidity on turbulence statistics and structure. Boundary-Layer Meteorol 167(1):99–121
Reardon GF, Holmes JD (1981) Wind tunnel research on low rise buildings. James Cook University of North Queensland, North Queensland
Sessa V, Xie ZT, Herring S (2018) Turbulence and dispersion below and above the interface of the internal and the external boundary layers. J Wind Eng Ind Aerodyn 182:189–201
Sessa V, Xie ZT, Herring S (2020) Thermal stratification effects on turbulence and dispersion in internal and external boundary layers. Boundary-Layer Meteorol 176(1):61–83

Stoesser T, Mathey F, Frohlich J, Rodi W (2003) LES of flow over multiple cubes. Ercoftac Bull 56:15–19
Suter I, Grylls T, Sützl B, van Reeuwijk M (2021) uDALES 1.0.0: a large-eddy-simulation model for urban environments. Geosci Model Dev Dis: 15:5309–5335
Tomas JM, Pourquie MJBM, Jonker HJJ (2016) Stable stratification effects on flow and pollutant dispersion in boundary layers entering a generic urban environment. Boundary-Layer Meteorol 159(2):221–239
Tomas JM, Eisma HE, Pourquie MJBM, Elsinga GE, Jonker HJJ, Westerweel J (2017) Pollutant dispersion in boundary layers exposed to rural-to-urban transitions: varying the spanwise length scale of the roughness. Boundary-Layer Meteorol 163:225–251
Tominaga Y, Si Akabayashi, Kitahara T, Arinami Y (2015) Air flow around isolated gable-roof buildings with different roof pitches: wind tunnel experiments and CFD simulations. Build Environ 84:204–213
Tsutsumi J, Katayama T, Nishida M (1992) Wind tunnel tests of wind pressure on regularly aligned buildings. J Wind Eng Ind Aerodyn 43(1–3):1799–1810
Vanderwel C, Ganapathisubramani B (2015) Effects of spanwise spacing on large-scale secondary flows in rough-wall turbulent boundary layers. J Fluid Mech 774:R2
Willingham D, Anderson W, Christensen KT, Barros JM (2014) Turbulent boundary layer flow over transverse aerodynamic roughness transitions: induced mixing and flow characterization. Phys Fluids 26(2):025,111
Woodward H, Gallacher D, Robins AG, ApSimon H (2021) A review of the applicability of gaussian modelling techniques to near-field dispersion. In: Publications of the ADMLC, atmospheric dispersion modelling Liaison committee, vol ADMLC-R11, pp 1–79
Xie ZT, Castro IP (2006) LES and RANS for turbulent flow over arrays of wall-mounted obstacles. Flow Turbul Combust 76(3):291
Xie ZT, Castro IP (2008) Efficient generation of inflow conditions for large eddy simulation of street-scale flows. Flow Turbul Combust 81(3):449–470
Xie ZT, Castro IP (2009) Large-eddy simulation for flow and dispersion in urban streets. Atmos Environ 43(13):2174–2185
Xie ZT, Fuka V (2018) A note on spatial averaging and shear stresses within urban canopies. Boundary-Layer Meteorol 167(1):171–179
Xie ZT, Coceal O, Castro IP (2008) Large-eddy simulation of flows over random urban-like obstacles. Boundary-Layer Meteorol 129(1):1–23
Xie ZT, Hayden P, Wood CR (2013) Large-eddy simulation of approaching-flow stratification on dispersion over arrays of buildings. Atmos Environ 71:64–74
Xie ZT, Voke PR, Hayden P, Robins AG (2004) Large-eddy simulation of turbulent flow over a rough surface. Boundary-Layer Meteorol 111(3):417–440
Yassin MF (2011) Impact of height and shape of building roof on air quality in urban street canyons. Atmos Environ 45(29):5220–5229

References

R. J. Adrian and J. Westerweel. *Particle image velocimetry*. Number 30. Cambridge university press, 2011.

R. Antonia and R. Luxton. The response of a turbulent boundary layer to an upstanding step change in surface roughness. 1971a.

R. Antonia and R. Luxton. The response of a turbulent boundary layer to a step change in surface roughness part 1. smooth to rough. *Journal of Fluid Mechanics*, 48 (4):721–761, 1971b.

N. Antoniou, H. Montazeri, H. Wigo, M. K.-A. Neophytou, B. Blocken, and M. Sandberg. Cfd and wind-tunnel analysis of outdoor ventilation in a real compact heterogeneous urban area: Evaluation using "air delay". *Building and Environment*, 126:355–372, 2017.

D. D. Apsley and I. P. Castro. Flow and dispersion over hills: comparison between numerical predictions and experimental data. *Journal of Wind Engineering and Industrial Aerodynamics*, 67:375–386, 1997.

S. Arnold, H. ApSimon, J. Barlow, S. Belcher, M. Bell, J. Boddy, R. Britter, H. Cheng, R. Clark, R. Colvile, et al. Introduction to the dapple air pollution project. *Science of the Total Environment*, 332(1-3):139–153, 2004.

M. G. Badas, S. Ferrari, M. Garau, and G. Querzoli. On the effect of gable roof on natural ventilation in two-dimensional urban canyons. *Journal of Wind Engineering and Industrial Aerodynamics*, 162:24–34, 2017.

A. Bailey and N. Vincent. Wind-pressure on buildings including effects of adjacent buildings. *Journal of the Institution of Civil Engineers*, 20(8):243–275, 1943.

J. Barlow and O. Coceal. A review of urban roughness sublayer turbulence. 2008.

J. Barlow, M. Best, S. I. Bohnenstengel, P. Clark, S. Grimmond, H. Lean, A. Christen, S. Emeis, M. Haeffelin, I. N. Harman, et al. Developing a research strategy to better understand, observe, and simulate urban atmospheric processes at kilometer to subkilometer scales. *Bulletin of the American Meteorological Society*, 98(10): ES261–ES264, 2017a.

J. Barlow, M. Best, S. I. Bohnenstengel, P. Clark, S. Grimmond, H. Lean, A. Christen, S. Emeis, M. Haeffelin, I. N. Harman, et al. Developing a research strategy to better understand, observe, and simulate urban atmospheric processes at kilometer to subkilometer scales. *Bulletin of the American Meteorological Society*, 98(10): ES261–ES264, 2017b.

J. F. Barlow, I. N. Harman, and S. E. Belcher. Scalar fluxes from urban street canyons. part i: Laboratory simulation. *Boundary-Layer Meteorology*, 113(3):369–385, 2004.

J. M. Barros and K. T. Christensen. Observations of turbulent secondary flows in a rough-wall boundary layer. *Journal of Fluid Mechanics*, 748, 2014.

B. Blocken, A. van der Hout, J. Dekker, and O. Weiler. Cfd simulation of wind flow over natural complex terrain: Case study with validation by field measurements for ria de ferrol, galicia, spain. *Journal of Wind Engineering and Industrial Aerodynamics*, 147:43–57, 2015.

V. Boppana, Z.-T. Xie, and I. Castro. Thermal stratification effects on flow over a generic urban canopy. *Boundary-layer meteorology*, 153(1):141–162, 2014.

R. Britter and S. Hanna. Flow and dispersion in urban areas. *Annual review of fluid mechanics*, 35(1):469–496, 2003.

I. P. Castro. Are urban-canopy velocity profiles exponential? *Boundary-Layer Meteorology*, 164(3):337–351, 2017.

I. P. Castro, H. Cheng, and R. Reynolds. Turbulence over urban-type roughness: deductions from wind-tunnel measurements. *Boundary-Layer Meteorology*, 118(1): 109–131, 2006.

I. P. Castro, Z.-T. Xie, V. Fuka, A. G. Robins, M. Carpentieri, P. Hayden, D. Hertwig, and O. Coceal. Measurements and computations of flow in an urban street system. *Boundary-Layer Meteorology*, 162(2):207–230, 2017.

H. Cheng and I. P. Castro. Near wall flow over urban-like roughness. *Boundary-Layer Meteorology*, 104(2):229–259, 2002.

H. Cheng, P. Hayden, A. Robins, and I. Castro. Flow over cube arrays of different packing densities. *Journal of Wind Engineering and Industrial Aerodynamics*, 95(8): 715–740, 2007.

M. Cindori, I. Džijan, F. Juretić, and H. Kozmar. The atmospheric boundary layer above generic hills: computational model of a unidirectional body force-driven flow. *Boundary-Layer Meteorology*, 176(2):159–196, 2020.

M. Coburn, Z.-T. Xie, and C. Vanderwel. Approching city scale flows, 13^{th} uk conference on wind engineering, leeds, uk., received award for *'top young presenter'*, 2018.

M. Coburn, Z.-T. Xie, and C. Vanderwel. Approaching city scale flows using les – an urban aerodynamics case study, UFMSIG conference, surrey, uk., 2019.

M. Coburn, Z.-T. Xie, and C. Vanderwel. Modelling airflow over idealized, semi-realistic suburban and realistic urban areas, UFMSIG conference, 2021.

M. Coburn, Z.-T. Xie, and S. J. Herring. Numerical simulations of boundary-layer airflow over pitched-roof buildings. *Boundary-Layer Meteorology*, 185(3):415–442, 2022.

O. Coceal, T. Thomas, I. Castro, and S. Belcher. Mean flow and turbulence statistics over groups of urban-like cubical obstacles. *Boundary-Layer Meteorology*, 121(3): 491–519, 2006.

E. Comm. *EN 1991-1-4, Eurocode 1: Actions on structures -Part 1-4: General actions -Wind actions*. doi:ICS 91.010.30; 93.040, 2005.

B. Conan, A. Chaudhari, S. Aubrun, J. van Beeck, J. Hämäläinen, and A. Hellsten. Experimental and numerical modelling of flow over complex terrain: the bolund hill. *Boundary-layer meteorology*, 158(2):183–208, 2016.

J. Counihan. An improved method of simulating an atmospheric boundary layer in a wind tunnel. *Atmospheric Environment (1967)*, 3(2):197–214, 1969.

S. J. Daniels, I. P. Castro, and Z.-T. Xie. Peak loading and surface pressure fluctuations of a tall model building. *Journal of wind engineering and industrial aerodynamics*, 120: 19–28, 2013.

Department for Communities and Local Government. *English Housing Survey*. Department for Communities and Local Government Publications, www.communities.gov.uk, 2008.

J. Dudhia. A history of mesoscale model development. *Asia-Pacific Journal of Atmospheric Sciences*, 50(1):121–131, 2014.

V. Efros and P.-Å. Krogstad. Development of a turbulent boundary layer after a step from smooth to rough surface. *Experiments in fluids*, 51(6):1563–1575, 2011.

W. P. Elliott. The growth of the atmospheric internal boundary layer. *Eos, Transactions American Geophysical Union*, 39(6):1048–1054, 1958.

B. En et al. Eurocode 1: Actions on structures—part 1–4: General actions—wind actions. *NA to BS EN, Brussels, Belgium*, 1991.

H. Fernando. Fluid dynamics of urban atmospheres in complex terrain. *Annual review of fluid mechanics*, 42:365–389, 2010.

S. Ferrari, M. G. Badas, M. Garau, A. Seoni, and G. Querzoli. The air quality in two-dimensional urban canyons with gable roof buildings: A numerical and laboratory investigation. In *17th International Conference on Harmonisation within Atmospheric Dispersion Modelling for Regulatory Purposes, HARMO 2016*, volume 2016, pages 351–356. Hungarian Meteorological Service, 2016.

H. E. Fossum and A. Helgeland. Computational fluid dynamics simulations of local wind in large urban areas. 2020.

N. S. Fouad, G. H. Mahmoud, and N. E. Nasr. Comparative study of international codes wind loads and cfd results for low rise buildings. *Alexandria engineering journal*, 57(4):3623–3639, 2018.

V. Fuka, Z.-T. Xie, I. P. Castro, P. Hayden, M. Carpentieri, and A. G. Robins. Scalar fluxes near a tall building in an aligned array of rectangular buildings. *Boundary-layer meteorology*, 167(1):53–76, 2018.

M. Garau, M. G. Badas, S. Ferrari, A. Seoni, and G. Querzoli. Turbulence and air exchange in a two-dimensional urban street canyon between gable roof buildings. *Boundary-Layer Meteorology*, 167(1):123–143, 2018.

J. Garratt. The internal boundary layer—a review. *Boundary-layer meteorology*, 50(1): 171–203, 1990.

A. Georgoulias, D. Papanastasiou, D. Melas, V. Amiridis, and G. Alexandri. Statistical analysis of boundary layer heights in a suburban environment. *Meteorology and Atmospheric Physics*, 104(1):103–111, 2009.

M. Germano, U. Piomelli, P. Moin, and W. H. Cabot. A dynamic subgrid-scale eddy viscosity model. *Physics of Fluids A: Fluid Dynamics*, 3(7):1760–1765, 1991.

J. Ginger and C. Letchford. Pressure factors for edge regions on low rise building roofs. *Journal of wind engineering and industrial aerodynamics*, 54:337–344, 1995.

B. Golding. The uk meteorological office mesoscale model. In *Interactions between Energy Transformations and Atmospheric Phenomena. A Survey of Recent Research*, pages 97–107. Springer, 1987.

E. V. Goulart, N. Reis Jr, V. F. Lavor, I. P. Castro, J. M. Santos, and Z.-T. Xie. Local and non-local effects of building arrangements on pollutant fluxes within the urban canopy. *Building and Environment*, 147:23–34, 2019.

C. Grimmond and T. R. Oke. Aerodynamic properties of urban areas derived from analysis of surface form. *Journal of Applied Meteorology and Climatology*, 38(9): 1262–1292, 1999.

T. Gronemeier, K. Surm, F. Harms, B. Leitl, B. Maronga, and S. Raasch. Validation of the dynamic core of the palm model system 6.0 in urban environments: Les and wind-tunnel experiments. *Geosci Model Develop Discuss*, pages 1–26, 2020.

T. Grylls, I. Suter, and M. van Reeuwijk. Steady-state large-eddy simulations of convective and stable urban boundary layers. *Boundary-Layer Meteorology*, 175(3): 309–341, 2020.

B.-S. Han, S.-B. Park, J.-J. Baik, J. Park, and K.-H. Kwak. Large-eddy simulation of vortex streets and pollutant dispersion behind high-rise buildings. *Quarterly Journal of the Royal Meteorological Society*, 143(708):2714–2726, 2017.

S. Hanna, S. Tehranian, B. Carissimo, R. Macdonald, and R. Lohner. Comparisons of model simulations with observations of mean flow and turbulence within simple obstacle arrays. *Atmospheric Environment*, 36(32):5067–5079, 2002.

I. N. Harman, J. F. Barlow, and S. E. Belcher. Scalar fluxes from urban street canyons part ii: model. *Boundary-Layer Meteorology*, 113(3):387–410, 2004.

D. Hertwig, G. C. Efthimiou, J. G. Bartzis, and B. Leitl. Cfd-rans model validation of turbulent flow in a semi-idealized urban canopy. *Journal of Wind Engineering and Industrial Aerodynamics*, 111:61–72, 2012.

D. Hertwig, L. Soulhac, V. Fuka, T. Auerswald, M. Carpentieri, P. Hayden, A. Robins, Z.-T. Xie, and O. Coceal. Evaluation of fast atmospheric dispersion models in a regular street network. *Environmental Fluid Mechanics*, 18(4):1007–1044, 2018.

D. Hertwig, H. L. Gough, S. Grimmond, J. F. Barlow, C. W. Kent, W. E. Lin, A. G. Robins, and P. Hayden. Wake characteristics of tall buildings in a realistic urban canopy. *Boundary-Layer Meteorology*, 172(2):239–270, 2019.

T. Heus, C. C. van Heerwaarden, H. J. Jonker, A. Pier Siebesma, S. Axelsen, K. Van Den Dries, O. Geoffroy, A. Moene, D. Pino, S. De Roode, et al. Formulation of the dutch atmospheric large-eddy simulation (dales) and overview of its applications. *Geoscientific Model Development*, 3(2):415–444, 2010.

J. D. Holmes. Wind pressures on tropical housing. *Journal of Wind Engineering and Industrial Aerodynamics*, 53(1-2):105–123, 1994.

J. D. Holmes. *Wind loading of structures*. CRC press, 2007.

A. Inagaki, M. Kanda, N. H. Ahmad, A. Yagi, N. Onodera, and T. Aoki. A numerical study of turbulence statistics and the structure of a spatially-developing boundary layer over a realistic urban geometry. *Boundary-Layer Meteorology*, 164(2):161–181, 2017.

M. Inagaki, T. Kondoh, and Y. Nagano. A mixed-time-scale sgs model with fixed model-parameters for practical les. *J. Fluids Eng.*, 127(1):1–13, 2005.

P. Jackson. On the displacement height in the logarithmic velocity profile. *Journal of fluid mechanics*, 111:15–25, 1981.

J. C. Kaimal and J. J. Finnigan. *Atmospheric boundary layer flows: their structure and measurement*. Oxford university press, 1994.

I. Kanda and Y. Yamao. Passive scalar diffusion in and above urban-like roughness under weakly stable and unstable thermal stratification conditions. *Journal of Wind Engineering and Industrial Aerodynamics*, 148:18–33, 2016.

M. Kanda, R. Moriwaki, and F. Kasamatsu. Large-eddy simulation of turbulent organized structures within and above explicitly resolved cube arrays. *Boundary-Layer Meteorology*, 112(2):343–368, 2004.

N. D. Katopodes. *Free-Surface Flow:: Shallow Water Dynamics*. Butterworth-Heinemann, 2018.

P. Krč, J. Resler, M. Sühring, S. Schubert, M. H. Salim, and V. Fuka. Radiative transfer model 3.0 integrated into the palm model system 6.0. *Geoscientific Model Development*, 14(5):3095–3120, 2021.

P.-A. Krogstad. Modification of the van driest damping function to include the effects of surface roughness. *AIAA journal*, 29(6):888–894, 1991.

H. Lim, D. Hertwig, T. Grylls, H. Gough, M. v. Reeuwijk, S. Grimmond, and C. Vanderwel. Pollutant dispersion by tall buildings: Laboratory experiments and large-eddy simulation. *Experiments in Fluids*, 63(6):1–20, 2022.

E. G. Limbrey, J. H. Macdonald, J. Rees, and Z. T. Xie. the clifton suspension bridge site.

Y. Liu, C.-H. Liu, G. P. Brasseur, and C. Y. Chao. Wavelet analysis of the atmospheric flows over real urban morphology. *Science of the Total Environment*, 859:160209, 2023.

M. Llaguno-Munitxa, E. Bou-Zeid, and M. Hultmark. The influence of building geometry on street canyon air flow: validation of large eddy simulations against wind tunnel experiments. *Journal of Wind Engineering and Industrial Aerodynamics*, 165:115–130, 2017.

T. S. Lund, X. Wu, and K. D. Squires. Generation of turbulent inflow data for spatially-developing boundary layer simulations. *Journal of computational physics*, 140(2):233–258, 1998.

B. Maronga, S. Banzhaf, C. Burmeister, T. Esch, R. Forkel, D. Fröhlich, V. Fuka, K. F. Gehrke, J. Geletič, S. Giersch, et al. Overview of the palm model system 6.0. *Geoscientific Model Development*, 13(3):1335–1372, 2020.

D. Marucci and M. Carpentieri. Dispersion in an array of buildings in stable and convective atmospheric conditions. *Atmospheric Environment*, 222:117100, 2020.

D. Marucci, M. Carpentieri, and P. Hayden. On the simulation of thick non-neutral boundary layers for urban studies in a wind tunnel. *International Journal of Heat and Fluid Flow*, 72:37–51, 2018.

Š. Nosek, L. Kukačka, R. Kellnerová, K. Jurčáková, and Z. Jaňour. Ventilation processes in a three-dimensional street canyon. *Boundary-layer meteorology*, 159(2): 259–284, 2016.

Š. Nosek, L. Kukačka, K. Jurčáková, R. Kellnerová, and Z. Jaňour. Impact of roof height non-uniformity on pollutant transport between a street canyon and intersections. *Environmental Pollution*, 227:125–138, 2017.

A. S. of Civil Engineers. Minimum design loads for buildings and other structures. American Society of Civil Engineers, 2013. .

Y. Ohya. Wind-tunnel study of atmospheric stable boundary layers over a rough surface. *Boundary-Layer Meteorology*, 98(1):57–82, 2001.

T. R. Oke. Street design and urban canopy layer climate. *Energy and buildings*, 11(1-3): 103–113, 1988.

T. R. Oke. *Boundary layer climates*. Routledge, 2002.

T. R. Oke, G. Mills, A. Christen, and J. A. Voogt. *Urban climates*. Cambridge University Press, 2017.

P. J. Oliveira and B. A. Younis. On the prediction of turbulent flows around full-scale buildings. *Journal of Wind Engineering and Industrial Aerodynamics*, 86(2-3):203–220, 2000.

Y. Ozmen, E. Baydar, and J. Van Beeck. Wind flow over the low-rise building models with gabled roofs having different pitch angles. *Building and Environment*, 95:63–74, 2016.

A. Pelliccioni, P. Monti, and G. Leuzzi. Wind-speed profile and roughness sublayer depth modelling in urban boundary layers. *Boundary-layer meteorology*, 160(2): 225–248, 2016.

M. Placidi and B. Ganapathisubramani. Effects of frontal and plan solidities on aerodynamic parameters and the roughness sublayer in turbulent boundary layers. *Journal of Fluid Mechanics*, 782:541–566, 2015.

M. Placidi and B. Ganapathisubramani. Turbulent flow over large roughness elements: effect of frontal and plan solidity on turbulence statistics and structure. *Boundary-layer meteorology*, 167(1):99–121, 2018.

E. Plate. Urban climates and urban climate modelling: An introduction. In *Wind climate in cities*, pages 23–39. Springer, 1995.

S. Rafailidis. Influence of building areal density and roof shape on the wind characteristics above a town. *Boundary-layer meteorology*, 85(2):255–271, 1997.

S. Rafailidis and M. Schatzmann. Physical modeling of car exhaust dispersion in urban street canyons—the effect of slanted roofs. In *Air Pollution Modeling and Its Application XI*, pages 653–654. Springer, 1996.

M. R. Raupach, R. A. Antonia, and S. Rajagopalan. Rough-wall turbulent boundary layers. 1991.

G. F. Reardon and J. D. Holmes. *Wind tunnel research on low rise buildings*. Department of Civil and Systems Engineering, James Cook University of North . . . , 1981.

A. Ricci, I. Kalkman, B. Blocken, M. Burlando, and M. Repetto. Impact of turbulence models and roughness height in 3d steady rans simulations of wind flow in an urban environment. *Building and Environment*, 171:106617, 2020.

A. A. Safaei Pirooz and R. G. Flay. Comparison of speed-up over hills derived from wind-tunnel experiments, wind-loading standards, and numerical modelling. *Boundary-Layer Meteorology*, 168(2):213–246, 2018.

V. Sessa, Z.-T. Xie, and S. Herring. Turbulence and dispersion below and above the interface of the internal and the external boundary layers. *Journal of Wind Engineering and Industrial Aerodynamics*, 182:189–201, 2018.

V. Sessa, Z.-T. Xie, and S. Herring. Thermal stratification effects on turbulence and dispersion in internal and external boundary layers. *Boundary-Layer Meteorology*, 176 (1):61–83, 2020.

A. Smits and D. Wood. The response of turbulent boundary layers to sudden perturbations. *Annual Review of Fluid Mechanics*, 17(1):321–358, 1985.

L. Soulhac, R. J. Perkins, and P. Salizzoni. Flow in a street canyon for any external wind direction. *Boundary-Layer Meteorology*, 126(3):365–388, 2008.

T. Stoesser, F. Mathey, J. Frohlich, and W. Rodi. Les of flow over multiple cubes. *Ercoftac Bulletin*, 56:15–19, 2003.

R. B. Stull. *An introduction to boundary layer meteorology*, volume 13. Springer Science & Business Media, 1988.

I. Suter, T. Grylls, B. S. Sützl, S. O. Owens, C. E. Wilson, and M. van Reeuwijk. udales 1.0: a large-eddy simulation model for urban environments. *Geoscientific Model Development*, 15(13):5309–5335, 2022.

P. A. Taylor. Turbulent boundary-layer flow over low and moderate slope hills. *Journal of Wind Engineering and Industrial Aerodynamics*, 74:25–47, 1998.

I. Tolias, N. Koutsourakis, D. Hertwig, G. Efthimiou, A. Venetsanos, and J. Bartzis. Large eddy simulation study on the structure of turbulent flow in a complex city. *Journal of Wind Engineering and Industrial Aerodynamics*, 177:101–116, 2018.

J. Tomas, M. Pourquie, and H. Jonker. Stable stratification effects on flow and pollutant dispersion in boundary layers entering a generic urban environment. *Boundary-Layer Meteorology*, 159(2):221–239, 2016.

J. Tomas, H. Eisma, M. Pourquie, G. Elsinga, H. Jonker, and J. Westerweel. Pollutant dispersion in boundary layers exposed to rural-to-urban transitions: varying the spanwise length scale of the roughness. *Boundary-Layer Meteorology*, 163(2):225–251, 2017.

Y. Tominaga, A. Mochida, T. Shirasawa, R. Yoshie, H. Kataoka, K. Harimoto, and T. Nozu. Cross comparisons of cfd results of wind environment at pedestrian level around a high-rise building and within a building complex. *Journal of Asian architecture and building engineering*, 3(1):63–70, 2004.

Y. Tominaga, S.-i. Akabayashi, T. Kitahara, and Y. Arinami. Air flow around isolated gable-roof buildings with different roof pitches: Wind tunnel experiments and cfd simulations. *Building and Environment*, 84:204–213, 2015.

J. Tsutsumi, T. Katayama, and M. Nishida. Wind tunnel tests of wind pressure on regularly aligned buildings. *Journal of Wind Engineering and Industrial Aerodynamics*, 43(1-3):1799–1810, 1992.

C. Vanderwel and B. Ganapathisubramani. Effects of spanwise spacing on large-scale secondary flows in rough-wall turbulent boundary layers. *Journal of Fluid Mechanics*, 774, 2015.

D. Willingham, W. Anderson, K. T. Christensen, and J. M. Barros. Turbulent boundary layer flow over transverse aerodynamic roughness transitions: induced mixing and flow characterization. *Physics of Fluids*, 26(2):025111, 2014.

D. Wood. The growth of the internal layer following a step change in surface roughness. *Report TN–FM*, 57, 1981.

D. Wood. Internal boundary layer growth following a step change in surface roughness. *Boundary-Layer Meteorology*, 22(2):241–244, 1982.

H. Woodward, D. Gallacher, A. Robins, and H. ApSimon. A review of the applicability of gaussian modelling techniques to near-field dispersion. *Publications of the ADMLC, atmospheric dispersion modelling Liaison committee, vol ADMLC-R11*, pages 1–79, 2021.

Z. Xie and I. P. Castro. Les and rans for turbulent flow over arrays of wall-mounted obstacles. *Flow, Turbulence and Combustion*, 76(3):291–312, 2006.

Z. Xie, P. Hayden, P. R. Voke, and A. G. Robins. Large-eddy simulation of dispersion: comparison between elevated and ground-level sources. *Journal of Turbulence*, 5(1): 031, 2004.

Z.-T. Xie and I. P. Castro. Efficient generation of inflow conditions for large eddy simulation of street-scale flows. *Flow, turbulence and combustion*, 81(3):449–470, 2008.

Z.-T. Xie and I. P. Castro. Large-eddy simulation for flow and dispersion in urban streets. *Atmospheric Environment*, 43(13):2174–2185, 2009.

Z.-T. Xie and V. Fuka. A note on spatial averaging and shear stresses within urban canopies. *Boundary-layer meteorology*, 167(1):171–179, 2018.

Z.-T. Xie, O. Coceal, and I. P. Castro. Large-eddy simulation of flows over random urban-like obstacles. *Boundary-layer meteorology*, 129(1):1–23, 2008.

Z.-T. Xie, P. Hayden, and C. R. Wood. Large-eddy simulation of approaching-flow stratification on dispersion over arrays of buildings. *Atmospheric Environment*, 71: 64–74, 2013.

A. Yakhot, H. Liu, and N. Nikitin. Turbulent flow around a wall-mounted cube: A direct numerical simulation. *International journal of heat and fluid flow*, 27(6): 994–1009, 2006.

J. Yang and W. Anderson. Numerical study of turbulent channel flow over surfaces with variable spanwise heterogeneities: topographically-driven secondary flows affect outer-layer similarity of turbulent length scales. *Flow, Turbulence and Combustion*, 100(1):1–17, 2018.

M. F. Yassin. Impact of height and shape of building roof on air quality in urban street canyons. *Atmospheric Environment*, 45(29):5220–5229, 2011.